



ScuDo

Scuola di Dottorato ~ Doctoral School

WHAT YOU ARE, TAKES YOU FAR



Doctoral Dissertation  
Doctoral Program in Material Science and Technology (31<sup>th</sup> Cycle)

# **Boronizing of Ti6Al4V alloy as a biomaterial with enhanced surface mechanical properties**

**Veronica Peretti**

\*\*\*\*\*

**Supervisors**  
Prof. S. Spriano

Politecnico di Torino  
2018



# Declaration

I hereby declare that, the contents and organisation of this dissertation constitute my own original work and does not compromise in any way the rights of third parties, including those relating to the security of personal data.

Veronica Peretti  
Turin, 2018



# Summary

Total hip arthroplasty (THA) is a widespread treatment for diseases of hip joint. The ever increasing number of THA and young patients who need this kind of surgical treatment has led to the need to improve the lifespan of the hip implants, that is 10-15 years nowadays.

Generally speaking, a THA is composed of a stem and a head that joints with an acetabular cup through an insert. Depending on the used materials the hip implants are classified in metal on polyethylene (MoP), metal on metal (MoM), ceramic on ceramic (CoC) and ceramic on polyethylene (CoP). The first material refers to the one of the head while second to the one of the insert. Both CoC/CoP and MoM couplings allow to reduce the wear rate of the implant, nevertheless other issues are related to these couplings. On one side, ceramic materials are brittle, need a strict proper positioning, have high costs and squeaking can occur under motion. On the other side, MoM coupling is associated to adverse reaction to metal debris and ions release.

Gold standard for THA is MoP coupling, where CoCrMo alloy (or stainless steel) are used for the femoral head and ultrahigh molecular weight polyethylene is employed for the insert. The stem, instead, can be made of Ti6Al4V alloy (cementless prostheses) or stainless steel (cemented prostheses).

Ti6Al4V alloy has high biocompatibility, good mechanical properties and corrosion resistance, nevertheless it has low wear and fretting resistance. For these reasons, it is used for orthopaedic implants in contact with bone, but it is not used where wear and fretting occur (femoral head or cemented stem) and it can be damaged at the head–neck junction (self-interlocking taper connection).

Taking into account all these aspects, the aim of this PhD thesis is to focus on improving the bio-tribological properties of Ti6Al4V by means of a surface modification treatment.

A low cost process of surface ceramic conversion was performed; it consists of a solid pack diffusion process by thermal treatment in a mixture of boriding powders.

The aim is to obtain a titanium borided coating on Ti6Al4V alloy substrate, in order to combine the good lubricant and tribological properties of a ceramic coating with the good mechanical properties of the metallic substrate.

Five different mixtures of boriding powders were compared, but only one allowed to develop an effective coating. Once selected the mixture of boriding powder, the process was performed following several strategies: without any pre/post treatment of the substrate, with a pre-treatment of surface deoxidation, with a pre-treatment of surface oxidation and with a post thermal treatment. Moreover, the effect of temperature and time of treatment was also evaluated.

All the treated samples were characterised in terms of chemical composition, microstructure, structure, coating thickness, hardness, roughness, wettability, coating adhesion and friction coefficient. From this analyses, it was assessed that time and temperature of treatment have mainly effect on thickness, hardness and adhesion of the coating, because of the different boron diffusion rate, and on the microstructure of the substrate, because of the occurrence of different phase transformations. While chemical composition, wettability and friction coefficient are approximately the same for all the conditions tested according to similarity of composition of the external layer of the coating.

According to these results, the samples treated at the highest temperature and for the longest time, without any pre/post treatment, were selected to evaluate wear and fretting behaviour, as well as interaction with physiological fluids.

In both cases, pin on disk/palate tests showed an enhanced tribological behaviour in comparison to reference material such as untreated Ti6Al4V and CoCrMo alloys. It is of relevance the change of wear mechanism of UHMWPE from adhesion (in current used couplings) to abrasion (in contact with the treated Ti6Al4V alloy), the high resistance to wear of the coating when tested on itself (as it could occur at the head-neck junction) and the ability of the treated Ti6Al4V surface to chemically bind PMMA (as it could occur at the stem-cement interface). Moreover, the treated material would be used in contact with biological fluids, thus the treated samples were analysed by means of zeta potential measurement and XPS analyses before and after protein adsorption. The titanium borided coating shows attitude to chemically bind proteins at physiological pH.

This PhD thesis, even if it is not an exhaustive analysis of all the properties of the titanium borided coating, gives good results based on which it is possible to think to a future application of it as biomaterial.

# Acknowledgment

I would especially like to thank my tutor Prpf.Silvia Spriano to have believed in this research, for her help, her support and the possibility to improve my knowledge.

I would like also to acknowledge all the people who have collaborated at this research work, sharing knowledge, skills and facilities.

My special thanks to Dr. Sara Ferraris from the Department of Applied Science and Thecnology of Politecnico di Torino, to Prof. Rossana Bellopede from Dipartimento di Ingegneria dell'Ambiente, del Territorio e delle Infrastrutture of Politecnico di Torino, to Dr. Giovanna Gautier from IMAMOTER (CNR di Torino), to Dr. Alex Lanzutti from Polytechnic Department of Engineering and Architecture of Università di Udine, to Dr. Seiji Yamaguchi from Department of Biomedical Science Center for Clinical Examination Practicum Support Biomedical Sciences of Chubu University, to Prof. Christian Hellmich from Institute for Mechanics of Materials and Structures of Thecnische Universität Wien, to the KMM-VIN and to Dr. Deepak Veeregowda, Miss. Angela Tortora and Mr. Fabio Alemanno from Ducom Instruments.

Thank you to the boys/girls of the "covo": Martina, Cristina, Gianfranco, Stefano, Alessandra e Fabiana, who are not only colleagues but also friend and they have been by my side during this journey. Thank you also all the other colleagues of Glance Group for they support, the laughter and love.

Finally, thank you to Simon, who encourages me to become a better and better person, to Manu, Malu and my parents, who always believe in me.





# Contents

Introduction.....	1
Chapter 1: Hip replacement prostheses and related issues of wear or fretting.....	3
1.1 Hip replacement prostheses.....	3
1.2 Metal on Metal coupling.....	7
1.2.1 Metal on Metal coupling issues.....	7
1.3 Metal on Polyethylene coupling.....	11
1.3.1 Metal on Polyethylene coupling issues.....	12
1.4 Cemented prostheses.....	13
1.4.1 Implant-Cement coupling issues.....	14
1.5 The neck-head interface.....	16
1.5.1 Neck-Head coupling issues.....	16
References.....	19
Chapter 2: Wear and fretting of Titanium and Titanium alloys.....	23
2.1 Introduction to the mechanical properties of Titanium and Titanium alloys.....	23
2.2 Wear mechanism.....	28
2.2.1 Adhesive wear.....	28
2.2.2 Abrasive wear.....	30
2.2.3 Fatigue wear.....	32
2.2.4 Fretting wear and fretting corrosion.....	33
2.3 Surface modification treatments.....	34
2.3.1 Physical vapour deposition.....	35
Beam-line ion implantation.....	35
Plasma immersion ion implantation.....	36
2.3.2 Thermal spray.....	38
Cold spray.....	40

2.3.3 Chemical vapour deposition.....	41
Plasma assisted chemical vapour deposition.....	41
2.3.4 Laser surface modification.....	43
2.3.5 Thermochemical treatments.....	45
Ceramic conversion treatment: oxidation.....	45
Boronizing.....	46
Gas Nitriding.....	51
Carburizing.....	52
2.3.6 Electrochemical treatments.....	54
Anodising.....	54
Plasma electrolytic oxidation treatment.....	55
Electrolytic boronizing.....	57
2.3.7 Duplex surface treatment.....	58
2.4 Commercial coatings for hip prostheses.....	58
References.....	61
Chapter 3: The mechanism of adhesion of proteins and their role in lubrication..	67
3.1 Mechanisms of protein adsorption.....	67
3.2 Serum Albumin.....	70
3.3 Fibronectin.....	72
3.4 Fetal Bovine Serum.....	75
3.5 Synovial fluid and its lubricant effect.....	77
3.5.1 Lubricantsfor in vitro test .....	79
References.....	81
Chapter 4: Experimental .....	85
4.1 Materials.....	85
4.2 Polishing process.....	86
4.2.1 Polishing process of the disks and the rectangles.....	86
4.2.2 Polishing process of the pins.....	86
4.3 Washing process.....	87
4.4 Thermochemical boronizing process.....	87
4.4.1 Surface oxidation pre-treatment.....	88
4.4.2 Surface deoxidation pre-treatment.....	88
4.4.3 Mixtures of powders.....	89
First composition: B – Activated Charcoal – Na <sub>2</sub> B <sub>4</sub> O <sub>7</sub> ... ..	89
Second composition: B <sub>4</sub> C – KBF <sub>4</sub> .....	91
Third composition: B <sub>4</sub> C – SiC – KBF <sub>4</sub> .....	92
Fourth composition: B <sub>4</sub> C – KCl+KBF <sub>4</sub> .....	92
Fifth composition: B <sub>2</sub> O <sub>3</sub> – Activated Charcoal – LiCl+KCl.....	94

4.5 Washing process after the boronizing treatment.....	95
4.6 Samples characterisation.....	95
4.6.1 XRD analysis.....	95
4.6.2 Observation of substrate microstructure and coating morphology and thickness.....	95
4.6.3 Hardness.....	96
4.6.4 Roughness.....	98
4.6.5 Wettability.....	98
4.6.6 Polishing of the coatings.....	98
4.6.7 Scratch test.....	98
4.6.8 Wear test and ICP analysis.....	99
4.6.9 Fretting test.....	90
4.6.10 Protein adsorption.....	101
Zeta potential analysis.....	102
X-ray Photoelectron Spectroscopy.....	103
BCA Protein Assay Kit analysis.....	103
4.6.11 In vitro bioactivity.....	104
References.....	107
Chapter 5: Results and Discussions .....	109
5.1 Overview of the plan of the experiments.....	109
5.2 Comparison of Ti6Al4V alloy grade 5 and ELI.....	111
5.3 Characterization of the Ti6Al4V alloy grade 5 samples treated with the first composition of powder mixture (50%wt B – 35%wt Activated Charcoal – 15%wt Na <sub>2</sub> B <sub>4</sub> O <sub>7</sub> ).....	112
5.3.1 XRD analysis.....	113
5.3.2 Substrate microstructure.....	120
5.3.3 Coating morphology and thickness.....	122
5.3.4 Coating hardness.....	127
5.3.5 Roughness .....	139
5.3.6 Wettability.....	144
5.3.7 Friction coefficients and scratch resistance derived from scratch tests	147
5.3.8 Wear tests (soft on hard and hard on hard condition).....	158
Friction coefficient.....	158
Wear resistance.....	163
Wear mechanisms.....	166
ICP analysis and ion release evaluation.....	177
5.3.9 Fretting tests.....	179
Friction coefficients.....	179

Wear mechanism.....	181
Wear resistance.....	188
5.3.10 Summary of titanium borided coatings properties.....	192
5.3.11 Protein adsorption evaluation.....	192
Zeta potential analysis: before protein adsorption.....	193
Zeta potential analysis: after BSA adsorption.....	197
Zeta potential analysis: after FN adsorption.....	202
Zeta potential analysis: after FBS adsorption.....	204
XPS analyses: survey analysis.....	207
XPS analyses: high resolution analysis of surfaces before protein adsorption .....	211
XPS analyses: high resolution analysis of surfaces after BSA adsorption .....	214
XPS analyses: high resolution analysis of surfaces after FN adsorption .....	216
XPS analyses: high resolution analysis of surfaces after FBS adsorption .....	218
XPS analyses: high resolution analysis of boron region.....	220
BCA Protein Assay Kit analysis.....	222
5.3.12 In vitro bioactivity evaluation.....	223
5.4 Analysis of further mixtures of powders.....	225
5.4.1 Characterization of the Ti6Al4V alloy grade 5 samples treated with the second composition of powder mixture (90%wt B <sub>4</sub> C – 10%wt KBF <sub>4</sub> ) .....	225
5.4.3 Characterization of the Ti6Al4V alloy grade 5 samples treated with the fourth composition of powder mixture (5%wt B <sub>4</sub> C – 95%wt KCl+KBF <sub>4</sub> ) .....	227
5.4.4 Characterization of the Ti6Al4V alloy grade 5 samples treated with the fifth composition of powder mixture (30%wt B <sub>2</sub> O <sub>3</sub> – 35%wt Activated Charcoal – 35%wt LiCl+KCl).....	228
References.....	231
Chapter 6: Conclusions and future trends.....	235

# List of Tables

- Table 1.1 Possible coupling for hip joint implant
- Table 1.2. Chemical composition of the native oxide layer of material after polishing in deionized water and of oxide layer of material after biological fluid exposition
- Table 1.3. Sterilisation methods
- Table 1.4 Cement generations
- Table 2.1 Properties of titanium and titanium alloys
- Table 2.2 Surface modification treatments and developed coatings
- Table 2.3 Possible heat source for thermal spray and their parameters
- Table 2.4 Thickness of borided coatings
- Table 2.5 Commercial powder composition for boronizing
- Table 2.6 Common salts bath composition for electroless liquid boronizing
- Table 2.7 Temperature and time of treatment and thickness and hardness of the nitride coatings in function of the process
- Table 2.8 Temperature and time of treatment and thickness and hardness of the nitride coatings in function of the process
- Table 2.9 Comparison between PEO process and conventional anodizing
- Table 2.10 Comparison between pack boronizing and electrolytic boronizing
- Table 3.1 Constituents of Serum and differences between human serum and bovine serum
- Table 4.1 Polishing protocol for the disks and the rectangles
- Table 4.2 Polishing protocol for the pins
- Table 4.3 Type of samples and process parameters
- Table 4.4 Polishing protocol
- Table 4.5 Materials and conditions of the wear test
- Table 4.6 Dilution scheme for standard test tube protocol

- Table 5.1 Summary of powder composition and characterizations
- Table 5.2 Average values of coatings thickness of the samples treated at 800°C and 750°C with pre-treatment of deoxidation
- Table 5.3 Knoop (HK) and Vickers Hardness (HV) of the treated samples
- Table 5.4 Average values of hardness, elastic modulus and contact depth
- Table 5.5 Roughness
- Table 5.6 Average values of hardness, elastic modulus and contact depth
- Table 5.7 Roughness of the treated samples without any pre/post treatment and with pre-treatment of deoxidation
- Table 5.8 Contact angles of the treated samples
- Table 5.9 The contact angles of CoCrMo alloy and alumina
- Table 5.10 Weight of the pins and disks before and after the wear tests of the untreated Ti6AL4V alloy
- Table 5.11 Weight of the pins and disks before and after the wear tests of the CoCrMo alloy
- Table 5.12 Weight of the pins and disks before and after the wear tests of the treated Ti6Al4V alloy without any pre/post treatment
- Table 5.13 Weight of the pins and disks before and after the wear tests of the treated Ti6Al4V alloy with pre-treatment of deoxidation
- Table 5.14 Weight of the pins and disks before and after the wear test of a treated Ti6Al4V alloy with post treatment
- Table 5.15 Average values of Ra for the cement plate and the AISI 316L, untreated and treated Ti6AL4V alloy pins before the fretting test
- Table 5.16 Average values of Ra and weight of the cement plate and the untreated Ti6AL4V alloy pins
- Table 5.17 Average values of Ra and weight of the cement plate and the AISI 316L pins
- Table 5.18 Average values of Ra and weight of the cement plate and the treated Ti6Al4V alloy pins
- Table 5.19 Characteristics of the borided coatings
- Table 5.20 Summary of material surface characteristic
- Table 5.21 IEP of the materials after BSA adsorption, dissolving the protein once in PBS and once in double distilled water
- Table 5.22 Atomic % from the survey analyses
- Table 5.23 N/Metal and N/C ratios
- Table 5.24 Width at the half height of the signals before protein adsorption
- Table 5.25 Width at the half height of the signals after BSA adsorption
- Table 5.26 Width at the half height of the signals after FN adsorption

- Table 5.27 Width at the half height of the signals after FBS adsorption
- Table 5.28 pH values of SBF
- Table 6.1 Characteristics of the boride coating and commercial coatings





# List of Figures

- Figure 1.1 Anatomy of hip joint
- Figure 1.2 Total Hip Arthroplasty (a) partial hip replacement (b) hip resurfacing (c)
- Figure 1.3 Currently used soft and hard material couplings
- Figure 1.4 Wear rate per years of different kinds of material coupling
- Figure 1.5 Photographs of the completed worn polymeric insert and metal cup by the metal head
- Figure 1.6 Mechanism of ion release
- Figure 1.7 Titanium alloy stem with fretting marks
- Figure 1.8 optical micrograph of a) a damaged titanium alloy stem b) cement counterface
- Figure 1.9 a) fretting marks on CoCr alloy head combined with Ti alloy taper b) CoCr alloy head dislocated from the Ti alloy neck
- Figure 2.1 Titanium crystal structures
- Figure 2.2 Classification of titanium alloys in a three-dimensional phase diagram
- Figure 2.3 Ternary phase diagram
- Figure 2.4 Microstructure of Ti6Al4V alloy a) furnace cooling and b) water quenching from 1050°C
- Figure 2.5 Microstructure of Ti6Al4V alloy a) furnace cooling and b) water quenching from 800°C
- Figure 2.6 Microstructure of  $\alpha$  and  $\omega$  phase
- Figure 2.7 Microstructure of Ti6Al4V alloy a) furnace cooling and b) water quenching from 600°C
- Figure 2.8 Microstructure of Ti6Al4V alloy a) fine equiaxed, b) coarse equiaxed and c) bimodal
- Figure 2.9 Adhesive wear mechanism
- Figure 2.10 Wear tracks of Ti6AL4V disk after unidirectional sliding against a WC ball slider in air. r points out the adhesive spots, while p the grooves due to the ploughing
- Figure 2.11 Two body and here body abrasive wear mechanism
- Figure 2.12 Softer surface ploughed by a hard conical asperity

- Figure 2.13 Summary of the factors acting on the fatigue strength
- Figure 2.14 Fretting of the surface of a modular hip component
- Figure 2.15 Equipment for ion implantation
- Figure 2.16 Breakthrough load of Ti and Ti6Al4V after C<sup>+</sup> and N<sup>+</sup> implantation tested against a ruby ball
- Figure 2.17 PIII process
- Figure 2.18 Hardness of Ti6Al4V subjected to nitrogen PIII at a bias voltage of 20 kV for different treatment times
- Figure 2.19 Thermal spray process
- Figure 2.20 Cold spray process
- Figure 2.21 PA CVD process
- Figure 2.22 wear volume in a) dry and b) lubricated condition after 3000 cycles
- Figure 2.23 Number of cycles before the DLC failure
- Figure 2.24 Laser nitriding process
- Figure 2.25 Trend of the friction coefficient of a) untreated titanium, b) nitride titanium by melting of a pre-deposited TiN powder layer, c) nitride titanium by gas nitriding and c) nitride titanium by mix process
- Figure 2.26 Ti-B phase diagram
- Figure 2.27 Self-diffusion of titanium in  $\alpha$  and  $\beta$  phases
- Figure 2.28 Ti-N phase diagram
- Figure 2.29 Pack carburizing vessel
- Figure 2.30 Dental screws with different thickness of the TiO<sub>2</sub> layer
- Figure 2.31 PEO process
- Figure 3.1 Molecular (a) and dissociative (b) adsorption of water on Titanium surface
- Figure 3.2 Vroman Effect: Protein A is adsorbed and over the time protein A increases the contact surface between protein and surface. This causes an increase of the free energy of the system. The gained energy is spent to desorb protein B, through the break of focal contact between protein B and surface
- Figure 3.3 Subdomain A and B of HAS
- Figure 3.4 (a) Titanium oxide surface (b) interaction between Titanium oxide surface and proteins (c) interaction between proteins and cells
- Figure 3.5 Modular structure of a FN domain, composed by repetition of modules F1, F2 and F3
- Figure 3.6 Interaction between RGD sequence of protein and integrins of cell
- Figure 3.7 Different orientation of FN in function of surface charge. (a) end-orientation on positive surface (b) side-orientation on negative surface
- Figure 3.8 Interaction between proteins and surface and between cells and proteins on different types of TiO<sub>2</sub> surfaces
- Figure 3.9 UHMWPE wear rate in function of protein and lipid concentrations

- Figure 4.1 Shape and dimensions of pins for a) wear tests and b) fretting tests
- Figure 4.2 Samples after polishing: a) Ti6Al4V alloy grade 5, b) Ti6Al4V alloy ELI, c) CoCrMo alloy and d) Alumina.
- Figure 4.3 Pin a) Ti6Al4V alloy grade 5 and b) CoCrMo alloy
- Figure 4.4 Different strategies for the thermal boronizing treatment
- Figure 4.5 The treated samples a) without any pre/post treatment, b) with pre-treatment of oxidation, c) with pre-treatment of deoxidation and d) subjected to post thermal treatment.
- Figure 4.6 The sample treated with the second composition of powder mixture
- Figure 4.7 The sample treated with the third composition of powder mixture at a) 800°C and b) 700°C.
- Figure 4.8 a)  $\text{KBF}_4 - \text{KF}$  phase diagram [13] and b)  $\text{KBF}_4 - \text{KCl}$  phase diagram
- Figure 4.9 The sample treated with the fourth composition of powder mixture
- Figure 4.10  $\text{LiCl} - \text{KCl}$  phase diagram [16]
- Figure 4.11 The sample treated with the fifth composition of powder mixture at a) 400°C and b) 500°C.
- Figure 4.12 a) AISI 316L, b) treated Ti6Al4V alloy without any pre/post treatment and c) untreated Ti6Al4V alloy pins for fretting test
- Figure 4.13 Bone cement plates for fretting test
- Figure 5.1 Different treatment process carried out on the samples: a) sample treated without any pre/post treatment, b) sample treated with pre-treatment of deoxidation, c) sample treated with pre-treatment of oxidation and d) sample subjected to post thermal treatment
- Figure 5.2 Bragg-Brentano spectra of the untreated Ti6Al4V alloy grade 5 and ELI
- Figure 5.3 Picture of the a) untreated and b) sample without any pre/post treatment treated at 1050°C for 4.5 h.
- Figure 5.4 XRD patterns collected with Bragg-Brentano geometry and grazing angle at 1° and 3° of samples without any pre/post treatment treated at 1050°C for 4.5 h
- Figure 5.5 XRD patterns collected with Bragg-Brentano geometry of samples treated at 1050°C for 4.5 h without any pre/post treatment and subjected to the post thermal treatment
- Figure 5.6 XRD patterns collected with 1° grazing angle measurement of samples treated at 1050°C for 4.5 h without any pre/post treatment and subjected to the post thermal treatment
- Figure 5.7 XRD patterns collected with Bragg-Brentano geometry of the samples treated at different temperatures for 4.5 h
- Figure 5.8 XRD patterns collected with 1° grazing angle measurement of the samples treated at different temperatures for 4.5 h

- Figure 5.9 XRD patterns collected with Bragg-Brentano geometry of the treated samples without any pre/post treatment
- Figure 5.10 XRD patterns collected with Bragg-Brentano geometry of the treated samples with pre-treatment of deoxidation
- Figure 5.11 XRD patterns collected with Bragg-Brentano geometry of the samples treated at 800°C for 4.5 h and 3.5 h
- Figure 5.12 XRD patterns collected with 1° grazing angle measurement of the samples treated at 800°C for 4.5 h and 3.5 h
- Figure 5.13 XRD patterns collected with Bragg-Brentano geometry of the samples treated at 750°C for 4.5 h, 3.5 h and 2.5 h
- Figure 5.14 XRD patterns collected with 1° grazing angle measurement of the samples treated at 750°C for 4.5 h, 3.5 h and 2.5 h
- Figure 5.15 Bragg-Brentano spectra of the samples treated at 800°C for 3.5 h without any pre/post treatment or pre-treatment of oxidation
- Figure 5.16 Optical microscope image of the cross section of the untreated sample
- Figure 5.17 Optical microscope images of the cross section of the samples without any pre/post treatment treated at a) 1050°C b) 900°C c) 800°C and d) 750°C
- Figure 5.18 Optical microscope images of the cross section of the samples without any pre/post treatment treated at 800°C for a) 4.5 h and b) 3.5 h
- Figure 5.19 Optical microscope images of the cross section of the samples without any pre/post treatment treated at 750°C for a) 4.5 h, b) 3.5 h and c) 2.5 h
- Figure 5.20 Cross-sectional FESEM micrographs of the samples without any pre/post treatment treated at a) 1050°C, b) 900°C, c) 800°C, d) 750°C and of the samples with pre-treatment of deoxidation treated at e) 1050°C f) 900°C, g) 800°C and h) 750°C
- Figure 5.21 Thickness of the samples treated at different temperature for 4.5 without any pre/post treatment and with pre-treatment of deoxidation
- Figure 5.22 Cross-sections FESEM micrographs of a) the sample treated at 800°C for 4.5 h without any pre/post treatment, b) the sample treated at 800°C for 3.5 h without any pre/post treatment, c) the sample treated at 800°C for 4.5 h with pre-treatment of deoxidation and d) the sample treated at 800°C for 3.5 h with pre-treatment of deoxidation
- Figure 5.23 Cross-section FESEM micrographs of a) the sample treated at 750°C for 4.5 h without any pre/post treatment, b) the sample treated at 750°C for 3.5 h without any pre/post treatment, c) the sample treated at 750°C for 2.5 h without any pre/post treatment, d) the sample treated at 750°C for 4.5 h with pre-treatment of deoxidation, e) the sample treated at 750°C for 3.5 h with pre-treatment of deoxidation and f) the sample treated at 750°C for 2.5 h with pre-treatment of deoxidation
- Figure 5.24 Thickness of the samples treated at 800°C and 750°C for different time of treatment without any pre-post treatment and with pre-treatment of deoxidation
- Figure 5.25 Cross-section FESEM micrographs of a) the sample treated at 1050°C for 4.5 h without any pre/post treatment and b) the sample treated

at 1050°C for 4.5 h and subjected to the post thermal treatment at 1050°C for 4.5 h

- Figure 5.26 Thickness of samples treated at 1050°C for 4.5 h without any pre/post treatment, with pre-treatment of deoxidation and subjected to the post thermal treatment
- Figure 5.27 Cross-section FESEM micrographs of the samples treated at 800°C for 3.5 h a) without any pre/post treatment and b) with pre-treatment of deoxidation
- Figure 5.28 Thickness of samples treated at 800°C for 3.5 h without any pre/post treatment, with pre-treatment of deoxidation and with pre-treatment of oxidation
- Figure 5.29 Vickers microindentations: hardness of the samples without any pre/post treatment treated at different temperatures for 4.5 h
- Figure 5.30 Vickers microindentations: hardness of the samples without any pre/post treatment treated for different times
- Figure 5.31 Comparison between the coating thickness and theoretical values
- Figure 5.32 Comparison between the coating thickness and theoretical values
- Figure 5.33 Knoop microindentations: hardness of the samples without any pre/post treatment and with pre-treatment of deoxidation treated at different temperatures for 4.5
- Figure 5.34 Knoop microindentations: hardness of the samples without any pre/post treatment and with pre-treatment of deoxidation treated for different times
- Figure 5.35 Knoop microindentations: hardness of the sample without any pre/post treatment and the sample subjected to the post thermal treatment
- Figure 5.36 Knoop microindentations: hardness of the samples without any pre/post treatment and with pre-treatment of deoxidation
- Figure 5.37 Displacement control: load vs penetration depth curves
- Figures 5.38 a) Hardness vs contact depth and b) elastic modulus vs contact depth
- Figure 5.39 Load control: load vs penetration depth curves
- Figures 5.40 a) Hardness vs contact depth and b) elastic modulus vs contact depth
- Figure 5.41 Hardness vs contact depth
- Figure 5.42 Elastic modulus vs contact depth.
- Figure 5.43 Surface profile scanning of a) unpolished surface and b) polished surface of a samples treated at 800°C for 3.5 h
- Figure 5.44 Surface profile scanning a) before and b) after the nanoindentation test (sample treated at 800°C for 3.5 h without any pre/post treatment)
- Figure 5.45 Load control: load vs penetration depth curves
- Figures 5.46 a) Hardness vs contact depth and b) elastic modulus vs contact depth

- Figure 5.47 Hardness vs contact depth
- Figure 5.48 Elastic Modulus vs contact depth
- Figure 5.49 Load control: load vs penetration depth curves
- Figures 5.50 a) Hardness vs contact depth and b) elastic modulus vs contact depth
- Figures 5.51 Roughness of the samples without any pre/post treatment and with pre-treatment of deoxidation treated at different temperatures for 4.5
- Figures 5.52 Roughness of the samples without any pre/post treatment and with pre-treatment of deoxidation treated for different times
- Figures 5.53 Roughness of a) the samples without any pre/post treatment and subjected to the post thermal treatment and b) the samples without any pre/post treatment and with pre-treatment of oxidation
- Figure 5.54 Comparison between roughness and coating thickness
- Figure 5.55 Surface roughness of the a) untreated sample, b) the sample treated at 750°C for 4.5 h and c) the sample treated at 1050°C for 4.5 h without any pre/post treatment
- Figure 5.56 Comparison between the roughness of the unpolished samples and the polished samples with a) diamond pasts (3+1 $\mu$ m) and b) diamond suspensions (3+1 $\mu$ m) ((a) samples treated at 1050°C for 3.5 h and (b) 800°C for 3.5 h both without any pre/post treatment)
- Figure 5.57 a) Sample treated at 750°C for 2.5h after being polished with diamond pasts of 3 and 1  $\mu$ m and b) optical microscope image of an area of the sample surface
- Figure 5.58 a) Sample treated at 800°C for 3.5h after being polished with diamond suspensions of 3 and 1  $\mu$ m and b) optical microscope image of an area of the sample
- Figures 5.59 Contact angles of the samples without any pre/post treatment and with pre-treatment of deoxidation treated at different temperature for 4.5 h
- Figure 5.60 Contact angles of the samples without any pre/post treatment and with pre-treatment of deoxidation treated for different time
- Figure 5.61 Contact angles of a) the samples without any pre/post treatment and subjected to the post thermal treatment and b) the samples without any pre/post treatment and pre-treatment of oxidation
- Figure 5.62 Comparison between the contact angles and roughness of the treated samples
- Figure 5.63 Comparison among the contact angles of the reference materials and the average value of the treated ones.
- Figure 5.64 COFs and AEs of the reference materials
- Figure 5.65 COFs and AEs of the Ti6Al4V alloy samples without any pre/post treatment treated at different temperatures for 4.5 h
- Figure 5.66 COFs and AEs of the Ti6Al4V alloy samples with pre-treatment of deoxidation treated at different temperatures for 4.5 h
- Figure 5.67 Thickness, roughness and detachment load of samples without any pre/post treatment and with pre-treatment of deoxidation treated for 4.5 h at different temperatures

- Figure 5.68 COFs and AEs of the Ti6Al4V alloy samples without any pre/post treatment treated at 800°C and 750°C for different times
- Figure 5.69 COFs and AEs of the Ti6Al4V alloy samples with pre-treatment of deoxidation treated at 800°C and 750°C for different times
- Figure 5.70 Thickness, roughness and detachment load of the samples without any pre/post treatment and with pre-treatment of deoxidation treated at 800°C and 750°C for different times
- Figure 5.71 COFs and AEs of the sample with pre-treatment of oxidation treated at 800°C for 3.5 h and of the sample subjected to the post thermal treatment<sup>5</sup>
- Figure 5.72 Normal displacement vs time
- Figure 5.73 FESEM images and EDS analyses of samples treated at 1050°C for 4.5 a) without any pre/post treatment, b) with pre-treatment of deoxidation and c) subjected to post thermal treatment
- Figure 5.74 COF of the untreated Ti6Al4V alloy in hard on hard and soft on hard conditions
- Figure 5.75 COF of the CoCrMo alloy in hard on hard and soft on hard conditions
- Figure 5.76 COF of the treated Ti6Al4V alloy without any pre/post treatment in hard on hard and soft on hard conditions
- Figure 5.77 COF of the treated Ti6Al4V alloy with pre-treatment of deoxidation in hard on hard and soft on hard conditions
- Figure 5.78 COF of the treated Ti6Al4V alloy subjected to the post thermal treatment in hard on hard and soft on hard conditions
- Figure 5.79 Comparison of COFs
- Figure 5.80 Average roughness and COF of the disk of the treated samples in soft on hard contact before the test
- Figure 5.81 Average roughness and COF of the pin and disk of the treated samples in hard on hard contact before the test
- Figure 5.82 Linear wear of the untreated Ti6Al4V alloy in hard on hard and soft on hard conditions
- Figure 5.83 Linear wear of the CoCrMo alloy in hard on hard and soft on hard conditions
- Figure 5.84 Linear wear of the treated Ti6Al4V alloy without any pre/post treatment in hard on hard and soft on hard conditions
- Figure 5.85 Linear wear of the treated Ti6Al4V alloy with pre-treatment of deoxidation in hard on hard and soft on hard conditions
- Figure 5.86 Linear wear of the treated Ti6Al4V alloy subjected to the post thermal treatment in hard on hard and soft on hard conditions
- Figure 5.87 Comparison of linear wear rates
- Figure 5.88 Pins and disks of a) soft on hard and b) hard on hard test of the untreated Ti6Al4V alloy
- Figure 5.89 Optical micrographs of the pins and disks surfaces in a) soft on hard and b) hard on hard contact of the untreated Ti6Al4V alloy

- Figure 5.90 SEM images and EDS analyses of the UHMWPE pin surface tested against the untreated Ti6Al4V alloy disk
- Figure 5.91 Pins and disks of a) soft on hard and b) hard on hard test of the CoCrMo alloy
- Figure 5.92 Optical micrographs of the pins and disks surfaces in a) soft on hard and b) hard on hard contact of the CoCrMo alloy
- Figure 5.93 SEM images and EDS analyses of the UHMWPE pin surface tested against the CoCrMo alloy disk
- Figure 5.94 Pins and disks of a) soft on hard and b) hard on hard test of the treated Ti6Al4V alloy without any pre/post treatment
- Figure 5.95 Optical micrographs of the pins and disks surfaces in a) soft on hard and b) hard on hard contact of the treated Ti6Al4V alloy without any pre/post treatment
- Figure 5.96 SEM images and EDS analysis of the pins and disks surfaces in a) soft on hard condition and b) hard on hard condition of the treated Ti6Al4V alloy without any pre/post treatment
- Figure 5.97 Pins and disks of a) soft on hard and b) hard on hard test of the treated Ti6Al4V alloy with pre-treatment of deoxidation
- Figure 5.98 Optical micrographs of the pins and disks surfaces in a) soft on hard and b) hard on hard contact
- Figure 5.99 SEM images and EDS analysis of the pins and disks surfaces in a) soft on hard condition and b) hard on hard condition of the treated Ti6Al4V alloy with pre-treatment of deoxidation
- Figure 5.100 Pins and disks of a) soft on hard and b) hard on hard test of the treated Ti6Al4V alloy subjected to post thermal treatment
- Figure 5.101 Optical micrographs of the pins and disks surfaces in a) soft on hard and b) hard on hard contact of the treated Ti6Al4V alloy subjected to post thermal treatment
- Figure 5.102 SEM images and EDS analysis of the pins and disks surfaces in a) soft on hard condition and b) hard on hard condition of the Ti6Al4V alloy subjected to the post thermal treatment
- Figure 5.103 Roughness of pins and disks surface in soft on hard contact
- Figure 5.104 Roughness of pins and disks surface in hard on hard contact
- Figure 5.105 Metallic ion release of the untreated Ti6Al4V alloy and the three cases of treated Ti6Al4V alloy tested under hard on hard and soft on hard wear condition
- Figure 5.106 COFs of the untreated Ti6Al4V alloy, AISI 316L and Ti6Al4V alloy without any pre/post treatment treated at 1050°C for 4.5 h
- Figure 5.107 COFs of the untreated Ti6Al4V alloy, AISI 316L and Ti6Al4V alloy without any pre/post treatment treated at 1050°C for 4.5 h after median filter
- Figure 5.108 Comparison between COFs and roughness of the untreated Ti6Al4V alloy, AISI 316L and Ti6Al4V alloy without any pre/post treatment treated at 1050°C
- Figure 5.109 Untreated Ti6Al4V alloy pin and PMMA plate



- Figure 5.110 SEM images and EDS analyses of untreated Ti6Al4V pin and PMMA plate
- Figure 5.111 AISI 316L pin and PMMA plate after the fretting test
- Figure 5.112 SEM images and EDS analyses of AISI 316L pin and PMMA plate after the fretting test
- Figure 5.113 treated Ti6Al4V alloy pin and PMMA plate after the fretting test
- Figure 5.114 SEM images and EDS analyses of treated Ti6Al4V alloy pin and PMMA plate after the fretting test
- Figure 5.115 Profilometric images of cement plate a) before the fretting test, b) after the fretting test against AISI 316L pin, c) after the fretting test against untreated Ti6Al4V alloy pin and d) after the fretting test against treated Ti6Al4V alloy pin
- Figure 5.116 Profilometric images of AISI 316L pin a) before the fretting test and b) after the fretting test; untreated Ti6Al4V alloy pin c) before the fretting test and d) after the fretting test; treated Ti6Al4V alloy pin e) before the fretting test and f) after the fretting test
- Figure 5.117 Wear rate of AISI 316L pin, untreated Ti6Al4V alloy pin and treated Ti6Al4V alloy pin
- Figure 5.118 Zeta potential curves before protein adsorption
- Figure 5.119 Charge at the solid-liquid interface for hydrophobic materials
- Figure 5.120 Charge at the solid-liquid interface for hydrophilic materials
- Figure 5.121 Comparison of the zeta potential curves before protein adsorption
- Figure 5.122 Comparison of the zeta potential curves before and after BSA adsorption
- Figure 5.123 Comparison of the zeta potential curves of materials after protein adsorption and pure BSA
- Figure 5.124 Outline of the BSA in solution
- Figure 5.125 a) secondary structure, b) spatial surface potential distribution (red: negative potential and blue: positive potential) and c) hydrophilic/hydrophobic regions (green: hydrophilic and white: hydrophobic) [19]
- Figure 5.126 Interaction between the BSA and hydrophobic/hydrophilic surfaces
- Figure 5.127 Comparison of the zeta potential curves before and after FN adsorption
- Figure 5.128 Comparison of the zeta potential curves of materials after protein adsorption and FN in PBS solution
- Figure 5.129 Comparison of the zeta potential curves before and after FBS adsorption
- Figure 5.130 Comparison of the zeta potential curves of materials after protein adsorption and FBS.
- Figure 5.131 Comparison of the zeta potential curves of materials after BSA and FBS adsorption

- Figure 5.132 Comparison of the zeta potential curves of pure BSA and FBS in solution
- Figure 5.133 Carbon region of the a) untreated Ti6Al4V alloy, b) CoCrMo alloy, c) alumina and d) treated Ti6Al4V alloy before protein adsorption
- Figure 5.134 Oxygen region of the a) untreated Ti6Al4V alloy, b) CoCrMo alloy, c) alumina and d) treated Ti6Al4V alloy before protein adsorption
- Figure 5.135 Nitrogen region of the treated Ti6Al4V alloy before protein adsorption
- Figure 5.136 Titanium region of the a) untreated and b) treated Ti6Al4V alloy before protein adsorption
- Figure 5.137 Carbon region of the a) untreated Ti6Al4V alloy, b) CoCrMo alloy, c) alumina and d) treated Ti6Al4V alloy after BSA adsorption
- Figure 5.138 Nitrogen region of the a) untreated Ti6Al4V alloy, b) CoCrMo alloy, c) alumina and d) treated Ti6Al4V alloy after BSA adsorption
- Figure 5.139 Oxygen region of the a) untreated Ti6Al4V alloy, b) CoCrMo alloy, c) alumina and d) treated Ti6Al4V alloy after BSA adsorption
- Figure 5.140 Carbon region of the a) untreated and b) treated Ti6Al4V alloy after FN adsorption
- Figure 5.141 Nitrogen region of the a) untreated and b) treated Ti6Al4V alloy after FN adsorption
- Figure 5.142 Oxygen region of the a) untreated and b) treated Ti6Al4V alloy after FN adsorption
- Figure 5.143 Carbon region of the a) untreated Ti6Al4V alloy, b) CoCrMo alloy, c) alumina and d) treated Ti6Al4V alloy after FBS adsorption
- Figure 5.144 Nitrogen region of the a) untreated Ti6Al4V alloy, b) CoCrMo alloy, c) alumina and d) treated Ti6Al4V alloy after FBS adsorption
- Figure 5.145 Oxygen region of the a) untreated Ti6Al4V alloy, b) CoCrMo alloy, c) alumina and d) treated Ti6Al4V alloy after FBS adsorption
- Figure 5.146 Boron region of the treated Ti6Al4V alloy a) before protein adsorption b) after BSA adsorption, c) FN adsorption and d) FBS adsorption
- Figure 5.147 Scheme of the titanium borided coating for the samples without any pre/post treatment
- Figure 5.148 a) Standards and b) samples
- Figure 5.149 Standard curve and concentration of untreated and Treated Ti6Al4V alloy
- Figure 5.150 FESEM images and EDS analyses of the surface of a Ti6Al4V alloy sample without any pre/post treatment treated at 1050°C for 4.5 h and soaked in SBF for 14 days
- Figure 5.151 FESEM images and EDS analyses of the surface of a Ti6Al4V alloy sample without any pre/post treatment treated at 1050°C for 4.5 h and soaked in SBF for 28 days.
- Figure 5.152 Picture of a) untreated sample and b) treated sample
- Figure 5.153 XRD patterns collected with Bragg-Brentano geometry on a sample treated at 800°C for 3.5 h

- Figure 5.154 Picture of a) untreated sample, b) sample treated at 800°C for 3.5h and c) samples treated at 700°C for 3.5h
- Figure 5.155 Picture of samples treated at 700°C with a) unpolished surface and b) polished surface
- Figure 5.156 XRD patterns collected with Bragg-Brentano geometry of the sample treated at 800°C and at 700°C, the last one after polishing
- Figure 5.157 Picture of a) untreated sample and b) sample treated at 550°C for 3.5 h
- Figure 5.158 XRD patterns collected with Bragg-Brentano geometry of the sample treated at 550°C for 3.5 h
- Figure 5.159 Picture of a) untreated samples, b) sample treated at 500°C and c) sample treated at 400°C
- Figure 5.160 XRD patterns collected with Bragg-Brentano geometry of the samples treated at 500°C and at 400°C



# Introduction

Total hip arthroplasty (THA) is a well-established surgical treatment for restoring joint mobility in case of end-stage degenerative osteoarthritis or damage from trauma of the hip joint.

Gold standard for THA is metal on polyethylene (MoP) coupling, that means a metallic head coupled to a polymeric insert in the acetabular cup. CoCrMo alloy and stainless steel are the main materials used for the femoral head, while ultrahigh molecular weight polyethylene (UHMWPE) is usually used for the insert. For the stem, instead, it is usually used Ti6Al4V alloy in case of cementless implant and stainless steel in case of cemented implants. Usually titanium is not used for the head component due to its low wear and fretting resistance, while it is employed at the interface with bone, for its high biocompatibility.

The main issue related to THA is the short lifespan, about 10-15 years, due to the wear and degradation of UHMWPE.

To overcome this limit, other solutions were introduced in the last decades, such as ceramic on ceramic (CoC), ceramic on UHMWPE (CoP) and metal on metal couplings.

CoC and CoP couplings are characterised by high wear resistance, superior lubrication ability and moderate friction coefficient (COF), nevertheless, negative aspects of these implants are intrinsic brittle nature of ceramics, squeaking, lack of familiarity by surgeons, the need for a strict proper positioning and high cost.

MoM coupling shows a low wear rate and it was taken into account for the treatment of young and active patients in the last decades, nevertheless, a huge correlation to adverse reaction to metal debris comes out from clinical studies.

Other solutions focused on the use of coatings, such as Diamond Like Carbon and TiN coatings. Nowadays, this solution is not widespread, due to problems of delamination and spallation of the coatings.

Another issue of THA is fretting of stems in the case of cemented hip joint and at the neck-head interface of modular joints. The damage at the stem-cement interface is due to tribocorrosion, caused by micromotions between stem and cement in an aggressive environment. Fretting at the neck-head interface, instead, is mainly related to the use of large heads.

The aim of this PhD thesis is to focus on the most biocompatible metallic material used for artroprosthesis components, that is Ti6Al4V alloy and to enhance its wear and fretting resistance, in order to allow its use for interfaces where wear or fretting occur.

To face this limit of Ti6Al4V alloy, a surface ceramic conversion treatment was carried out in order to combine the good mechanical properties of the Ti6Al4V alloy and the good tribological and lubricant properties of ceramic materials.

The followed strategy was the one of developing a titanium borided coating by means of a low cost process, based on a solid state pack diffusion.

The obtained coating was then characterized in order to perform a preliminary analysis for future application as biomaterial for arthroprostheses where wear or fretting occur.

In order to analyse all these points, the present thesis is organised as following described.

**Chapter 1** gives an overview of the state of art of the THA, focusing on the used materials and possible couplings. In particular, the MoM and MoP coupling are described with an analysis of their main issues. Moreover, the problematics of the cemented prostheses and the ones at the neck-head interface are taken into account. **Chapter 2** deals with the classification of the titanium alloy and their properties, focusing on the wear mechanism. Adhesive, abrasive, and fatigue wear, as well as fretting corrosion are evaluated. In the same chapter, the main surface modification processes, to obtain a hard coating on a Ti6Al4V alloy substrate, are also described. The main characteristics and the limits of each technique are reported, as well as examples of commercialised coatings. In **Chapter 3**, the mechanism of protein adsorption and the role of proteins as lubricants is reported. The attention was focused in particular on bovine serum albumin, fibronectin and fetal serum bovine. **Chapter 4** summarizes the materials used in this research and the preparation process of the samples. In this chapter, the surface ceramic conversion treatment is described and analysed in function of the variation of the process parameters. In particular, several mix of powders, times and temperatures of treatment were taken into account. Moreover, the effects of pre-treatments of deoxidation/oxidation and post thermal treatment were evaluated, mainly as regards the thickness and the adhesion of the coating. The characterization of the obtained coatings is reported in **Chapter 5**. They were analysed in terms of chemical composition, microstructure, structure, thickness, hardness, roughness, wettability, adhesion and COF (scratch tests). Wear and fretting behaviours were evaluated by means of pin on disk/plate tests and finally it was study the ability to adsorb proteins and the in vitro bioactivity. A summary of the results is reported in **Chapter 6**, that allows to get conclusions of the performed research and to outline possible further developments.

# Chapter 1

## Hip replacement prostheses and related issues of wear or fretting

### 1.1 Hip replacement prostheses

Hip replacement is a surgical reconstructive procedure, in which the hip is totally or partially substituted by an artificial implant.

The hip joint is an enarthrosis, in which the femoral head articulates with the acetabulum of the pelvis. The femoral head has a  $2/3$  sphere-like shape, while the acetabulum looks like a semi-spherical cup depression. Between the two surfaces there is a cushion of about 2.5 cm of white cartilage, lubricated by synovial fluid. The hip joint is wrapped in a joint capsule and it is stabilised by tendons, ligaments and muscles, that prevent dislocation of the femoral head from the acetabular cup [1]. The anatomy of hip joint is shown in Figure 1.1.

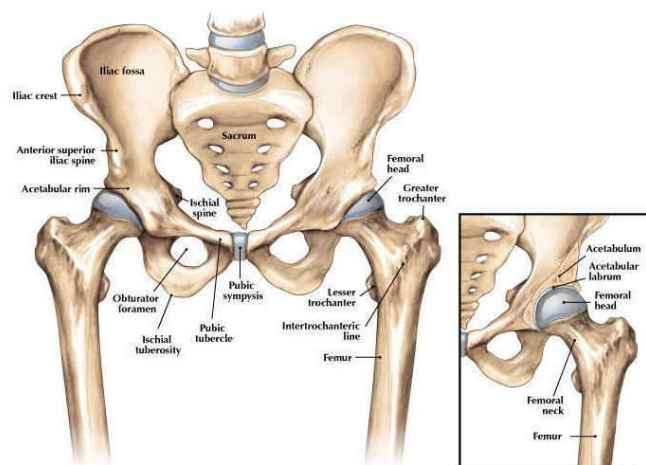
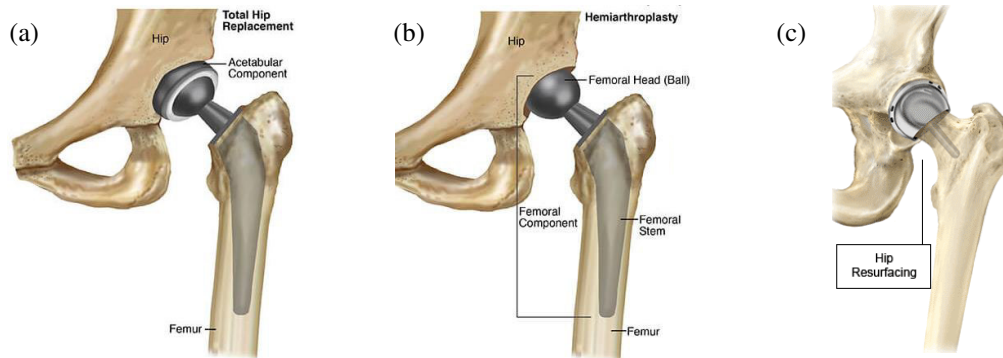


Figure 1.1 Anatomy of hip joint [2]

There are several possibilities for a hip replacement:

- Total hip arthroplasty (THA), where both the femoral head and the acetabular cup are replaced by a prosthetic implant (Figure 1.2a).
- Partial hip replacement, where only the femoral head is substituted (Figure 1.2b).
- Hip resurfacing (HR), where the femoral head is covered with a cup and the acetabular is replaced (Figure 1.2c).



**Figure 1.2 Total Hip Arthroplasty (a) partial hip replacement (b) [3] hip resurfacing (c) [4]**

Generally speaking, the hip prosthesis is composed of a femoral stem, a femoral head, an acetabular cup and/or an insert. The average lifespan of this kind of implant is about 10-15 years. Concerning the increasing of young patients that in the last decades need a hip replacement, nowadays, the lifespan of the implants is the main issue.

Revision surgery to replace the primary implant is a more complex and difficult procedure, with more postoperative complications and longer rehabilitation time [1].

The gold standard for hip joint implants is the combination of a metal head to a metal acetabular cup with an ultra-high molecular weight polyethylene insert (Metal on Polyethylene coupling (MoP)). The advantages of this kind of coupling are low costs, consolidated surgical techniques, possibility to immediate load-bearing. Nevertheless, the main disadvantage is the wear of polyethylene.

To overlap this issue, new technologies, materials and couplings have been studied. The clinically used material couplings are reported in Table 1.1 and shown in Figure 1.3.



Table 1.1 Possible coupling for hip joint implant [5]

Femoral head	Insert	Acetabular cup	Coupling	Note
Metal	Cross linked ultrahigh molecular weight polyethylene	Metal	MoP	
Metal	-	Metal	MoM	Insert and acetabular cup can be a mono-block
Ceramic	Cross linked ultrahigh molecular weight polyethylene	Metal	CoP	
Ceramic	Ceramic	Metal	CoC	Insert and acetabular cup can be a mono-block
Ceramic	-	Metal	CoM	Few clinical trials. Not currently in use



Figure 1.3 Currently used soft and hard material couplings [6]

Figure 1.4 compares the wear rate of the different kinds of coupling.

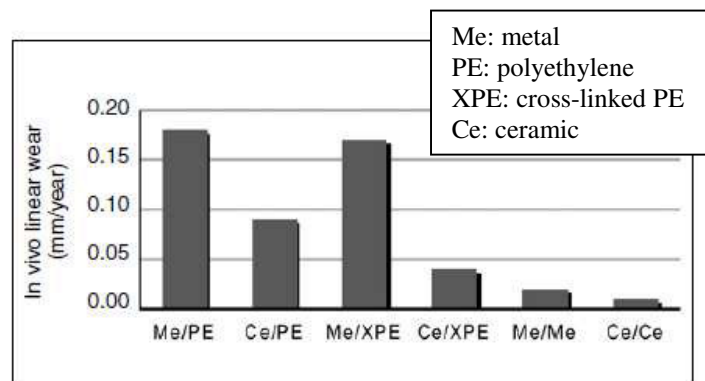


Figure 1.4 Wear rate per years of different kinds of material coupling [5]

Figure 1.4 underlines how MoP coupling results to be the coupling with the highest wear rate. A reduction of the wear rate can be reached using cross-linked ultrahigh molecular weight polyethylene (UHMWPE). The lowest wear rate is

obtained using a ceramic-ceramic coupling (CoC), due to the high corrosion resistance and the hard and smooth surface of the material. Limits of this kind of coupling is related to the ceramic intrinsic brittleness and the lack of data about follow-up over long time [5]. Low wear rate is reached also using a MoM coupling, nevertheless, early failure and serious systemic secondary effects were registered by the FDA, therefore this kind of system nowadays is not implanted any more [7].

The main factor from which depends the lifespan of an artificial implant is the wear rate at head and acetabular cup interface. Due to the different hardness of the bearing surfaces, abrasive and adhesive wear mechanisms take place.

The wear process is observed both in MoP and MoM coupling and it depends on many factors: materials, dimensions, positioning and cement versus cementless components [8].

In the first case, MoP coupling, the component that undergoes mainly to wear is the polymeric insert. The wear of UHMWPE can cause dislocation of the implant, due to the mobilization of the insert and the loosening of the head and osteolysis, as consequence of the reaction of the body to the release of micron and submicron UHMWPE debris. UHMWPE under wear condition produces particles in the range of 100 nm – 1 µm with several shapes (spheroid, plates fibrils or shreds). MoP wear rate is approximately 40-80 mm<sup>2</sup>/year, one to three orders of magnitude higher than the one of MoM coupling and depends on type of polyethylene, loading condition and positioning of the prosthesis components [9].

In 2015 a case of study was published about a catastrophic failure of an THA (Figure 1.5) [10]. The polymeric insert underwent to completely wear and the CoCr femoral head impacted and articulated directly against the Ti alloy acetabular cup. As consequence a strict wear of the Ti alloy cup occurred, due to the soft nature of the Ti alloy and its low wear resistance in comparison to CoCr alloy. The rubbing between the two metallic surfaces caused the releases of metallic debris and ions into the surrounding tissues, that showed beginning of adverse reactions to metal debris (ARMD).



**Figure 1.5 Photographs of the completed worn polymeric insert and metal cup by the metal head [10]**

In the second case, the ARMD is the main and most problematic issues related to wear process of MoM implants. In this case the rolling between the metallic femoral head and the metallic acetabular cup causes the wear of both surfaces and the release of metallic debris. Metallic debris have mainly a nanoscale size, that is lower than the one of UHMWPE debris but they are more reactive and undergo to tribocorrosion process, releasing toxic metallic ions. The wear process is faster when different kinds of metals are coupled. In addition, the degree of wear in MoM coupling is strongly related to the head dimension and the inclination angle of acetabular cup. The higher the head dimension and the inclination angle are, the higher the wear [11].

The reaction of the body can be local or systemic, symptomatic or asymptomatic [9] and depends on many factors such as the amount of metallic ions releases, the gender and the health condition of the patient [12].

## **1.2 Metal on Metal coupling**

MoM joint implants are characterised by metallic components: stem, head and acetabular cup. Metals used are stainless steel, Ti alloys and CoCr alloys. For their mechanical properties stainless steel and CoCrMo alloy are mainly used for stem and head, while for its low wear resistance and good biocompatibility Ti alloy is principally used for the acetabular cup and cementless stem.

Advantages of this coupling are the reduction of volumetric wear rate, that results to be 200 times lower than the one of MoP coupling and the increase of implant stability, due to the possibility to use larger femoral head.

The first MoM bearing was implanted in 1938 by Smith-Peterson and Wiles, their kind of implant made of stainless steel showed poor stability. In 1960 McKee-Farrar tried to solve the problem using the newly developed polymethylmethacrylate bone cement to stabilised the stem. For decades, until the nineties, this system was superseded by the standard MoP coupling introduced by Charnley. At the end of the eighties, MoM couplings began to be take into account again for the treatment of young and active patients, due to the lower volumetric wear rate than MoP coupling and the possibility to maximise the head-neck ratio and redact the risk of impingement between neck and acetabular cup.

In 2008, in USA 40% of THA were performed using MoM coupling, nevertheless in 2009 a warning about the use of this kind of coupling was issued by FDA, concerning the high early failure rate of MoM joint implant [13].

### **1.2.1 Metal on Metal coupling issues**

The main issue related to MoM joint implant is the adverse reactions to metal debris (ARMD). Biological fluids are corrosive environments for metallic materials, due to the presence of electrolytes, such as amino acids and proteins and high concentrations of chloride,  $113 \text{ mEqL}^{-1}$  in serum and  $117 \text{ mEqL}^{-1}$  in interstitial fluid. In addition, the pH decreases to 5.2 after surgery, making acid the environment for two weeks before recovering a normal level of 7.4. The corrosion

and the ion release is favoured by the lower oxygen concentration of body fluids than in air. The oxygen level within the physiological fluids is one fourth of that in air and this causes a delay of the re-generation (in case of removal for wear or abrasion) of the surface protective oxide film. The corrosion is also increased by material wear and fretting, that cause the partial desegregation of the oxide layer. When the oxide film is disrupted the corrosion process and the release of ions continue until the oxide film is regenerated. The process is shown in Figure 1.6. The amount of ions release depends on the regeneration time of the surface oxide layer on the material. Open circuit potential measurements after abrasion show that Ti6Al4V takes 8.2 min, Co28Cr6Mo 12.7 min and 316L stainless steel 35.3 min to regenerate their oxide layers when soaked in physiological fluids [14].

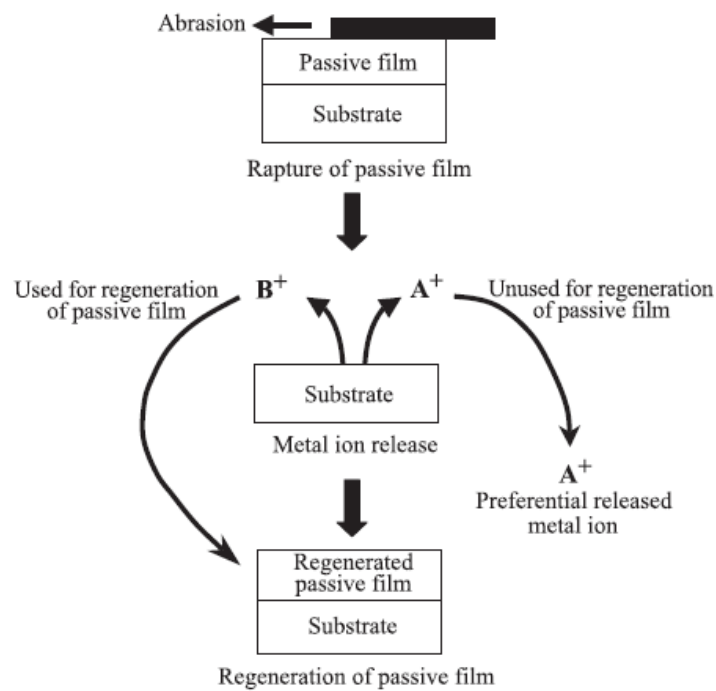


**Figure 1.6 Mechanism of ion release [14]**

The mechanism of desegregation and regeneration of the oxide layer involves a change of the composition of the oxide film as it is reported in Table 1.2.

**Table 1.2. Chemical composition of the native oxide layer of material after polishing in deionized water and of oxide layer of material after biological fluid exposition [14]**

<b>Material</b>	<b>Native oxide film composition</b>	<b>Regenerated oxide film composition</b>
316L stainless steel	The upper part of the oxide film hydrated or oxyhydroxided because of a large amount of OH <sup>-</sup> and it is enriched of Fe. The inner part presents oxidic species of Cr, Ni, Mo and Mn.	The upper part of the oxide film contains Fe and Cr oxides with a small amount of Mo oxide. Cr results to be in association with S while Fe with P. Ni and Mn oxides are located in the inner part.
CoCrMo alloy	The upper part of the oxide film hydrated or oxyhydroxided because of a large amount of OH <sup>-</sup> and it is enriched of Co. The inner part presents oxidic species of Cr and Mo.	Co dissolves and the oxide layer result to be composed of Cr and Mo oxides. On surface in addition calcium phosphates precipitate.
Ti and Ti6Al4V	The oxide layer is composed of amorphous or low-crystalline and non-stoichiometric TiO <sub>2</sub> . The oxide film contains Ti <sup>4+</sup> , Ti <sup>3+</sup> and Ti <sup>2+</sup> . There are a small amount of Al oxide in Ti6Al4V alloy.	The oxide film incorporate Ca, S and P and interact with ions and molecules.

In particular, during the clinical life of a MoM prosthesis, the femoral head rubs against the acetabular cup, this causes a smoothing of the irregularities of the CoCrMo surfaces. As consequence metal particles are produced and metal ions are released into the periprosthetic space. These particles are smaller than the ones produced by the wear of UHMWPE and very reactive [15].

There are two mechanisms through which metallic ions are released. On one side, when a metallic material is in contact with aqueous solutions, such as biological fluid, a cyclic process of partial dissolution and reprecipitation of the surface oxide film occurs. Amino acids and proteins can accelerate the dissolution process. On the other side, there is the action of macrophages. An implant is recognised as a foreign body, macrophages adhere to the surface and generate active oxygen species, such as O<sub>2</sub><sup>-</sup>. The higher the amount of phagocytosed particles is, the higher the amount of active oxygen species. The O<sub>2</sub><sup>-</sup> specie are catalysed by superoxide dismutase to produce H<sub>2</sub>O<sub>2</sub>. H<sub>2</sub>O<sub>2</sub> reacts with the surface metallic oxides generating OH<sup>-</sup> and radicals, that accumulate.

High concentrations of Cobalt and Chromium ions result toxic and interfere with biological functions [15].

Several studies have underlined how patients with MoM implant have Co and Cr serum levels at least one order of magnitude higher than patients with other types of implant (MoP or CoC) or without implants [12,16,17].

The femoral head dimension and positioning of the acetabular cup during surgery are the main factors that influence the amount of the ions released. The bigger the femoral head is, the bigger the contact surface with the acetabular cup. Increasing the contact area also the surface that can undergo to wear increases and thus the formation of metal particles and the release of Cobalt and Chromium ions. Consequently, the hypotheses of advantages from the use of larger femoral heads has been disproved in the clinical experience. In addition, an accurate and right

positioning of the acetabular cup is extremely important for MoM implants, to avoid and to prevent abnormal loading of the implant, that can accelerate wear of the components [13]. MoM implant failures have been reported in case of high acetabular cup inclination angle ( $>50^\circ$ ) and it was also related to high levels of metal ions [11].

Nowadays, data about the normal and toxic levels of metal ions in the human body are not universally defined. Several studies have been conducted and each one reported a different ion range. The Medicines and Healthcare products Regulatory Agency suggests a cut-off level of 7 ppb for Cobalt and Chromium ions [11], while De Smet et al. reported that metallosis can be associated to Cr-ion levels higher than 17 ppb and Co-ion levels higher than 19 ppb [16]. As consequence, it is difficult to define an exact toxicity threshold for metallic ion levels. Nevertheless, several are the diseases correlated to metallosis, in particular to high level of Cobalt and Chromium ions:

- **Cardiomyopathy.** High level of Cobalt causes inhibition of mitochondrial dehydrogenase and thus the inhibition of cellular respiration, alteration of transmembrane transport and, as consequence, the damage of the electrochemical matching of myocardial tissue and the alteration of the beta-adrenergic system and the delayed type IV hypersensitivity (activation of T lymphocytes) [15].
- **Carcinogenicity.** It is demonstrated that abnormal levels of Co and Cr ions cause genetic changes such as DNA damage and chromosomal aberrations [15]. The potential risk of carcinogenicity of MoM prostheses has been often assumed, but actually it was not clinically proved.
- **Polyneuropathy.** Metallosis is associated to thyroid abnormal function, peripheral neuropathy, hearing and vision loss [15]. In a case of study [18] has been reported the follow up of a patient with Parkinson disease after a bilateral hip substitution with MoM implant. The patient exhibited high level of Co ions in serum and a rapid acceleration of Parkinson disease symptoms. He was subjected to a revision surgery after that he exhibited a reduction of Parkinson symptoms and a natural follow up of the disease.
- **Renal effect.** Patients with MoM implant show high level of Co, Cr and Ni into urine, this is due to the fact that metal particles are only degraded by renal and gastrointestinal system [15].
- **Aseptic lymphocyte dominated vasculitis associated lesion (ALVAL).** Local vascular system can be altered by a chronic inflammation, caused by a lymphocyte inflammatory reaction at metal debris [15]. A study conducted by Hart et al. [19] reported a reduction of peripheral blood count of T-lymphocytes and B-lymphocytes in patient with MoM implants.
- **Pseudotumor.** Pseudotumors look like cyst or granulomatous. They can be asymptomatic or related to pain [15]. Even if the directly correlation between pseudotumors and MoM implant have not been confirmed, cases of reduction of metal ion levels and pseudotumour mass dimensions after revision surgeries are reported in literature [20].

- Osteolysis. Accumulation of metal debris on periprosthetic tissues causes an inflammatory response of the system and the activation of macrophages, that lead to a bone resorption [21].

Several studies have been carried out to confirm or not the correlation between MoM implant and the diseases reported above. They focus on many factors such as patient history, age and gender, implant design, type of hip prostheses and mixing of components from different manufactures [15]. In particular, it is observed that women exhibit higher Co and Cr levels than men and that patients with MoM HR have serum Cr levels higher than patients with MoM THA. The last phenomenon is related to the different volume, size and morphology of debris of the two kinds of implant. HR implants generate particles that are half in size than the ones of THA implants, and so at the same wear volume, the amount of particles release is higher [12,17,21]. Nevertheless, data are not homogeneous and define a correlation is difficult. In any case, all these diseases are related to high values of metal ions and thus can be considered as a potential risk. Different orthopaedic associations in different countries gave indications of threshold of metal ions concentrations in blood and/or urine for revision of the MoM implants [13].

The wear at the head neck taper junction causes, instead, the wear of titanium surface with the release of Al ions. Al is not a physiological element and its high serum levels can be dangerous as well as Co and Cr high levels. Diseases like anemia, encephalopathy and osteoporosis are related to high Al ion concentrations [22].

### **1.3 Metal on Polyethylene coupling**

MoP joint implants are composed of a metallic stem, metallic head and metallic acetabular cup connected by a polymeric insert, as mentioned previously. The metallic material used are stainless steel, CoCrMo alloy and Ti alloy, as in the case of MoM coupling, while the polymeric liner is based on polyethylene.

This kind of system is the most common implanted all over the world, even if in the last decades the percentage of others kinds of prosthetic solutions is increasing.

MoP implants were introduced in 1960s by Charely. At the beginning the liner was composed of ultrahigh molecular weight polyethylene (UHMWPE) and the stability of the components were secured by the acrylic bone cement. In the last decades, cementless approaches, using osteointegrable stem and acetabular cup and new kinds of polyethylene (cross-linked UHMWPE and cross-linked UHMWPE with Vitamin E) were introduced, in order to increase the wear properties of the materials and thus the lifespan of the implants [23].

The femoral head is mainly composed of CoCrMo alloy or stainless steel, while Ti6Al4V alloy is not usually used for femoral head. This is due to its low wear resistance and limited resistance to hydrogen diffusion, that causes embrittlement of the material.

The tribological interaction between titanium and UHMWPE promotes a hydrogen assisted wear mechanism. Friction between the surfaces causes the release of hydrogen by the synovial fluid and the UHMWPE. In the first case the degradation is due to a thermodegradation process, while in the second case, a physicochemical dissociation occurs. In addition, the hydrogen diffusion is promoted by local plastic deformations, that occur at the contact areas during the rubbing between the metallic and polymeric surfaces. The hydrogen diffusion is usually retarded by the natural oxide layer present on the titanium surface. Nevertheless, defects of the oxide layer can allow the diffusion of the hydrogen released by the dissociation of the UHMWPE and thus the formation of titanium hydride at the interface oxide-metal, when the concentration of the hydrogen reaches the saturation limit. The presence of titanium hydride reduces the bonding strength at the interface oxide-metal, as consequence particles of oxide can detach, developing debris and/or being embedded in the UHMWPE surface. Two body and three body abrasion wear occurs, promoting the damage of the surface and the formation of micro-cracks that lead to the detachment of titanium and titanium hydride clouds. These clouds develop debris and can be embedded into the UHMWPE surface as well as the detached oxide particles. This phenomenon feeds the wear mechanism and the degradation of the surfaces [24].

### **1.3.1 Metal on Polyethylene coupling issues**

The wear at the interface between the metallic head and the UHMWPE liner is the main issue of the MoP system. The wear of the UHMWPE causes the release of debris, that lead to a cellular response of the periprosthetic tissues. The inflammatory response of the tissues consists in the phagocytosis of the debris by the macrophages and the activation of the osteoclasts. As consequence, locally, the bone is resorbed and the prosthesis can mobilize and thus undergoes to failure. Osteolysis and aseptic loosening are the main causes of failure of the MoP joint implants.

The UHMWPE, nevertheless, was substituted by the cross-linker UHMWPE (XLPE) in the 98% of the cases in the last 15 years. The XLPE consists on a UHMWPE irradiated with at least 50kGy of gamma/beta/electron beam irradiations. The process causes a cross-linking between the PE molecules and the development of free radicals. The first increases the wear resistance of the material while the second reduces the mechanical properties of the material if oxidised. Therefore, in the choice of the suitable XLPE, the kind of irradiation, melting technique and annealing must be taken into account. When annealing is carried out at temperatures below the melting point, wear resistance and mechanical properties are increased, but the material shows low oxidation resistance, because the process does not neutralise all the free radicals. While, when annealing is performed at temperatures above the melting point, oxidation resistance is increased, but fatigue resistance is reduced.

Recently, to enhance the oxygen resistance of the XLPE without re-melting the material and preserving its mechanical properties, it was introduced the Vitamin E.



The Vitamin E is an antioxidant, its addition wants allow the free radicals to react preferably with the vitamin instead of oxygen. Nowadays, the data about this kind of XLPE are not sufficient for a well-defined risk analysis. Nevertheless, the medium-term follow-up shows that the Vitamin E XLPE allows the use of thinner liners coupled with large head with a low wear rate. This suggests enhanced wear properties in comparison to the standard PE, that shows high wear rate with high possibility of osteolysis if coupled with large head.

The tribological and mechanical properties of the UHMWPE depends not only on the kind of polyethylene but also by the sterilization process.

**Table 1.3. Sterilisation methods [25]**

<b>Sterilization method</b>	<b>Advantages</b>	<b>Disadvantages</b>
Gamma irradiation in oxygen	Increment of wear resistance through the increment of cross-linking between PE molecules	Increment of PE brittleness, caused by the oxidation of the free radicals produced by the gamma irradiation
Thermal sterilization with gas plasma	Increment of wear and oxidation resistance	
Gamma sterilisation in an air-free environment + oxygen-free packaging	Reduction of the free radicals oxidation and increment of wear resistance	
Ethylene oxide	Reduction of the free radicals oxidation	

Table 1.3 reports the principal sterilisation methods for UHMWPE with the advantages and disadvantages of each process.

Nowadays, the main employed processes are the gamma sterilisation in an air-free environment with oxygen-free packaging and the used of ethylene oxides. These methods allow to better preserve the mechanical properties of the material.

In conclusion in the valuation of the UHMWPE several factors must be considered such as the production process, sterilization method and prosthesis design [25].

## **1.4 Cemented prostheses**

Cemented prostheses consist on implants where the stem and the acetabular cup are fixed by the use of an acrylic bone cement based on polymethylmethacrylate (PMMA). This technique to stabilise the components was employed since the first generation of prostheses introduced by Charnely in 1960s.

In the last decades, cement underwent to evolution in terms of the method of bon and cement preparation and cement delivery. Three generations of cement can be identified, their characteristics are reported in Table 1.4.

**Table 1.4 Cement generations [26]**

Generation	Mixing/Porosity Reduction	Canal Preparation	Insertion	Centralization
First	Hand mix	Rasp only, leave cancellous bone	Manual insertion with finger packing	None
Second	Hand mix	More aggressive rasp, brushing pulsatile lavage	Cement gun Distal canal plug	Early distal centralizers
Third	Vacuum mix/ centrifugation	More aggressive rasp, brushing pulsatile lavage	Cement gun with pressurization Distal canal plug	Proximal and distal centralizers

A suitable preparation of the bone bed and a correct insertion of the bone are essential for a good connection between bone and cement and thus for a long lifespan of the implants.

The introduction of the vacuum mix and centrifugation allows to reduce the porosity of the cement and to increase its mechanical properties. A more aggressive rasp with a brushing pulsate lavage, instead, favour the removal of blood and loose cancellous bone and thus the adhesion of the cement to the health bone. While, the use of gun and the pressurisation of the mantel, lead to a better filling of the canal. Finally, the use of centralizers allows to have a more uniform circumferential cement mantel around the stem.

Important factors that must be taken into account in the choice of the cement, are the viscosity, working time and setting. The determination of these factors depends on the kind of stem/cup, that have to be implanted.

If the surface of the implant component is rough, the component should be inserted in the earlier phase of the cement polymerization, thus it is preferable to use a cement with a long liquid phase. While if the surface is smooth, the component should be inserted in a doughier phase, so a cement with a long polymerization phase is preferable [26].

### 1.4.1 Implant-Cement coupling issues

The main issue of the implant-cement interface is the tribocorrosion. The main factors that act on the wear process are the presence of micromotions and pores at the interface between cement and stem, the chemical composition of the cement, the presence of radiopacifiers and the design of the stem [27]. Microotions are due to the shrinkage of the cement after the curing. It correspond to the 4% reduction of the volume [23]. To have the primary stability after the implant and to avoid instability of the prostheses, these micromotions have to be lower than 150  $\mu\text{m}$  [28].

During the normal walking cycle the hip joint bears up to five time the body weight with an average of 1-2 million step per annum. Therefore, under physiological loading and due to the presence of the shrinkage gap low-amplitude oscillatory micromotions occur at the interface between stem and cement.

These micromotions are the main cause of fretting at the interface between stem and cement. Moreover, the body fluids can be considered an aggressive environment, thus the fretting is correlated to corrosion of the surfaces and wear products. The wear process at the interface involves the development of wear debris, subsequent activation of macrophage response, followed by bone resorption and aseptic loosening [23].

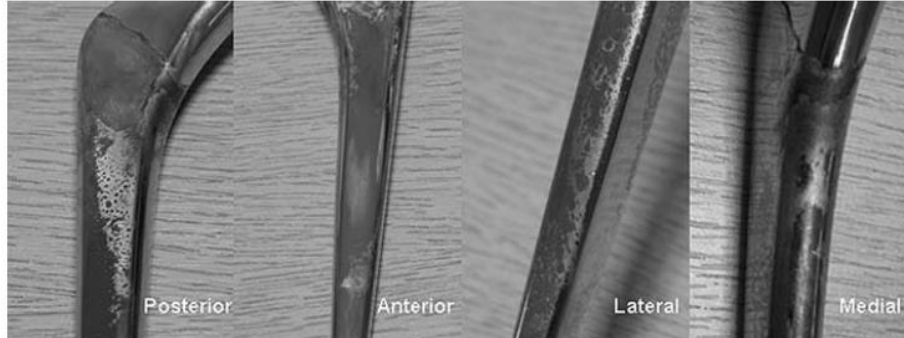


**Figure 1.7 Titanium alloy stem with fretting marks [29]**

As it is shown by Brown et al. [29] the wear mechanism depends on the morphology of the surface: matt stems undergo to abrasive wear due to an in vivo polishing process, while polished stems show crater and pitting on the surface due to fretting wear. Nevertheless, the wear location is similar for all kinds of stem, the main worn zones are the anterolateral, posteromedial and underneck areas of the stem. They correspond to the sites where there are the maximum concentrations of stress (Figure 1.7). The wear mechanism is due to the combination of the presence of micropores into the cement and stress caused by the physiological loading. Pores are sites where the interfacial bonding strength between cement and stem is low and debris accumulates. On one site, they correspond to unworn areas on the stem surfaces while on the other site, they behave as stress concentrator and, as consequence, they act as site where fatigue cracks can generate into the cement mantle (Figure 1.8). Through the fatigue cracks, debris can reach the surrounding tissues, breaking out the macrophage response. The bone resorption causes micromotions at the cement-stem interface, that is the main factor that triggers the fretting wear [29,30].

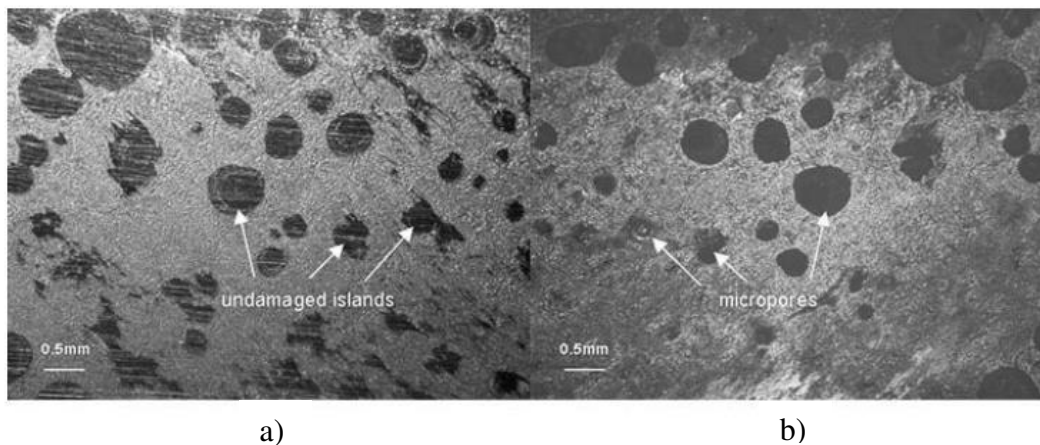


**Figure 1.8 optical micrograph of a) a damaged titanium alloy stem b) cement counterface [29]**

The bone resorption can be caused not only by metal and cement debris, but it can also be due to tissue necrosis. The bone cells undergo to apoptosis when exposed to 47°C for 1 min or to a higher temperature for a shorter time; during cement polymerization, the temperature at the interface bone-cement reaches values of 40-70°C for some seconds, damaging the surrounding cells. In some cases, new bone is generated in order to heal the damage, in other cases macrophages are activated and bone is resorbed (implant failure) [31]. Moreover, a small percentage of methylmethacrylate monomer can remain after curing of the cement. This monomer is toxic for the body and can cause secondary collateral effects [23].

## **1.5 The neck-head interface**

Focusing on the head – neck junction, the taper connection consists on the self-interlocking between the neck and the head. The mechanical assembly of the components causes an intrinsic damage of the surfaces due to the contact of the asperities of the surfaces. The rubbing of the surfaces during the joint of the components lead to abrasion of the oxide films, the cracking of the surfaces layer and localised plastic deformation. The damage is greater in case of mixed materials.

In the most common implants the taper connection is composed of a CoCr femoral stem and CoCr head or of a Ti alloy femoral stem and CoCr head, thus it is important to take into account the mechanical and chemical properties of these materials.

Generally speaking, Ti alloy has lower wear resistance and higher corrosion properties than CoCr alloy, these properties influence the mechanism of damage of these metals. The strong passive film of Ti alloy prevents it from electrochemical degradation, but the soft nature of the metal makes it more susceptible to mechanical damage; inversely, in the case of CoCr alloys [32].

### **1.5.1 Neck-Head coupling issues**

The degradation of taper junction at the interface between the head and stem is one of the main cause of failure of total hip arthroplasty (THA)[33].

The functionality of this interface depends on many factors, such as: material, dimensions, positioning and surface roughness of the head and neck, shape and mechanical coupling of the tapers [34].

For a greater knowledge of the mechanism of damage of these couplings, a retrieval study was conducted by Hall D.J. et al. [33]. Analyses conducted on explanted implants show that both the heads and stems of the Co/Co coupling and Co/Ti couplings present local flattening of machining mark peaks by plastic deformation, due to the assembly process of the head onto the stem. In the case of the Co/Ti stem tapers, plastic deformation is also associated with grooves and toggle damage, caused by cycling rubbing over time.

The contact between the hard Co head and the soft Ti taper can cause fretting, toggling and wear of the Ti taper with eventual loosening of the head and formation of Ti, Co and Mo-oxides debris (Figure 1.9). Debris can go through the system and accumulate in organs, causing adverse local tissue reactions.

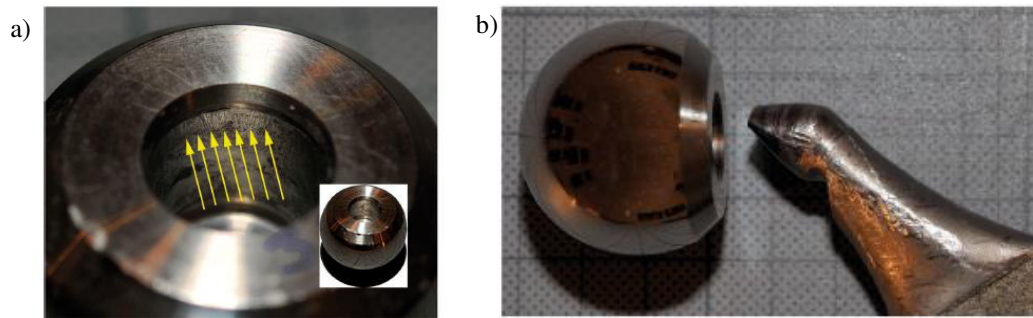


**Figure 1.9 a) fretting marks on CoCr alloy head combined with Ti alloy taper b) CoCr alloy head dislocated from the Ti alloy neck [35]**

Co/Co and Co/Ti tapers show also material transfer: in the first case small flakes detach from the stem and transfer to the head and the other way around, in the second case large flakes detach from the stem, leaving large depression, and transfer onto the Co head. On one hand, the material transfer has a positive aspect because the transfer of the Ti alloy onto the Co alloy causes micro-joints between the two taper surfaces, that enhances the joint stability and prevents further micromotions, fretting and imprinting. On the other hand, the material transfers in Co/Co coupling gives rise to the removal of chromium oxide film in some surface areas, that stay exposed to fretting, fretting corrosion and pitting corrosion. In addition, when the corrosion is along the grain boundaries, the Co stem tapers undergo to intergranular corrosion. The dissolution of some areas leaves trenches and holes, that can be refilled with organic matter, due to the contact with the physiological fluids.

Fretting can be induced not only by the micromotions between the two taper surfaces, but also by the imprinting of the rougher topography of the stem into the smoother head taper [34]. In the case of the Co/Ti coupling, the damage of the Co surface by the Ti alloy is due to a hardening process of the Ti alloy, through the formation of a hard, inert, stable and amorphous oxide layer on the Ti surface [36].

Implants are set in an aggressive environment, due to the presence of synovial fluid, that contains chlorides and hydroxides. For this reason, heads and necks undergo to a tribocorrosion process. Factors that influence the wear and corrosion of taper and head are the design, type of assembly and loading. Greater fretting and corrosion effects were shown by thin tapers, large heads, varus stem and high offset stems. Fretting, crevice and galvanic corrosion are also triggered by a non-correct positioning of the components. A wrong positioning causes loads applied on an axis not aligned to the taper one and thus non-symmetrical compressive radial stress distribution. As consequence, micro-motions and loss of contact take place, allowing synovial fluid to enter the interface, that causes the corrosion of the

components, mainly of the taper surfaces. Micro-motions can develop also due to an insufficient assembly force [35,37].

## References

- [1] Derar H, Shahinpoor M. Recent patents and designs on hip replacement prostheses. *The Open Biomedical Engineering Journal* 2015;9:92–102. doi:10.2174/1874120701509010092.
- [2] Anatomy of the hip 2017. [www.howtorelief.com](http://www.howtorelief.com).
- [3] Total hip replacement 2017. [www.imotionpt.com](http://www.imotionpt.com).
- [4] Hip resurfacing 2018. [www.medadvisor.co](http://www.medadvisor.co).
- [5] Schwartzmann CR, Boschin LC, Gonçalves RZ, Yépez AK, de Freitas Spinelli L. New Bearing Surfaces in Total Hip Replacement. *Revista Brasileira de Ortopedia* 2012;47:154–9. doi:10.1016/S2255-4971(15)30079-3.
- [6] Di Puccio F, Mattei L. Biotribology of artificial hip joints. *World Journal of Orthopedics* 2015;6:77–94. doi:10.5312/wjo.v6.i1.77.
- [7] Concerns about Metal-on-Metal Hip Implants. 2018 n.d. [www.fda.gov](http://www.fda.gov).
- [8] Del Schutte Jr H, Lipman AJ, Bannar SM, Livermore JT, Ilstrup D, F MB. Effects of acetabular abduction on cup wear rates in total hip arthroplasty. *The Journal of Arthroplasty* 1998;13:621–6.
- [9] Sullivan SJL, Topoleski LDT. Surface Modifications for Improved Wear Performance in Artificial Joints: A Review. *Jom* 2015;67:2502–17. doi:10.1007/s11837-015-1543-0.
- [10] Knudsen ML, Coobs BR, Kyle RF. Complete Wear-Through of a Polyethylene Liner and Metal-Backed Acetabular Cup Resulting in a Unique Form of Catastrophic Total Hip Arthroplasty Failure: A Case Report. *JBJS Case Connector* 2015;5:e12.
- [11] Hart AJ, Sabah SA, Bandi AS, Maggiore P, Tarassoli P, Sampson B, et al. Sensitivity and specificity of blood cobalt and chromium metal ions for predicting failure of metal-on-metal hip replacement. *The Bone & Joint Journal* 2011;93–B:1308–13. doi:10.1302/0301-620X.93B10.26249.
- [12] Moroni A, Savarino L, Hoque M, Cadossi M, Baldini N. Do ion levels in hip resurfacing differ from metal-on-metal THA at midterm? *Clinical Orthopaedics and Related Research* 2011;469:180–7. doi:10.1007/s11999-010-1424-3.
- [13] Neuwirth AL, Ashley BS, Hardaker WM, Sheth NP. Metal-on-Metal Hip Implants : Progress and Problems. *Biomedical Applications of Metals*, 2018, p. 73–93.

- [14] Hanawa T. Metal ion release from metal implants. *Materials Science and Engineering C* 2004;24:745–52. doi:10.1016/j.msec.2004.08.018.
- [15] Campbell JR, Estey MP. Metal release from hip prostheses: Cobalt and chromium toxicity and the role of the clinical laboratory. *Clinical Chemistry and Laboratory Medicine* 2013;51:213–20. doi:10.1515/cclm-2012-0492.
- [16] Smet K De, Haan R De, Calistri A, Campbell P, Ebramzadeh E, Pattyn C, et al. Metal Ion Measurement as a Diagnostic Tool to Identify Problems with Metal-on-Metal Hip Resurfacing. *The Journal of Bone and Joint Surgery-American Volume* 2008;90:202–8. doi:10.2106/JBJS.H.00672.
- [17] Savarino L, Cadossi M, Chiarello E, Baldini N, Giannini S. Do ion levels in metal-on-metal hip resurfacing differ from those in metal-on-metal THA at long-term followup? *Clinical Orthopaedics and Related Research* 2013;471:2964–71. doi:10.1007/s11999-013-2981-z.
- [18] Woelber E, Van Citters DW, Steck T, Glass GA, Tower S. Explant analysis from a patient exhibiting rapid acceleration of Parkinson disease symptoms and hypercobaltemia following metal-on-metal total hip arthroplasty a case report. *JBJS Case Connector* 2016;6:6–9. doi:10.2106/JBJS.CC.15.00063.
- [19] Hart AJ, Skinner JA, Winship P, Faria N, Kulinskaya E, Webster D, et al. Circulating levels of cobalt and chromium from metal-on-metal hip replacement are associated with CD8 + T-cell lymphopenia. *J Bone Joint Surg [Br]* 2009;9191:835–42. doi:10.1302/0301-620X.91B6.
- [20] Almousa SA, Greidanus N V., Masri BA, Duncan CP, Garbuz DS. The natural history of inflammatory pseudotumors in asymptomatic patients after metal-on-metal hip arthroplasty. *Clinical Orthopaedics and Related Research* 2013;471:3814–21. doi:10.1007/s11999-013-2944-4.
- [21] Langton DJ, Sidaginamale RP, Joyce TJ, Nattu S, Blain P, Jefferson RD, et al. The clinical implications of elevated blood metal ion concentrations in asymptomatic patients with MoM hip resurfacings: A cohort study. *BMJ Open* 2013;3. doi:10.1136/bmjopen-2012-001541.
- [22] Glenske K, Donkiewicz P, Köwitsch A, Milosevic-Oljaca N, Rider P, Rofall S, et al. Applications of metals for bone regeneration. *International Journal of Molecular Sciences* 2018;19:1–32. doi:10.3390/ijms19030826.
- [23] Turner IG. Orthopaedic coatings. In: Driver M, editor. *Coatings for biomedical applications*, 2012.
- [24] Li XY, Dong H, Shi W. New insights into wear of Ti6Al4V by ultra-high molecular weight polyethylene under water lubricated conditions. *Wear* 2001;250–251:553–60. doi:10.1016/S0043-1648(01)00637-8.
- [25] Zagra L, Gallazzi E. Bearing surfaces in primary total hip arthroplasty. *EFORT Open Reviews* 2018;3:217–24. doi:10.1302/2058-5241.3.180300.
- [26] *The Technique of Cemented Total Hip Replacement* 2005. www.healio.com.



- [27] Cook RB, Shearwood-Porter NR, Latham JM, Wood RJK. Volumetric assessment of material loss from retrieved cemented metal hip replacement stems. *Tribology International* 2015;89:105–8. doi:10.1016/j.triboint.2014.12.026.
- [28] Bignardi C. *Artroplastica dell'anca* 2008.
- [29] Brown L, Zhang H, Blunt L, Barrans S. Reproduction of fretting wear at the stem-cement interface in total hip replacement. *Proceedings of the Institution of Mechanical Engineers, Part H: Journal of Engineering in Medicine* 2007;221:963–71. doi:10.1243/09544119JEIM333.
- [30] Zhang H, Brown L, Blunt L, S. B. Generation of fretting wear debris at the stem-cement interface in total hip replacement. *Proceedings of Computing and Engineering Annual Researchers' Conference 2007*, 2007, p. 1–4.
- [31] Mjoberg B. Loosening of the cemented hip prosthesis. *Acta Orthopaedica Scandinavica* 1986;57:3–40. doi:10.3109/17453678609157925.
- [32] Ryu JJ, Shrotriya P. Mechanical load assisted dissolution response of biomedical cobalt-chromium and titanium metallic alloys: Influence of in-plane stress and chemical environment. *Wear* 2015;332–333:662–8. doi:10.1016/j.wear.2015.01.071.
- [33] Hall DJ, Pourzal R, Lundberg HJ, Mathew MT, Jacobs JJ, Urban RM. Mechanical, chemical and biological damage modes within head-neck tapers of CoCrMo and Ti6Al4V contemporary hip replacements. *Journal of Biomedical Materials Research - Part B Applied Biomaterials* 2017;106:1672–85. doi:10.1002/jbm.b.33972.
- [34] Langton DJ, Sidaginamale RP, Joyce TJ, Meek RD, Bowsher JG, Deehan D, et al. A comparison study of stem taper material loss at similar and mixed metal head-neck taper junctions. *Bone and Joint Journal* 2017;99B:1304–12. doi:10.1302/0301-620X.99B10.BJJ-2016-1005.R1.
- [35] Morlock M, Bünte D, Gührs J, Bishop N. Corrosion of the Head-Stem Taper Junction—Are We on the Verge of an Epidemic?: Review Article. *HSS Journal* 2017;13:42–9. doi:10.1007/s11420-016-9526-4.
- [36] Bull SJ, Moharrami N, Langton D. Mechanistic Study of the Wear of Ceramic Heads by Metallic Stems in Modular Implants. *Journal of Bio- and Tribo-Corrosion* 2017;3:1–8. doi:10.1007/s40735-016-0066-8.
- [37] Cook SD, Barrack RL, Baffes GC, Clemow a J, Serekian P, Dong N, et al. Wear and corrosion of modular interfaces in total hip replacements. *Clinical Orthopaedics and Related Research* 1994;298:80–8. doi:10.1097/00003086-199401000-00013.



## Chapter 2

# Wear and fretting of Titanium and Titanium alloys

## 2.1 Introduction to the mechanical properties of Titanium and Titanium alloys

Titanium and its alloys present two crystal structures, each one stable in a particular temperature range. At low temperatures titanium has a hexagonal close packed structure (hcp), while at high temperatures the structure is body centred cubic (bcc). The hcp and bcc structures are respectively called  $\alpha$  phase and  $\beta$  phase (Figure 2.1).

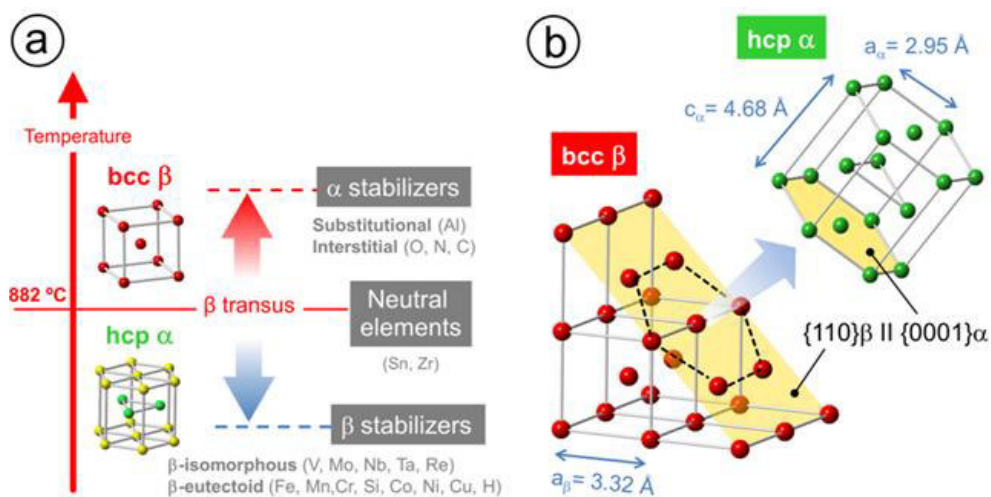


Figure 2.1 Titanium crystal structures [1]

The allotropic transformation from the  $\beta$  phase to the  $\alpha$  phase consists in the transformation of the  $\{110\}$  planes of the bcc  $\beta$  phase into the  $\{0001\}$  planes of the hcp  $\alpha$  phase. The distance between the basal planes in the  $\alpha$  and  $\beta$  phase is different, the  $\alpha$  phase has a greater distance between  $\{0001\}$  planes than the  $\beta$  phase between

the {110} planes. This causes a slight atomic distortion, that at a macroscopy level corresponds to an increment of volume (Figure 2.1b).

The temperature at which the transformation between  $\alpha$  and  $\beta$  phase occurs, is called  $\beta$  transus temperature and it depends on the alloying elements. For example, the  $\beta$  transus temperature of the commercially pure titanium is about 882°C, while for the titanium alloy used in this research (Ti6Al4V) the  $\beta$  transus temperature is around 910°C.

The alloying elements are classified into  $\alpha$  stabilizer or  $\beta$  stabiliser, the first ones rise the  $\beta$  transus temperature extending the  $\alpha$  phase field to higher temperatures, while the second ones reduce the  $\beta$  transus temperature shifting the  $\beta$  phase field to lower temperatures. The extension of the  $\alpha$  phase field allows the formation of a two phases  $\alpha+\beta$  field. As consequences titanium alloys are classified in  $\alpha$ ,  $\alpha+\beta$  and  $\beta$  alloy in function of the alloying element present and the microstructure. A schematic classification of titanium alloys is reported in Figure 2.2 [2].

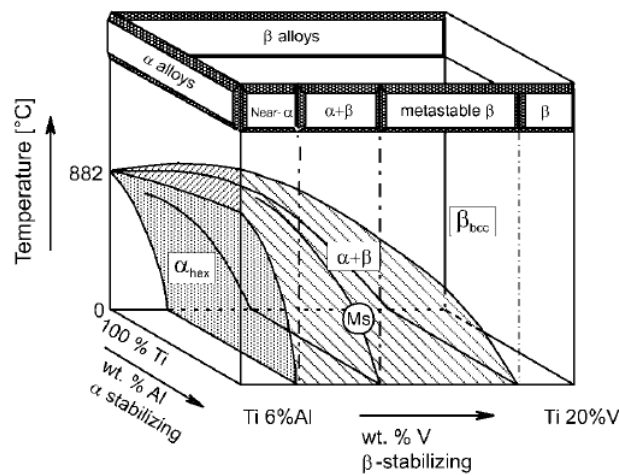


Figure 2.2 Classification of titanium alloys in a three-dimensional phase diagram [2]

The size, shape and distribution of the  $\alpha$  and  $\beta$  phases define the microstructure of the titanium alloys and they are function of the thermochemical treatment applied (Figure 2.3).

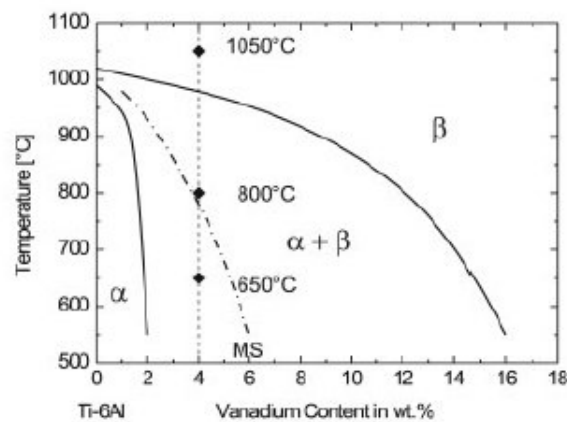
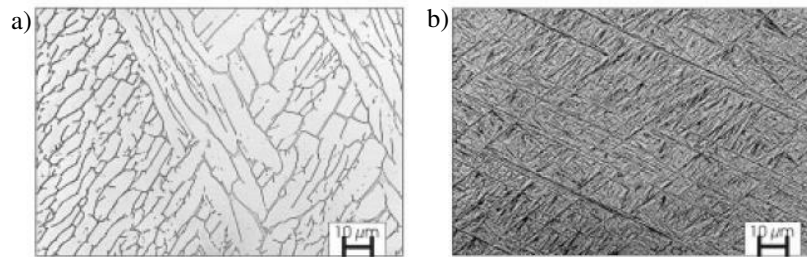


Figure 2.3 Ternary phase diagram [2]

Thermal treatments carried out at temperatures above the  $\beta$  transus temperature lead to the development of lamellar microstructures. During the cooling, when the temperature falls below the  $\beta$  transus temperature,  $\alpha$  phase nucleates at  $\beta$  grain boundaries, growing as lamellae. The cooling rate influence the lamellae dimensions, the faster the cooling rate is, the finer the lamellae, while decreasing the cooling rate, the lamellae become coarser.

In addition, a slow cooling rate leads to a microstructure composed of pure lamellae of primary  $\alpha$ , while a fast cooling rate leads to a fine needle-like microstructure, due to a martensitic transformation of  $\beta$  phases (Figure 2.4).



**Figure 2.4** Microstructure of Ti6Al4V alloy a) furnace cooling and b) water quenching from 1050°C [2]

In the  $\alpha+\beta$  field, when the cooling is slow, the microstructure consists in coarse  $\alpha$  lamellar with around small seam of  $\beta$  phase. While, when the cooling is fast and from temperatures above the martensitic start temperature, the  $\beta$  phase transforms into martensite, that is, the bcc  $\beta$  phase transforms completely into hcp  $\alpha$  phase by means of a diffusionless process (Figure 2.5).

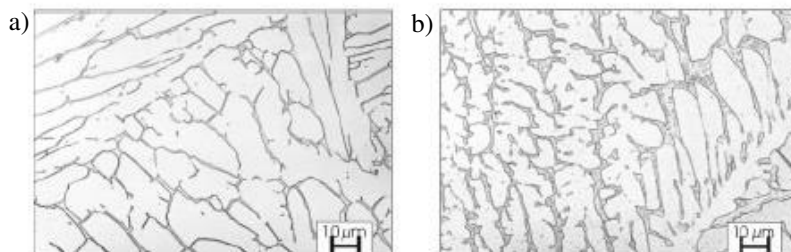


**Figure 2.5** Microstructure of Ti6Al4V alloy a) furnace cooling and b) water quenching from 800°C [2]

The microstructure and the crystal structure of the martensite depend respectively on the amount of alloy elements and the martensitic start temperature. In particular, low amount of alloy elements leads to a hcp martensite, while an orthorhombic martensite is obtained when the amount of alloy elements is high. Moreover, when the martensitic start temperature is low the martensite is massive, while it is acicular when the martensitic start temperature is high. The martensitic start temperature is function of the starting structure and the homogeneity of the microstructure.

In some cases, depending on the cooling rate, the amount of alloy elements and internal stresses, the transformation of the  $\beta$  phase in  $\alpha$  phase goes through a precursor  $\omega$  phase [3]. Both  $\alpha$  and  $\omega$  phase have a hexagonal structure as it is possible to see in Figure 2.6, nevertheless, the transformation between  $\alpha$  and  $\omega$  phase causes a distortion of the crystallographic lattice and a change of the

interstitial impurity sites. Each phase contains an octahedral (o), tetrahedral (t), and hexahedral (h) sites for interstitial impurities. The octahedral site of  $\alpha$  phase transforms into the octahedral and hexahedral sites of  $\omega$  phase. The octahedral site is the one occupied by O, C or N impurities in both phases. As it will be mentioned below in Paragraph 2.3.4 about the boronizing process, the  $\omega$  phase can be relevant for the diffusion of elements into the titanium and its alloy substrate. The sites indexed as A and B in the  $\omega$  phase, instead, are two substitutional impurity sites resulting from the unique substitutional impurity site of  $\alpha$  phase. These are sites occupied by Al and V impurities.

The presence of all these impurities causes a retard of the martensitic transformation [4].

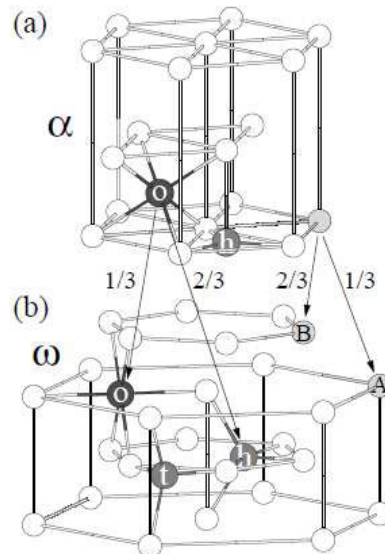


Figure 2.6 Microstructure of  $\alpha$  and  $\omega$  phase [4]

Thermal treatments at temperatures below the martensitic start temperature in the  $\alpha+\beta$  field, instead, influence the thickness of the  $\alpha$  lamellar, but there are not further martensitic transformations (Figure 2.7).

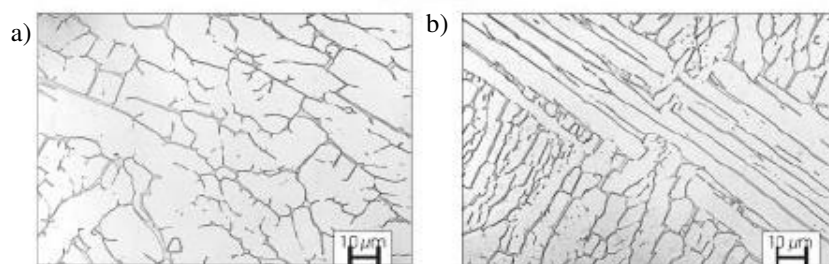


Figure 2.7 Microstructure of Ti6Al4V alloy a) furnace cooling and b) water quenching from 600°C [2]

A equiaxed microstructure is obtained through a recrystallization process. This process requests a mechanical deformation of the material and a subsequent solution heat treatment in the  $\alpha+\beta$  field. Temperatures of treatment closed to the  $\beta$  transus temperature lead to a bimodal microstructure composed of equiaxed primary  $\alpha$  and  $\alpha$  lamellar, while a pure equiaxed primary  $\alpha$  microstructure is obtained at lower temperatures (Figure 2.8) [2].

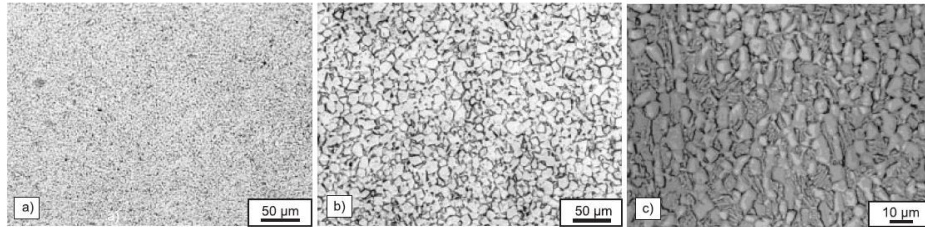


Figure 2.8 Microstructure of Ti6Al4V alloy a) fine equiaxed, b) coarse equiaxed and c) bimodal [2]

The microstructure and the chemical composition have effects on the properties of titanium alloys. Table 2.1 shows the main properties of titanium and its alloys in function of the microstructure [2].

Table 2.1 Properties of titanium and titanium alloys [2]

Property	$\alpha$	$\alpha+\beta$	$\beta$
Density	+	+	-
Strength	-	+	++
Ductility	-/+	+	+/-
Fracture toughness	+	-/+	+/-
Creep strength	+	+/-	-
Corrosion behaviour	++	+	+/-
Oxidation behaviour	++	+/-	-
Fatigue strength	+	+/-	-
Wettability	+	+/-	-
Cold formability	--	-	-/+

Some properties depend mainly on the crystal structure of the alloy, such as density, ductility and plastic deformation. The hcp structure is more densely packed than the bcc structure, the number of slip system is 3 for the first one and 12 for the second one. As consequence, there is a reduction of ease of plastic deformation and ductility of the  $\alpha$  alloys compared to the  $\beta$  alloys.

Other properties, such as strength, creep strength and fatigue strength, depend also on the microstructure. For example, fine microstructure increases the strength and retards crack nucleation, while coarse microstructure increases the creep strength and slows down fatigue crack growth. Equiaxed microstructure has high fatigue strength, while lamellar microstructure present high fracture toughness and high resistance to creep and fatigue crack growth [2].

Generally, titanium and its alloys are widely used in particular for their high strength to weight ratio, good corrosion resistance and bio-compatibility. The limit

to their use depends on the poor tribological properties, such as: high and unstable friction coefficient, abrasive wear and low resistance to adhesion and fretting wear.

## 2.2 Wear mechanism

Generally speaking, when titanium surface is put in contact under motion with another surface (ceramic, polymeric or metallic), several wear mechanisms can occur individually or combined: adhesive wear, abrasive wear, fatigue wear, fretting and corrosion. The mechanical damage caused by wear induces an alteration of the passive layer, that grows on titanium surface naturally when the material is in contact with an environment rich in oxygen, that is why tribo-corrosion phenomena are of great relevance [2].

### 2.2.1 Adhesive wear

The effective contact area between two surfaces depends on their topography, roughness, elastic and plastic properties and on the acting force. The real contact happens between surface asperities, so the real contact area is smaller than the apparent one [5].

At the points of contact, during the sliding of the two surfaces, asperities become flatten by plastic deformation, adhesion and cold welding occur, causing a cyclic growth and breaking out of junctions between the two surfaces. The rupture of junctions causes material transfer from one surface to the other and in some cases the formation of particle debris [6].

The transfer phenomenon depends on the micro topography of the surfaces, in particular on roughness and presence of surface defects. Transferred material formed micrometer sized smooth patches on the counterface after the first passages, then the next sliding steps cause the formation of large smooth patches on different surface levels. As consequence, there is an increase of surface roughness and the detachment of particle debris. The harder particles and asperities can groove the softer surface, in this way the effect of the abrasive wear overlaps the one of adhesive wear [7].

The adhesive wear mechanism is shown in Figure 2.9.

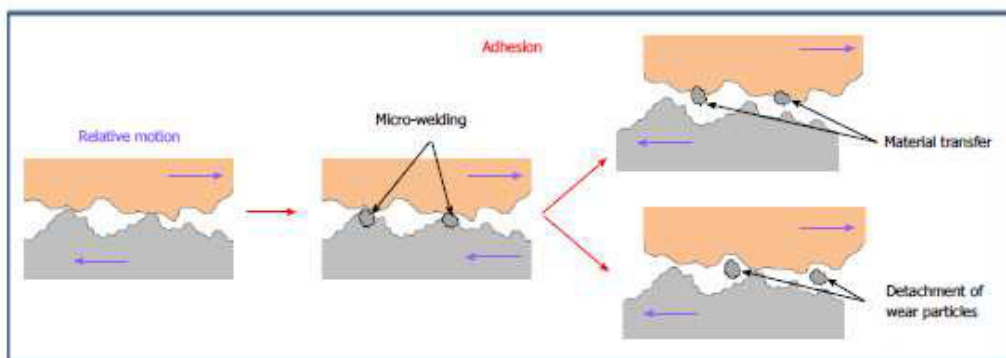


Figure 2.9 Adhesive wear mechanism [8]



The adhesive wear can be explained by the theoretical law introduced by Archard on 1953. The total wear  $Q$  results to be:

$$Q = KN/H \quad (1)$$

Where  $K$  is the wear coefficient,  $N$  is the total load and  $H$  the hardness of softer material.

$K$  and  $N$  depend on the mechanism of wear. In case of adhesive wear, the contact area is supposed to be made up circular spots, in this case  $K$  and  $N$  correspond to:

$$K = k/3 \quad (2)$$

$$N = n\pi a^2 \quad (3)$$

Where  $k$  is the fraction of contacts that produces wear particles,  $n$  is the number of produced particles and  $a$  the radius of contact asperities.

As concern the practical mechanism, junctions grow between the thin oxide layer that usually cover a metallic surface: during rubbing, the oxide is removed and the metal substrate is exposed, then in contact to the atmosphere the metal re-oxidizes. When the process of re-oxidation predominates, an oxide film splits the two sliding surface and, as a result, friction and wear are low, surfaces are smooth and debris correspond to the oxidised particles. When the oxide removal process predominates, instead, surfaces undergo to wear (scuffing, galling and seizure), become rough and produce metal debris. In this case, adhesive mechanism is associated to abrasive mechanism, caused by transferred material and particles debris [5].

The force necessary to break up the junctions corresponds to the friction force, therefore stronger the junctions, greater is the friction. Moreover, during the sliding contact the friction level increases more or less gradually due to the material transfer [7].

In particular, titanium and its alloys show a stick-slip behaviour (Figure 2.10) due to their high adhesion tendency during sliding. As the tangential forces increase, the contact area increases too, junctions grow between the surfaces, that show stick, remaining in adhesive contact. The slip occurs when the applied force exceeds the adhesive strength, breaking the junctions. This mechanism is associated to the transfer of material onto the counterpart and to an abrasive action of the transferred material. This phenomenon can explain the high and unstable friction coefficient of titanium and its alloys [6].

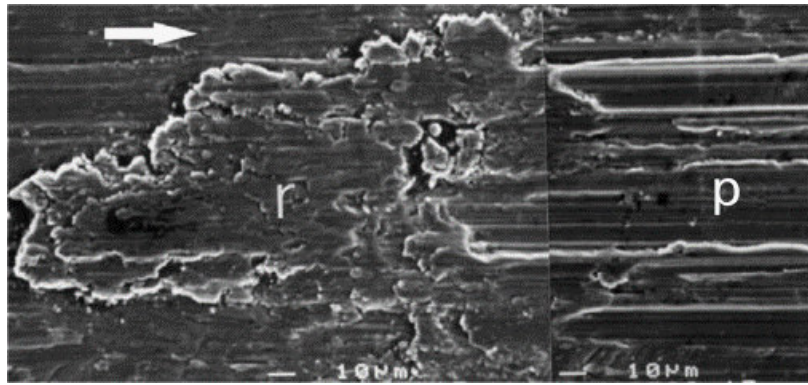


**Figure 2.10** Wear tracks of Ti6AL4V disk after unidirectional sliding against a WC ball slider in air. r points out the adhesive spots, while p the grooves due to the ploughing [6]

The adhesive process is related to plastic deformation and ductility of the metal, that respectively depend on its crystal structure and microstructure [6].

The commercially pure titanium is a  $\alpha$  metal, but its crystal lattice ratios make it behaves more similar to a cubic metal, showing a high ductility, easy plastic deformation and low tribological properties and as consequence a low wear resistance. Considering the titanium alloy family and taking into account the crystal structure and the relative mechanical properties (Table 2.1), the  $\beta$  alloys show a lower adhesive resistance than the  $\alpha+\beta$  alloys due to their higher ductility [9].

Another factor that influences the wear process of titanium and its alloys is the ineffectiveness of the main common lubricants with these materials. In general, lubricants act reducing friction and wear. The presence of a lubricant film between the surfaces can reduce adhesion, friction heating and prevent three-body abrasion by carry wear debris away [5].

In case of titanium, during contact it undergoes to a boundary lubrication because the oxide layer does not adsorb lubricant molecules in an effective way. This issue is enhanced by the low thermal conductivity of titanium: at the contacting surfaces, the temperature increases causing a partial desorption of the boundary lubricant [2]. Moreover, the low thermal conductivity, allowing the accumulation of thermal energy at the surfaces interface, promotes the plastic deformation and the diffusion and growth of junctions between the surfaces, thus the adhesive wear tendency [6].

### 2.2.2 Abrasive wear

The abrasive wear consists in the removal of material from a softer surface by harder asperities under load. It is classified into two-body abrasion and three-body abrasion: in the first case the harder material ploughs the softer material, while in the second case hard particles located at the interface between the two surfaces, damage one or both the surfaces [5]. The two wear mechanisms are shown in Figure 2.11.

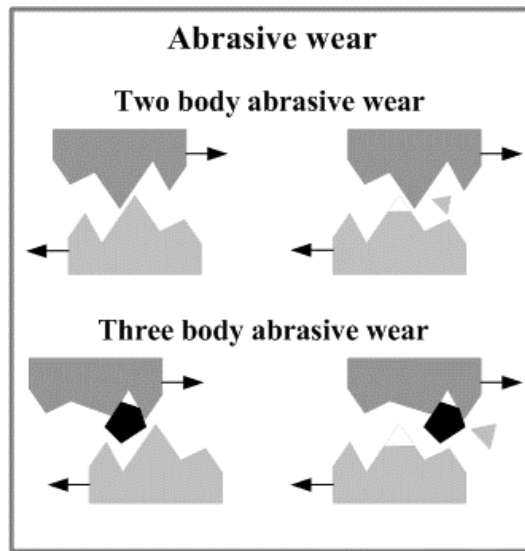


Figure 2.11 Two body and here body abrasive wear mechanism [10]

The surface damage at the micro-level can be classified in ploughing, cutting and cracking. In the first case, the material is not removed but it is shifted to the sides of the grooves, in the second case the volume of removed material from the surface is equal to the one of the wear track. In the third case, instead, the volume of removed material is higher than the one of the wear track, due to the creaking of the subsurface areas around the grooves [10].

The abrasive wear can be explained by Archard's theoretical law (eq. 1), as well as the adhesive wear.

In this case the hard asperities are considered to have a conical shape with a semi top angle of  $\theta$  as it is shown in Figure 2.12.

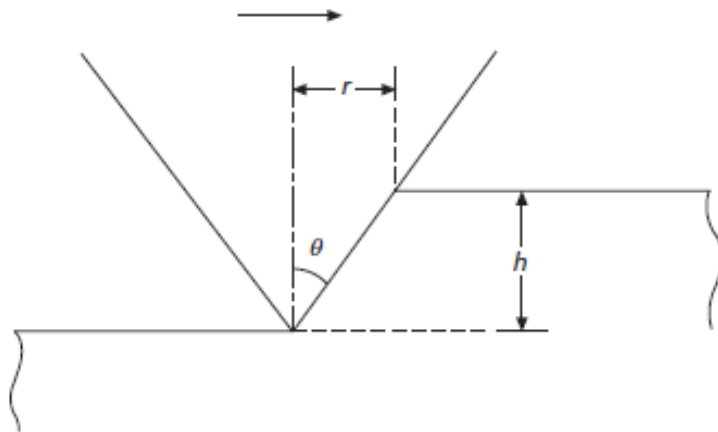


Figure 2.12 Softer surface ploughed by a hard conical asperity [5]

In this case,  $K$  and  $N$  result to be:

$$K = k \tan \theta / \pi \quad (4)$$

$$N = 0.5\pi r^2 H \quad (5)$$

Where  $k$  is the fraction of contacts that produces wear particles,  $n$  is the number of produced particles and  $r$  the distance as Figure 2.11 shows.

Titanium and its alloy are considered soft materials, thus they have a poor abrasive wear resistance. As mentioned in the previous paragraph, the abrasive wear can be a consequence or overlaps to the adhesive wear due to the transfer of material between the surfaces [6].

### **2.2.3 Fatigue wear**

Fatigue wear is related to cyclic movements and defines the lifespan of a material. Fatigue occurs at the macroscale between non-conforming surfaces under load and at the microscale at the contact asperities.

The repetition of stress cycling causes an accumulation of fatigue damage and thus the propagation of fatigue cracks. The crack propagation process shows two phases, a first stage of microcrack growth, followed by a second stage of macrocrack growth. This phenomenon causes a fatigue failure and the production of wear fragments. During the contact, asperities are subjected to elastic deformation and sub-surface stresses. These stresses cause local plastic deformations, that results in an accumulate damage from which a local fatigue failure derives. This wear process can explain the wear of harder material by softer one [2,5].

The fatigue strength is also affected by the mechanical surface treatments. Treatments such as deep rolling, shot peening and mechanical polishing act on surface roughness, dislocation density and residual stresses. Fatigue strength can behave as primary crack initiator, when the surface is smooth or as crack propagation controlled, when surface is rough. In addition, when cracks are present, the propagation of microcracks is deferred in presence of compressive residual stress on surface [2].

In the case of titanium and its alloys, the fatigue strength as well as fatigue wear resistance depends strongly on the microstructure of the alloy, in particular they are influenced by grain size, phase dimension, phase morphology, elastic modulus, crystallographic texture, interstitial oxygen content, degree of work hardening and age hardening condition.

In the case of titanium and  $\alpha$  alloys, the fatigue strength is mainly influenced by the  $\alpha$  grain size, interstitial oxygen content and degree of age hardening. The reduction of grain size as well as the increment of the oxygen content and an age hardening process improves the fatigue strength. Nevertheless, the fine grained microstructures allow to hinder the propagation of microcracks, while the growth of macrocracks is mainly reduced in coarser microstructures.

The fatigue resistance of the  $\alpha+\beta$  alloys is also influenced by the morphology and the arrangements of the  $\alpha$  and  $\beta$  phases. This family of alloy can show a lamellar, equiaxed or bimodal (primary  $\alpha$  in  $\alpha$  lamellar matrix) microstructure, thus the main parameters that have to be taken into account are the  $\beta$  grain size and the colony size of  $\alpha$  and  $\beta$  lamellae, in addition to the  $\alpha$  grain/lamellae size, volume

fraction of primary  $\alpha$  oxygen content and age hardening process. The reduction of  $\alpha$  lamellar width or  $\alpha$  grain size allows to increase the fatigue strength. [2].

In case of  $\beta$  alloys, instead, the main factors that influence the fatigue strength are the  $\beta$  grain size, precipitate-free zones and degree of age hardening. The fatigue strength is increased by the reduction of  $\beta$  grains in lamellae, while it decreases, increasing the  $\alpha$  volume fraction, maybe due to the absence of a continuous  $\alpha$  grain boundary that can improve the cracks diffusion. The age hardening process influences the homogeneity of the precipitation of the  $\alpha$  phase within the  $\beta$  grains, thus the presence of precipitate-free zones. These areas are sites with lower local yield stress than homogeneous areas and where cracks can nucleate, therefore the lower the amount of these zones is, the greater the fatigue resistance [2].

Finally, the fatigue strength depends also on the degree of crystallographic textures and the direction of applied load. For example, the Ti6Al4V alloy with an equiaxed microstructure has the highest fatigue strength in case of mixed texture and load applied parallel to the rolling direction. While the lower fatigue strength is found in case of transversal texture loaded perpendicular to the rolling direction.

Figure 2.13 summarises the main factors that influence the fatigue strength.

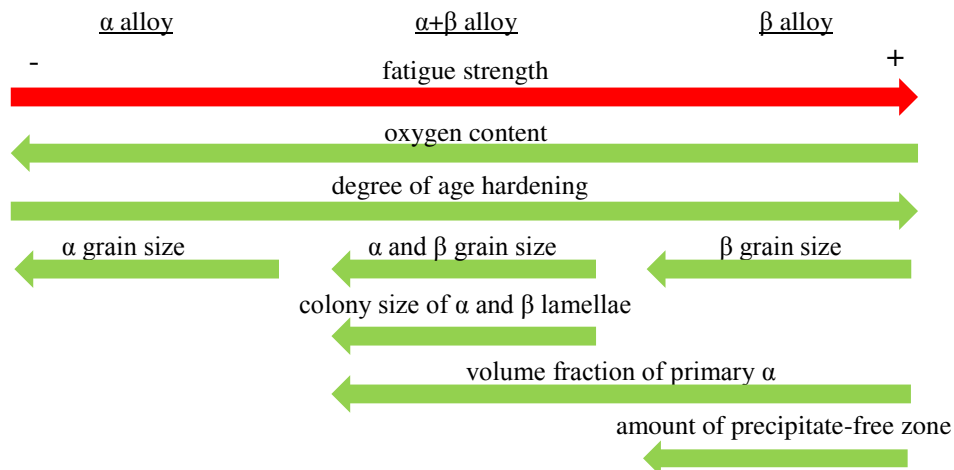


Figure 2.13 Summary of the factors acting on the fatigue strength

## 2.2.4 Fretting wear and fretting corrosion

Fretting wear is induced when under load the movements at the interface of two contacting surfaces are in the range of microns. The micromotions can involve the whole contact interface or only the areas near the edges of the contact zone with no slip in the central zone. In mechanical application different from artificial joints, fretting is also related to high frequency oscillators, but this is not the case.

The fretting wear is a combination of different wear mechanism such as adhesive, abrasive and oxidative wear that can occurs concurrently or subsequently. The oscillatory motions cause fatigue wear that can enhance the adhesive wear, moreover, in some case, when materials are in contact with an aggressive environment, fretting wear can combine with corrosion process and corrosion products can induce abrasive wear [5]. A tribocorrosion phenomenon, fretting corrosion, develops, due to the overlapping of chemical stimuli to mechanical stimuli [11].

Tribocorrosion phenomenon is controlled by the kinetic of passivation and re-passivation of the material; a strict wear can accelerate the corrosion of the surface material, vice versa corrosion can accelerate wear of the surface [12].

In the case of titanium and its alloys, the severity of this wear mechanism depends on the counterface material, the harder the opposite material is, the lower the fretting wear. Fretting damages act as crack initiator sites, causing a reduction of fatigue strength of the material [2]. Moreover, the material can be subjected to corrosion in a reactive environment, even if the rate of damage is usually low, due to the passive film on the metal surface. Nevertheless, when the surface presents defects or there is a damage of the passive film, a local corrosion, called pitting corrosion, can develop, due to the exposition of the bulk material.

A local form of corrosion similar to pitting corrosion is crevice corrosion, it takes places on gaps and contact areas between surfaces when there is stagnation of aggressive fluid [13].

The corrosion resistance of titanium and its alloys depends on many factors, such as alloying elements, formed oxides, microstructure of the bulk and thermal treatment applied to the material. Heat treatments can cause a redistribution of alloying elements and thus the development of singular oxide layers. The re-passivated film, in addition, results to be different from the native oxides film, due to the incorporation of ions from the surrounding environment during its growth and thus it changes by changing the environment [13].

Figure 2.14 shows an example of fretting wear on titanium surface.

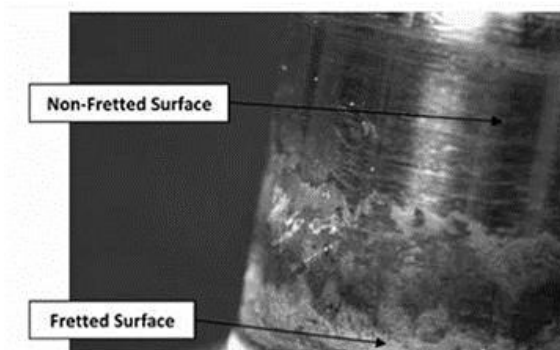


Figure 2.14 Fretting of the surface of a modular hip component [14]

## 2.3 Surface modification treatments

To enhance wear resistance of titanium and titanium alloys, different surface modification treatments have been investigated. The aim of these treatments is to obtain a hard and well adherent coating on titanium surfaces, because hardness results to be one of the main factor that defines the degree of wear resistance of bearing materials [15]. These treatments can be classified in Physical Vapour Deposition treatments, Chemical Vapour Deposition, thermomechanical, thermochemical and electrochemical treatments. On titanium and its alloys, the main deposited coatings are usually titanium carbides, titanium nitrides, titanium borides, diamond-like carbon and combinations of them.

**Table 2.2 Surface modification treatments and developed coatings**

Techniques	Process	Coating
Physical Vapour Deposition	Beam-line ion implantation	TiC - TiN/TiN <sub>2</sub> - TiO <sub>2</sub>
	Plasma immersion ion implantation	TiC - TiN/TiN <sub>2</sub> - TiO <sub>2</sub> - DLC
Thermal spray	Thermal spray	Al <sub>2</sub> O <sub>3</sub> - ZrO <sub>2</sub> - TiO <sub>2</sub>
	Cold spray	Al <sub>2</sub> O <sub>3</sub>
Chemical Vapour Deposition	Plasma Assisted Chemical Vapour Deposition	DLC
Laser surface modification		TiN - TiC
Thermochemical treatment	Ceramic Conversion Treatment	TiO <sub>2</sub>
	Boronizing	TiB/TiB <sub>2</sub>
	Nitriding	TiN
	Carburizing	TiC
Electrochemical treatment	Anodising	TiO <sub>2</sub>
	Plasma electrolytic oxidation treatment	TiO <sub>2</sub>
	Electrolytic boronizing	TiB/TiB <sub>2</sub>

### 2.3.1 Physical vapour deposition

Physical Vapour Deposition (PVD) is a class of processes used to deposit thin coatings, in which a target or combination of targets are evaporated by means of several techniques such as laser beam, arc discharge and plasma. The formation of the coating is due to the acceleration of the generated ions that impact and condense on the substrate to be coated. The process is usually carried out in vacuum to have as much as possible a collisionless pathway of the ionised atoms [16].

#### Beam-line ion implantation

Ions implantation is a PVD line-of-sight technique that allows to obtain thin coatings on substrates at low temperatures.

Facilities are composed of an ionisation chamber, an accelerator and a target chamber (Figure 2.15). Accelerated ions impact on the surface substrate generating a coating, which thickness can be between 10 nm and 1µm, in function of the process parameters [17,18].

It is a useful technique for modifying biomedical material, due to the low temperature and the good reproducibility of the process.

The ion penetration involves only the near-surface region, thus the bulk properties are not modified [19].

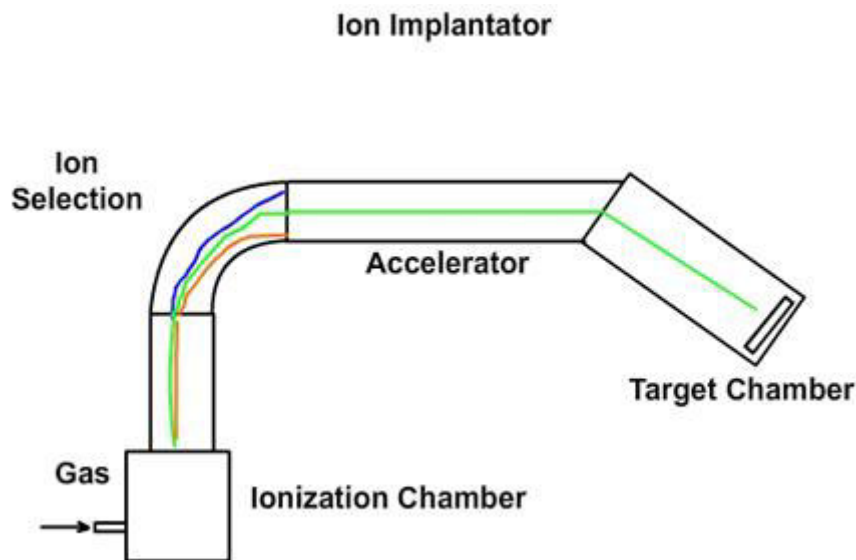


Figure 2.15 Equipment for ion implantation [17]

The main elements that are implanted on titanium are carbon, nitrogen and oxygen. Kustas et al. [18] report a ball on disk test performed testing a commercial pure titanium disk and a Ti6Al4V disk after ion implantation against a ruby ball. In case of commercially pure titanium substrate, nitrogen and carbon implantation have almost the same breakthrough load, while in case of Ti6Al4V alloy, nitrogen implantation is more effective than carbon implantation in enhancing breakthrough load. The relative data are reported in Figure 2.16.

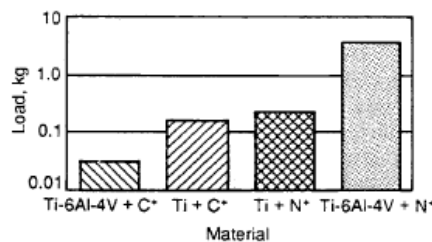


Figure 2.16 Breakthrough load of Ti and Ti6Al4V after C<sup>+</sup> and N<sup>+</sup> implantation tested against a ruby ball [18]

Schmidt et al. [20], instead, studied the tribological behaviour of Ti6Al4V against UHMWPE after ion implantation of carbon and nitrogen. They reached a hardness of 5.2 GPa and 6.4 GPa respectively after carbon and nitrogen implantation and in both cases no scratches of the surfaces were observed after more than 50000 revolutions of the polymeric pin on the coated metallic disk surfaces.

## Plasma immersion ion implantation

Plasma immersion ion implantation (PIII) is a simpler and cheaper evolution of the beam-line ion implantation. This technique allows to coat samples or devices with complex shapes; the thickness of the coating is from several nanometers to micrometers and the bulk properties are not modified as in the case of beam-line ion implantation.



The differences between the two techniques are that in PIII the samples are surrounded by a low temperature plasma and a high differential of potential is used (Figure 2.17).

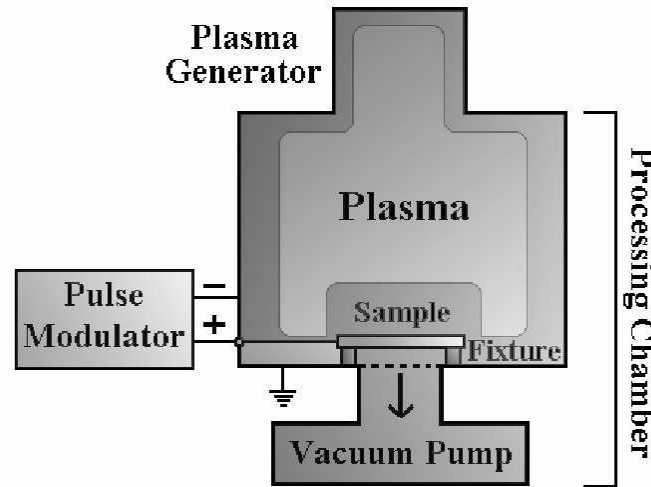


Figure 2.17 PIII process [21]

The plasma required by PIII is at low temperature and with high-density, generally, it is generated by electrical discharge, but depending on the nature of implanted ions it is classified into gaseous plasma discharge, glow discharge and metal plasma discharge.

PIII is a versatile technique that can be combined with other process, such as nitriding and deposition.

Nitriding PIII is one of the main technique used to enhance the hardness and wear resistance of titanium alloys. The process can be carried out by playing on several parameters, such as the bias voltage, substrate condition (heated or not heated) and the treatment time. The longer the treatment time is, the higher the hardness, as it is shown in Figure 2.18.

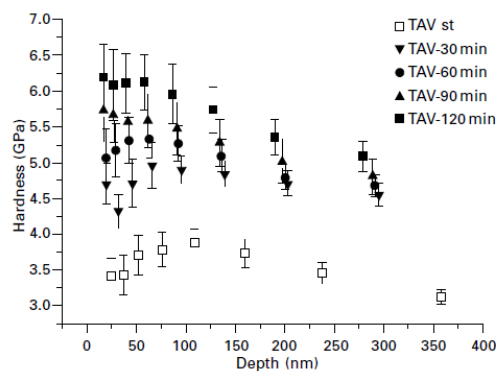


Figure 2.18 Hardness of Ti6Al4V subjected to nitrogen PIII at a bias voltage of 20 kV for different treatment times [22]

Without heating of the substrate, the thickness of the coating can be several tens of nanometers, while heating the substrate, the penetration depth of ions increases and reaches over than one hundred nanometers. Using a pure nitrogen gas, inclusion of carbon can occur, while by using a mixture of gases such as  $N_2/H_2$  it

can be avoided. Generally, this process causes a change of the surface morphology, due to a sputtering damage. This is more evident when a mixture of gases is used.

Concerning the titanium properties, hardness of surfaces treated by nitrogen PIII is several fold higher and the friction coefficient of the surface is reduced of one third. Nevertheless, the process has slight negative effect on the corrosion resistance.

Other process carried out on titanium alloy are oxygen and carbon PIII. Loinaz et al. [23] show that the oxygen implantation on Ti6Al4V substrate can increase the surface hardness. This leads to an improvement of the wear resistance. Pin on disk tests, where implanted Ti6Al4V alloy disks were tested against a UHMWPE pins, show that the friction coefficient is between 0.2-0.3 both for implanted and unimplanted Ti6Al4V disks, but the breakthrough resistance of the oxide layer is improved for implanted disks. The improvement of hardness depends mainly on the retained dose. The use of a denser plasma allows to generate high current intensities, that cause the heating of the substrate. As consequence there is an oxide diffusion that leads to the formation of oxide precipitates at deeper region and a greater enhancement of the hardness. This process, nevertheless, causes also an increment of the roughness of the surface, that has bad effect on the friction coefficient. In fact, when the process is performed with a denser plasma the friction coefficient rises to a values of 0.5 and abrasive wear mechanism is observed, while on the surfaces of the others implanted disks no damages were visible.

The oxygen implantation was compared to nitrogen and carbon implantation by Han et al. [24]. In this case, it was observed that the carbon implantation allows to greater enhance the surface hardness of the Ti6Al4V alloy. At low load, where measurement is less affected by the influence of the substrate, because the penetration depth of the indenter is within the thickness of the implanted layer, the carbon implantation leads to an increment of the hardness of a factor higher than 1.5. While in case of nitrogen and oxygen the enhancement corresponds respectively to a factor of about 1.4 and 1.3.

PIII process on titanium can also be used to activate the surface and to make it bioactive [22], in fact, even if this technique allows to enhance the tribological properties of titanium, nowadays it is mainly employed to perform TiN and DLC thin coating on biomedical device to improve the biocompatibility and the hemocompatibility [21,25].

### **2.3.2 Thermal spray**

Thermal spray is a fast and relatively low cost process. It takes place in three steps (Figure 2.19), first of all a stream of melted or partially melted droplets is created, then particles are heated by a heat or power source and accelerated by a gas or plasma, finally droplets impact on the substrate, creating a lamellar coating through rapid cooling and solidification.

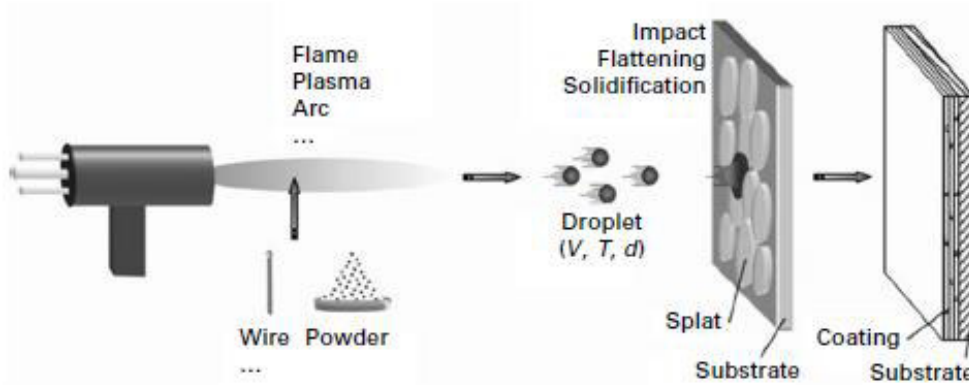


Figure 2.19 Thermal spray process [26]

The heating and the acceleration phase is an extremely crucial and important stage. During this phase, droplets have to acquire the opportune kinetic and thermal energy up to or over the melting point, in addition it is possible that particles interact chemically with the surrounding environment or with the flame atmosphere and undergo to oxidation or compositional change. This can alter the final properties of the coating.

On one side, this technique allows to work at low temperatures, the temperature of the bulk usually does not exceed  $150^{\circ}\text{C}$ , in addition, the process does not deform the shape of the samples or damage the substrate microstructure or the properties.

Changing the process parameters such as temperature, velocity and size of droplets, it is possible to obtain coatings with a thickness from several tens of micrometers to several millimetres; it is also possible to cover the whole surface or a local part.

On the other side, the coating results to be rough, so further surface finishes are necessary, moreover it presents a porosity up to 20% in function of the process parameters (the higher the velocity and the temperature are, the denser the coating). These interconnected pores can act as lubricant reservoir, but they also do not allow a corrosion protection of the whole surface. As last, the coating material is heated at very high and not perfectly controlled temperature with eventual degradation phenomena.

The coating is anisotropic with properties in longitudinal direction very different to the ones of normal direction to the surface and the adhesion to the substrate is lower compared to other techniques.

To coat samples with complex shape, it is necessary to use a multiaxial source, as it is a line-of-sight process.

Thermal spray is a class of process that change name in function of the kind of the heat source in use (gas flame, electric arc or plasma jets). The Table 2.3 reports the possible heat sources and their parameters.

**Table 2.3 Possible heat source for thermal spray and their parameters [26]**

Thermal spray methods	Temperature of heat source (K)	Particle velocity (m/s)
Powder flame spray	~ 3500	30 ~ 50
Wire flame spray	~ 3500	100 ~ 200
Detonation gun (D-gun)	4200	500 ~ 700
High-Velocity Oxy-Fuel (HVOF)	~ 3500	300 ~ 700
Air Plasma spray	10000 ~ 15000	100 ~ 400
Arc spray	5000 ~ 6000	100 ~ 200
Cold spray	RT ~ 900	300 ~ 1000

In general, thermal spray process is carried out at atmospheric pressure, while plasma spray can be performed in inert environment at a reduced pressure to prevent oxidation.

Thermal spray can be used on titanium and titanium alloy to create a hard coating to enhance the wear and corrosion resistance, nevertheless tensile adhesion results to be lower than 70 MPa for most thermal spray coating. Therefore this technique is mainly employed on implant for bioactive coatings such as hydroxyapatite and bioinert coatings such as  $\text{Al}_2\text{O}_3$ ,  $\text{ZrO}_2$  and  $\text{TiO}_2$  [26].

## Cold spray

Cold spray is a subcategory of thermal spray. The process is illustrated in Figure 2.20.

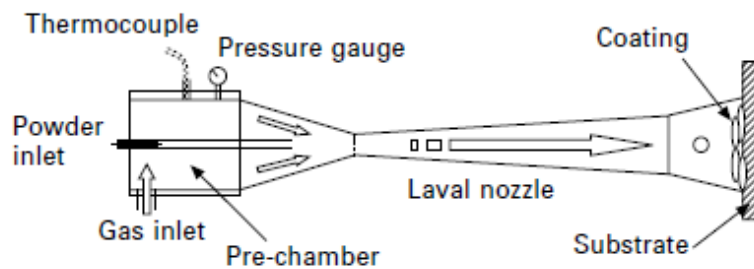


**Figure 2.20 Cold spray process [27]**

A high pressure gas is pre-heated and injected in the Laval nozzle, where particles are accelerated and impact against the substrate. The coating is obtained by plastic deformation of the particles during the impact.

The working temperature is between atmosphere temperature and  $700^\circ\text{C}$ , very below of the melting point of the particles, thus the process is performed in a complete solid state. This allows to avoid chemical reactions (oxidation and compositional changes) between particles and surrounding environment and solidification stresses [27].

No commercial coatings for biomedical applications are produced by means of this technique, nevertheless some study are being conducted for obtaining a dense  $\alpha$  alumina coating on titanium substrate for head and acetabular cup component. The aim is to combine the good mechanical properties of the titanium with the good tribological properties of the alumina.

The idea is a three steps process. The first step consists in depositing a 2  $\mu\text{m}$  layer of Al on Ti6Al4V alloy substrate by means of cold spray technique. In the second step the system must be subjected to a thermal treatment at 640°C for 1 h in air to develop an intermediate layer of  $\text{TiAl}_3$  for enhancing the adhesion. And finally, a micro arc oxidation treatment would be carried out to convert the Al layer into an alumina layer [28].

### **2.3.3 Chemical vapour deposition**

Chemical Vapour Deposition (CVD) is a class of deposition techniques for thin films. The process is performed in a chamber at high temperature. The source material is a gas that reacts with the heated substrate, developing a solid product and a gas. The first is deposited on the substrate, generating the coating; the second is evacuated from the chamber. The chamber is filled with inert gas such as argon, nitrogen, helium that transport uniformly the gas precursor [16].

### **Plasma assisted chemical vapour deposition**

Plasma assisted chemical vapour deposition (PA CVD) is a CVD process in which the precursor reacting gas is ionised through a plasma generated by radio frequency (Figure 2.21). This process allows to work at lower temperature respect to the traditional CVD technique. This allows to reduce the possibility to damage the substrate and to use a wider range of materials both as substrates and precursors [16].

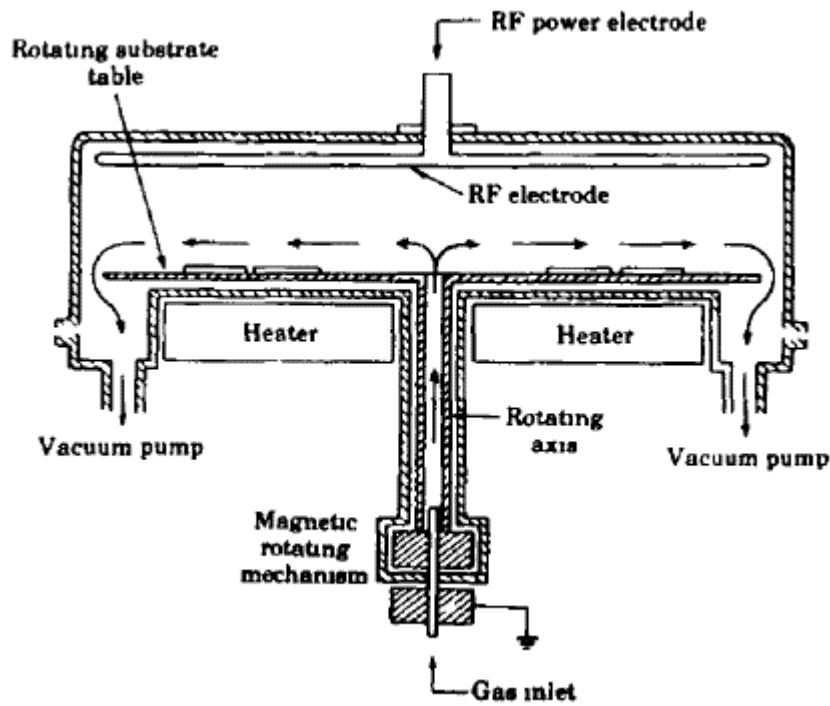


Figure 2.21 PA CVD process [16]

PA CVD is the main process used to deposit diamond-like carbon (DLC) coating of some microns on titanium substrates.

DLC is a metastable form of amorphous carbon. It is composed of  $sp^2$  bonds like graphite and  $sp^3$  bonds like diamond. It is a material with a wide range of applicability due to its interesting properties, such as high biocompatibility, haemocompatibility, anty-trombogenicity, high hardness, good wear and corrosion resistance, low friction coefficient and self-lubricant behaviour. The mechanical properties of DLC are controlled by the  $sp^3$  bond fraction and the content of hydrogen. Tailoring the composition of DLC it is possible to obtain coating with different properties in function of the desired application. Possible gases used to deposit DLC coating are methane and acetylene [29,30].

DLC coatings are employed on the articulating surface of medical-grade titanium and Ti6Al4V alloy as protective coating for wear, corrosion and ion release. The increment of the wear resistance of both the substrate was confirmed by Kim et al. [31]. A pin on ball test was performed, putting in contact a ruby ball against a commercially pure titanium and Ti6Al4V disk with DLC coating of  $1\ \mu\text{m}$ . The test was carried out both in dry and lubricated conditions. In both cases, for both the substrates a reduction of the wear rate was observed in comparison to the data of the test performed on uncoated substrates (Figure 2.22).

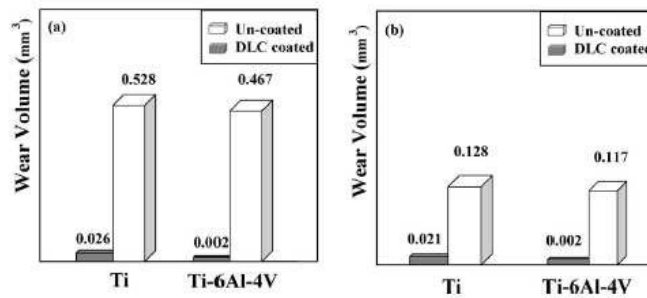


Figure 2.22 wear volume in a) dry and b) lubricated condition after 3000 cycles [31]

The wear rate is the same for the coated substrates in both the test conditions, nevertheless differences were observed as regards the number of cycles that the coatings borne before the failure (Figure 2.23).

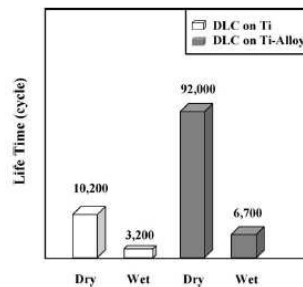


Figure 2.23 Number of cycles before the DLC failure [31]

In dry condition the coated Ti6Al4V shows a high wear resistance and the substrate was damaged only after the completely damaged of the DLC coating. In case of commercial pure titanium cracks and delamination were observed at a low number of cycles. This can be due to the soft nature of the commercially pure titanium that under load deform plastically and it is not followed by the rigid coatings. In wet condition, instead, both the coated substrates bear a low number of cycles before failing. The humid environment dramatically reduced the wear resistance of the DLC coating.

This phenomenon, whose causes are not well-defined yet, can explain the reported failure of DLC coatings in orthopaedic implant. Retrieved femoral head can show delamination or spallation of the coating or moreover pits on the surface coated [32].

### 2.3.4 Laser surface modification

Laser surface modification is a class of treatments in which a laser is used to heat the surface of a substrate, to modify it and to enhance its properties. Different results can be achieved by varying the process parameters such as the laser power, beam radius and mode (stationary or pulse), samples velocity, concentration and composition of alloying additives and concentration and flow rate of the gas.

The process is called laser surface melting when there is a modification of the surface without alterations of the surface chemical composition. In this case, the laser is used to heat the surface, the near-surface melts developing a liquid phase, inside which an inter-diffusion starts. The hardening is due to the rapid

solidification of the surface, that induces crystalline defects and residual stresses. The last ones can be reduced by post thermal treatment of the substrate at low temperature. When this process is applied on a Ti6Al4V substrate, the surface exhibits a titanium oxide film that increases the wear resistance of the material.

When the laser is used to melt an alloy addition onto the surface the process is called cladding. The alloy addition that can be powder, wire or foil, is melted in the highest possible concentration with a thin layer of the substrate. After the solidification phase a layer with strong metallurgical bond with the substrate and an increase hardness is obtained. This technique allows to cover both large and small areas and to precipitate borides, carbides, nitrides and silicides both single or combined.

Laser surface modification usually is performed in an inert environment to avoid oxidation of the substrate. In particular case when the substrate is a metal related to oxygen. When the substrate is titanium or titanium alloy it is possible to replace the inert gas with nitrogen. In this case, the process is referred to laser nitriding and it is described in Figure 2.24.

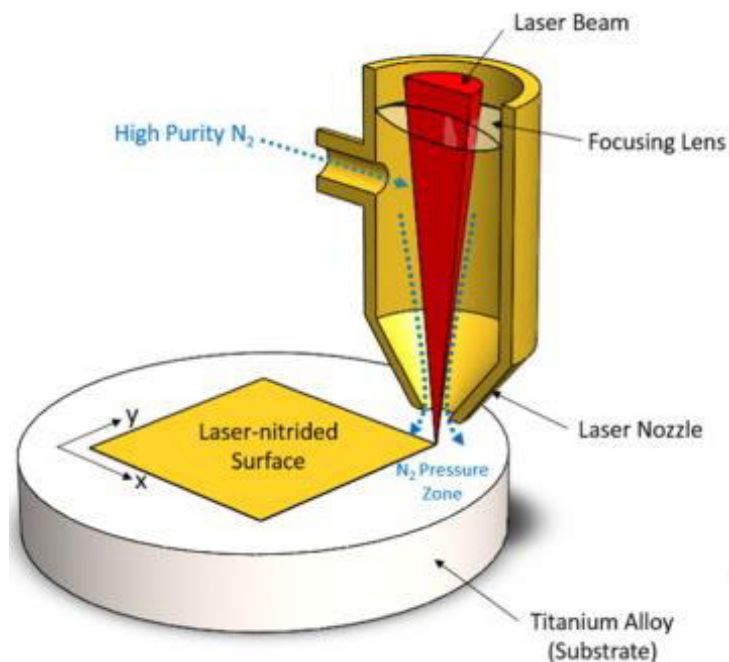


**Figure 2.24 Laser nitriding process [33]**

Laser nitriding on titanium or titanium alloy surface using a 100% nitrogen atmosphere allows to obtain a coating 5-10  $\mu\text{m}$  thick, with hardness between 1000-2000 HV, improved wear and corrosion resistance and low friction coefficient [34]. The tribological properties of nitride commercially pure titanium by means of pulse laser were investigated by Ettaqi et al. [35]. A ball on disk test was performed testing the nitride titanium disk against a ruby ball. Three kinds of nitriding process were followed: gas nitriding under nitrogen flow, melting of a pre-deposited TiN powder layer and the combination of gas nitriding and melting of TiN powder. Comparing the friction coefficient of the nitride samples with the untreated one it was observed that in all cases the friction coefficient was reduced. The nitride



samples have a friction coefficient between 0.2-0.4 while the untreated one shows a friction coefficient of 0.6. (Figure 2.25).

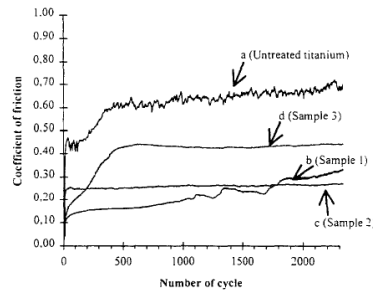


**Figure 2.25** Trend of the friction coefficient of a) untreated titanium, b) nitride titanium by melting of a pre-deposited TiN powder layer, c) nitride titanium by gas nitriding and d) nitride titanium by mix process [35]

Nevertheless, the nitride coatings often present cracking. This issues can be reduced or avoid by pre-heating the substrate in order to reduce the cooling rate and controlling the amount of residual stresses or by using a dilute nitrogen atmosphere. The last solution allows to avoid the formation of cracks, but reduces the final surface hardness.

It is possible to use the same process to obtain TiC coating, in this case nitrogen atmosphere is substituted by CO<sub>2</sub>. A TiC hardened layer was obtained on Ti6Al4V substrate by Saleh et al. [36]. The properties of the TiC layer were dependent on the used type of laser and power. The higher the power is, the higher the carburised depth, but lower the surface hardness. With low power (1-1.5kW) surface hardness of 1050 HV was reached, nevertheless the hardness decreased fast from the surface to the bulk, while using higher power (3 kW) the hardness resulted to be 650 HV up to a carburised depth of about 0.5 mm. In any cases, the hardness of the substrate (200 HV) was improved.

It is also possible to mix N<sub>2</sub> and CO<sub>2</sub> atmosphere, in this case the coatings have wear resistance higher than the one reached by coatings obtained with single gases. This process can also be combined with cladding to obtain coatings without any cracks [34].

### 2.3.5 Thermochemical treatments

#### Ceramic conversion treatment: oxidation

Conversion ceramic treatment is a thermal oxidation process performed in a controlled atmosphere containing oxygen at 550-650°C for 50-120 h. It is also possible to carry out the process at higher temperature such as 700-900°C for a shorter time, that means some hours in a gas mixture or in plasma.

During the process, the titanium surface reacts with oxygen, oxygen diffuses into the substrate, creating a harder interstitial solid solution, while the surface is converted into a TiO<sub>2</sub> rutile layer. Coating results to be composed of a thick oxygen diffuse zone of about tens of microns and a thin, dense e adherent oxygen layer of about some microns. The thickness of the coating can be increased, increasing

temperature and time of treatment, nevertheless damage of the surface and porous and poorly adherent coatings can be obtained by using too high temperature and too long time of treatment.

This treatment allows to increase hardness and wear or fretting resistance and to reduce the friction coefficient of titanium and its alloys. In case of Ti6Al4V, hardness of 106 GPa and young modulus of 146.7 GPa can be reached. While the friction coefficient results to be 0.1-0.2 in lubricated condition and 0.2-0.3 in dry condition for the Ti6Al4V after conversion ceramic treatment in a ball on disk test against a WC ball. The corresponding values for the untreated Ti6Al4V are 0.5-0.6 and 0.4-0.5 respectively in lubricated and dry conditions.

On one side, the rutile layer enhances wettability by lubricants, the corrosion resistance and the resistance to galling and scuffing of titanium and its alloys. While on the other side, there is a reduction of fatigue properties, due to the rough surface and the presence of residual stresses after the treatment. Residual stresses are caused by the different elastic modulus between the substrate (about 114 GPa) and the ceramic layer (230 GPa). They can lead to the formation of cracks both within the rutile layer and at the interface between the compact layer and the diffusion zone.

It is an effective technique to avoid or reduce the hydrogen-induced embrittlement of titanium surface that allows UHMWPE to damage titanium surface when these materials are put in contact under motion and load [37].

## **Boronizing**

Boronizing is a thermochemical treatment, based on the diffusion of boron into a metal substrate to form a hard borided layer on the surface. During the process, boron atoms diffuse into the substrate forming intermetallic compounds. The chemical composition of the coating depends on several parameters such as the chemical composition of the substrate, the concentration of boron donor and the time and temperature of the treatment. The thickness of the coating is time and temperature dependent; its growth follows a parabolic law:

$$x^2 = kt \quad (5)$$

Where  $x$  is the thickness of the coating,  $k$  a constant depending on the treatment temperature and  $t$  is the treatment time.

Boron diffuses into the substrate forming at the interface a columnar or tooth-like structure, this allows to enhance the adhesion of the coating compared to cementation and nitriding process.

This process allows to obtain a borided layer with high hardness, low friction coefficient and high melting point, that involves an increment of the wear, corrosion and high temperature oxidation resistance and mechanical strength.

The process is usually carried out between 700°C to 1200°C for a period of time from 1 h to 12 h by solid-state diffusion, liquids or gas atmosphere.

Table 2.4 shows the average thickness of the coatings in function of the boronizing process, boron donor, time and temperature of treatment and kind of substrate.

**Table 2.4 Thickness of borided coatings**

<b>Boronizing process</b>	<b>Substrate</b>	<b>Boron source</b>	<b>Time and temperature ranges</b>	<b>Thickness range (<math>\mu\text{m}</math>)</b>
Pack boronizing [38]	Steel	90% B <sub>4</sub> C +	850°C 4 h	20-80
	Ti6Al4V	10% KBF <sub>4</sub>	900°C 4 h	3-5
Pack boronizing [39]	cp-Ti	50% B + Na <sub>2</sub> CO <sub>3</sub> + C	800-1100°C 1-24 h	10-80
Pack boronizing [40]	Ti6Al4V	50% B + 15% Na <sub>2</sub> CO <sub>3</sub> + 35% C	750-1050°C 2.5-4.5 h	4-28
		70% Na <sub>2</sub> B <sub>4</sub> O <sub>7</sub> + 30% B <sub>4</sub> C		105-150
Electroless liquid boronizing [41]	Steel	65% Na <sub>2</sub> B <sub>4</sub> O <sub>7</sub> + 10% B <sub>4</sub> C + 10% SiC	900-950°C	90-130
		65% Na <sub>2</sub> B <sub>4</sub> O <sub>7</sub> + 35% SiC		70-100
Gas boronizing [42]	Steel	HB <sub>3</sub> N(C <sub>2</sub> H <sub>5</sub> ) <sub>3</sub>	800-1000°C	5-12

In the solid-diffusion process the boron donor can be solid powder or paste.

When boron is added as a solid powder, the process is called pack boronizing. In this case the samples are embedded into the powder mixture into a crucible, that have to be sealed. Then, the samples are thermally treated in a furnace at the desiderate temperature and for the suitable time in an inert or vacuum environment to avoid oxidation. The mixture of powder is usually composed of a boron donor (amorphous boron, ferrous boron or boron carbide), an activator (NaBF<sub>4</sub>, KBF<sub>4</sub>, (NH<sub>4</sub>)<sub>3</sub>BF<sub>3</sub>, NH<sub>4</sub>Cl, Na<sub>2</sub>CO<sub>3</sub>, Na<sub>2</sub>B<sub>4</sub>O<sub>7</sub> and BaF<sub>2</sub>) and a filler or diluent (activated carbon, silicon carbide or alumina) [43].

The main commercial powder compositions for boronizing are reported in Table 2.5.

**Table 2.5 Commercial powder composition for boronizing [44]**

Boron donor	Activator	Filler
5% B <sub>4</sub> C	5% KBF <sub>4</sub>	90% SiC
50% B <sub>4</sub> C	5% KBF <sub>4</sub>	45% SiC
85% B <sub>4</sub> C	15% Na <sub>2</sub> CO <sub>3</sub>	
95% B <sub>4</sub> C	5% Na <sub>2</sub> B <sub>4</sub> O <sub>7</sub>	
84% B <sub>4</sub> C	16% Na <sub>2</sub> B <sub>4</sub> O <sub>7</sub>	
Amorphous Boron		
5% Amorphous Boron	5% KBF <sub>4</sub>	

When the boron source is a paste, the process is similar: the paste is applied on the surface to be treated, lets dry and then the samples are treated as in the pack boronizing. At the end, the past needs to be removed by washing, blast cleaning or brushing [43]. Common pasts contain 55% B<sub>4</sub>C and 45% cryolite or commercial boron powder mixture (B<sub>4</sub>C-KBF<sub>4</sub>-SiC) in nitrocellulose dissolved in butylacetate or an aqueous solution of methyl cellulose [41].

In case of a liquid boronizing the component to be coated is dipped in a salts bath. This process is not useful for components with complex shape and low resistance to thermal shock. The immersion and removal of the component from the molten salts can cause distortions and cracks. Moreover, it has high maintenance costs for the recharging of the salts bath and the cleaning of the components after the treatment. It is important to recharge the salt bath for the repeatability of the treatment and to well clean the components to remove the unreacted boron and the excess salts. The process can be a electroless or electrolytic treatment. In the first case, the process is thermochemical and it is based on the reduction of molten borax. The borax has a melting point around 741°C, thus the process is usually carried out at temperatures higher than 900°C. in Table 2.6 are reported the main common salts bath compositions.

**Table 2.6 Common salts bath composition for electroless liquid boronizing**

Boron donor	Reducer
70% Na <sub>2</sub> B <sub>4</sub> O <sub>7</sub>	30% B <sub>4</sub> C
65% Na <sub>2</sub> B <sub>4</sub> O <sub>7</sub>	25% SiC + 10% B <sub>4</sub> C
65% Na <sub>2</sub> B <sub>4</sub> O <sub>7</sub>	35% SiC

In the second case, the process is electrochemical and it is described in paragraph 2.3.4 [41].

Using a boron source in the gas form (BCl<sub>3</sub> or B<sub>2</sub>H<sub>6</sub>) is not very common, because the process results to be dangerous and toxic. It consists in a thermal decomposition of B<sub>2</sub>H<sub>6</sub> or in the reduction of BCl<sub>3</sub> with hydrogen [41].

Generally speaking, the boronizing process carried out on titanium and titanium alloys substrates allows to obtain a hard coating composed of a monolithic upper layer, containing TiB and TiB<sub>2</sub> and whiskers penetrating the substrate

composed of TiB, TiB and TiB<sub>2</sub>, that are the main compounds between Ti and B as the phase diagram shows (Figure 2.26)

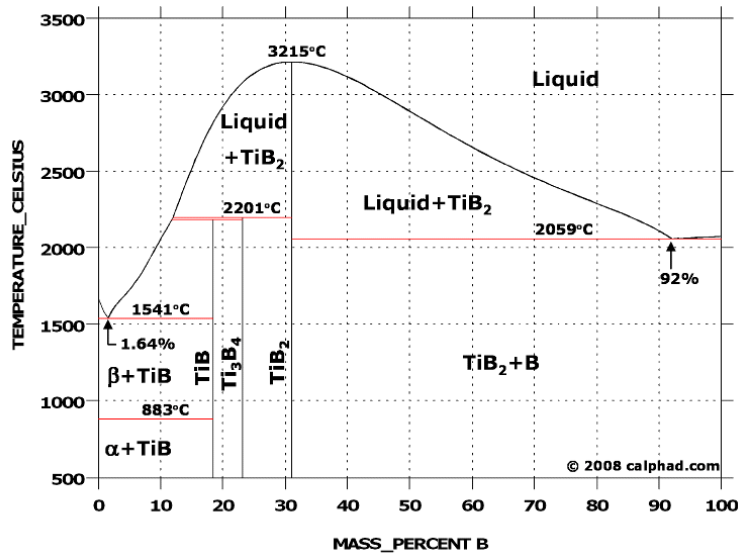


Figure 2.26 Ti-B phase diagram [45]

At the interface between the boron donor and substrate the following reactions take place:



At the beginning of the reaction and at the interface with the substrate, where titanium concentration exceeds, the reaction number (6) mainly develops, forming whiskers of TiB. The reaction number (7) is the main one during the formation of the external layer of the coating. The reaction number (8) is the one with the most negative free energy of formation and it is the reaction that occurs on a later stage, when the coated material is still in contact with an environment containing boron. When the concentration of boron in the reaction zone is less than 18wt%, Ti and TiB<sub>2</sub> can react again to form TiB, this reaction has a less negative free energy than the one of TiB<sub>2</sub>. [39].

When the process is performed in the α phase of titanium, TiB layer grows faster than TiB<sub>2</sub> layer, while in the β phase of titanium, a thicker TiB<sub>2</sub> layer is obtained. In addition, at the β transus temperature (temperature at which the transformation from α to β titanium phase occurs) an acceleration of the growth kinetic was observed. As consequence, a deeper penetration of whiskers is obtained for the treatment around the β transus temperature. This can be related to the enhanced self-diffusion of titanium near its β transus temperature, as Figure 2.27 shows.

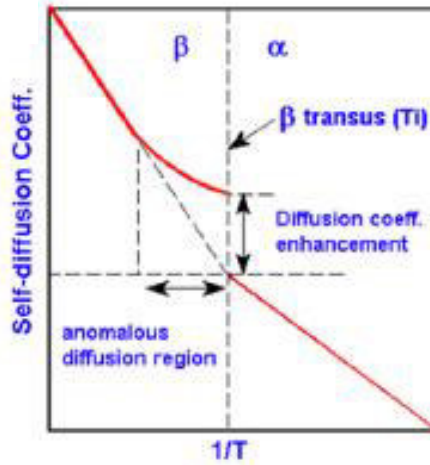


Figure 2.27 Self-diffusion of titanium in  $\alpha$  and  $\beta$  phases [3]

This phenomenon has been explained by Sanchez and de Forntaine, who suppose that the enhanced diffusivity is related to a  $\omega$ -like fluctuation at the  $\alpha \rightarrow \beta$  transformation point, where  $\omega$  is a precursor for the equilibrium of  $\alpha$  phase.

The  $\omega$  phase is a trigonal phase, which is metastable with respecting to an equilibrium mixture of ( $\alpha + \beta$ ) phases.

To explain this phenomenon, they modified the Arrhenius relation by introducing a factor related to the contribution of  $\omega$  fluctuation:

$$D = D_0 e^{\frac{-Q}{RT}} + D_0 e^{\frac{-\Delta S_m}{R}} c_\omega e^{\frac{-\Delta H_f}{RT}} \quad (9)$$

Arrhenius eq.  
Self-diffusion part

Contribution of  
 $\omega$  fluctuations

Where  $D_0$  is the frequency factor,  $Q$  the activation energy,  $R$  the ideal gas constant,  $T$  the absolute temperature,  $S_m$  the entropy of vacancy migration,  $c_\omega$  the concentration of  $\omega$  fluctuations and  $H_f$  the enthalpy of vacancy formation [3].

Hardness of the coating decreases from the surface to the diffusion zone and it is dependent on the volume of fraction of TiB phase: the higher the amount of TiB whiskers is, the higher the hardness [39].

The thermal expansion coefficient of Ti, TiB and TiB<sub>2</sub> are  $8.6 \times 10^{-6} \text{ K}^{-1}$ ,  $8.5 \times 10^{-6} \text{ K}^{-1}$  and  $8.1 \times 10^{-6} \text{ K}^{-1}$  respectively. This allows to reduce the residual stresses at the interface between substrate and coating and so to limit distortions at the interface and to decrease the probability of delamination of the coating.

Boronizing is a well-established process on steel to enhance the wear resistance for mechanical components and cutting tools. Nevertheless, this process can be also useful to improve the wear resistance and to reduce the friction coefficient of the titanium and its alloys.

The tribology of a borided Ti6Al4V alloy ball against an alumina disk was studied by Lee et al. in lubricated condition. The friction coefficient resulted to be 0.11-0.12, values closed to the one of the alumina ball (0.12) and lower than the one of the untreated Ti6Al4V alloy ball (0.3-0.4), tested as reference materials.

Tests and considerations about the friction coefficient of borided coatings on Ti6Al4V were also reported in the Chapter 5 of this research. The data confirm an improvement of the tribological properties of the titanium alloy.

## Gas Nitriding

Nitriding is a thermochemical process used to enhance wear, corrosion, friction and fatigue properties of some metals.

It is a diffusion process depending on time and temperature of the treatment. The nitrogen diffusion causes distortions and the growth of samples dimensions. To limit the distortions and not to damage the surface of the material temperature and time of treatment have to be opportunely tailored.

When this process is applied on titanium and titanium alloys substrates, the hardened layer results composed of  $Ti_2N$  and  $TiN$  with a diffusion zone containing interstitial solution of N and Ti (Figure 2.28). The diffusion zone allows to enhance the adhesion of the nitride layer, reducing the possibility of spalling [46].

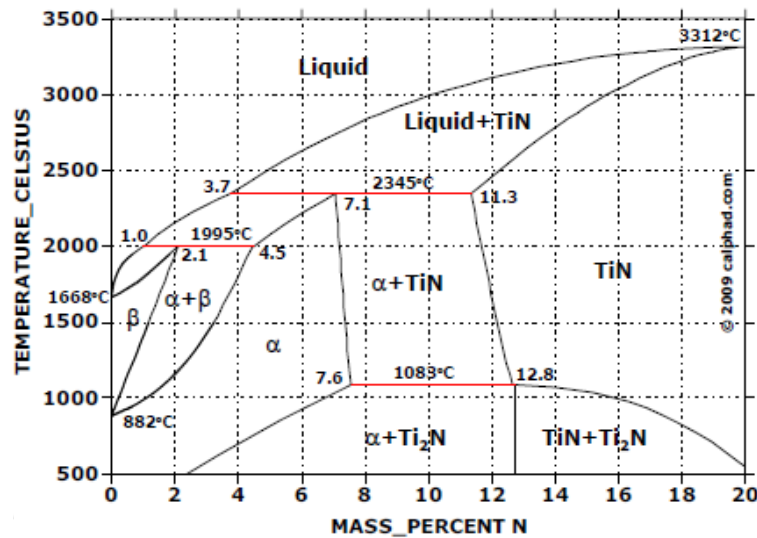


Figure 2.28 Ti-N phase diagram [45]

Working at temperature below the  $\beta$  transus temperature, the microstructure of titanium alloys is homogeneous. While working at temperature above the  $\beta$  transus temperature the microstructure of titanium alloys is inhomogeneous due to the phase transformation at the  $\beta$  transus temperature.

Generally speaking, the process is carried out between 650°C and 1000°C for 1-100 h and it allows to obtain coating of 2-15  $\mu m$  on Ti6Al4V alloy with hardness values of 450-1800 HV. The thickness and the hardness are mainly dependent on the time and temperature of treatment [47].

Table 2.7 compare the time and temperature of treatment and the thickness of the nitride coatings obtained through different techniques.

**Table 2.7 Temperature and time of treatment and thickness and hardness of the nitride coatings in function of the process [47]**

Process	Temperature	Time	Thickness ( $\mu\text{m}$ )	Hardness (HV)
Ion-beam nitriding (PVC)	500 – 900°C	30 min – 20 h	5 – 8	800 – 1200
Plasma nitriding (PVD)	400 – 950°C	15 min – 12 h	1 – 50	600 – 2000
Laser nitriding (PVD)	-	-	5-10	900 – 1300
Gas nitriding	650 – 1000°C	1 h – 100 h	2 – 15	450 – 1800

## Carburizing

Carburizing is a heat thermal treatment. It involves the diffusion of carbon into a metal substrate, with the formation of metal carbides used to increase wear resistance and strength of the material, without modifying the bulk properties.

The process consists on embedding the samples into the carbon source and heating them. The carbon source can be solid (mixture of carbon powder), liquid (cyanide) or gas (carbon monoxide gas). In case of a solid boron source, the metal surface reacts with carbon monoxide, produced during the heating by reduction of the powder compounds at the interface with the substrate. In case of a gas source, the carbon monoxide is blown into the furnace directly.

The hardened layer results to be composed of a combination of metal carbides and oxides. To avoid oxidation, it is also possible to work in an oxygen-free environment, performing the process in vacuum. This allows to carry out the process at higher temperature avoiding oxidation of the samples [48].

On titanium and its alloy substrates, a vacuum carburizing is usually performed due to the high affinity of titanium with oxygen. Nevertheless, Bailey and Sun [49] carried out a carburizing process in a controlled air environment to study the properties of the obtained hardened carbide layer. The process was performed in a muffle at 925°C for 20 h. A commercially pure titanium sample was embedded into a mix of powders composed of hardwood charcoal, barium carbonate, sodium carbonate and calcium carbonate in a sealed steel container, leaving oxygen inside (Figure 2.29).



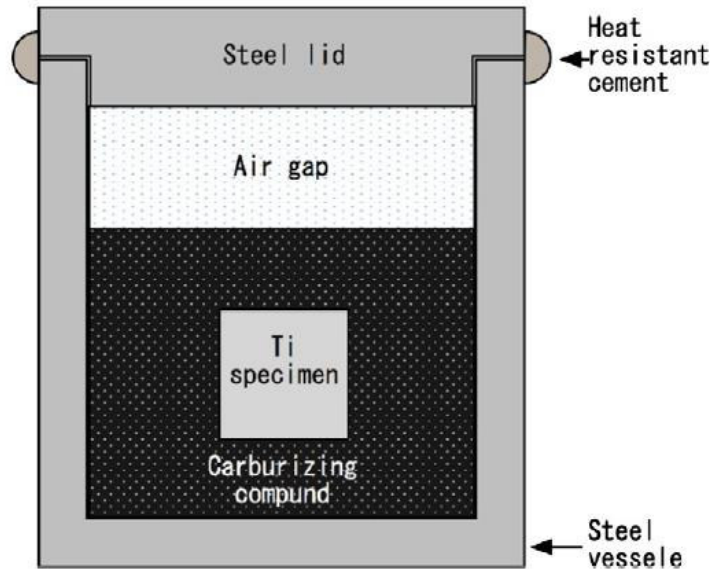
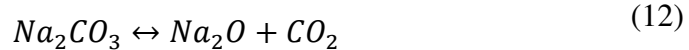
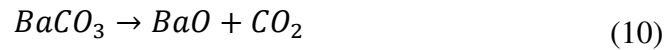


Figure 2.29 Pack carburizing vessel [49]

During the heating, first of all titanium oxidation occurs above 550/600°C. When the available oxygen is exhausted, the diffusion of oxygen continues inside the substrate, allowing to generate a diffusion zone.

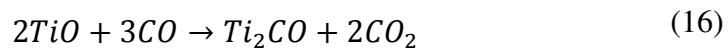
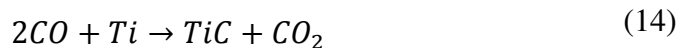
Then at 800°C carbonates decompose releasing carbon dioxide:



Carbon dioxide reacts with carbon to produce carbon monoxide, necessary to the diffusion of carbon inside the titanium:



Carbon diffuses in titanium reacting both with Ti and TiO<sub>2</sub> to form the TiC upper layer. During the reaction TiO<sub>2</sub> is reduced and intermediate oxycarbide are produced:



The process lets to obtain a diffusion zone of about 200 μm and a TiC layer of about 8 μm. The diffusion zone gives an increase of the load bearing capacity, while the TiC layer gives a higher surface hardness (2100 HV), an increase of the wear resistance and a reduction of the friction coefficient. Sliding tests against a Al<sub>2</sub>O<sub>3</sub> ball show that the friction coefficient at different load (5-40 N) is stable around 0.2,

while the one of the untreated Ti6Al4V alloy is 0.6. Moreover, the TiC layer shows a higher breakthrough threshold than a thermally oxidised layer. The friction coefficient of the TiC is low (0.2) and stable up to a load of 40 N while the one of the TiO<sub>2</sub> layer is low (0.3) only for load below 1 N [49].

The characteristics of the thermochemical carburizing process are compared to the one of the laser carburizing in Table 2.8.

**Table 2.8 Temperature and time of treatment and thickness and hardness of the nitride coatings in function of the process [47]**

Process	Temperature/ Power	Time	Thickness (µm)	Hardness (HV)
Laser carburizing (PVD)	1-3 kW	-	200-500	500-1050
Thermochemical Carburizing	925°C	20 h	About 200	2100

## 2.3.6 Electrochemical treatments

### Anodising

Anodising is an electrochemical process, based on an electrolytic cell. The material that needs to be covered plays as anode to that negatively charged ions of the electrolytic solution migrate. At the interface between the metal and aqueous electrolytic solution, chemical anodic reactions occur, allowing the formation of an oxide layer on the metal surface. Metal dissolves forming cations, that react with ionic oxygen, causing the formation of the coating. When the reaction products are insoluble in the electrolyte a strongly adherent film grows on the substrate until the current passage is prevented by the film resistance. When the products of the chemical reaction are partially soluble, instead, there is a localized dissolution of the film during its growth that cause the presence of pore inside the coating.

The final properties depend strongly by the electrolyte used, because electrolyte anions are incorporated into the coating during its growth. The presence of defects and non-uniformity of the coating cause residual stresses, that act on properties such as fatigue resistance; compressive stresses enhance the fatigue resistance while tensile stresses reduce fatigue resistance and adhesion of the coating.

Titanium can be anodised through acid anodising or alkaline anodising. In the first case, the component is put in an acid bath of electrolytes such as 80% phosphoric acid, 10% sulphuric acid and 10% water and a thin colourful film of TiO<sub>2</sub> is obtain. The colour of the later depends on the thickness of the layer, that is a function of the voltage applied. This because white light is in part adsorbed, partially reflected, partially transmitted and partially refracted within the oxide film, the degree of adsorption and the number of reflections are function of the oxide layer thickness. Generally, the thickness reached is below 0.1 µm as maximum, thus

this technique is mainly applied for aesthetic application, in particular it is used for medical and dental instruments (Figure 2.30). Due to the low thickness of the coating, this is not a useful technique to enhance wear resistance, but it can increase the resistance to galling and it is advantageous from the biological standpoint if coupled to coating of nanotubes [50].

In the second case, it is used an alkaline bath of electrolytes and it is possible to obtain films with higher thickness, up to 4  $\mu\text{m}$ , that can enhance the hardness of the surface and its wear resistance. In this case due to the thicker oxide layer the surface appears visually grey [51].



Figure 2.30 Dental screws with different thickness of the  $\text{TiO}_2$  layer [52]

This process is mainly used for dental component to enhance the corrosion resistance and the osteointegrability of the implants.

### Plasma electrolytic oxidation treatment

Plasma electrolytic oxidation treatment (PEO) is an anodic oxidation carried out above the breakdown voltage in an acid or alkaline electrolytic solution, using an appropriate power source (DC source, DC pulsed sources or AC source). This allows to obtain coatings composed of complex oxides, the one of the substrate and the ones of the element present in the aqueous electrolytic solution. The process is schematized in Figure 2.31.

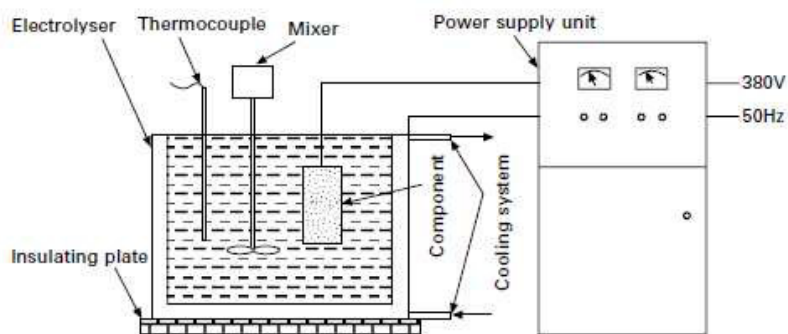
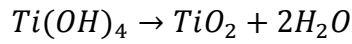
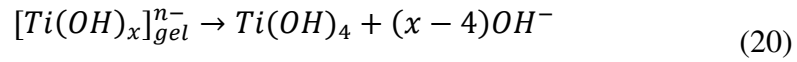
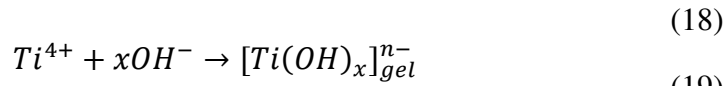
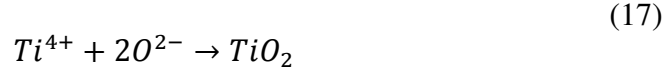


Figure 2.31 PEO process [53]

The process can be divided in stages, first of all the traditional anodising process takes place, an increased voltage is applied and a porous insulation film with a columnar structure perpendicular to the substrate grows. Secondly, the voltage exceeds the breakdown voltage and spark discharges develops across the insulating film. The generation of sparks causes the formation of small uniform pores. During this phase, anions from the electrolytic solution, such as  $\text{PO}_4^{3-}$  and

$\text{SiO}_3^{2-}$ , move into the discharge channels under the electric field forces. At the same time, due to the high temperature and pressure induced by the spark discharge, alloy elements of the substrate melt or diffuse into the discharge channel. The electrolyte solution causes a rapid cooling, during this phase, the produced oxides solidify and deposit on the channels walls. Finally, the produced gases flow away leaving holes with a volcano shape. At the interface between the titanium substrate and electrolytic solution, a chemical reaction develops:



During the solidification phase, the oxides products deposit generating a nano-crystalline layer with uniform nano grains. These grains grow during the PEO process, as soon as the oxide layer grows at the interface between the coating and substrate under the out breaking of spark discharges.

The microstructure and chemical composition of the coatings depend strongly by the electrical parameters and the composition and concentration of electrolytic solution. Acting on the electrical parameters and optimizing the electrolyte composition it is possible to limit the growth of the porous layer. It is not possible to eliminate the pores completely, on one hand they can act as reservoir for lubricant on the other hand they reduce hardness and so wear resistance and they also allow the penetration of corrosive liquid in aggressive environment that causes a low corrosion resistance.

The adhesion of the coating results to be quiet strong, nevertheless it depends on the amount of residual stresses at the interface and on the thickness of the coatings, the higher the thickness is, the lower the adhesion of the coating.

$\text{TiO}_2$  coatings on titanium alloy substrate obtain with this technique allow to reach hardness between 400-700 HV and to reduce the friction coefficient at values of 0.1-0.2.

Several properties can be enhanced or achieved through this techniques, such as wear and corrosion resistance, thermos-optical, thermal and dielectric properties, without changing the mechanical properties of the substrate.

In addition, PEO process, as other techniques above mentioned, allows to create also bioactive coating on titanium and titanium alloys substrates.

It is also an eco-friendly, low cost and easy techniques that can be applied to samples with complex shapes [53].

Table 2.9 compares the PEO process and the conventional anodizing.

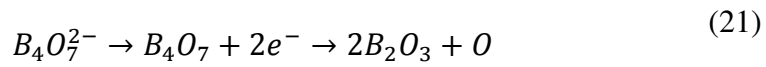
**Table 2.9 Comparison between PEO process and conventional anodizing**

Process	Temperature	Time	Thickness ( $\mu\text{m}$ )	Hardness (HV)
PEO	<50°C	Tens of min	up to 200	400 – 700
Anodizing	<30°C	10 – 60 min	0.1 – 4	150 – 300

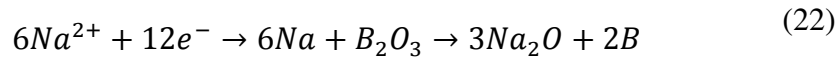
### Electrolytic boronizing

Electrolytic boronizing is an anodization process that consists on immersing the samples attached to the cathode and a graphite anode into a molten borax ( $\text{Na}_2\text{B}_4\text{O}_7$ ), used as salt bath.

Sodium and tetraborate ions flow towards the cathode and the anode respectively under the electric field. Tetraborate ions are neutralized and reduced to boric acid according to the following reaction:



Oxygen reacts with C of graphite cathode, while at the cathode sodium ions are neutralised and react with the boric acid releasing boron:



To obtain a uniform deposit layer on the surface, a strictly control of the current density is necessary [41].

This is an effective process for boronizing of ferrous material, nevertheless some studies were carried out on the electrolytic boronizing of the titanium. Kartal et al. [54] performed the electrolytic boronizing of commercially pure titanium plates. The process was carried out in a salts bath composed of 90% borax and 10% sodium carbonate at the temperature of 950°C and with a current density of 300 mA/cm<sup>2</sup>. Depending on the process parameters and time of treatment the thickness of the TiB<sub>2</sub> compact coating resulted to be between 1.85 and 8.5  $\mu\text{m}$  for a range time of treatment between 5 min and 2 h, while the hardness reached values of 40 GPa.

A comparison between the pack boronizing and the electrolytic boronizing performed on commercially pure titanium is shown in Table 2.10.

**Table 2.10 Comparison between pack boronizing and electrolytic boronizing [54,55]**

Process	Temperature	Time	TiB <sub>2</sub> Thickness ( $\mu\text{m}$ )	Hardness (HV)
Pack boronizing	890 – 1050°C	3 – 24 h	1.2 – 6.4	about 4000
Electrolytic boronizing	950°C	5 min – 2 h	1.85 – 8.5	4079 (40GPa)

### **2.3.7 Duplex surface treatment**

Duplex surface treatments consist on the sequential application of two or more surface modification techniques above described.

The single processes do not always allow to obtain the desired surface properties or present some issues such as distortions, deformations and changes in sample dimensions in case of thermal diffusion processes and spallation of the coating in case of deposition processes. The deposition of hard layer on soft substrate, such as titanium and its alloys, can cause the delamination or spallation of the coating due to a non-opportune support of the substrate to the hard coating. The different hardness and elastic modulus of the substrate and the coating, the residual stresses at the interface and the plastic deformation of the substrate involve fractures and cracks in the hard and brittle coating.

Duplex processes allow overlap these limits. The use of more techniques allows to obtain an intermediate hardening layer on which a thin hard film is deposit.

The main commercial duplex techniques consist on low temperature plasma nitriding followed by deposition of amorphous  $CN_x$ , TiN, TiCN and DLC. The process allows to generate an intermediate layer that enhance the load bearing capacity and the adhesion of the upper hard layer, improving as consequence the wear resistance. The hard layer results also to be deposited uniformly and this enhances the corrosion resistance.

Another process used to enhance the adhesion of DLC coating consist on a plasma nitride layer, followed by a plasma carbonitrided layer, that is used as precursor for the nucleation and the growth of diamond crystals.

The tribological properties of titanium can also be improved by a Ti-O/Ti-N duplex coating, obtained by PIII and subsequent plasma nitriding/oxidation. In this way is also enhanced the titanium haemocompatibility.

The interlayer can be generated by nitrogen diffusion or oxygen diffusion. In case of oxygen diffusion, a boot diffusion oxidation (BDO) process has been developed.

In BDO process titanium substrate is thermally oxidised in air and then diffusion treated in vacuum. It is possible to obtain a hard oxygen diffusion interlayer of about 300  $\mu m$  with good adhesion to the substrate. BDO can be combined with DLC deposition to obtain coatings with high adhesion, good tribological properties and excellent load bearing. The intermediate layer enhances the adhesion providing a strong bonding strength between substrate and DLC coating and support the DLC coating by suppressing plastic deformation [56].

## **2.4 Commercial coatings for hip prostheses**

Nowadays, it is possible to find commercial head of hip implant coated with TiN or DLC.

TiN coatings deposited via PVD were used since 1980s, however data about clinical use are still limited. Lapaj et al. carried out a study on retrieved implant to compare the old and current generation of implants.

The current technologies allow to perform TiN coatings with a greater wear resistance than older ones, nevertheless retrieved femoral heads show evident damage. The coatings are still subjected to scratches, delamination and spallation with formation of debris that can abrade the exposed substrate through a wear mechanism of three body abrasion. It was also reported an increment of the roughness of the polymeric counterface. Moreover, the presence of defects and impurities into the TiN layer decreases drastically the wear resistance of the coatings. Defects are identified as initiated sites where the adhesive wear of polyethylene starts, while impurities and contaminations reduce the adhesion strength of the coatings.

These data show that, not only the technologies but also a great control of the quality process is extremely important to produce component suitable for the clinical use [57].

Several failures were also reported about DLC layer deposited via CVD on femoral heads [32]. DLC has good wear resistance and tribological properties in dry condition but in humid condition as well as in physiological environment it is not stable and subjected to spallation and delamination as previously mentioned.





## References

- [1] Barriobero Vila P. Phase transformation kinetics during continuous heating of  $\alpha+\beta$  and metastable  $\beta$  titanium alloys. 2015.
- [2] Leyens C, Peters M, editors. Titanium and Titanium Alloys: Fundamentals and Applications. 2003.
- [3] Sarma B, Ravi Chandran KS. Accelerated kinetics of surface hardening by diffusion near phase transition temperature: Mechanism of growth of boride layers on titanium. *Acta Materialia* 2011;59:4216–28. doi:10.1016/j.actamat.2011.03.046.
- [4] Hennig RG, Trinkle DR, Bouchet J, Srinivasan SG, Albers RC, Wilkins JW. Impurities block the  $\alpha$  to  $\omega$  martensitic transformation in titanium. *Nature Materials* 2005;4:129–33. doi:10.1038/nmat1292.
- [5] Arnell D. Mechanisms and laws of friction and wear. *Tribology and Dynamics of Engine and Powertrain: Fundamentals, Applications and Future Trends*, 2010, p. 41–72. doi:10.1533/9781845699932.1.41.
- [6] Dong H. Tribological properties of titanium-based alloys. In: Dong H, editor. *Surface engineering of light alloys*, 2010, p. 58–80.
- [7] Heinrichs J, Olsson M, Jenei IZ, Jacobson S. Transfer of titanium in sliding contacts-New discoveries and insights revealed by in situ studies in the SEM. *Wear* 2014;315:87–94. doi:10.1016/j.wear.2014.04.006.
- [8] Di Puccio F, Mattei L. Biotribology of artificial hip joints. *World Journal of Orthopedics* 2015;6:77–94. doi:10.5312/wjo.v6.i1.77.
- [9] Kubiak KJ, Wilson MCT, Mathia TG, Carval P. Wettability versus roughness of engineering surfaces. *Wear* 2011;271:523–8. doi:10.1016/j.wear.2010.03.029.
- [10] Mechanisms of wear 2018. <http://www.substech.com>.
- [11] Ryu JJ, Shrotriya P. Mechanical load assisted dissolution response of biomedical cobalt-chromium and titanium metallic alloys: Influence of in-plane stress and chemical environment. *Wear* 2015;332–333:662–8. doi:10.1016/j.wear.2015.01.071.
- [12] Priya R, Mallika C, Kamachi Mudali U. Wear and tribocorrosion behaviour of 304L SS, Zr-702, Zircaloy-4 and Ti-grade2. *Wear* 2014;310:90–100. doi:10.1016/j.wear.2013.11.051.
- [13] Geetha M, Singh AK, Asokamani R, Gogia AK. Ti based biomaterials, the ultimate choice for orthopaedic implants - A review. *Progress in Materials Science* 2009;54:397–425. doi:10.1016/j.pmatsci.2008.06.004.

- [14] The Limitations of Neck Modularity in High-Demand Primary Total Hip Arthroplasty n.d. <http://exactech.co.jp/uk>.
- [15] Sullivan SJL, Topoleski LDT. Surface Modifications for Improved Wear Performance in Artificial Joints: A Review. *Jom* 2015;67:2502–17. doi:10.1007/s11837-015-1543-0.
- [16] Carey P. Plasma Enhanced Chemical Vapour Deposition of Thin Carbon Films. 1989.
- [17] Equipment for ion implantation 2012. [www.nptel.ac.in/courses](http://www.nptel.ac.in/courses).
- [18] Kustas FM, Misra MS. Friction and Wear of Titanium Alloys. *ASM International* 1992;18:1169–76.
- [19] Sioshansi P, Tobin EJ. Surface treatment of biomaterials by ion beam processe. *Surface and Coatings Technology* 1996;83:175–82.
- [20] Schmidt H, Schminke A, Riick DM. Tribological behaviour of ion-implanted Ti6Al4V sliding against polymers. *Wear* 1997;209:49–56.
- [21] Gupta D. Plasma Immersion Ion Implantation (PIII) Process - Physics AND Technology. *International Journal of Advancements in Technology* 2011;2:471–90.
- [22] Xin YC, Chu PK. Plasma immersion ion implantation (PIII) of light alloys. In: Dong H, editor. *Surface Engineering of Light Alloys: Aluminium, Magnesium and Titanium Alloys*, 2010, p. 362–97. doi:10.1533/9781845699451.2.362.
- [23] Loinaz A, Rinner M, Alonso A, Onate JI, Ensinger E. Effects of plasma immersion ion implantation of oxygen on mechanical properties and microstructure of Ti6Al4V. *Surface and Coatings Technology* 1998;103–104:262–7.
- [24] Han S, Kim H, Lee Y, Lee J, Kim S-G. Plasma source ion implantation of nitrogen, carbon and oxygen into Ti-6Al-4V alloy. *Surface and Coating Technology* 1996;82:270–6.
- [25] Chu PK. Recent developments and applications of plasma immersion ion implantation. *Journal of Vacuum Science & Technology B: Microelectronics and Nanometer Structures Processing, Measurement, and Phenomena* 2004;22:289–96. doi:10.1116/1.1632920.
- [26] Li CJ. Thermal spraying of light alloys. In: Dong H, editor. *Surface Engineering of Light Alloys: Aluminium, Magnesium and Titanium Alloys*, 2010, p. 184–241. doi:10.1533/9781845699451.2.184.
- [27] Li W, Liao H, Wang H. Cold spraying of light alloys. In: Dong H, editor. *Surface Engineering of Light Alloys: Aluminium, Magnesium and Titanium Alloys*, 2010, p. 242–93. doi:10.1533/9781845699451.2.242.
- [28] Khanna R, Ong J, Oral E, Narayan R. *Progress in Wear Resistant Materials*

- for Total Hip Arthroplasty. Coatings 2017;7:99. doi:10.3390/coatings7070099.
- [29] Ma WJ, Ruys AJ, Mason RS, Martin PJ, Bendavid A, Liu Z, et al. DLC coatings: Effects of physical and chemical properties on biological response. *Biomaterials* 2007;28:1620–8. doi:10.1016/j.biomaterials.2006.12.010.
- [30] McNamara BP, Murphy H, Morshed MM. Adhesion properties of diamond-like coated orthopaedic biomaterials. *Diamond and Related Materials* 2001;10:1098–102. doi:10.1016/S0925-9635(00)00567-7.
- [31] Kim DH, Kim HE, Lee KR, Whang CN, Lee IS. Characterization of diamond-like carbon films deposited on commercially pure Ti and Ti-6Al-4V. *Materials Science and Engineering C* 2002;22:9–14. doi:10.1016/S0928-4931(02)00106-6.
- [32] Roy RK, Lee K-R. Biomedical Applications of Diamond-Like Carbon Coatings: A Review. *Journal of Biomedical Materials Research Part B: Applied Biomaterials: An Official Journal of The Society for Biomaterials, The Japanese Society for Biomaterials, and The Australian Society for Biomaterials and the Korean Society for Biomaterials* 2007;83:72–84. doi:10.1002/jbmb.
- [33] Chan C-W, Lee S, Smith GC, Donaghy C. Fibre laser nitriding of titanium and its alloy in open atmosphere for orthopaedic implant applications: Investigations on surface quality, microstructure and tribological properties. *Surface and Coating Technology* 2017;309:628–40.
- [34] Baker TN. Laser surface modification of titanium alloys. In: Dong H, editor. *Surface Engineering of Light Alloys: Aluminium, Magnesium and Titanium Alloys*, 2010, p. 398–443. doi:10.1533/9781845699451.2.398.
- [35] Ettaqi S, Hays V, Hantzpergue JJ, Saindrenan G, Remy JC. Mechanical, structural and tribological properties of titanium nitrided by a pulsed laser. *Surface and Coatings Technology* 1998;100–101:428–32. doi:10.1016/S0257-8972(97)00664-6.
- [36] Saleh AF, Abboud JH, Benyounis KY. Surface carburizing of Ti-6Al-4V alloy by laser melting. *Optics and Lasers in Engineering* 2010;48:257–67. doi:10.1016/j.optlaseng.2009.11.001.
- [37] Li X, Dong H. Ceramic conversion treatment of titanium-based materials. *Surface Engineering of Light Alloys: Aluminium, Magnesium and Titanium Alloys* 2010:475–500. doi:10.1533/9781845699451.2.475.
- [38] Petrova RS, Suwattananont N, Samardzic V. The Effect of Boronizing on Metallic Alloys for Automotive Applications. *Journal of Materials Engineering and Performance* 2008;17:340–5.
- [39] Aich S, Ravi Chandran KS. TiB whisker coating on titanium surfaces by solid-state diffusion: Synthesis, microstructure, and mechanical properties. *Metallurgical and Materials Transactions A* 2002;33:3489–98. doi:10.1007/s11661-002-0336-6.

- [40] Peretti V, Ferraris S, Gautier G, Hellmich C, Lahayne O, Stella B, et al. Surface treatments for boriding of Ti6Al4V alloy in view of applications as a biomaterial. *Tribology International* 2018;126:21–8. doi:10.1016/j.triboint.2018.05.006.
- [41] Dearnley PA, Bell T. Engineering the surface with boron based materials. *Surface Engineering* 1985;1:203–17. doi:10.1179/sur.1985.1.3.203.
- [42] Küper A, Qiao X, Stock HR, Mayr P. A novel approach to gas boronizing. *Surface and Coatings Technology* 2000;130:87–94. doi:10.1016/S0257-8972(00)00682-4.
- [43] Vangaveti R. Boron induced surface modification of transition metals. 2006. doi:10.3141/2100-07.
- [44] Balasubramanian K, Venkatarama B, Krishna KG, Sundararajan G, Jain V, Sampath K. An Improved Boronizing Composition. 220370, 2008.
- [45] Ti-B phase diagram 2011. <http://www.calphad.com>.
- [46] Nitriding of Titanium and Titanium Alloys 2009. [www.totalmateria.com](http://www.totalmateria.com).
- [47] Zhecheva A, Sha W, Malinov S, Long A. Enhancing the microstructure and properties of titanium alloys through nitriding and other surface engineering methods. *Surface and Coatings Technology* 2005;200:2192–207. doi:10.1016/j.surfcoat.2004.07.115.
- [48] Carburizing Techniques: What Is Carburization? 2011. [www.brightengineering.com](http://www.brightengineering.com).
- [49] Bailey R, Sun Y. Pack carburisation of commercially pure titanium with limited oxygen diffusion for improved tribological properties. *Surface and Coatings Technology* 2015;261:28–34. doi:10.1016/j.surfcoat.2014.11.071.
- [50] Webster TJ, Ross AP. Anodizing color coded anodized Ti6Al4V medical devices for increasing bone cell functions 2013;8:109–17.
- [51] Yerokhin A, Khan RHU. Anodising of light alloys. In: Dong H, editor. *Surface Engineering of Light Alloys: Aluminium, Magnesium and Titanium Alloys*, 2010, p. 83–109. doi:10.1533/9781845699451.2.83.
- [52] Titanium dental screw 2018. [www.medicalexpo.it](http://www.medicalexpo.it).
- [53] Jiang BL, Wang YM. Plasma electrolytic oxidation treatment of aluminium and titanium alloys. In: Dong H, editor. *Surface Engineering of Light Alloys: Aluminium, Magnesium and Titanium Alloys*, 2010, p. 110–54. doi:10.1533/9781845699451.2.110.
- [54] Kartal G, Timur S, Urgan M, Erdemir A. Electrochemical boriding of titanium for improved mechanical properties. *Surface and Coatings Technology* 2010;204:3935–9. doi:10.1016/j.surfcoat.2010.05.021.
- [55] Tikekar NM, Ravi Chandran KS, Sanders A. Nature of growth of dual

titanium boride layers with nanostructured titanium boride whiskers on the surface of titanium. *Scripta Materialia* 2007;57:273–6. doi:10.1016/j.scriptamat.2007.03.050.

- [56] Fu RYQ. Duplex surface treatments of light alloys. In: Dong H, editor. *Surface Engineering of Light Alloys: Aluminium, Magnesium and Titanium Alloys*, 2010, p. 501–45. doi:10.1533/9781845699451.2.501.
- [57] Łapaj Ł, Wendland J, Markuszewski J, Mróz A, Wiśniewski T. Retrieval analysis of titanium nitride (TiN) coated prosthetic femoral heads articulating with polyethylene. *Journal of the Mechanical Behavior of Biomedical Materials* 2016;55:127–39. doi:10.1016/j.jmbbm.2015.10.012.



## **Chapter 3**

# **The mechanism of adhesion of proteins and their role in lubrication**

### **3.1 Mechanisms of protein adsorption**

Hip joints are usually soaked by synovial fluid, whose amount and quality (composition and viscosity) change, when the joint is replaced by a hip implant, as better described in the following paragraphs. Thus it is extremely important to understand the interactions between the synovial fluid and/or its compounds and the materials surface: the ability of an artificial surface to be well lubricated by even just a small amount of synovial fluid can be relevant for the positive outcome of the prostheses. In particular, in the following paragraphs, serum bovine albumin, fibronectin and fetal bovine serum will be described. They are the proteins and the biological fluid used as lubricants for the tribological tests and the adsorption analyses discussed in Chapter 5.

Generally speaking, when an implanted material is exposed to biological fluids a sequence of interactions takes place.

First of all, the surface comes in contact with water molecules and ions, subsequently proteins interact with the surface, developing a protein layer [1]. The kind of adsorbed protein layer influences the response of cells and their biological activities [2]. Focusing on adsorption on titanium surface, water adsorption can be molecular or dissociative. Adsorption mechanisms are shown in Figure 3.1.

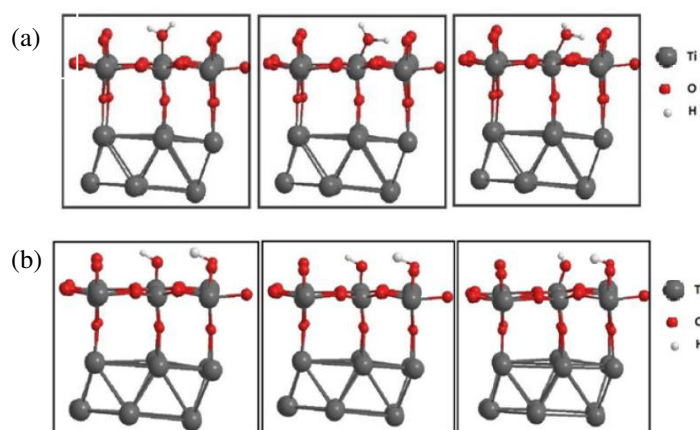


**Figure 3.1 Molecular (a) and dissociative (b) adsorption of water on Titanium surface [1]**

In the first case there is double protonation of the oxygen atom caused by binding between the water molecule and the Ti atom. In the second case there is single protonation of the oxygen atom due to binding between the Ti atom and the hydroxyl group, the remaining hydrogen atom is transferred to the next oxygen atom.

The reactivity of water molecules to the surface is increased by the presence of surface defects, that increase surface energy acting as additional reactive adsorption sites.

After water adsorption, the interaction between the surface and proteins is driven by four forces:

- ionic or electrostatic interactions among surface charge and the net charge of the protein and among water molecules and charged amino-acid chains of proteins.
- hydrogen bonding among polar groups of proteins and water molecules.
- hydrophobic interactions, that cause a rearrangement of the protein structure to decrease the internal free energy.
- charge transfer interactions, that have a key role in the stabilisation of the proteins on the surface [1].

The initial reaction and the characteristics of the adsorbed layer depend on several factors, some belonging to the surface (topography, chemistry, charge, wettability, hydrophobicity, heterogeneity and potential) and some belonging to the proteins (size, charge, structure stability and unfolding rate) [1,2].

Surface topography, in terms of porosity, pore size, pore distribution, roughness and particles size, determines the amount of surface area available for the interaction with proteins. The higher the surface area is, the higher the number of interaction sites for protein adsorption. What is important is the relationship between the surface roughness scale ( $\mu\text{m}$  –  $\text{nm}$  range) or pore size (micro and nano pores) and protein or cell size (from tens to angstrom to tens of  $\mu\text{m}$ ): a surface can result smooth or rough for a protein in relation to its size, in addition, when the protein dimensions are bigger than the one of the pores, proteins cannot be adsorbed.



Protein adsorption and their rearrangement depend also on the interaction between the charged ions/groups exposed by the surface and the functional groups of the proteins. The electrostatic interaction between the proteins and substrate surface is influenced by several parameters: presence of vacancies, defects, substitutions that affect the surface charge density and the binding sites distribution. The incubator environment inhibits or improves the protein adsorption due to the presence of ions, that interact with the charged surface, changing the solution properties around the surface. Very important is the pH of the solution. The pH influences the ions distribution in the solution and also the conformation of proteins. The protein adsorption is higher when the pH is near the isoelectric point of the protein [2]. The study of Z.G. Peng et al., carried out on magnetic particle, shows that adsorption of bovine serum albumin is maximum when the pH is closed to the isoelectric point of the protein [3]. The same is observed for the adsorption of lysozymes in the study of M. Van der Veen et al.[4]. This phenomenon can be explained taking into account that at the isoelectric point the protein has not a net charge, so the electrostatic repulsion between protein and surface are at the minimum; in addition at the isoelectric point the spreading of proteins is low due to the high structural stability of proteins [3,4]. pH affects both kinetic and thermodynamic of protein adsorption and the structure of adsorbed proteins. Changing in pH causes the protonation and deprotonation of functional groups of both protein and surface. This influence the nature (favourable or unfavourable) of electrostatic interactions that develops between surface and protein [5].

A higher amount of protein is adsorbed on hydrophobic surface than on hydrophilic surface. Proteins tend to unfold and spread the hydrophobic core over the surface and to expose the charged functional groups to the surface in order to reduce the net hydrophobic surface area of the system [2]. The exposure of the inner hydrophobic core to the hydrophobic surface, leaving the hydrophilic domains of the protein hydrate, requests a rearrangement of the protein, with a loss of protein ternary structure. Nevertheless, this kind of interaction results to be stronger and proteins cannot be easily separated from the surface. Hydrophilic surfaces in contact with aqueous solution tend to interact easily with water and to be covered with a hydration layer, that can act as a barrier between the protein and surface. In this case, the interaction between protein and surface is weak and adsorption process is reversible. Proteins conserve their ternary structure, they are only reoriented due to electrostatic interactions developed between the charged groups of the hydrophilic surface and the functional groups of the protein [5].

From the point of view of proteins, they are composed by an inner hydrophobic core and a surface dominated by charged and neutral hydrophilic groups. The protein stability depends on the organization of protein domains and strength of their interactions. The more stable the protein is, the less its ability to unfold and reorganize. Generally speaking, proteins can be classified as hard and soft proteins. Hard proteins such as lysozyme and ribonuclease are more stable than soft proteins and tend to conserve their ternary structure and to be adsorbed slowly and less strongly than the others [5].

Soft proteins such as fibrinogen and fibronectin usually are larger than hard proteins and as a consequence they have more binding sites to interact with the surface than smaller one, more over soft proteins, having a less stable structure can unfold, spread and form more contact points with the surface than protein with a stable structure. Their change in protein conformation during the adsorption has a big influence on the cell response to the material [2,5]. This is due to the fact the protein functions depend on second and ternary protein structure [6].

The other parameter that influences protein adsorption is temperature. At high temperature proteins denature, because the enthalpy free energy due to the folding is outweighed by the entropic instabilities [5].

In the biological environment, the adsorption process is a complex competitive process, time – concentration dependent. It can be described by the Vroman effect: in a mixed protein solution, first proteins interact each other, then a series of adsorption and displacement steps occur. First of all, at short time, proteins with low weight and high concentration are adsorbed. Then at long time they are replaced by proteins with high weight, less concentration but higher affinity to the surface.

To understand this process P. Turbill et al. study the amount of adsorbed albumin and fibrinogen in function of the concentration of plasma. Albumin and fibrinogen, proteins with low molecular weight and high concentration in plasma are adsorbed firstly and then displaced by other proteins with high molecular weight and low concentration in plasma [7]. The mechanism is shown in Figure 3.2 [2,8].

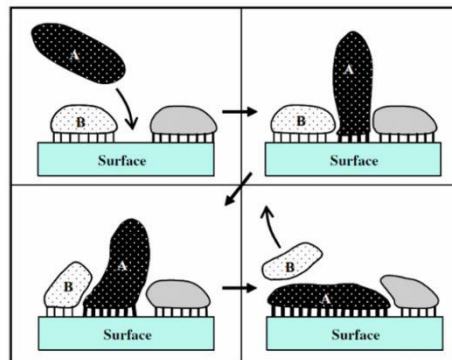


**Figure 3.2 Vroman Effect: Protein A is adsorbed and over the time protein A increases the contact surface between protein and surface. This causes an increase of the free energy of the system. The gained energy is spent to desorb protein B, through the break of focal contact between protein B and surface [5]**

## 3.2 Serum Albumin

Serum albumins are a multigene family of proteins and the most abundant proteins in the blood. They perform several physiological function, such as aiding in the transport, distribution and metabolism of several ligands and contributing to osmotic blood pressure. Human serum albumin (HAS) is a relatively low mass weight protein and it is one of the proteins with the highest concentration in the blood. It has a mass weight of 66.5 kDa and a concentration in the blood in a range of 35-50 mg/mL [9]. It consists of 585 amino acids, composed by 17 disulphide bridges, a single tryptophan (Trp 214) and one free thiol (Cys 34). There are eight

sequential Cys-Cys pairs, around which the disulphides are positioned, organized in series of nine loop-link-loop structures. HAS as a heart asymmetric shape, composed by six helical subdomains. The internal amino-acid sequence is organized in three domains homologous in structure (I II III). These domains are composed by two smaller subdomains (A and B). Each domain contains 10 helices (h1-h10). Helices h1, h2, h3, h4 and h7, h8, h9, h10 form common motif for subdomains A and B respectively. Subdomain IA differs from the other because it does not contain the disulphide bridge that connects h1 and h3. Subdomains A in addition have two short antiparallel helices (h5 and h6). A pair of disulphide bridges links the two helices, forming a smaller disulphide double loop. Subdomain B present an N-terminal portion, that looks like an up-down helical bundle. Subdomains IA-IB, IIA-IIB, IIIA-IIIB are intra-connected by extended polypeptide, while inter-connections between subdomains IB-IIA and IIB-IIA are formed by helices from C-terminal portion of IB/IIB and the N-terminal portion of IIA/IIIA (Figure 3.3) [10].

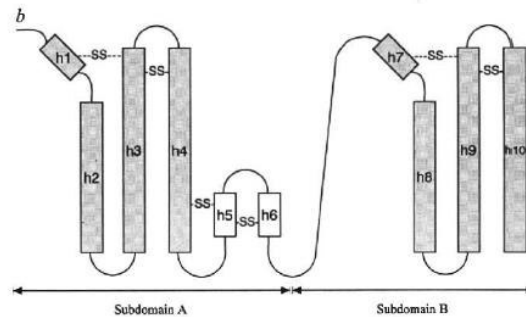


**Figure 3.3 Subdomain A and B of HAS [10]**

The secondary structure of HAS results to be composed of  $\alpha$ -helix (67%) and other structures divided between turns and  $\beta$ -sheet [11,12].

HAS conformation is influenced by the pH of the surrounding solution, at acid pH the protein denatures. Until pH 4-4.5, the amount of helical content decrease, due to a partial opening of albumin structure. At pH below 4, the albumin structure riches its maximum spreading. Limit to its uncoiling is due to the repulsion between loops and positive domains [13].

For laboratory purpose, bovine serum albumin (BSA) usually is used instead of HAS. These two proteins share 76% of amino acid sequences [11].

BSA conformation, as well as that of HAS, depends on pH and characteristics/features of the surface on which it interacts. BSA can perform a side or end-orientation on surface (Figure 3.4). This depend on the charge of the surface. Hu and Yang [12] studied the conformation of BSA adsorbed on three different Ti surface: commercial pure Ti, Ti subjected to alkali-heat treatment and acid-alkali treatment. The change of BSA conformation was studied by FTIR analysis, data show that the treatments cause an increase of surface hydrophilicity and of the amount of OH groups on surface. The OH groups are not the same on the surfaces, they are divided in basic and acid hydroxyl groups, as consequence the surfaces result charged differently and albumin interacts differently with the surfaces. On commercial pure Ti and on acid-alkali Ti, albumin has a side-orientation, while on

alkali-head Ti it has an end-orientation. The different orientation depends on the interaction between basic hydroxyl groups and protein  $\text{NH}_3^+$  and between acid hydroxyl groups and protein  $\text{COO}^-$ .

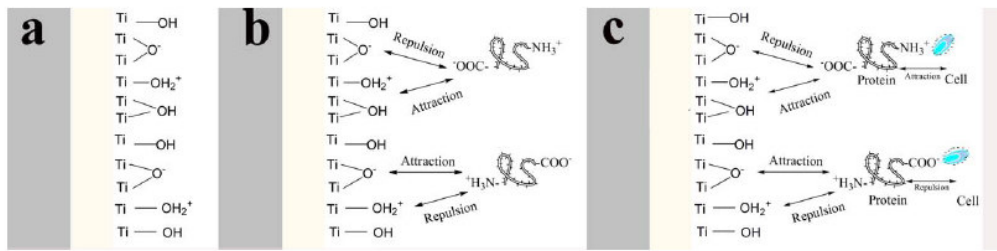


**Figure 3.4 (a) Titanium oxide surface (b) interaction between Titanium oxide surface and proteins (c) interaction between proteins and cells [12]**

Albumin after adsorption on different surface not only presents a different orientation, but also a different conformation. In comparison of native BSA, after adsorption there is a decrease of amount of  $\alpha$ -helix, mainly for treated Ti, and an increase of  $\beta$ -sheet in the case of commercial pure Ti and alkali-head Ti. BSA adsorbed on commercial pure Ti does not present turn, the one adsorbed on acid-alkali Ti increases the amount of turn, while the one adsorbed on alkali-head Ti has not turn, but part of the structure become unordered [12].

Several studies [14,15] confirm that the highest albumin adsorption on a surface occurs at pH close to the one of protein IEP. BSA has an isoelectric point (IEP) in the range 4.7-5.1 when measured with zeta potential method [16].

### 3.3 Fibronectin

Fibronectin (FN) is a high molecular weight glycoprotein of 450 kDa, that contains specific functional groups, through which it interacts with integrins of cells. Due to the interactions between protein sites for cell binding and integrins on cell membranes, FN is important for cell adhesion, spreading, differentiation and phagocytosis. These biological activities of FN depend on its conformation [17,18].

FN is a disulphide-linked dimer with negatively charged ends, composed of 2265 residues. The two domains are composed by the combination of three modules (F1, F2, F3), as shows by Figure 3.5. Each domain contains twelve F1 modules, two F2 modules, fifteen F3 modules and six connecting strands [18].

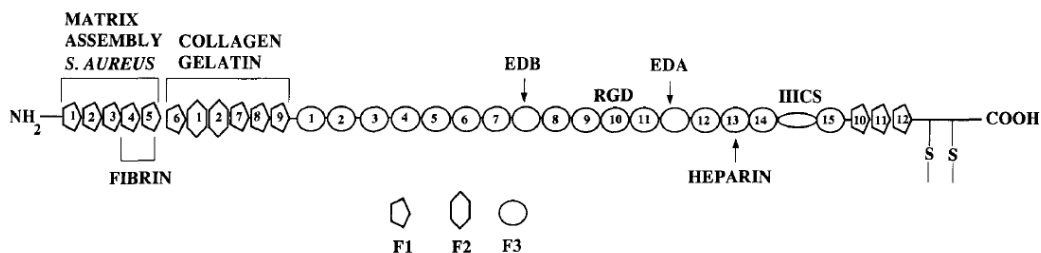


**Figure 3.5 Modular structure of a FN domain, composed by repetition of modules F1, F2 and F3 [19]**

F1 module corresponds to a sequence of 45 amino acids with four cysteines, that form two disulphide bonds with configuration 1-3, 2-4. The amino acids sequence folds forming a short double-stranded anti-parallel  $\beta$ -sheet (A, B) over a triple-stranded anti-parallel  $\beta$ -sheet (C, D, E). The structure is stabilised by the two disulphide bonds between strands A and D and between strands D and E. At the two opposite sides of the chain, there are a N-terminal end and a C-terminal end. A covalent and a non-covalent fibrin binding sites are placed at the N-terminal end, these binding sites are important for FN physiological functions [19].

F2 module is composed by two perpendicular short double-strands anti-parallel  $\beta$ -sheet and two irregular loops. One loop is placed between the strands of the second  $\beta$ -sheet, the other divides the two  $\beta$ -sheet. As in F1 module, the structure is stabilized by two perpendicular disulphide bonds. This module contains the collagen binding fragment [19,20].

F3 module consists on a sandwich of two anti-parallel  $\beta$ -sheets, composed of three and four  $\beta$ -strands, respectively. The main functions of this module are the maintenance of the correct space between the functional sites and the mediations of protein-protein interaction, through the RGD sequence contained in the 10F3 module. RGD sequence allows the identification and the binding of integrins and so it is important for the biocompatibility of the implant (Figure 3.6) [19,21].

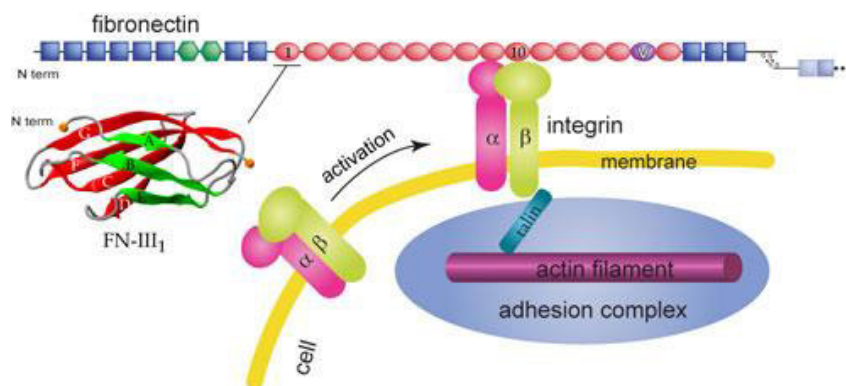


**Figure 3.6 Interaction between RGD sequence of protein and integrins of cell [22].**

Bovine fibronectin (BFN) and Human fibronectin (HFN) differ for 146 residues, as consequence they result to have a homology of 93% [20].

The concentration of FN in human plasma is about 0.3 mg/ml while in the bovine plasma is about 0.2 mg/ml [23].

FN conformation in the adsorbed condition depends on several factors, such as pH, temperature, protein concentration, surface charge and surface hydrophilicity.

A. P. Ngankam et al., using an optical waveguide light-mode spectroscopy system, observed that at physiological pH FN tends to be adsorbed in a linear end-orientation on positive surface and in a side-orientation on negative surface (Figure 3.7) [18].

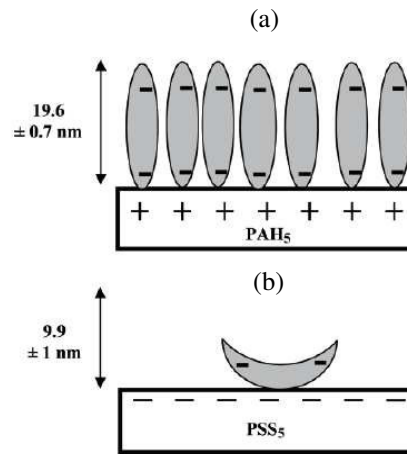


**Figure 3.7** Different orientation of FN in function of surface charge. (a) end-orientation on positive surface (b) side-orientation on negative surface [18]

It was also observed that the increase of the net negative charge of a material surface, and as consequence of its hydrophilicity, involves the increase of the intrinsic bioactivity of fibronectin. Treatments that cause changing in the chemistry of surface M-OH groups with an increase of the amount of [M-O]<sup>-</sup> groups, have effects on the fibronectin conformation. More binding sites for the integrins result to be exposed by the protein and as consequence there is an increase of the amount of attached cells [24].

When there is high affinity between surface and FN, such as between FN and TiO<sub>2</sub> surface, the conformation of adsorbed FN depends on FN concentration. At low concentration, FN tends to be adsorbed in an unfolded conformation, while at high concentration the adsorbed layer is more compressed and adsorbed protein is present with different degrees of unfolding conformation [25].

The conformation of FN is also influenced by the kind of TiO<sub>2</sub> layer. Lv et al. show that anatase surfaces are more osteogenic than rutile ones. Anatase surface results to have more Ti-OH groups than rutile surface, the formation of Ti-OH groups is facilitated by the low distances between oxygen vacancy and the adjacent oxygen, that decreases the dissociation of H<sub>2</sub>O. Electrostatic interactions develop between the surface hydroxyl groups and protein amino acid groups; this causes a change in protein conformation that exposes more binding sites for integrines, through with cells can attached, spread and proliferate on surface (Figure 3.8) [26].

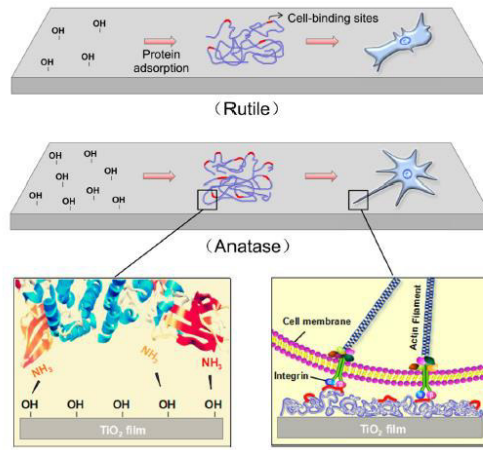


**Figure 3.8** Interaction between proteins and surface and between cells and proteins on different types of TiO<sub>2</sub> surfaces [26]

### **3.4 Fetal Bovine Serum**

Fetal bovine serum (FBS) is the liquid fraction of blood plasma after blood coagulation. It is free of cell, fibrin and clotting factors, but rich in nutrients and growth factors. It is composed by proteins, hormones, sugar, lipids and amino acids as shown in Table 3.1.

**Table 3.1 Constituents of Serum and differences between human serum and bovine serum [27]**

Elements	Concentration Range	Notes
Albumin	20–50 mg/mL	
Amino acids	0.01–1.0 $\mu$ M	
Calcium	4–7 mM	
Chlorides	100 $\mu$ M	
Cholesterol	10 $\mu$ M	
Fatty acids	0.1–1.0 $\mu$ M	
Fetuin		In FB only
Fibronectin	1–10 $\mu$ g/mL	
Globulins	1–15 mg/mL	
Glucose	0.6–1.2 mg/ml	
Growth Factors: EGF, PDGF, IGF,FGF, IL-1, IL-6, Insulin	1–100 ng/mL	
Hydrocortisone	10–200 nM	
Hexosamine	0.0–1.2 mg/mL	Highest in human
Iron	1–10 $\mu$ M	
Lactic acid	0.5–2.0 mg/mL	Highest in FB
Linoleic acid	0.01–0.1 $\mu$ M	
Phospholipids	0.7–3.0 mg/mL	
Polyamines putrescine,spermidine	0.1–1.0 $\mu$ M	
Potassium	5–15 mM	
Proteinase inhibitors:a1-antitrypsin, a2-macroglobulin	0.5–2.5 mg/mL	
Protein, total	40–80 mg/mL	
Pyruvic acid	2–10 $\mu$ g/mL	
Selenium	0.01 $\mu$ M	
Sodium	135–155 mM	
Total lipids	2–10 mg/mL	
Transferrin	2–4 mg/mL	
Tri-iodotyrosine		
Urea	170–300 $\mu$ g/mL	
Vitamins	10 ng–10 $\mu$ g/mL	
Vitamin A	10–100 ng/mL	
Zinc	0.1–1.0 $\mu$ M	



For the presence of growth factors and nutrients FBS, is widely used in cell cultures and it is also involved in the production of vaccines and drug [28].

The protein fraction of serum is composed for 99% of 22 high concentration proteins and for 1% of low concentration proteins. The most abundant high concentration proteins are serum albumin (55%), fibrinogen (7%) and globulins (38%), while proteins with low concentrations are mainly secreted by livers, necrotic and apoptotic cells. Several are the functions of serum proteins, such as lactate dehydrogenase and alkaline phosphatase act as enzymes, high and low molecular weight kininogen are kinin precursors, C1, C2 and C4 are complement components, while globulins are involved in the transport of minerals, hormones, lipids and vitamins, in the functioning of immune system and in the regulation of acellular activity [29].

From the point of view of adsorption mechanism, serum is a mix of protein solution thus it follows the Vroman effect. The kind of adsorbed layer depends on protein-protein interaction and protein-surface interaction.

### **3.5 Synovial fluid and its lubricant effect**

Synovial fluid is a non-Newtonian fluid secreted by the synovial membrane by filtration from blood. It is composed by hyaluronic acid, lubricin, protein and interstitial fluid.

Proteins and interstitial fluid derive from plasma by filtration. The concentration of proteins in synovial fluid is 18-20 mg/ml, the 20% of the one of plasma.

Hyaluronic acid is a polymer of disaccharides produced by cell Type B (fibroblast-like cells) of synovial membrane. The viscosity of synovial fluid depends on hyaluronic acid, that is present in a concentration of 3-4 mg/ml in normal synovial fluid.

Lubricin is the second lubricating component, secreted by chondrocytes and its functions is to reduce the friction between the two cartilaginous surfaces.

Synovial membrane, in addition, contains cells type A (macrophage-like), that have a phagocytosis function, removing microbes and wear debris from synovial fluid. Synovial fluid is present in synovial joint, such as hip, knee, shoulder, ankle and it forms a layer of about 50 nm on cartilaginous surface. During movement and under load, synovial fluid is squeezed out from cartilage in order to preserve the fluid layer between articular cartilage. Its main functions are: lubricating cartilaginous surfaces, cushioning of loads and transporting nutrients and waste. Variations in synovial fluid viscosity and permeability are induced by inflammatory responses, that cause changes in the synovial fluid composition [30].

After a total joint arthroplasty an inflammatory response develops and a periprosthetic fluid is produced instead the normal synovial fluid. Differences between periprosthetic fluid and synovial fluid consist on protein and hyaluronic acid concentrations and pH values. Synovial fluid contains proteins in a concentration of 18-20 mg/ml, this value increases to 30-50 mg/ml in periprosthetic fluid [31]. The main proteins present in synovial fluid are albumin and  $\gamma$ -globulin,

the concentrations are in the range 7-18 mg/ml and 0.5-2.9 mg/ml, respectively. While in periprosthetic fluid albumin concentration ranges the ranges of 20-39 mg/ml and  $\gamma$ -globulin concentration the one of 4.6-15.4 mg/ml. The pH is between 7.3-7.43 for synovial fluid and 7.5-8.5 for periprosthetic fluid [32].

The lubrication action of periprosthetic fluid depends on material with it is in contact, this is due to the different affinity and adsorption mechanism of proteins on surfaces. Serro et al., show that albumin adsorption onto joint surfaces enhances boundary lubrication and it inhibits the transfer of polymeric material on counter-faces. The protective effect is proportional to the amount of albumin adsorbed. Focusing on the main joint material (stainless steel, CoCrMo and alumina), the study shows that the transfer of UHMWPE on metal surface is inhibited and there is a decrease of the friction coefficient while on alumina the polymeric transfer persists and the friction coefficient increases. This is because albumin adsorption is higher on metal than on alumina [33]. Generally speaking, normal synovial film is thicker than periprosthetic film, nevertheless the use of head with big size and small clearance can reduce the contact pressure and thus it can increase the thickness of periprosthetic synovial layer [31]. The increase of head size however involves an increase of toxic metal ions releases and a more invasive surgical procedure as it has been already reported in Chapter 1.

To better understand the proteins and phospholipids lubricant effect and their influence on UHMWPE wear process, the wear rate of polyethylene was studied considering solutions with different amount of proteins and lipids. Figure 3.9 shows the average UHMWPE wear rate. The wear rate of polyethylene mainly depends on protein concentration. Wear increases, increasing protein concentration. This is due to the fact that under sliding condition protein can denature and their unfold condition promotes their adsorption on the hydrophobic surface of polyethylene. Thus the tribological behaviours of UHMWPE can be changed by this adsorbed layer of proteins, that causes an increase of adhesion friction. The effect of phospholipids also depends on protein concentration. When the protein concentration is lower than physiological value, increasing the lipids concentration the wear rate of polyethylene decreases, while at physiological value of protein concentration and above, the increase of lipid concentration causes an increase of wear rate. This could be due to the interaction between proteins and phospholipids. Ex vivo analyses of polyethylene acetabular cup show that while proteins adsorb only on the surface of the material, lipids diffuse into the material. The diffusion of lipids into the bulk of the material causes a plasticizing effect, decreasing the compressive modulus and the compressive strength of the UHMWPE [34].

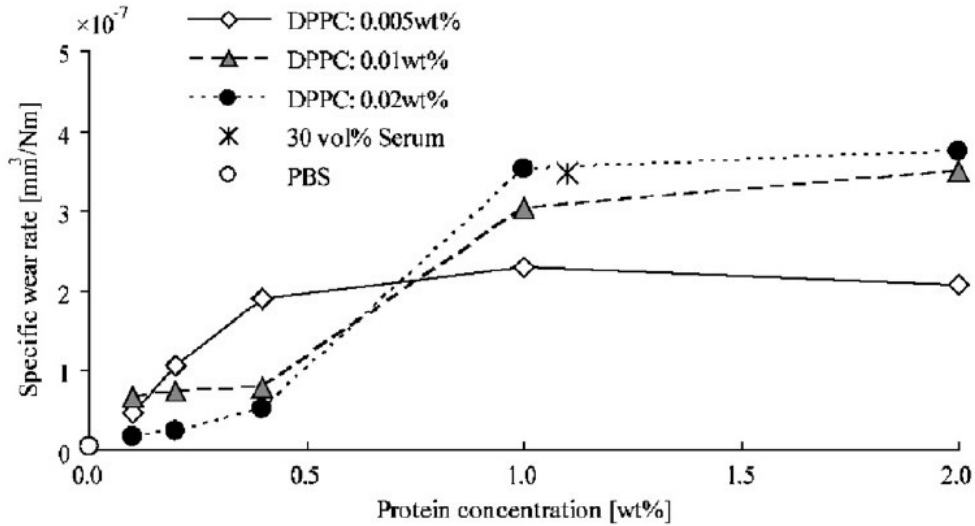


Figure 3.9 UHMWPE wear rate in function of protein and lipid concentrations [34]

### 3.5.1 Lubricants for in vitro test

Nowadays there is not a standard lubricant for in-vitro wear tests for implant joint. Using human synovial or periprosthetic synovial fluid is difficult due to issues related to collection and preservation of the fluid in the right amount. Bovine serum (BS) is usually used as lubricant to simulate synovial fluid in in-vitro wear test. Nevertheless, there are some relevant differences between BS and human periprosthetic and bovine synovial fluid. Human periprosthetic and bovine synovial fluid are non-Newtonian fluid, due to the presence of hyaluronic acid, while BS is a Newtonian fluid. In addition, BS has a lower viscosity than the other two fluids, that have the same viscosity. Protein concentration and protein distribution are significantly different for all these fluids: BS has the highest protein concentration, while human periprosthetic fluid has the lowest one, which is three time higher than protein concentration of bovine synovial fluid. Also the ratio between albumin and globulins is different, BS has the highest albumin/globulins ration, while human synovial fluid the lowest one.

These differences in chemical composition and rheological properties of lubricants influence the value of friction coefficient (COF) in in vitro test. Experiments show that human synovial fluid is the lubricant fluid that allows to obtain the lower COF in in-vitro wear tests [35].



## References

- [1] Bousnaki M, Koidis P. Advances on Biomedical Titanium Surface Interactions. *Journal of Biomimetics, Biomaterials, and Tissue Engineering* 2014;19:43–64. doi:10.4028/www.scientific.net/JBBTE.19.43.
- [2] Wang K, Zhou C, Hong Y, Zhang X. A review of protein adsorption on bioceramics. *Interface Focus* 2012;2:259–77. doi:10.1098/rsfs.2012.0012.
- [3] Peng ZG, Hidajat K, Uddin MS. Adsorption of bovine serum albumin on nanosized magnetic particles. *Journal of Colloid and Interface Science* 2004;271:277–83. doi:10.1016/j.jcis.2003.12.022.
- [4] Van Der Veen M, Norde W, Stuart MC. Electrostatic interactions in protein adsorption probed by comparing lysozyme and succinylated lysozyme. *Colloids and Surfaces B: Biointerfaces* 2004;35:33–40. doi:10.1016/j.colsurfb.2004.02.005.
- [5] Garland A, Shen L, Zhu X. Mobile precursor mediated protein adsorption on solid surfaces. *Progress in Surface Science* 2012;87:1–22. doi:10.1016/j.progsurf.2012.02.001.
- [6] Nguyen VH, Lee BJ. Protein corona: A new approach for nanomedicine design. *International Journal of Nanomedicine* 2017;12:3137–51. doi:10.2147/IJN.S129300.
- [7] Turbill P, Beugeling T, Poot a. a. Proteins involved in the Vroman effect during exposure of human blood plasma to glass and polyethylene. *Biomaterials* 1996;17:1279–87. doi:10.1016/S0142-9612(96)80004-4.
- [8] Treuel L, Docter D, Maskos M, Stauber RH. Protein corona - from molecular adsorption to physiological complexity. *Beilstein Journal of Nanotechnology* 2015;6:857–73. doi:10.3762/bjnano.6.88.
- [9] Roach P, Farrar D, Perry CC. Interpretation of protein adsorption: Surface-induced conformational changes. *Journal of the American Chemical Society* 2005;127:8168–73. doi:10.1021/ja042898o.
- [10] Xiao Min H, Carter DC. Atomic structure and chemistry of human serum albumin. *Nature* 1992;358:209–15.
- [11] Huang BX, Kim H, Dass C. Probing Three-Dimensional Structure of Bovine Serum Albumin by Chemical Cross-Linking and Mass Spectrometry. *Journal of the American Society for Mass Spectrometry* 2004;15:1237–47. doi:10.1016/j.jasms.2004.05.004.
- [12] Hu XN, Yang BC. Conformation change of bovine serum albumin induced by bioactive titanium metals and its effects on cell behaviors. *Journal of Biomedical Materials Research Part A* 2014;102:1053–62.

doi:10.1002/jbm.a.34768.

- [13] Bramanti E, Benedetti E. Determination of the Secondary Structure of Isomeric Forms of Human Serum Albumin by a Particular Frequency Deconvolution Procedure Applied to Fourier Transform IR Analysis. *Biopolymers* 1996;38:639–53.
- [14] Fukuzaki S, Urano H, Nagata K. Adsorption of Bovine Serum Albumin onto Metal Oxide Surfaces. *Journal of Fermentation and Bioengineering* 1996;81:163–7.
- [15] Rezwani K, Meier LP, Rezwani M, Vörös J, Textor M, Gauckler LJ. Bovine Serum Albumin Adsorption onto Colloidal Al<sub>2</sub>O<sub>3</sub> Particles : A New Model Based on Zeta Potential and UV - Vis Measurements. *Langmuir* 2004;20:10055–61.
- [16] Salis A, Boström M, Medda L, Cugia F, Barse B, Parsons DF, et al. Measurements and theoretical interpretation of points of zero charge/potential of BSA protein. *Langmuir* 2011;27:11597–604. doi:10.1021/la2024605.
- [17] Mosesson MW, Amrani DL. The structure and biologic activities of plasma fibronectin. *Blood* 2017;56:145–58.
- [18] Ngankam AP, Mao G, Van Tassel PR. Fibronectin adsorption onto polyelectrolyte multilayer films. *Langmuir* 2004;20:3362–70. doi:10.1021/la035479y.
- [19] Potts JR, Campbell ID. Structure and Function of Fibronectin Modules. *Matrix Biology* 1996;15:313–20. doi:10.1002/med.10052.
- [20] Skorstengaard K, Jensen MS, Sahl P, Petersen TE, Magnusson S. Complete primary structure of bovine plasma fibronectin. *The FEBS Journal* 1986;161:441–53. doi:10.1111/j.1432-1033.1986.tb10464.x.
- [21] Strehle MA, Rösch P, Petry R, Hauck A, Thull R, Kiefer W, et al. A Raman spectroscopic study of the adsorption of fibronectin and fibrinogen on titanium dioxide nanoparticles. *Physical Chemistry Chemical Physics* 2004;6:5232–6. doi:10.1039/B406524G.
- [22] [www.ks.uiuc.edu](http://www.ks.uiuc.edu).
- [23] Hayman EG, Ruoslahti E. Distribution of Fetal Bovine Serum Fibronectin and Endogenous Rat Cell Fibronectin in Extracellular Matrix. *The Journal of Cell Biology* 1979;83:255–9.
- [24] Rapuano BE, MacDonald DE. Surface oxide net charge of a titanium alloy: Modulation of fibronectin-activated attachment and spreading of osteogenic cells. *Colloids and Surfaces B: Biointerfaces* 2011;82:95–103. doi:10.1016/j.colsurfb.2010.08.023.
- [25] Sousa SR, Morada-Ferreira P, Barbosa MA. TiO<sub>2</sub> type influences fibronectin adsorption. *Journal of Materials Science: Materials in Medicine*

2005;16:1173–8.

- [26] Lv L, Li K, Xie Y, Cao Y, Zheng X. Enhanced osteogenic activity of anatase TiO<sub>2</sub> film: Surface hydroxyl groups induce conformational changes in fibronectin. *Materials Science and Engineering C* 2017;78:96–104. doi:10.1016/j.msec.2017.04.056.
- [27] Creighton TE. *The Encyclopedia of Molecular Biology*. 1999.
- [28] [www.labome.com](http://www.labome.com).
- [29] [www.rockland-inc.com](http://www.rockland-inc.com).
- [30] [www.boneandspine.com](http://www.boneandspine.com).
- [31] Myant C, Underwood R, Fan J, Cann PM. Lubrication of metal-on-metal hip joints: The effect of protein content and load on film formation and wear. *Journal of the Mechanical Behavior of Biomedical Materials* 2012;6:30–40. doi:10.1016/j.jmbbm.2011.09.008.
- [32] Kitano T, Ateshian GA, Mow VC, Kadoya Y, Yamano Y. Constituents and pH changes in protein rich hyaluronan solution affect the biotribological properties of artificial articular joints. *Journal of Biomechanics* 2001;34:1031–7. doi:10.1016/S0021-9290(01)00058-6.
- [33] Serro AP, Gispert MP, Martins MCL, Brogueira P, Colaço R, Saramago B. Adsorption of Albumin on Prosthetic Materials: Implication for Tribological Behavior. *Journal of Biomedical Materials Research Part A* 2006;78:581–9. doi:10.1002/jbm.a.
- [34] Sawae Y, Yamamoto A, Murakami T. Influence of protein and lipid concentration of the test lubricant on the wear of ultra high molecular weight polyethylene. *Tribology International* 2008;41:648–56. doi:10.1016/j.triboint.2007.11.010.
- [35] Yao JQ, Laurent MP, Johnson TS, Blanchard CR, Crowninshield RD. The influences of lubricant and material on polymer/CoCr sliding friction. *Wear* 2003;255:780–4. doi:10.1016/S0043-1648(03)00180-7.





# Chapter 4

## Experimental

### 4.1 Materials

The materials used in this research are Ti6Al4V alloy grade 5 and Ti6Al4V alloy ELI. They were undergone to a thermochemical boronizing process and they were characterized and compared to reference materials such as untreated Ti6Al4V alloy grade 5 and ELI, alumina, CoCrMo alloy and AISI 316L.

Ti6Al4V alloy grade 5 was supplied both as disks of 10 mm in diameter and 3 mm thick and as bars of 10 mm in diameter. Ti6Al4V alloy ELI and AISI 316L were provided as bars respectively of 30 mm and 12 mm in diameter. While alumina was supplied as 10x8 mm rectangles and CoCrMo alloy was provided as bars of 10 mm and 40 mm in diameter.

Ti6Al4V alloy ELI and CoCrMo alloy bars were cut in disks 5 mm thick by Brillant 200 cutting machine, using a transversal cutting mode, a ceramic blade and a cutting speed of 0.020 mm/s under lubrication condition.

From Ti6Al4V alloy grade 5 bars, AISI 316L bars and CoCrMo alloy bars of 10 mm in diameter some pins were obtained, using a lathe for the wear and fretting tests. Shapes and dimensions of the pins are reported in Figure 4.1

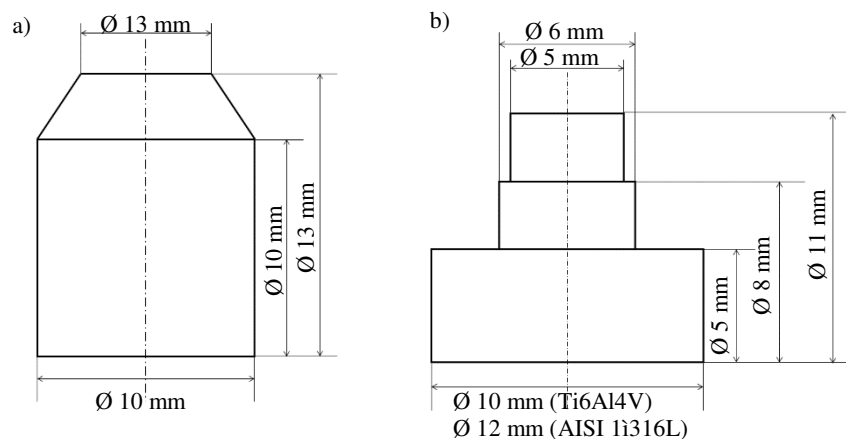


Figure 4.1 Shape and dimensions of pins for a) wear tests and b) fretting tests

Ultrahigh molecular weight polyethylene (UHMWPE) and Palacos bone cement based on poly methyl methacrylate (PMMA), with gentamicine and high viscosity were used as counterparts respectively in wear and fretting tests. UHMWPE was working as pins with the same shape and dimensions of the metallic pins (Figure 4.1a), while bone cement was used to make plates. The cement was mixed under hood and put in a stamp with dimensions of 20.3x30.5 mm.

## 4.2 Polishing process

### 4.2.1 Polishing process of the disks and the rectangles

Ti6Al4V alloy grade 5 and ELI disks, CoCrMo alloy disks and alumina rectangles were polished through Struers LaborForce-1 automatic polishing machine. Firstly, SiC abrasive sheets were used with different grid and water as lubricant. Then, polishing cloths with suitable suspensions were used to mirror polish the sample surfaces. Table 4.1 reports the polishing steps for each kind of sample.

**Table 4.1 Polishing protocol for the disks and the rectangles.**

Material	SiC abrasive sheet	Suspension
Ti6Al4V alloy grade 5	from 120 to 2500 grit	3 $\mu\text{m}$ diamond suspension
Ti6Al4V alloy ELI	from 120 to 2500 grit	3 $\mu\text{m}$ diamond suspension
CoCrMo alloy	from 120 to 2500 grit	0.04 $\mu\text{m}$ silica colloidal suspension
Alumina	from 2500 to 4000 grit	

Between one passage and another of the polishing process samples were observed under Reicher-Jung MeF3 optical microscope to verify the homogeneity of polishing. The process was carried out making attention to obtain flat disks. The final aspect of the samples can be observed in Figure 4.2.

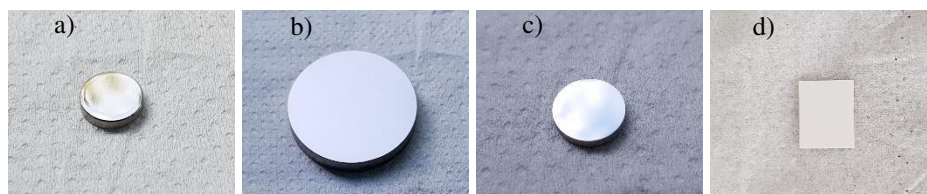


**Figure 4.2 Samples after polishing: a) Ti6Al4V alloy grade 5, b) Ti6Al4V alloy ELI, c) CoCrMo alloy and d) Alumina.**

### 4.2.2 Polishing process of the pins

Ti6Al4V alloy grade 5 and CoCrMo alloy pins (pins for wear test) were embedded into acrylic resin before to be polished.

The used resin was Struers acrylic resin, 1 part of LevoCit liquid and 2 parts of LevoCit powder were mixed in a beaker and spilt on the samples placed in suitable stamps. After 30 min the resin resulted to be dry and the samples could be easily polished.

The use of the resin helps to obtain flat surface during the polishing process. The polishing protocol of the pins is show in Table 4.2, the pins were polished as the correspondent disks. Figure 4.3 shows the samples after polishing.

**Table 4.2 Polishing protocol for the pins**

Material	SiC abrasive sheet	Suspension
Ti6Al4V alloy grade 5	from 120 to 2500 grit	3 $\mu\text{m}$ diamond suspension
CoCrMo alloy	from 120 to 2500 grit	0.04 $\mu\text{m}$ silica colloidal suspension

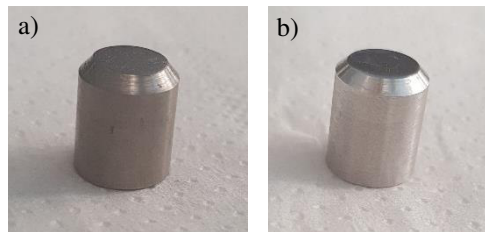


**Figure 4.3 Pin a) Ti6Al4V alloy grade 5 and b) CoCrMo alloy**

### 4.3 Washing process

All the samples were washed in the SONICA ultrasonic cleaner. The washing process took three steps, firstly the samples were washed for 5 min in acetone, then twice in double distilled water for 10 min. After washing the samples were let dry in air on a paper sheet at room temperature.

### 4.4 Thermochemical boronizing process

The boronizing process was performed on Ti6Al4V alloy grade 5 and ELI samples.

The samples were put on the bottom of a graphite crucible and covered with a powder mixture. Then the powders were pressed by using a pestle and the crucible was sealed and thermal treated. At the end of the treatment the samples were let to furnace cooling at room temperature and then extracted from the crucible.

The preparation of the crucible was carried out inside a glove box filled with argon (Ar) to work in an inert environment and to minimise the amount of oxygen.

The thermal treatment was performed in two types of furnace, a vertical tubular furnace closed with silicon caps with a continuous flow of Ar and a press oven filled of Ar. In both cases the thermal treatment was carried out in Ar to avoid oxidation of the samples. In the case of the vertical tubular furnace the thermal process required three steps. First of all, a Ar flow was allowed to flow for 30 min to be

sure to minimize the amount of oxygen, then the furnace reached the desired temperature of treatment through two ramps with a rate of heating of 10°C/min. The first ramp was set 20°C below the desired temperature with a dwell of 30 min. The second ramp allowed to reach the desired temperature of treatment for a suitable time of treatment. The Ar flow was switched off during the cooling at a temperature below 500°C, temperature at which the graphite burns.

In the case of the press oven, after having set the rate of heating (10°C/min) and the desired temperature and time of treatment, the oven performed the vacuum and filled the chamber with Ar automatically. After the cooling, the chamber was emptied manually and the samples extracted.

The powder mixture was composed of a boron source, a filler and an activator. The main task of the filler is to react with oxygen and avoid the oxidation of the samples, while the activator helps to trigger the reaction between boron and the sample surfaces. Several different mixtures of powders were tested. They are further described in the following paragraphs (4.4.3). The process was carried out following four different strategies as Figure 4.4 shows.

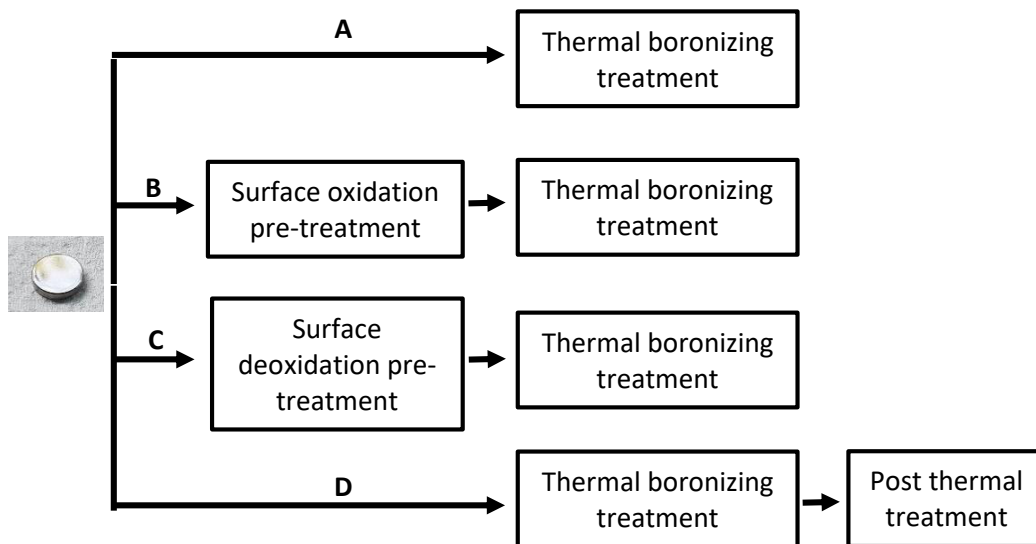


Figure 4.4 Different strategies for the thermal boronizing treatment

#### 4.4.1 Surface oxidation pre-treatment

Two Ti6Al4V alloy grade 5 samples were thermal treated at 300°C for 1 h in air. This step was performed before the thermal boronizing process to increase the surface oxide layer and to evaluate the effect of this oxide layer on the diffusion of boron and on the adhesion of the coating.

#### 4.4.2 Surface deoxidation pre-treatment

Some Ti6Al4V alloy grade 5 and ELI samples were subjected to a pre-treatment to remove the natural oxide layer on their surface. This step was carried out to evaluate the effect on the diffusion of boron and on the adhesion of the coating, such as in the case of the oxidation pre-treatment.

This step was performed inside the glove box before putting the samples into the crucible.

The samples were soaked in 5 ml of 5M HF solution for 1 min and following they were soaked in an acid washing solution (pH 1.5) for 2 min (composition under patent). Then the samples were taken from the washing solution and put into the crucible with a drop of washing solution on the surface to avoid the re-oxidation of the surface. Following, the thermal boronizing process was carried out as described on paragraph 4.4.

### 4.4.3 Mixtures of powders

Several powder mixtures were tested, as reported above (paragraph 4.4), to find the suitable composition for obtaining a uniform boron coating on the substrate. The starting point had been the literature, then combinations and variations of the commercial mixtures for boronizing were tried.

For each treatment a suitable amount of powder mixture was used, to ensure a complete coverage of the samples. Studies on steel show that 10 mm of powders above the samples are enough to obtain a borided coating [1]. In the present study the thickness of the powder ranged between 15 mm and 25 mm. All kinds of mixtures were weighted using a scale under chemical hood and blended in a WC ball milling.

#### **First composition: B – Activated Charcoal – Na<sub>2</sub>B<sub>4</sub>O<sub>7</sub>**

For the first composition of the powder mixture the works of Ravi Chandran et al. were taken into account [2–5].

10 g of powder mixture was employed to ensure a thickness of 2.5 mm of powder over the samples as suggested in literature [2,4,5]. The powders were blended for 6 h in the ball milling.

The powder mixture results to be composed of 50%wt amorphous boron, 35%wt activated charcoal and 15%wt Na<sub>2</sub>B<sub>7</sub>O<sub>4</sub>. In particular, for each treatment 5 g of B, 3.5 g of activated charcoal and 1.5 g of Na<sub>2</sub>B<sub>7</sub>O<sub>4</sub> was used. Amorphous boron corresponds to the boron donor, the activated charcoal to the filler and Na<sub>2</sub>B<sub>7</sub>O<sub>4</sub> to the activator.

The boronizing process with this kind of powder mixture was performed on Ti4Al4V alloy grade 5 disks and pins and on Ti6Al4V alloy ELI disks. The effect of the boronizing process was investigated on three types of surface (no pre/post treatment, oxidised and deoxidised) and after a post thermal treatment. The process was carried out at several temperatures (750 – 800 – 900 – 1050°C) and for several time (2.5 – 3.5 – 4.5 h) of treatment. Figure 4.5 shows samples with different processed surface, while Table 4.3 sums up the types of sample and the process parameters used.

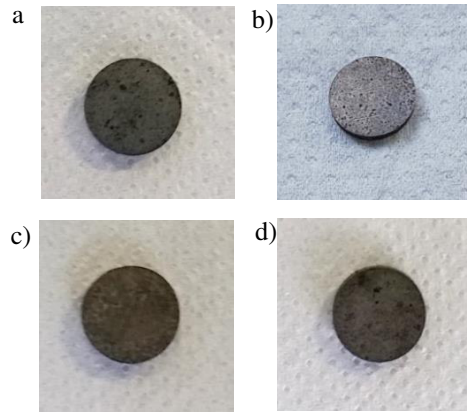


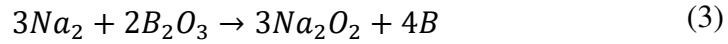
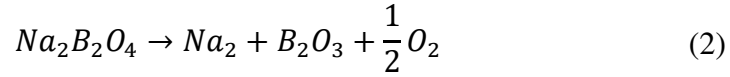
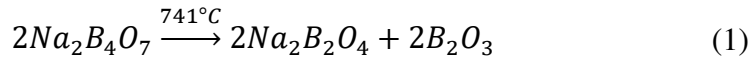
**Figure 4.5** The treated samples a) without any pre/post treatment, b) with pre-treatment of oxidation, c) with pre-treatment of deoxidation and d) subjected to post thermal treatment.

**Table 4.3** Type of samples and process parameters.

Material	Temperature of treatment (°C)	Time of treatment (h)	Pre-treatment or post thermal treatment
Ti6Al4V alloy grade 5 disks	1050	4.5	no pre/post treatment pre-treatment of deoxidation post thermal treatment*
	900	4.5	no pre/post treatment pre-treatment of deoxidation
	800	4.5	no pre/post treatment pre-treatment of deoxidation
	800	3.5	no pre/post treatment pre-treatment of deoxidation pre-treatment of oxidation
	750	4.5	no pre/post treatment pre-treatment of deoxidation
	750	3.5	no pre/post treatment pre-treatment of deoxidation
Ti6Al4V alloy grade 5 pins	750	2.5	no pre/post treatment pre-treatment of deoxidation
	1050	4.5	no pre/post treatment pre-treatment of deoxidation post thermal treatment*
	800	3.5	no pre/post treatment
Ti6Al4V alloy ELI disks	1050	4.5	no pre/post treatment pre-treatment of deoxidation post thermal treatment*
	800	3.5	no pre/post treatment

\* The post thermal treatments were carried out at the same temperature and for the same time of treatment of the corresponding boronizing process.

During the treatments  $\text{Na}_2\text{B}_4\text{O}_7$  melts around  $743^\circ\text{C}$  [6] while amorphous boron and activated charcoal have higher melting point ( $2075^\circ\text{C}$  and  $>3500^\circ\text{C}$  respectively [6]) and remain in the solid state. Between the samples surface and the powder mixture the following reaction takes place [7]:



### Second composition: $\text{B}_4\text{C} - \text{KBF}_4$

The second composition of powder mixture was used in literature to boronizing process on steel alloy and titanium alloy [8]. It is composed of 90%wt  $\text{B}_4\text{C}$  and 10%wt  $\text{KBF}_4$ , containing only the boron donor  $\text{B}_4\text{C}$  and the activator  $\text{KBF}_4$ .

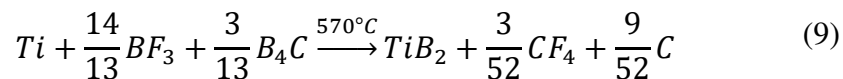
In this case 6 g of powders (5.4 g of  $\text{B}_4\text{C}$  and 0.6 g of  $\text{KBF}_4$ ) were blended for 30 min in the ball milling and a thickness of 15 mm of pack powder was ensured over the samples.

This boronizing process was carried out at  $800^\circ\text{C}$  for 3.5 h on Ti6Al4V alloy grade 5 disks without any pre/post treatment (Figure 4.6).



Figure 4.6 The sample treated with the second composition of powder mixture

The melting points of  $\text{B}_4\text{C}$  and  $\text{KBF}_4$  are  $<2780^\circ\text{C}$  [9] and  $530^\circ\text{C}$  [10], respectively. During the treatment  $\text{KBF}_4$  melts and the reaction that develops between the substrate and the powder mixture is the following [11]:



### Third composition: B<sub>4</sub>C – SiC – KBF<sub>4</sub>

The third composition of powder mixture refers to a commercial powder mixture used to treat steel. The boron source and the activator are the same of the second composition with the addition of the filler. The powder mixture results to be composed of 5%wt B<sub>4</sub>C, 90%wt SiC and 5%wt KBF<sub>4</sub>.

For the boronizing treatment 6 g of powders were used, corresponding to 0.3 g of B<sub>4</sub>C, 0.3 g of KBF<sub>4</sub> and 5.4 g of SiC. The powders were blended in the ball milling for 30 min as in the case of the second composition of powder mixture.

Two temperatures of treatment were used with this kind of powder mixture, 800°C and 700°C. In both cases the time of treatment was 3.5 h and the process was carried out on Ti6Al4V alloy grade 5 disks. They are shows in Figure 4.7.

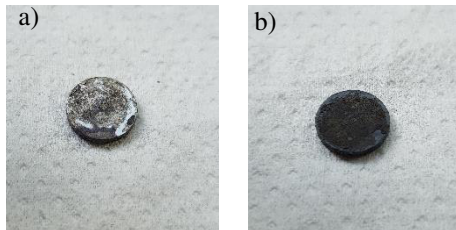
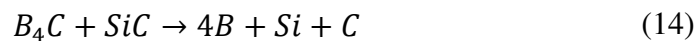
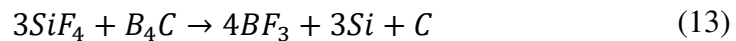
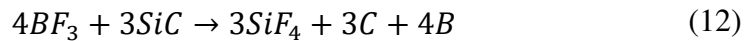


Figure 4.7 The sample treated with the third composition of powder mixture at a) 800°C and b) 700°C.

During the thermal treatment KBF<sub>4</sub> melts while SiC, that has a melting point of 2600°C [6], stay in the solid state as B<sub>4</sub>C. The substrate reacts with the powder mixture following the reaction reported below [11]:



### Fourth composition: B<sub>4</sub>C – KCl+KBF<sub>4</sub>

For the fourth composition of powder mixture the study of Koyama was taken into account [12]. In the study a blend of B<sub>4</sub>C, KBF<sub>4</sub> and KF was used.



Focusing on  $\text{KBF}_4 - \text{KF}$  phase diagram and comparing it with the one  $\text{KBF}_4 - \text{KCl}$ , it is possible to see that they are very similar. They are reported on Figure 4.8.

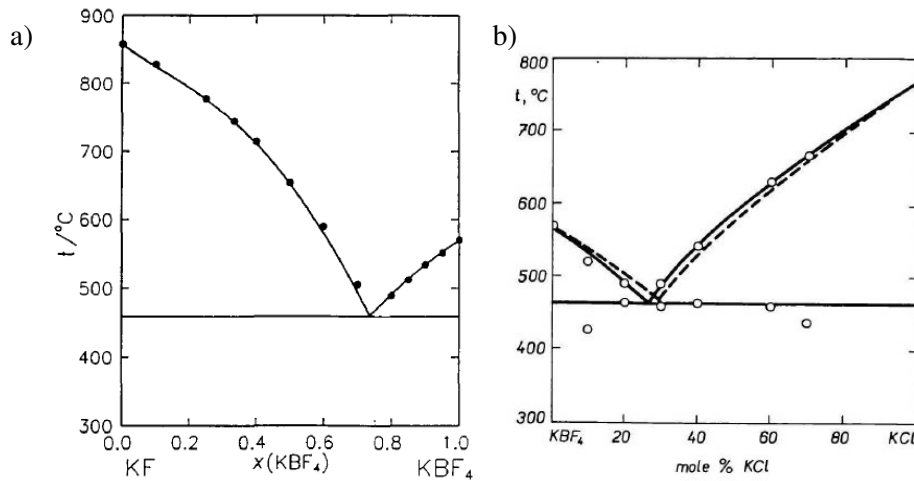


Figure 4.8 a)  $\text{KBF}_4 - \text{KF}$  phase diagram [13] and b)  $\text{KBF}_4 - \text{KCl}$  phase diagram [14]

$\text{KBF}_4 - \text{KF}$  phase diagram shows a eutectic point at  $460^\circ\text{C}$  for a composition of 74%mol  $\text{KBF}_4$  and 26%mol  $\text{KF}$  [13]. While the  $\text{KBF}_4 - \text{KCl}$  phase diagram presents a eutectic point at  $464^\circ\text{C}$  with a composition of 75%mol  $\text{KBF}_4$  and 25%mol  $\text{KCl}$  [14]. As consequence, in the present study the  $\text{KF}$  was replaced by  $\text{KCl}$ , that is less aggressive for the titanium substrates than  $\text{KF}$ .

The powder mixture resulted to be composed of 5%wt  $\text{B}_4\text{C}$  and 95%wt  $\text{KCl} + \text{KBF}_4$  (eutectic composition). 10 g of powders, containing 0.5 g of  $\text{B}_4\text{C}$ , 7.9 g of  $\text{KBF}_4$  and 1.6 g of  $\text{KCl}$ , were blended for 30 min in the ball milling.

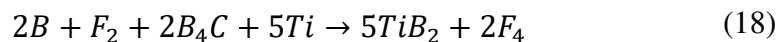
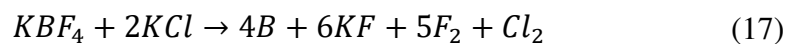
This kind of powder mixture was employed to decrease the temperature of treatment, thus to work at lower temperature and to reduce the microstructural modifications of the substrates, caused by the thermal treatment.

The process was carried out at  $550^\circ\text{C}$  for 3.5 h on  $\text{Ti6Al4V}$  alloy grade 5 disks. Treated samples are shown in Figure 4.9.



Figure 4.9 The sample treated with the fourth composition of powder mixture

At the temperature of about  $464^\circ\text{C}$  the activator ( $\text{KBF}_4 + \text{KCl}$ ) melts while the boron source  $\text{B}_4\text{C}$  is at the solid state and react with the substrate according to the following reaction [15]:



## Fifth composition: B<sub>2</sub>O<sub>3</sub> – Activated Charcoal – LiCl+KCl

The fifth composition of powder mixture was stabilised with the idea to work at low temperature and to avoid the used of fluorides that are aggressive for the titanium substrates.

In this case, B<sub>2</sub>O<sub>3</sub> was used as boron source, because it has a lower melting point (450° [6]) compared with other boron sources such as boron amorphous and B<sub>4</sub>C. LiCl and KCl were employed as activators and activated charcoal as filler. The phase diagram on Figure 4.10 shows that LiCl and KCl form a eutectic point at 352°C for a composition of 58.2%mol KCl and 41.8%mol LiCl [16].

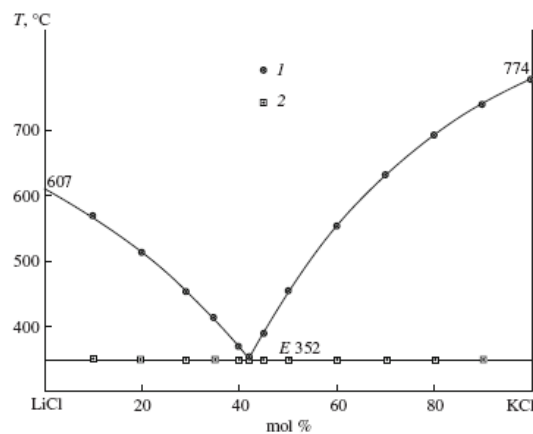


Figure 4.10 LiCl – KCl phase diagram [16]

The powder mixture was composed of 35%wt B<sub>2</sub>O<sub>3</sub>, 35%wt LiCl+KCl (eutectic composition) and 30%wt activated charcoal.

For the boronizing process 10 g of powders, containing 3.5 g of B<sub>2</sub>O<sub>3</sub>, 1.6 g of LiCl, 1.9 g of KCl (eutectic composition) and 3 g of activated charcoal, were blended for 30 min in the ball milling. The process was performed on Ti6Al4V alloy grade 5 disks at two temperatures of treatment, 400°C and 500°C for 3.5 h in both cases (Figure 4.11).

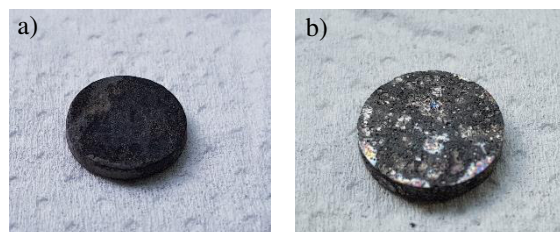
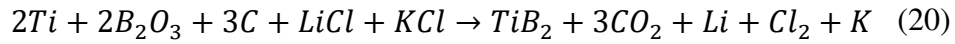


Figure 4.11 The sample treated with the fifth composition of powder mixture at a) 400°C and b) 500°C.

In this case, during the treatment both the activators and the boron source melt and the possible reaction between the substrate and the boron source is the following:



## 4.5 Washing process after the boronizing treatment

After the thermal treatment all the samples were washed in the SONICA ultrasonic bath twice for 10 min in double distilled water and then they were let dry in air on a paper sheet at room temperature.

## 4.6 Samples characterisation

The treated Ti6Al4V alloy disks were characterized in terms of chemical composition, microstructure, structure, thickness, roughness, hardness, adhesion of the coating, surface protein adsorption and surface bioactivity.

### 4.6.1 XRD analysis

All kinds of treated samples were analysed by means of Philips/PANalytical X'Pert Pro diffractometer. The instrument has a Cu  $K_\alpha$  anode and running parameters of 40 kV and 40 mA.

Tests were performed with both Bragg-Brentano geometry and grazing angle measurements. In the first case the X-ray diffraction patterns were collected in  $2\theta$  range of 10-120° with slits of 1/4-1/2. In the second case incident radiations with an incident angle of 1° and 3° were used with slits of 1/8-1/4. The X-ray diffraction patterns were collected in  $2\theta$  range of 26-90°.

Data were analysed using X'Pert highScore program and the International Centre for Diffraction Data (ICDD) database.

Data of the treated samples were compared with the ones of the untreated samples and with each other.

### 4.6.2 Observation of substrate microstructure and coating morphology and thickness

The untreated Ti6Al4V alloy grade 5 disks and the ones treated with the first powder composition (B – activated charcoal -  $Na_2B_4O_7$ ) were observed by means of Reicher-Jung MeF3 optical microscope and Zeiss supra 40 GEMINI Field Emission Scanning Electron Microscopy (FESEM). The optical microscope was used for evaluating the substrate microstructure, while FESEM for analysing the morphology and thickness of the coatings. Images, acquired through FESEM, were processed with ImageJ software, to determine the thickness of the coatings.

The samples, firstly, were cut transversely with the Brillant 200 cutting machine. Secondly, they were fixed on a Cu spring and encapsulated into a resin. Then they were polished with SiC abrasive sheets from 120 to 2500 grit and then the samples were chemically etched with 5M HF solution. Each sample was soaked

for 30 s in 10 ml of solution and washed with double distilled water in order to bring out its microstructure. Following, the samples were let dry and observed.

Three kinds of resins with low shrinkage were used: Struers epoxy resin, Struers acrylic resin and Presi phenolic resin. The first one is a cold epoxy resin composed of liquid EpoFix resin and liquid EpoFix hardener, that takes 24 h to stiffen. Every 15 ml of liquid resin need 2 ml of hardener. The second resin is a cold acrylic resin, that stiffens in 30 min and requires the mixing of 2 part of LevoCit liquid resin and 1 part of LevoCit powder hardener. The third resin is a hot powder phenolic resin, that under high temperature and pressure stiffening in 20 min. For each samples were used 20 ml of powder.

### 4.6.3 Hardness

Hardness was measured by means of Vickers and Knoop microindentations and nanoindentations.

Vickers microindentations were performed at Chubu University in Japan using the Shimadzu HMV Micro Hardness Tester. The measurements were carried out on Ti6Al4V alloy grade 5 disks without any pre/post treatment and treated with the first powder mixture. As reference material untreated Ti6Al4V alloy grade 5 disk was used. The measurements were performed with a diamond tip with straight pyramid shape with square base. Five indentations were done on each sample perpendicular to the surface. The time test was set at 10 s while the load at 0.490 N for samples treated below 900°C and at 0.980 N for samples treated above 900°C. A load of 0.490 N did not allow to obtain a visible footprint on the surface of samples treated at high temperatures. For each indentation the dimensions of the two diagonals of the footprint were collected and then the value of the hardness was calculated using the following equation as setting out in the UNI EN ISO 6507 standard:

$$HV = 0.1891 * \frac{F}{d^2} \quad (22)$$

Where 0.1891 is the penetrator constant, F the load expressed in N and d the mean value of the diagonals expressed in mm.

The thickness must be 1.5 times the average value of the diagonals in order to verify the standard. Thus the thickness values of the coating were compared with the calculated values.

To compare the Vickers hardness (HV) values with the Knoop (HK) ones and the ones collected through nanoindentations, the HV values were converted in GPa using the following equation:

$$H_{GPa} = HV * 0.009807 \quad (23)$$

Knoop microindentations were carried out at DIAT of Politecnico di Torino, with the Leitz DURIMET tester. The measurements were performed on all kinds of Ti6Al4V alloy grade 5 disks treated with the first powder mixture. Also in this case,

untreated Ti6Al4V alloy grade 5 disk was used as reference material. A diamond tip with straight pyramid shape with rhomboidal base was used. Three indentations were done on each sample perpendicular to the surface. The time test was set at 20 s and the load at 0.490 N. For each indentation the dimension of the longest diagonal of the footprint was collected and then the value of the hardness was calculated using the following equation as setting out in the UNI EN ISO 4516 standard:

$$HK = 1.451 * \frac{F}{d^2} \quad (24)$$

Where 1.451 is the penetrator constant, F the load expressed in N and d the mean value of the longest diagonal expressed in mm.

In this case the standard results to be verified if the thickness is 0.35 times the longest diagonal. As before the HK values were converted in GPa using the following equation:

$$HK_{GPa} = HK * 0.009807 \quad (25)$$

The nanoindentation tests were performed with the TI-900 TirboIndenter Hysitron at the TUWien in Austria. The tests were done with a Berkovich tip, a fall and rise time of 8 s and a dwell of 20 s. Both the hardness and the elastic modulus were taken into account during the tests. Measurements were carried out on an untreated Ti6Al4V alloy grade 5 pin and on a disks of Ti6Al4V alloy grade 5 treated at 800°C for 3.5 h without any pre/post treatment with the first powder composition.

Before doing the nanoindentations, a roughness measurement was performed using the Berkovic tip on an area of 50x50 µm on each sample. Roughness is extremely important because it can influence the nano-hardness values considerably.

On the treated samples two preliminary test were performed to define the most suitable one for the studied material. The first test consisted on a series of 3 single indentations under a displacement control of 100 nm. The second test, instead, corresponded to a 3 single indentations under a load control of 10000 µN. Then two tests consisting of a series of 34x25 indentations were done under a load control of 10000 µN.

The specimen was then hand polished, performing a figure 8 and following the polishing protocol reported in Table 4.4.

**Table 4.4 Polishing protocol**

<b>Diamond suspension 3µm</b>	<b>Diamond suspension 1µm</b>	<b>Diamond suspension 0.25µm</b>
40min	40min	40min

After the polishing, firstly, a preliminary test of 7 single indentations were performed, then a grid of 34x25 indentations were carried out. Both the tests were done under a load control of 10000 µN.

A series of 3x3 indentations, instead, was carried out on the untreated pin under a load control of 10000  $\mu\text{N}$ .

Samples were compared to each other and with literature data.

#### **4.6.4 Roughness**

The roughness was evaluated through Form Talysurf 120 contact profilometer at IMAMOTER in Torino.

The measurements were carried out on all kinds of Ti6Al4V alloy grade 5 disks treated with the first powder composition and on the reference materials (untreated Ti6Al4V alloy grade 5, CoCrMo alloy and alumina). Three measurements were done on each sample with a conical stylus type with a radius tip of 2  $\mu\text{m}$ . Each measurement was 3 mm in length, with a 0.8 mm cut off length. For each sample the average roughness was calculated and compared to each other and with the one of polished untreated material.

#### **4.6.5 Wettability**

The surface wettability was evaluated by means of KUSS DSA 100 Drop Shape Analyser, using the sessile drop method. Medium used was double distilled water and the analysed samples were all kinds of Ti6Al4V alloy grade 5 disks treated with the first powder composition and the reference materials (untreated Ti6Al4V alloy grade 5, CoCrMo alloy and alumina).

A drop of double distilled water was put on the surface of the samples at room temperature using a 5  $\mu\text{l}$  micropipette, an image of the drop was captured by the camera and the contact angle was collected automatically through the Drop Shape Analysis software of the instrument. Three measurements were carried out on each sample and then for each sample an average contact angle was calculated.

#### **4.6.6 Polishing of the coatings**

The polishing process causes an increase of roughness as reported in literature [17]. To reduce surface roughness several polishing approaches were evaluated.

In one case, the coating was polished with diamond pasts of 6, 3, 1  $\mu\text{m}$  and in the second case, the coating was polished by means of diamond suspensions of 3 and 1  $\mu\text{m}$ .

In all cases, samples were polished at least for few minutes for each grit and between one step and another of the polishing process the samples were observed by Reicher-Jung MeF3 optical microscope.

#### **4.6.7 Scratch test**

The adhesion of the coatings obtained with the first powder composition was evaluated by means of scratch tests using the Revetest Scratch Tester at IMAMOTER in Torino. The reference materials (untreated Ti6Al4V alloy grade 5, CoCrMo alloy and alumina) were also tested as comparison. Each sample was

tested three times using a Rockwell C diamond stylus 200  $\mu\text{m}$  in radius. Each scratch consists of a line scratch 4.9 mm long, under a normal load continuously increasing from 1N to 50N. The loading rate was 100 N/min with a speed of 10 mm/min. Normal load, friction force and acoustic emission were recorded during the tests. The tests were performed following the ASTM G171 standard.

The samples treated at 750°C for 3.5 h without any pre/post treatment were also tested with CSR-2000 Rhesca Co. Scratch Tester at Chubu University in Japan. Five scratches were performed on each sample, applying a normal load increasing up to 200 mN in 30 s with a diamond stylus 5  $\mu\text{m}$  in radius.

The sample treated at 800°C for 3.5 h without any pre/post treatment was, in addition, scratched at TUWien in Austria by means of the TI-900 TirboIndenter Hysitron. A linear nanoscratch 30  $\mu\text{m}$  long with progressive load up to 12000  $\mu\text{N}$  reached in 30 s was performed, using a cono-spherical probe with radii of 5.04  $\mu\text{m}$  and a cone angle of 62.54°.

#### 4.6.8 Wear test and ICP analysis

Wear tests were performed by means of Docum Biotribometer with multidirectional motion at Ducom Instruments Europe in Netherlands. Hard on hard contact and soft on hard contact were taken into account: in the first case metallic disks were put in contact with metallic pins, using a constant normal load of 400 N. While in the second case metallic disks were put in contact with UHMWPE pins, using a constant normal load of 100 N. The scheme of the tests done is reported in Table 4.5.

**Table 4.5 Materials and conditions of the wear test**

Contact	Disk	Pin	Kind of treatment	Note
Hard on hard	Ti6Al4V alloy ELI	Ti6Al4V alloy grade 5	First composition of powder mixture (800°C for 3.5h and 1050°C for 4.5h)	Any pre/post treatment
	Ti6Al4V alloy ELI	Ti6Al4V alloy grade 5		Pre-treatment of deoxidation
	Ti6Al4V alloy ELI	Ti6Al4V alloy grade 5		Post thermal treatment
	Ti6Al4V alloy ELI	Ti6Al4V alloy grade 5		Untreated
Soft on hard	CoCrMo alloy	CoCrMo alloy	Untreated	
	Ti6Al4V alloy ELI	UHMWPE	First composition of powder mixture (800°C for 3.5h and 1050°C for 4.5h)	Any pre/post treatment
	Ti6Al4V alloy ELI	UHMWPE		Pre-treatment of deoxidation
	Ti6Al4V alloy ELI	UHMWPE		Post thermal treatment
	Ti6Al4V alloy ELI	UHMWPE		Untreated
		CoCrMo alloy	UHMWPE	Untreated

CoCrMo alloy and untreated Ti6Al4V alloy were used as reference materials.

A 8 shape path was executed by pins on stationary disks, with a speed of 31.4 mm/s for 1 h. The tests were carried out in lubricant condition at 37°C, using FBS as lubricant. The lubricant was composed by FBS aqueous solution at 25% v/v plus 1g/l of NaN<sub>3</sub>; for each test 30 ml of lubricant were used. The UHMWPE pins before being tested were weighted, rinsed with ethanol, soaked in PBS for 60 min, soaked in the FBS solution for 60 min, rinsed again with ethanol, dried with compressed air, weighted again, rinsed with ethanol and soaked again in PBS for 60 min, then used for the tests.

During the tests wear was measured by means of Linear Variable Differential Transformer (LVDT). After the tests Phenom XL Scanning Electron Microscope was employed to observe wear tracks on samples.

2 ml of each lubricant, used in the wear tests, were collected and analysed by means of Thermo Fisher iCAP Q 5110 Inductively Coupled Plasma Mass Spectrometer (ICP-MS); in order to quantify the amount of metallic ions (Al, V, Ti and B) released.

When necessary, the collected lubricants were mineralized with the blood method (HNO<sub>3</sub>+H<sub>2</sub>O<sub>2</sub> in a ratio 4:1), using the ETHOS EASY Advanced Microwave Digestion System and diluted with triple distilled water, before to be analysed.

#### 4.6.9 Fretting test

Fretting tests were performed to simulate the condition at the interface between the stem of a hip prosthesis and the cement. The measurements were carried out at the Polytechnic Department of Engineering and Architecture of Università di Udine.

Pins of untreated Ti6Al4V alloy, AISI 316L and treated Ti6Al4V alloy without any pre/post treatment were tested against a plates of bone cement.

Figures 4.12 and 4.13 show the pins and the plates.



**Figure 4.12 a) AISI 316L, b) treated Ti6Al4V alloy without any pre/post treatment and c) untreated Ti6Al4V alloy pins for fretting test**



**Figure 4.13 Bone cement plates for fretting test**



Fretting tests were performed in triplicate on each kind of pin by means of CETR UMT-3. The instrument has a driver with alternate motion and 1 kN load cell. The cement plates were put in a titanium box filled with lubricant and set on the driver. While the pins were clasped to the holder and set on the load cell.

Each test was performed with a load of 49 N (2.5MPa), a frequency of 3 Hz and a displacement of 0.4 mm for 50000 cycles in lubricant condition at 37°C. As in the case of wear tests, the lubricant was composed by FBS aqueous solution at 25% v/v plus 1g/l of NaN<sub>3</sub>.

Data of normal force, tangential force, vertical displacement of the pins, COF, number of cycles and time were collected during the tests with a frequency of about 2 Hz. The data were then processed by means of Sigma Plot software, using a median filter.

The samples were weighted before and after the tests to evaluate changing in weight, moreover, data about roughness and wear rate were calculated on the base of profilometric analyses. Profilometric analyses were performed using a Veeco Dektak stylus profilometer, with a tip of 12.5 mm in radius. Profilometric maps of 1x1 mm and of 7x10 mm were acquired respectively for pins and plates. 100 and 200 multiple scans side-by-side were performed respectively for pins and plates.

Wear rate was detected calculating the wear volume on the base of the profilometric maps. Wear rate equation is reported below:

$$K = \frac{\text{removed volume}}{\text{displacement} * \text{load}} \quad (26)$$

Data were then elaborated through Veeco Vision software.

The surfaces were observed by means of SEM Zeiss Evo 40 with EDXS Oxford Inca X size probe after test.

#### **4.6.10 Protein adsorption**

The protein adsorption behaviour was taken into account due to the fact that the studied material would be used in contact with biological fluid. To evaluate the protein adsorption, the Ti6Al4V alloy grade 5 disks without any pre/post treatment and treated with the first powder composition at 1050°C for 4.5 h were soaked in several protein solutions. The same was done with the reference materials (untreated Ti6Al4V alloy grade 5, CoCrMo alloy and alumina).

For the tests Bovine Serum Albumin (BSA) solution, fibronectin solution and Fetal Bovine Serum (FBS) were used.

Fetal bovine serum was used as received, while BSA and fibronectin were dissolved in suitable medias. Two BSA solutions were prepared, one dissolving the protein in double distilled water and one dissolving the protein in Phosphate Buffered Saline (PBS). Fibronectin was dissolved only in PBS.

BSA solutions with a concentration of 20 mg/ml were prepared, in order to work in the same range of albumin content within FBS (20-36 mg/ml) [18]. The concentration of fibronectin solution was set at 0.2 mg/ml considering the serum

human values [19]. While the protein concentration of FBS is reported to be 50 mg/ml [20].

BSA and FBS adsorptions were performed using 1 ml of solution for each sample. The solution of fibronectin, instead, was available in less amount, so the samples were soaked all together in 1 ml of solution.

The pH of each solutions was registered.

The samples were soaked in each solution for 2 h at 37°C in an incubator, then they are washed in double distilled water, let dry under biochemical hood and analysed by means of SurPASS Anton Paar electrokinetic analyser and X-ray Photoelectron Spectroscopy (XPS) PHI 5000 VersaProbe - Physical Eletronics.

The untreated and treated Ti6Al4V alloy were tested using all the three protein solutions while the CoCrMo alloy and alumina were soaked only in the BSA and FBS solution. This because they are not used as osteointegrable materials.

The untreated and treated Ti6Al4V alloy samples after soaking in FBS were also analysed by BCA Protein Assay Kit, to evaluate the amount of adsorbed proteins.

## **Zeta potential analysis**

Zeta potential titration vs pH was evaluated by SurPASS Anton Paar electrokinetic analyser. Analysis were performed on samples after protein adsorption and on the corresponding samples without protein adsorption.

The instrument presents a cell, in which a couple of samples is put face to face with a gap of about 100 µm. Between the samples a flow of aqueous solution is forced and the reciprocal movement between the surfaces and the flow causes an electrokinetic effect. The measurement of this effect correspond to the zeta potential. When the surface is put in contact with the aqueous solution, the surface assumes a charge due to acid-basic reaction between the aqueous solution and the surface functional groups or due to the adsorption of water ions on hydrophobic surface. In this way the ion distribution at the interface between the solid surface and the aqueous solution results to be different from the ion distribution in the liquid phase. All this mechanism is strongly dependent on pH [21].

The surface zeta potential was determined in function of pH in a 0.001 M KCl electrolyte solution. The solution pH was varied by addition of 0.05M HCl or 0.05M NaOH through the instrument automatic titration unit. Two distinct couples of samples were used for the acid and alkaline sides of the curve. Usually the acid side was tested firstly.

At Università degli Studi di Torino (Dipartimento di Scienza e Tecnologia del Farmaco) the zeta potential of the single proteins solutions was measured by means of Malvern Nano ZS zetasizer. The zeta potential of each solution was evaluated in triplicate at the pH of 3,4,5,6,7,8. First of all, BSA and fibronectin were dissolved in PBS to obtain solution with the concentration of 35 mg/ml and 0.2 mg/ml, respectively. While the FBS with a concentration of 50 mg/ml was used as received. Then each solution was aliquoted in 0.001 M KCl solutions to obtain the final concentration of 5 mg/ml for BSA solution and FBS and of 0.01mg/ml for

fibronectin solution. Finally, the values of pH were tailored with HCl 0.05M or NaOH 0.05M. For each measurement 20  $\mu$ l of solution were used for each pH values.

### **X-ray Photoelectron Spectroscopy**

The surface chemical composition of the samples after protein adsorption and on the corresponding samples without protein adsorption was evaluated by means of X-ray Photoelectron spectroscopy (XPS) PHI 5000 VersaProbe - Physical Electronics. Measurements were carried out with a monochromatic aluminium K-alpha X-rays centred on 1486.6eV. Survey spectra and high resolution spectra were collected for each sample. The elements detected with the high resolution spectra were C, O, Ti, B and N. The hydrocarbon maximum peak in the C 1s spectra was set at 284.8 eV as reference of the binding energy scale for all the samples.

### **BCA Protein Assay Kit analysis**

The BCA Protein Assay is a colorimetric method to detect and quantify the total amount of adsorbed proteins on a surface. It is based on the reduction of  $\text{Cu}^{+2}$  to  $\text{Cu}^{+1}$  by protein in an alkaline medium, followed by the chelation of two molecules of bicinchoninic acid (BCA) with one  $\text{Cu}^{+1}$  ion. This is a purple-coloured reaction with absorbance at 562 nm.

The kit used is the one of the Thermo Scientific Pierce, performing the test tube procedure with a working range of 20-2000  $\mu$ m/ml.

First of all, the samples after FBS adsorption were soaked in 300  $\mu$ l of 2% sodium dodecyl sulfate (Fisher BioReagent) for 1 night and sonicated for 5 minutes to completely desorb the proteins attached on the surfaces. The solutions were then collected to be analysed by means of BCA Protein Assay Kit for quantifying the amount of adsorbed proteins.

The procedure consists on determining the protein concentration of the samples with reference to standard of BSA.

The first step was to prepare a series of BSA dilutions of known concentration to define the standard curve.

The dilutions were prepared following the volumes of diluent and BSA reported in Table 4.6.

**Table 4.6 Dilution scheme for standard test tube protocol**

Vial	Volume of diluent ( $\mu\text{l}$ )	Volume of BSA ( $\mu\text{l}$ )	BSA concentration ( $\mu\text{g/ml}$ )
A	0	300 of stock	2000
B	125	375 of stock	1500
C	325	325 of stock	1000
D	175	175 of vial B	750
E	325	325 of vial C	500
F	325	325 of vial E	250
G	325	325 of vial F	125
H	400	100 of vial G	25
I	400	0	0 (blank)

The prepared volumes were sufficient for three repetitions of each diluted standard.

Then it was prepared the working reagent, necessary to start the colorimetric reaction, by mixing 50 parts of a reagent A and 1 part of a reagent B. The reagent A is composed by sodium carbonate, sodium bicarbonate, bichinchonic acid and sodium tartrate in 0.1 M sodium hydroxide. While the reagent B contains 4% cupric sulfate. The amount of required working reagent was determined using the following formula:

$$\text{total volume of working reagent} = (\#standards + \#samples) * (\text{replicates}) * (\text{volume of working reagent per samples}) \quad (27)$$

9 standards and 2 samples were used, performing three replicates and using 2 ml of working reagent per sample as reported in the manual of the kit. Therefore, 66 ml of working reagent were needed.

At that point, 0.1 ml of each standard and sample in three replicates was mixed with 2 ml of working reagent. Then the solutions were incubated at 37°C for 30 minutes, cooled to room temperature and analysed by means of spectrophotometer (UV-2600 Shimadzu).

The instrument was set to 562 nm and the zero was carried out using double distilled water.

At the end, the data collected was plotted to define the standard curve and the concentration of the samples.

#### **4.6.11 In vitro bioactivity**

The bioactivity behaviour of Ti6Al4V alloy grade 5 disks treated at 1050°C for 4.5 h without any pre/post treatment and treated with the first powder composition was investigated by soaking the samples in simulated body fluid (SBF). The test was performed following the protocol of Kokubo [22].

The bioactivity was evaluated at 14 and 28 days, with solution refresh every 7 days. Two samples were used for each time point and each sample was soaked in 25 ml of FBS and kept at 37°C in an incubator.

The SBF was filtered using 0.2 µm filter and incubated for 24 h at 37°C in an incubator before the start of the test and before every solution refresh.

The samples were, finally, washed in double distilled water and let dry under chemical hood.

After the test the samples were observed with Zeiss supra 40 GEMINI FESEM equipped with Energy Dispersive Spectroscopy (EDS), to evaluate the deposition of hydroxyapatite.



## References

- [1] Jain V, Sundararajan G. Influence of the pack thickness of the boronizing mixture on the boriding of steel. *Surface and Coatings Technology* 2002;149:21–6. doi:10.1016/S0257-8972(01)01385-8.
- [2] Sarma B, Ravi Chandran KS. Accelerated kinetics of surface hardening by diffusion near phase transition temperature: Mechanism of growth of boride layers on titanium. *Acta Materialia* 2011;59:4216–28. doi:10.1016/j.actamat.2011.03.046.
- [3] Sivakumar B, Singh R, Pathak LC. Corrosion behavior of titanium boride composite coating fabricated on commercially pure titanium in Ringer's solution for bioimplant applications. *Materials Science and Engineering C* 2015;48:243–55. doi:10.1016/j.msec.2014.12.002.
- [4] Sarma B, Tikekar NM, Ravi Chandran KS. Kinetics of growth of superhard boride layers during solid state diffusion of boron into titanium. *Ceramics International* 2012;38:6795–805. doi:10.1016/j.ceramint.2012.05.077.
- [5] Tikekar NM, Ravi Chandran KS, Sanders A. Nature of growth of dual titanium boride layers with nanostructured titanium boride whiskers on the surface of titanium. *Scripta Materialia* 2007;57:273–6. doi:10.1016/j.scriptamat.2007.03.050.
- [6] [pubchem.ncbi.nlm.nih.gov](http://pubchem.ncbi.nlm.nih.gov).
- [7] Kartal G, Timur S, Urgen M, Erdemir A. Electrochemical boriding of titanium for improved mechanical properties. *Surface and Coatings Technology* 2010;204:3935–9. doi:10.1016/j.surfcoat.2010.05.021.
- [8] Petrova RS, Suwattananont N, Samardzic V. The Effect of Boronizing on Metallic Alloys for Automotive Applications. *Journal of Materials Engineering and Performance* 2008;17:340–5.
- [9] [www.azom.com](http://www.azom.com).
- [10] [www.chemicalbook.com](http://www.chemicalbook.com).
- [11] Spence TW, Makhlof MM. Characterization of the operative mechanism in potassium fluoborate activated pack boriding of steels. *Journal of Materials Processing Technology* 2005;168:127–36. doi:10.1016/j.jmatprotec.2004.10.015.
- [12] Koyama K, Shimotake H, Mrazek FC. Boriding of Nickel and Other Metals at Temperatures below 670°C. *Journal of the Electrochemical Society* 1983;130:147–51. doi:10.1149/1.2119643.
- [13] Chrenková M, Patařák O, Danek V. Phase diagram of the system KF-KBF<sub>4</sub>-

K2TiF 6. *Thermochimica Acta* 1996;273:157–67.

- [14] Daněk V, Votava I, Cherenková-Paucirová M, Matiasovsky K. Phase diagram of the ternary system KBF<sub>4</sub> — NaCl — KCl. *Chemical Papers* 1976;30:841–6.
- [15] C.Subramanian, A.K.Suri TSRCM. Development of Boron-based materials for nuclear applications. *Technology Development Article* 2010:14–22.
- [16] Basin AS, Kaplun AB, Meshalkin AB, Uvarov NF. The LiCl-KCl binary system. *Russian Journal of Inorganic Chemistry* 2008;53:1509–11. doi:10.1134/S003602360809026X.
- [17] Şahin S. Effects of boronizing process on the surface roughness and dimensions of AISI 1020, AISI 1040 and AISI 2714. *Journal of Materials Processing Technology* 2009;209:1736–41. doi:10.1016/j.jmatprotec.2008.04.040.
- [18] Gstraunthaler G, Lindl T. *Zell-und Gewebekultur: allgemeine Grundlagen und spezielle Anwendungen*. 2013.
- [19] Sousa SR, Lamghari M, Sampaio P, Moradas-Ferreira P, Barbosa MA. Osteoblast adhesion and morphology on TiO<sub>2</sub> depends on the competitive preadsorption of albumin and fibronectin. *Journal of Biomedical Materials Research Part A* 2008;84:281–90. doi:10.1002/jbm.a.
- [20] [www.sigmaaldrich.com](http://www.sigmaaldrich.com) 2018.
- [21] Luxbacher T. *The Zeta Guide Principles of the streaming potential technique*. 2014.
- [22] Kokubo T, Takadama H. How useful is SBF in predicting in vivo bone bioactivity? *Biomaterials* 2006;27:2907–15. doi:10.1016/j.biomaterials.2006.01.017.



# Chapter 5

## Results and Discussions

### 5.1 Overview of the plan of the experiments

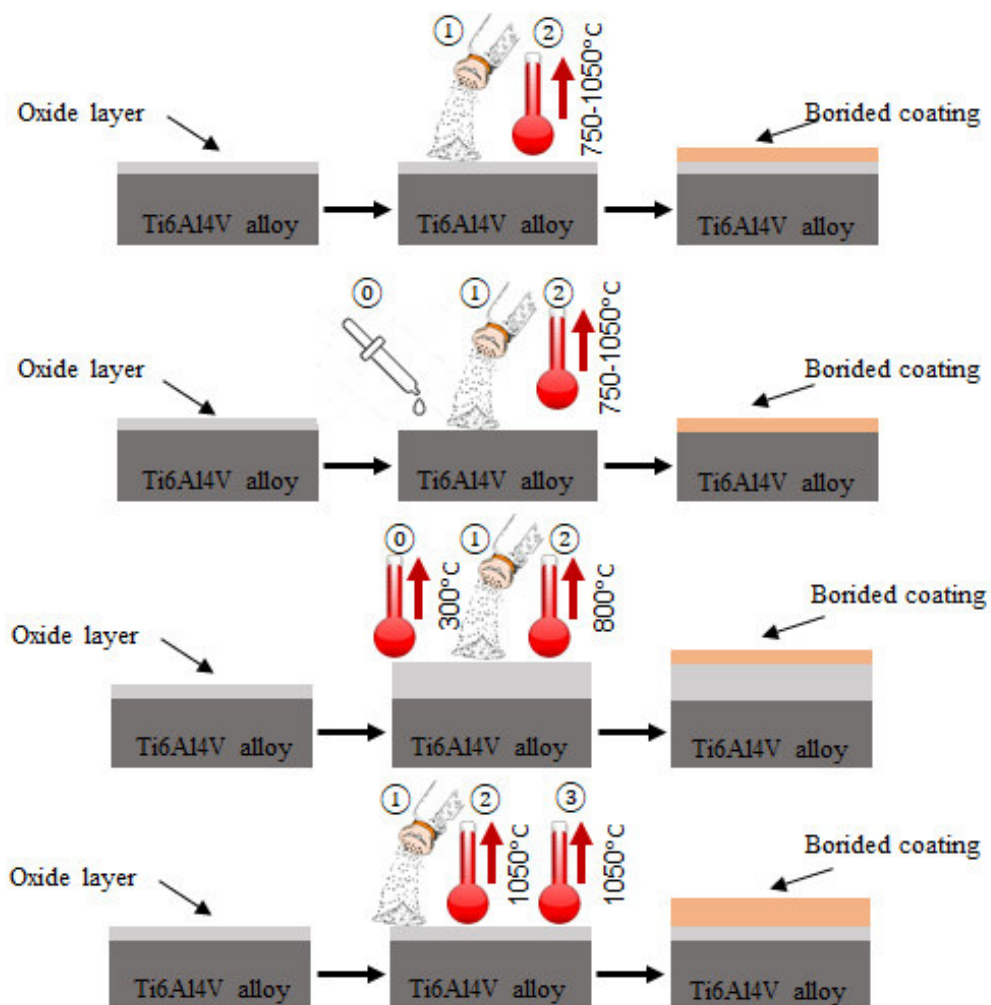


Figure 5.1 Different treatment process carried out on the samples: a) sample treated without any pre/post treatment, b) sample treated with pre-treatment of deoxidation, c) sample treated with pre-treatment of oxidation and d) sample subjected to post thermal treatment

Figure 5.1 summarizes the different treatment processes carried out on the samples. As mentioned in the Chapter 4, the coating was performed on samples with different surface: samples with natural oxide layer (Figure 5.1a), samples without the oxide layer (Figure 5.1b) and samples with an increased oxide layer (Figure 5.1c). Moreover, it was investigated the effect of a post thermal treatment (Figure 5.1d).

A summary of the kind of powder composition used and characterizations carried out on each sample are summarized in Table 5.1.

**Table 5.1 Summary of powder composition and characterizations**

<b>Powder composition</b>	<b>Substrate</b>	<b>Pre/post treatment</b>	<b>Temperature/Time</b>	<b>Characterization</b>
50%wt B – 35%wt Activated Charcoal – 15%wt Na <sub>2</sub> B <sub>4</sub> O <sub>7</sub>	Ti6Al4V alloy grade 5	No pre/post treatment	1050°C/900°C/ 800°C/750°C 4.5 h/3.5 h/2.5 h	XRD analysis – microstructure observation – coating thickness – micro/nano hardness
		Pre- treatment of deoxidation Pre- treatment of oxidation Post thermal treatment		– roughness – wettability – scratch test – wear test – zeta potential analysis – XPS analysis – BCA analysis – in vitro bioactivity
	Ti6Al4V alloy ELI	No pre/post treatment Pre- treatment of deoxidation Post thermal treatment	1050°C 4.5 h	XRD analysis – wear test
90%wt B <sub>4</sub> C – 10%wt KBF <sub>4</sub>	Ti6Al4V alloy grade 5	-	800°C 3.5 h	XRD analysis
5%wt B <sub>4</sub> C – 90%wt SiC – 5%wt KBF <sub>4</sub>	Ti6Al4V alloy grade 5	-	800°C/700°C 3.5 h	XRD analysis
5%wt B <sub>4</sub> C – 95%wt KCl+KBF <sub>4</sub>	Ti6Al4V alloy grade 5	-	550°C 3.5 h	XRD analysis
30%wt B <sub>2</sub> O <sub>3</sub> – 35%wt Activated Charcoal – 35%wt LiCl+KCl	Ti6Al4V alloy grade 5	-	500°C/400°C 3.5 h	XRD analysis

Visual inspection and XRD analyses were used as preliminary screening. The boronizing process has to preserve the samples in shape and dimensions and the coating has to be composed of titanium borides without any contaminations or additional compounds. Such characteristics were used as threshold for further analyses and evaluation of the properties of the coatings in terms of thickness, hardness, roughness, wettability and scratch test. According to the obtained results, a further screening was applied: wear tests and interaction with biological fluids.

## 5.2 Comparison of Ti6Al4V alloy grade 5 and ELI

Two kinds of Ti6Al4V alloy were used for this study: grade 5 and ELI. To verify the similarity of the two substrates and the possibility to compare the data obtained on them, the two substrates were, firstly, analysed by means of XRD measurements. XRD patterns of the untreated materials were collected as described in Chapter 4 and the crystallographic structure was evaluated and compared.

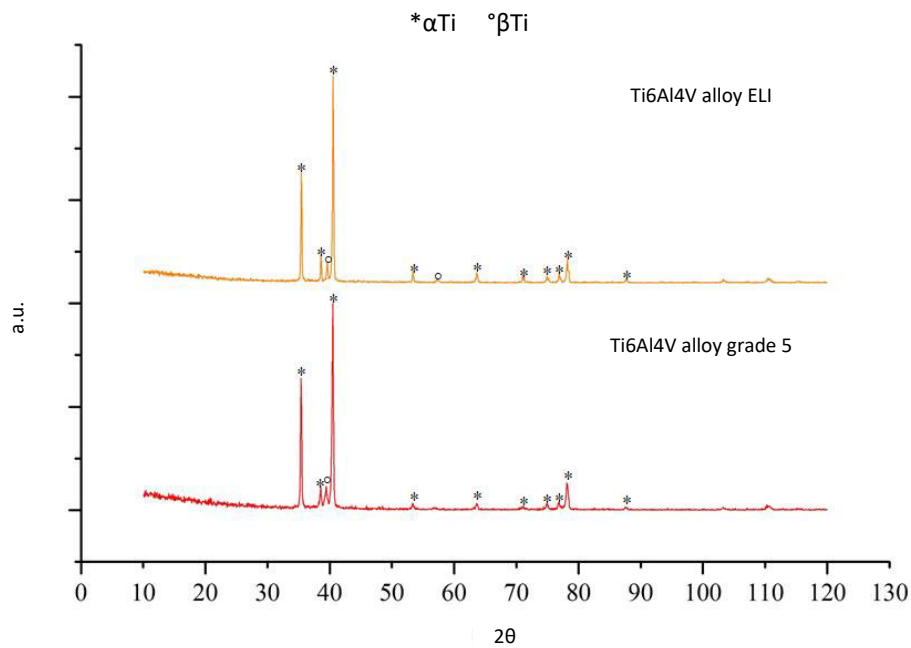


**Figure 5.2** Bragg-Brentano spectra of the untreated Ti6Al4V alloy grade 5 and ELI

As expected, being the Ti6Al4V alloy an  $\alpha$ - $\beta$  alloy, the XRD patterns (Figure 5.2) show the presence of  $\alpha$  and  $\beta$  phases in both substrates. In addition, the measurements were carried out at room temperature, thus, as usual, the amount of  $\alpha$  phase is higher than the one of  $\beta$  phase.

As the Figure 5.2 shows the patterns of two materials are similar both concerning position and intensity ratio of the peaks. The two substrates result to have the same crystallographic structure and they will be considered as comparable at this stage. The eventual effect of presence/absence of impurities on the diffusion of B will be considered in a second stage.

### 5.3 Characterization of the Ti6Al4V alloy grade 5 samples treated with the first composition of powder mixture (50% wt B – 35% wt Activated Charcoal – 15% wt Na<sub>2</sub>B<sub>4</sub>O<sub>7</sub>)

For a preliminary analysis, the samples were treated at 1050°C for 4.5h. After the treatment, the samples appeared uniformly covered and not deformed by means of visual inspection. The result of the treatment is shown in Figure 5.3.

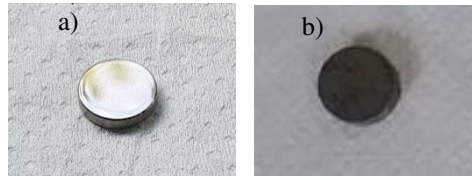


Figure 5.3 Picture of the a) untreated and b) sample without any pre/post treatment treated at 1050°C for 4.5 h.

XRD analysis reveals the presence of titanium borides on the surface, as it is possible to see in Figure 5.4. The principal titanium borided phases are TiB and TiB<sub>2</sub>. The first is the more thermodynamically stable and less hard phase (>15 GPa Hv), while the second is the less thermodynamically stable and harder phase (~30 GPa Hv) [1].

Grazing angle measurements at 1° and 3° suggest that the coating has a gradient chemical composition. The coating shows an external layer composed of TiB<sub>2</sub> phase and an inner part composed of TiB phase. This trend is in agreement with literature data about boriding treatments on c.p. Ti [2].

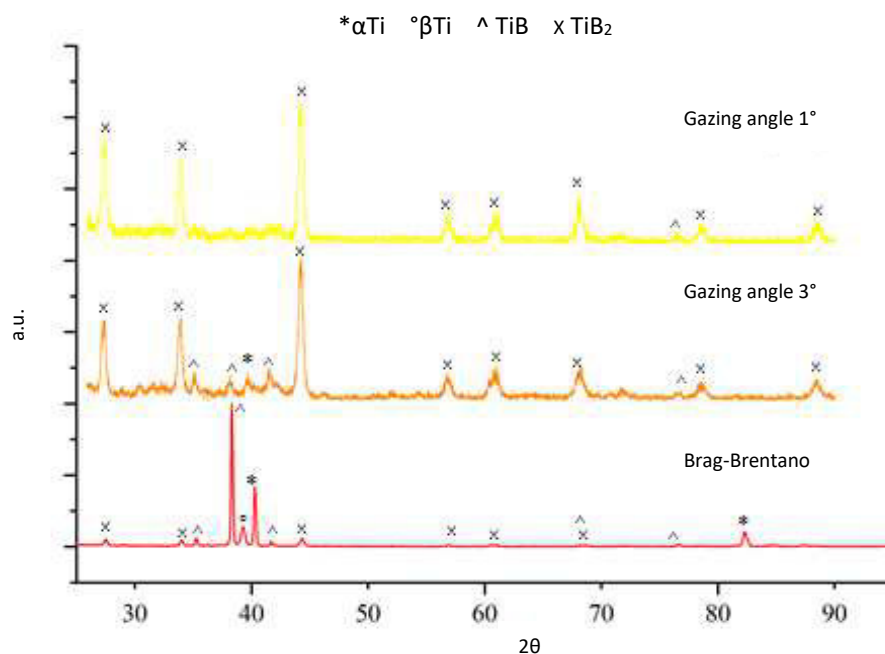


Figure 5.4 XRD patterns collected with Bragg-Brentano geometry and grazing angle at 1° and 3° of samples without any pre/post treatment treated at 1050°C for 4.5 h.

Brag-Brentano pattern shows both the peaks of the phases of the coating and the ones of the substrate: according to penetration depth of XR it is possible to suppose a thickness of the coating of some microns.

Due to the good results of the preliminary analysis, further considerations and analyses were carried out on this kind of samples. Several temperatures and times of treatment were investigated as well as substrates with different starting surfaces (without any pre/post treatment, with pre-treatment of deoxidation and oxidation) and the effect of a post thermal treatment. The obtained coatings were characterized by means of XRD analysis, optical microscope and FESEM observation, micro and nanoindentations, scratch and wear test, zeta potential analysis before and after proteins adsorption and in vitro bioactivity test.

### 5.3.1 XRD analysis

XRD analysis was used to evaluate the crystallographic structure of the coating when the parameters of treatment vary.

First of all, the effect of the post thermal treatment on the samples treated at 1050°C for 4.5 h was investigated.

The XRD patterns are reported in Figures 5.5 and 5.6.

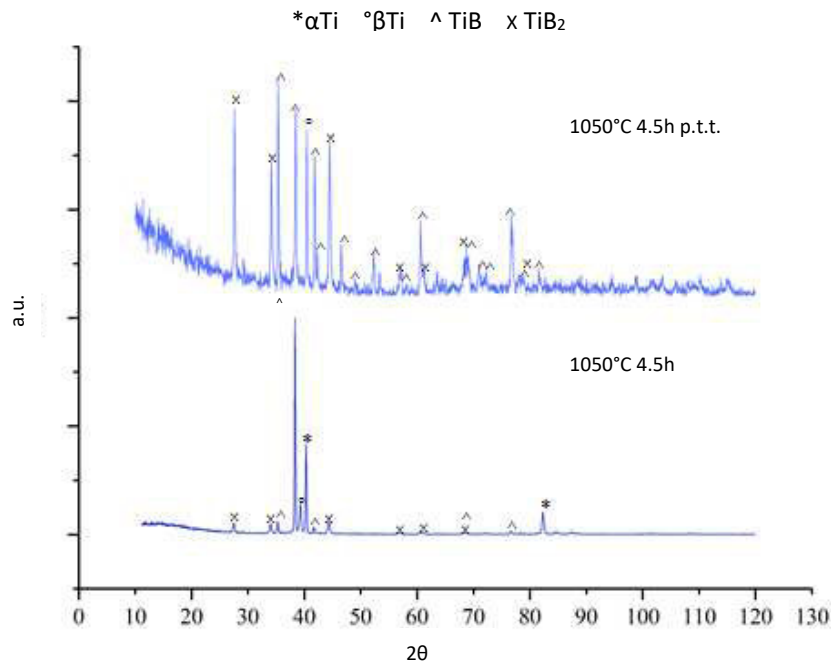


**Figure 5.5 XRD patterns collected with Bragg-Brentano geometry of samples treated at 1050°C for 4.5 h without any pre/post treatment and subjected to the post thermal treatment**

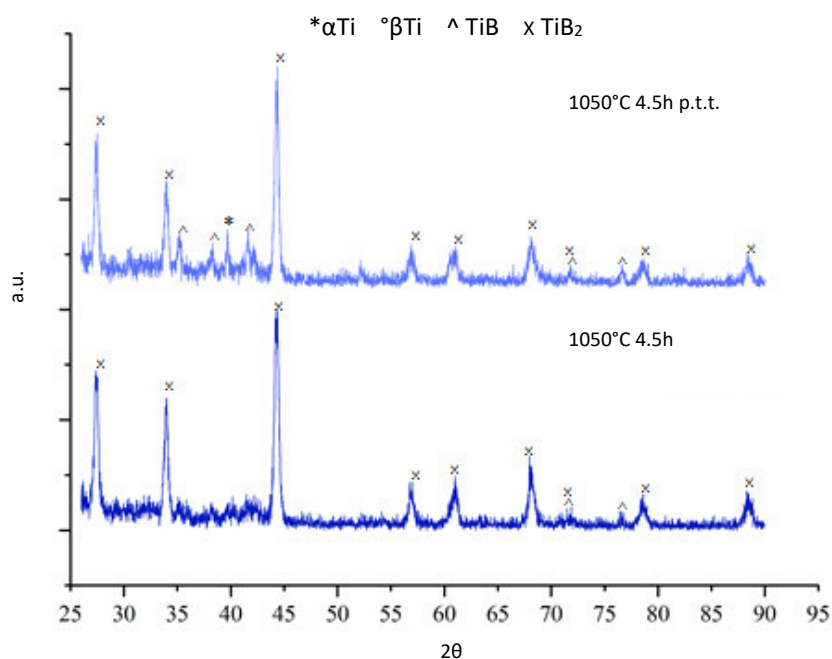


**Figure 5.6 XRD patterns collected with  $1^\circ$  grazing angle measurement of samples treated at  $1050^\circ\text{C}$  for 4.5 h without any pre/post treatment and subjected to the post thermal treatment**

Both XRD patterns obtained with Bragg-Brentano geometry show well evident TiB and  $\text{TiB}_2$  peaks (Figure 5.5). The intensity of the TiB and  $\text{TiB}_2$  peaks of the sample with the post thermal treatment is comparable to the one of the peaks of the substrate and higher than the one of the peaks of the sample without the post thermal treatment. This suggests a greater thickness of the coating of the sample with the post thermal treatment. Moreover, the comparison between the samples with and without the post thermal treatment highlights that, during the post thermal treatment, part of the  $\text{TiB}_2$  reacted to form TiB, the more stable borided phase. This is confirmed by the grazing angle patterns (Figure 5.6). The pattern of the treated sample without the post thermal treatment shows that the upper layer of the coating is composed only of  $\text{TiB}_2$  phase and the TiB phase of the inner part is not detected. While the pattern of the treated sample with the post thermal treatment has peaks both of the  $\text{TiB}_2$  and TiB phases. This suggests a mix composition of the upper layer of the coating and/or a lower thickness of the  $\text{TiB}_2$  upper layer.

Then, it was evaluated the effect of temperature, maintaining the same time of treatment. Figures 5.7 and 5.8 show the XRD patterns of the samples treated at different temperatures for 4.5 h.

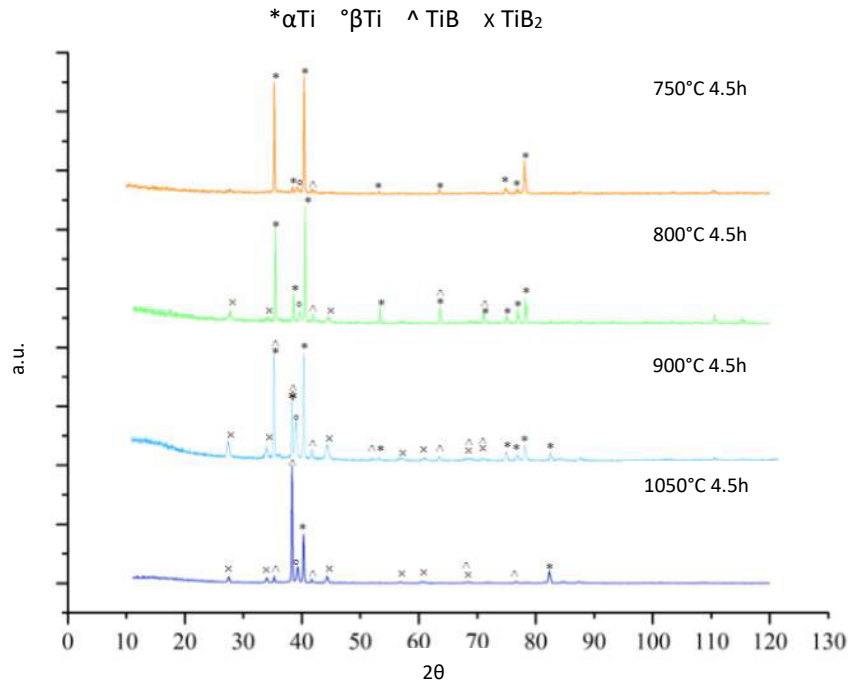


**Figure 5.7** XRD patterns collected with Bragg-Brentano geometry of the samples treated at different temperatures for 4.5 h

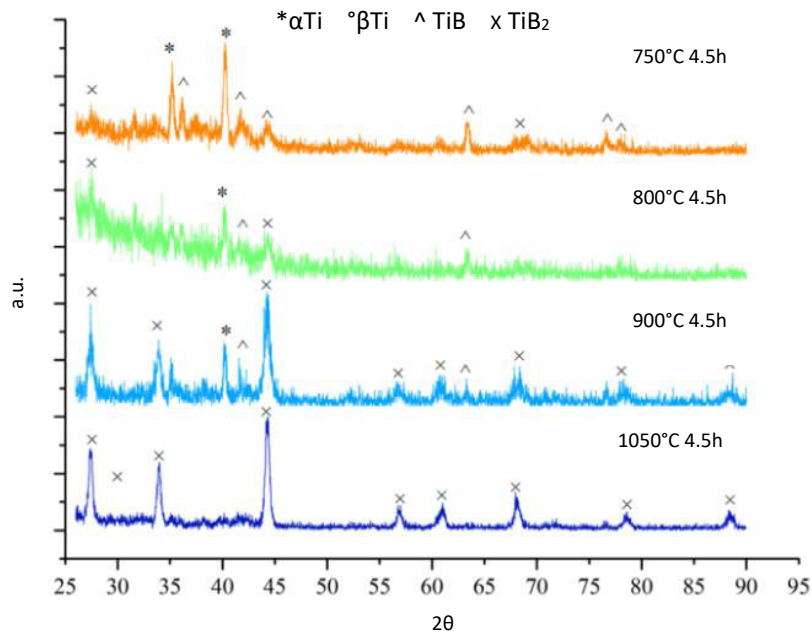


**Figure 5.8** XRD patterns collected with 1° grazing angle measurement of the samples treated at different temperatures for 4.5 h

Focusing on Bragg-Brentano patterns (Figure 5.7), the intensity of  $\text{TiB}_2$  and  $\text{TiB}$  peaks decreases with decreasing the temperature of treatment while the intensity of  $\text{Ti}$  peaks increases. At  $1050^\circ\text{C}$   $\text{TiB}_2$  and  $\text{TiB}$  phases are mainly detected while at  $750^\circ\text{C}$  only the substrate is detected. This suggests a difference of coating thickness that becomes much more thin as the temperature of treatment decreases.

Differences are also underlined by grazing angle measurements (Figure 5.8). At  $1050^\circ\text{C}$ , the surface layer is composed of  $\text{TiB}_2$  phase, as described before, while

decreasing the temperature of treatment, the TiB phase starts to be revived. At lower temperature, the mainly phase developed is TiB phase, that is the most stable one.

This trend agrees with literature data, in which it is reported that the highest boron diffusion happens around the  $\beta$  transus temperature, that is about 910°C for the material used in this research [2].

To evaluate the effect of the natural oxide layer on boron diffusion, the boronizing process was carried out both on samples without any pre/post treatment and with pre-treatment of deoxidation. The XRD patterns are compared in Figures 5.9 and 5.10.

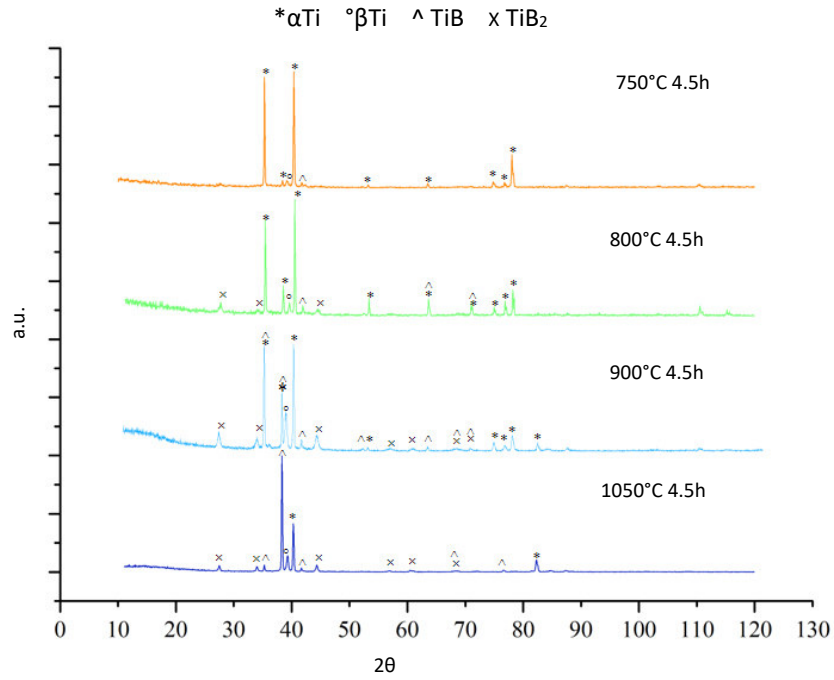


**Figure 5.9 XRD patterns collected with Bragg-Brentano geometry of the treated samples without any pre/post treatment**



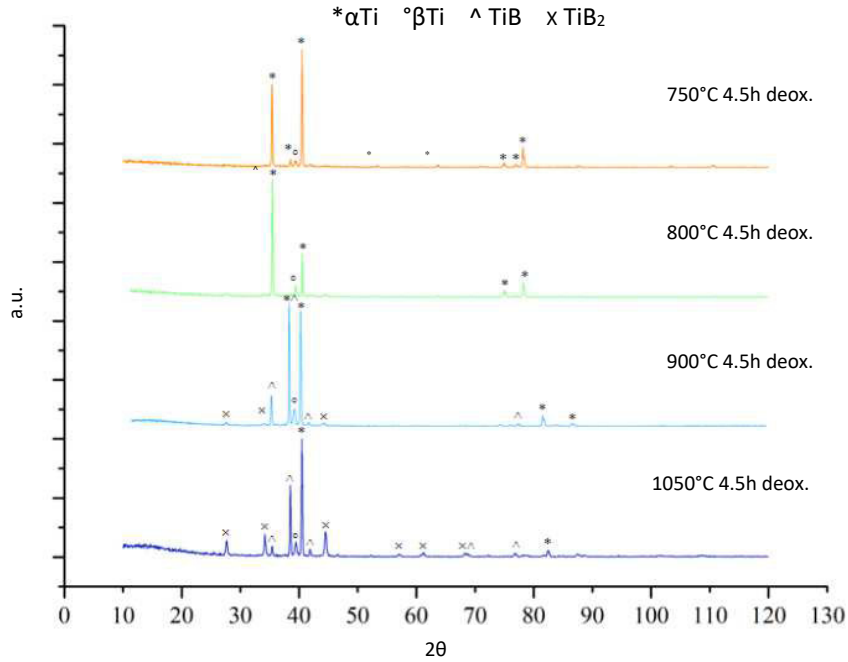


**Figure 5.10 XRD patterns collected with Bragg-Brentano geometry of the treated samples with pre-treatment of deoxidation**

It is possible to see that there are not substantial differences between the samples without any pre/post treatment and the ones with a pre-treatment of deoxidation. In both cases, decreasing the temperature of treatment, the intensity of the peaks of TiB and TiB<sub>2</sub> phases decreases and the number of peaks related to the substrate increases.

To conserve the microstructure of the substrates, as it will be discussed in the following paragraph, more attention is focused on the lowest temperatures of treatment. It was evaluated the effect of the time of treatment when the temperatures of treatment are 800°C and 750°C. Figures 5.11 and 5.12 show the XRD patterns of the samples treated at 800°C for 4.5 h and 3.5h, while Figures 5.13 and 5.14 report the XRD patterns of the samples treated at 750°C for 4.5 h, 3.5 h and 2.5 h. The samples without any pre/post treatment and with a pre-treatment of deoxidation were compared.

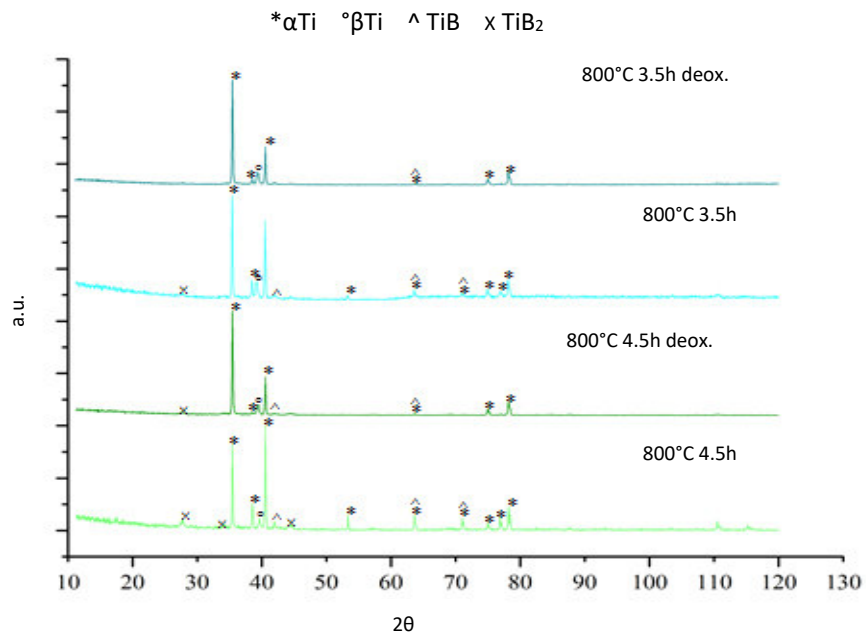


**Figure 5.11** XRD patterns collected with Bragg-Brentano geometry of the samples treated at 800°C for 4.5 h and 3.5 h

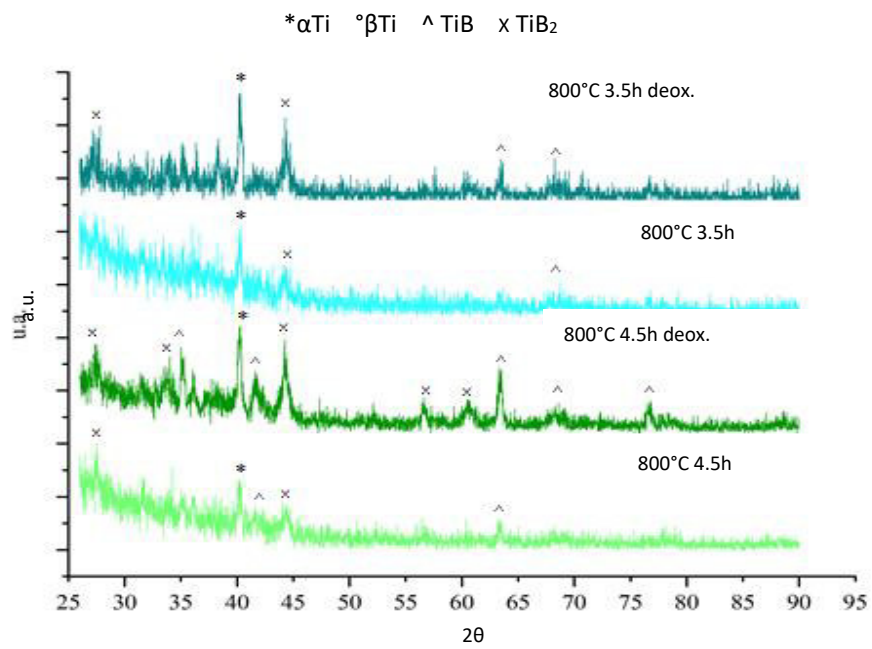


**Figure 5.12** XRD patterns collected with 1° grazing angle measurement of the samples treated at 800°C for 4.5 h and 3.5 h

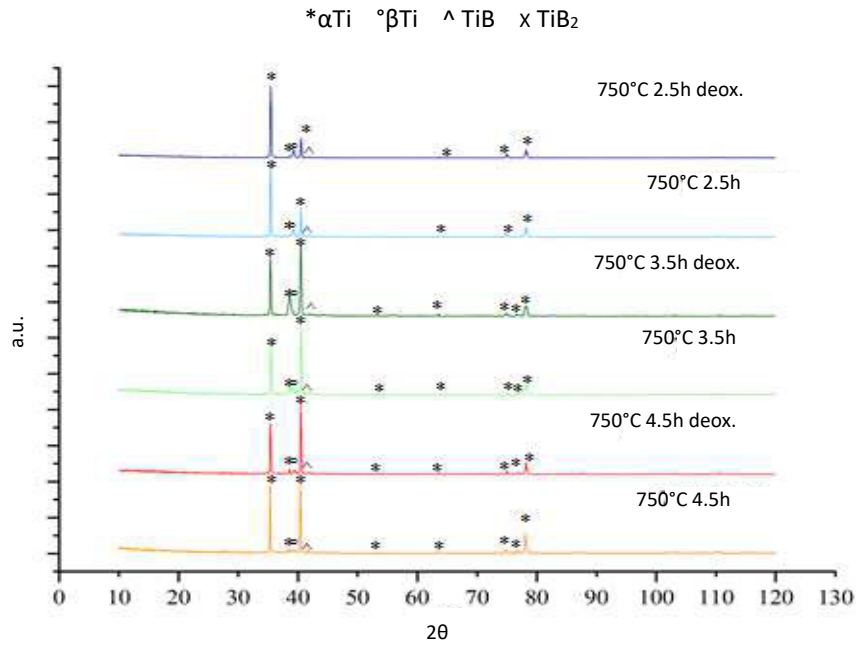


Figure 5.13 XRD patterns collected with Bragg-Brentano geometry of the samples treated at 750°C for 4.5 h, 3.5 h and 2.5 h

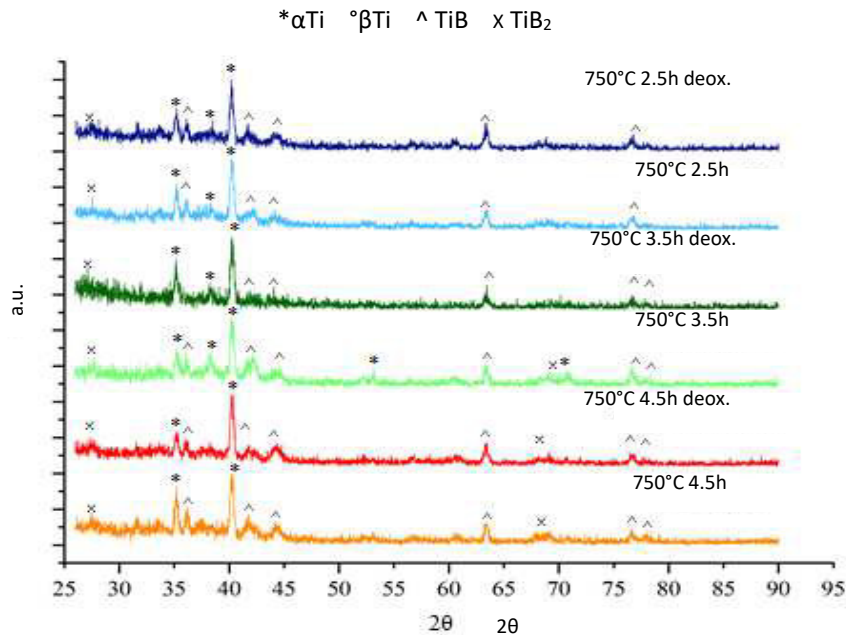
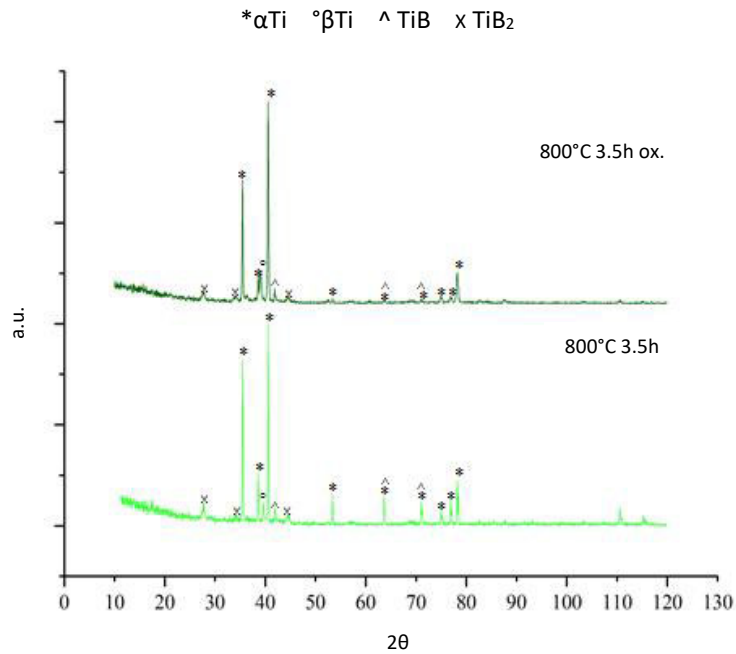


Figure 5.14 XRD patterns collected with 1° grazing angle measurement of the samples treated at 750°C for 4.5 h, 3.5 h and 2.5 h

At low temperature the variation of the time of treatment does not cause any significant variation in the XRD patterns both in Bragg-Brentano geometry and in grazing angle analysis. The temperature has no visible effect both on the samples without any pre/post treatment and on the ones with a pre-treatment of deoxidation. Bragg-Brentano analyses (Figures 5.11 and 5.13) detect mainly the phases related to the substrates, while 1° grazing angle analyses (Figures 5.12 and 5.14) show the peaks of TiB and TiB<sub>2</sub> phases.



**Figure 5.15** Bragg-Brentano spectra of the samples treated at 800°C for 3.5 h without any pre/post treatment or pre-treatment of oxidation

As last consideration, it was evaluated the effect of an increment of the thickness of the oxide layer on boron diffusion. The XRD patterns are shown in Figure 5.15.

The two XRD patterns look like similar, thus the oxidation process does not seem to have any effects on the chemical composition as well as the deoxidation process.

### 5.3.2 Substrate microstructure

Changes in microstructure due to the thermal treatment is a very important issue concerning Ti6Al4V alloys. The mechanical properties of Ti6Al4V alloys strictly depend on microstructure. The data reported in literature about similar boronizing process on c.p. Ti [2] do not concern microstructure of the substrate, one of the main point, instead, taken into account in this research.

Figure 5.16 shows the microstructure of an untreated sample, while the one of the treated substrates at different temperatures for 4.5 h without any pre/post treatment are shown and compared in Figure 5.17. The corresponding samples with a pre-treatment of deoxidation have the same microstructure so the images are not reported.

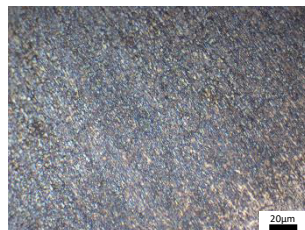


**Figure 5.16** Optical microscope image of the cross section of the untreated sample

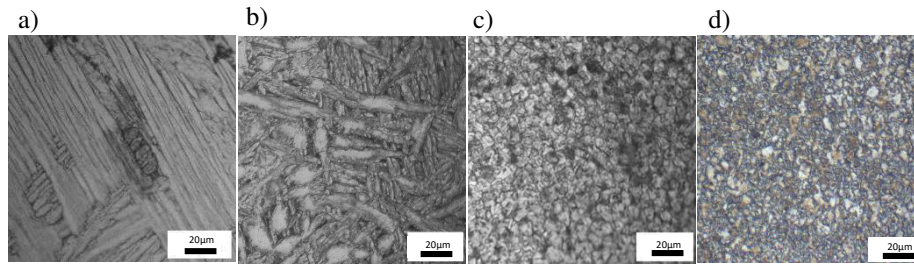


**Figure 5.17** Optical microscope images of the cross section of the samples without any pre/post treatment treated at a) 1050°C b) 900°C c) 800°C and d) 750°C

As expected, there is a change in microstructure for the samples treated above or next to the  $\beta$  transus temperature [3]. The untreated sample has a microstructure composed of small rounded grains, while the samples treated at 1050°C show a Widmanstätten microstructure, the ones treated at 900°C show acicular grains and the samples treated at 800°C and 750°C have rounded grains similar to the untreated sample; in these last two cases, it is possible to observe only a growth of grains size.

Growth of the grains seems to depend more by the temperature and less by the time of treatment referring to the range of considered temperatures and times.

Figures 5.18 and 5.19 show the microstructure of the samples without any pre/post treatment treated at 800°C and 750°C respectively for different times of treatment. As previously, the corresponding samples with a pre-treatment of deoxidation have the same microstructure so the images are not reported.

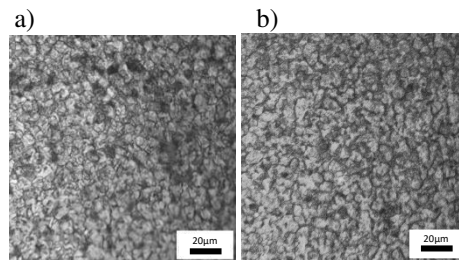


**Figure 5.18** Optical microscope images of the cross section of the samples without any pre/post treatment treated at 800°C for a) 4.5 h and b) 3.5 h

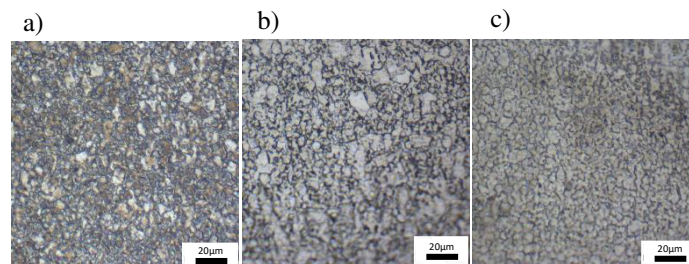


**Figure 5.19** Optical microscope images of the cross section of the samples without any pre/post treatment treated at 750°C for a) 4.5 h, b) 3.5 h and c) 2.5 h

The samples treated at 800°C have grains a little bit bigger in dimensions than the samples treated at 750°C, but there are not relevant differences by changing the time of treatment between 4.5 h and 3.5 h or among 4.5 h, 3.5h and 2.5 h, for temperature of treatment respectively of 800°C and 750°C.

### 5.3.3 Coating morphology and thickness

Figure 5.20 shows the cross-sectional micrographs of the samples treated at different temperatures for 4.5h.

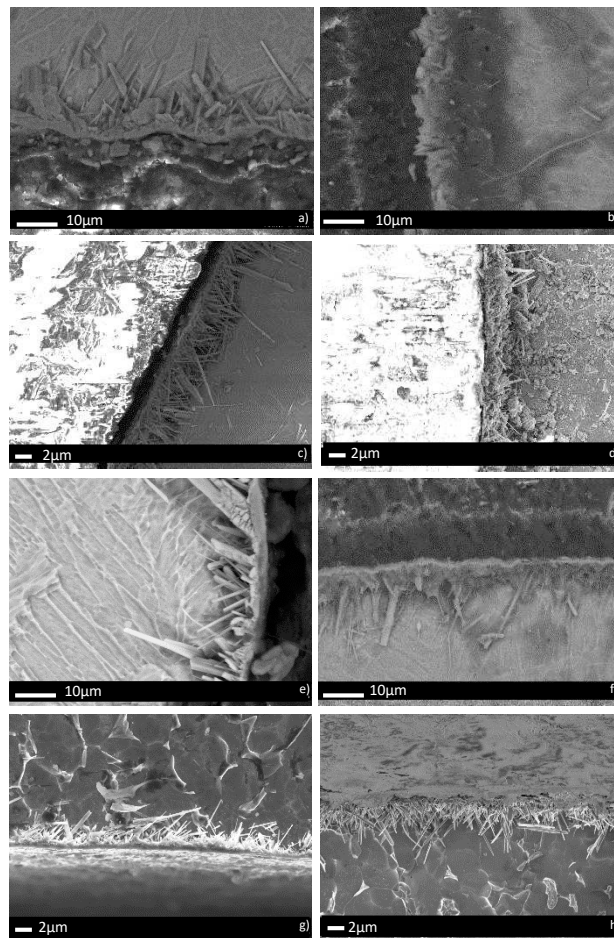


**Figure 5.20** Cross-sectional FESEM micrographs of the samples without any pre/post treatment treated at a) 1050°C, b) 900°C, c) 800°C, d) 750°C and of the samples with pre-treatment of deoxidation treated at e) 1050°C f) 900°C, g) 800°C and h) 750°C

The boride layer consists of an upper monolithic layer and whiskers entering the substrate. The morphology of the coatings is the same for all samples, regardless of the temperature and time of the treatment.

The temperature of treatment has effects on the penetration depth of the whiskers and on the thickness of the compact upper borided layer. As it is possible to see in Figure 5.21 the thickness of the coatings and the penetration depth of the whiskers decrease, decreasing the temperature of treatment.

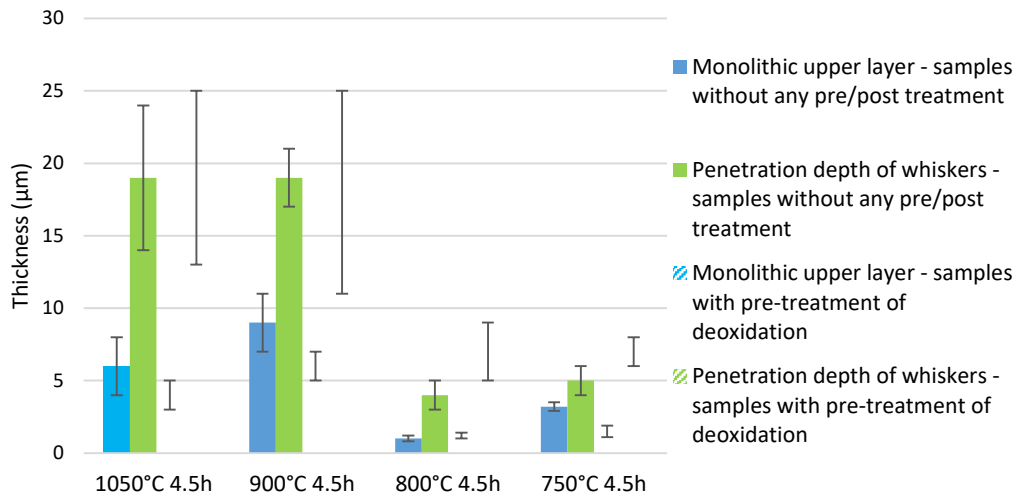


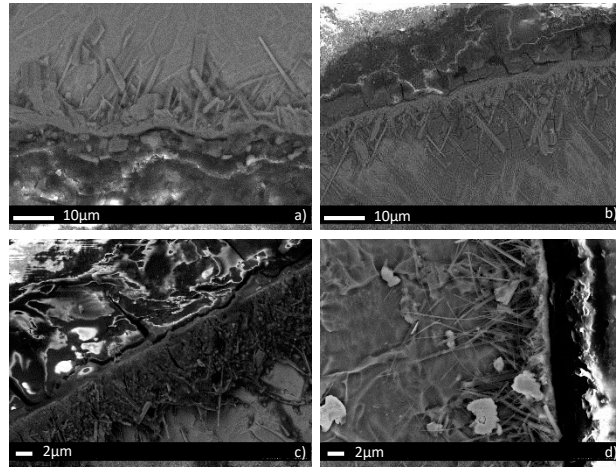
**Figure 5.21 Thickness of the samples treated at different temperature for 4.5 without any pre/post treatment and with pre-treatment of deoxidation**

Considering as first the treated samples without any pre/post treatment, the average thickness of the upper layer and the penetration depth of the whiskers are respectively in the range of 1-3  $\mu\text{m}$  and 4-5  $\mu\text{m}$  for the samples treated at the temperatures below the  $\beta$  transus temperature (800-750°C). In the case of the samples treated at temperatures above or close the  $\beta$  transus temperature (1050-900°C) the average thickness of the upper layer results to be in the range of 6-9  $\mu\text{m}$ , while the average of the penetration depth of the whiskers is 19  $\mu\text{m}$ . Even if a wider standard deviations of the thickness of the coating must be underlined in these samples. Nevertheless, decreasing the temperature of treatment there is a decrease of the thickness of the upper monolithic layer and the penetration depth of the whiskers.

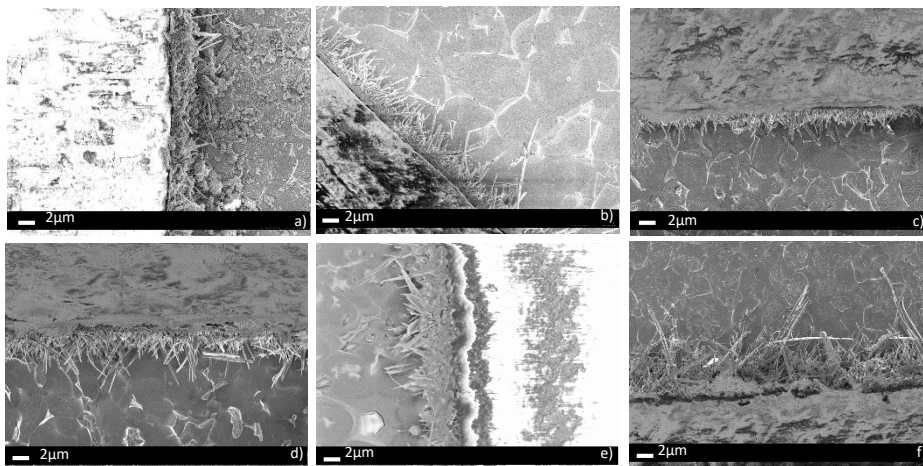
A similar treatment on pure commercial titanium was explored by K.S. Ravi Chandran et al. [1,2]. A coating of overall thickness (monolithic layer + whiskers) in the range of 42-60  $\mu\text{m}$  as maximum was obtained on the samples treated at 850-1000°C for 1-4 h. These values are higher even if not far from what obtained here in the case of the Ti6Al4V alloy. K.S. Ravi Chandran et al. [2] underline that, in the case of pure Ti, the highest coating thickness can be achieved at the highest possible temperature close to the  $\beta$  transus temperature, while no evident advantage comes from a further increase of the temperature of the treatment. Actually, this is in agreement with what it was observed in the case of the  $\alpha$ - $\beta$  alloy.

Figure 5.21 also shows that the treated samples with a pre-treatment of deoxidation have the same trend concerning the temperature. Comparing the treated samples without any pre/post treatment and the ones with a pre-treatment of deoxidation it is possible to evaluate the effect of the deoxidation process on boron diffusion. Figure 5.21 highlights that the deoxidation process results to be effective mainly in increasing the penetration depth of the whiskers when the temperature of treatment is below the  $\beta$  transus temperature. Instead, when the temperature of treatment is close or above the  $\beta$  transus temperature the deoxidation process has not significant effect on the penetration depth of the whiskers, while the thickness of the upper monolithic layer slightly decreases.

Further analyses were carried out to evaluate the effect of the time of treatment on boron diffusion at low temperature (800-750°C). Figures 5.22 and 5.23 report the micrographs of cross-sections of the samples treated respectively at 800°C and 750°C, varying the time of treatment.



**Figure 5.22** Cross-sections FESEM micrographs of a) the sample treated at 800°C for 4.5 h without any pre/post treatment, b) the sample treated at 800°C for 3.5 h without any pre/post treatment, c) the sample treated at 800°C for 4.5 h with pre-treatment of deoxidation and d) the sample treated at 800°C for 3.5 h with pre-treatment of deoxidation



**Figure 5.23** Cross-section FESEM micrographs of a) the sample treated at 750°C for 4.5 h without any pre/post treatment, b) the sample treated at 750°C for 3.5 h without any pre/post treatment, c) the sample treated at 750°C for 2.5 h without any pre/post treatment, d) the sample treated at 750°C for 4.5 h with pre-treatment of deoxidation, e) the sample treated at 750°C for 3.5 h with pre-treatment of deoxidation and f) the sample treated at 750°C for 2.5 h with pre-treatment of deoxidation

The morphology of the coatings is the same for all samples, the effect of the time variation and pre-treatment of deoxidation can be better understood looking at Figure 5.24.



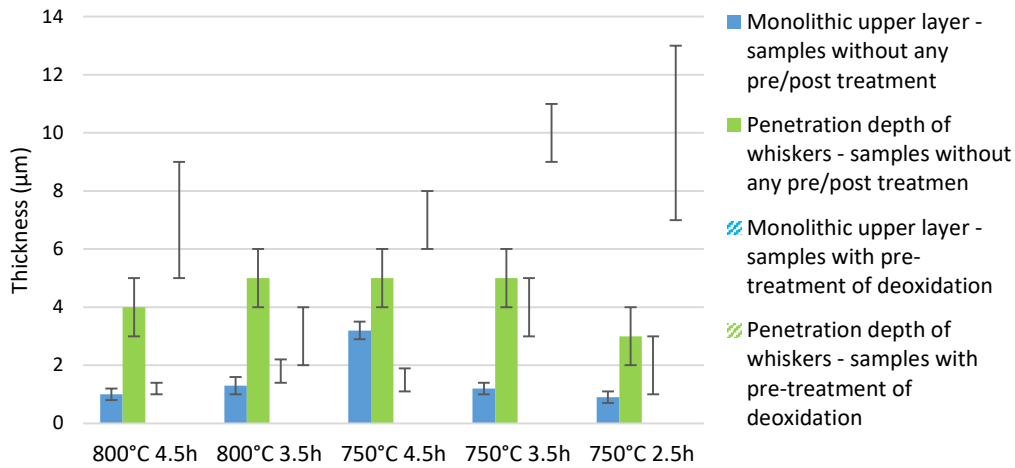


**Figure 5.24 Thickness of the samples treated at 800°C and 750°C for different time of treatment without any pre-post treatment and with pre-treatment of deoxidation**

Focusing on the samples without any pre/post treatment, it is possible to see that, taking into account the standard deviations, there are not a lot of differences between the samples treated at 800°C for 4.5 h and 3.5 h. The average thickness of the monolithic upper layer is  $1.0 \pm 0.2 \mu\text{m}$  and  $1.3 \pm 0.3 \mu\text{m}$  respectively for the samples treated for 4.5 h and 3.5 h. The corresponding average values of the penetration depth of whiskers are  $4 \pm 1 \mu\text{m}$  and  $5 \pm 1 \mu\text{m}$ .

Regarding, the samples treated at 750°C, reducing the time of treatment the thickness of the monolithic upper layer decreases as well as the penetration depth of whiskers. The average values of the monolithic upper layer are  $3.2 \pm 0.3 \mu\text{m}$  (4.5 h),  $1.2 \pm 0.2 \mu\text{m}$  (3.5 h) and  $0.9 \pm 0.2 \mu\text{m}$  (2.5 h), while the ones of the penetration depth of the whiskers are  $5 \pm 1 \mu\text{m}$  (4.5 h),  $5 \pm 1 \mu\text{m}$  (3.5 h) and  $3 \pm 1 \mu\text{m}$  (2.5 h). The thickness of the monolithic upper layer of the samples treated at 750°C for 4.5 h is little bit higher than the one of others samples treated at low temperature.

The deoxidation surface process seems to slight increase the thickness of the coating obtained at low temperatures, in particular it allows to increase the penetration depth of the whiskers. For the samples treated at 750°C the effect is evident also on the thickness of the monolithic upper layer. The average values are reported in Table 5.2.

Looking at Figure 5.24, the samples treated at 800°C for 3.5 h and at 750°C for 4.5 h result to be particular cases, regarding the samples treated at 750°C the thickness of the monolithic upper layer of the sample without any pre/post treatment is higher than the one of the sample with a pre-treatment of deoxidation. Similarly, focusing on the samples treated at 800°C the penetration depth of the whiskers of the sample without any pre/post treatment is higher than the one of the sample with a pre-treatment of deoxidation. This is an anomaly maybe linked to the preparation process of the samples for the metallographic evaluation, during which there were some complications.

**Table 5.2 Average values of coatings thickness of the samples treated at 800°C and 750°C with pre-treatment of deoxidation**

Sample with a pre-treatment of deoxidation	800°C 4.5 h	800°C 3.5 h	750°C 4.5 h	750°C 3.5 h	750°C 2.5 h
Monolithic upper layer (μm)	1.2±0.2	1.8±0.4	1.5±0.4	4.0±1.0	2.0±1.0
Penetration depth of the whiskers (μm)	7±2	3±1	7±1	10±1	10 ±3

Figures 5.25 and 5.26 show the effect of the post thermal treatment on the diffusion of boron.

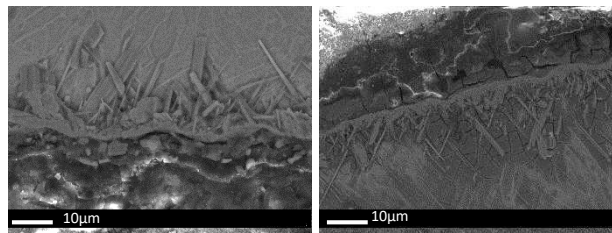


**Figure 5.25 Cross-section FESEM micrographs of a) the sample treated at 1050°C for 4.5 h without any pre/post treatment and b) the sample treated at 1050°C for 4.5 h and subjected to the post thermal treatment at 1050°C for 4.5 h**

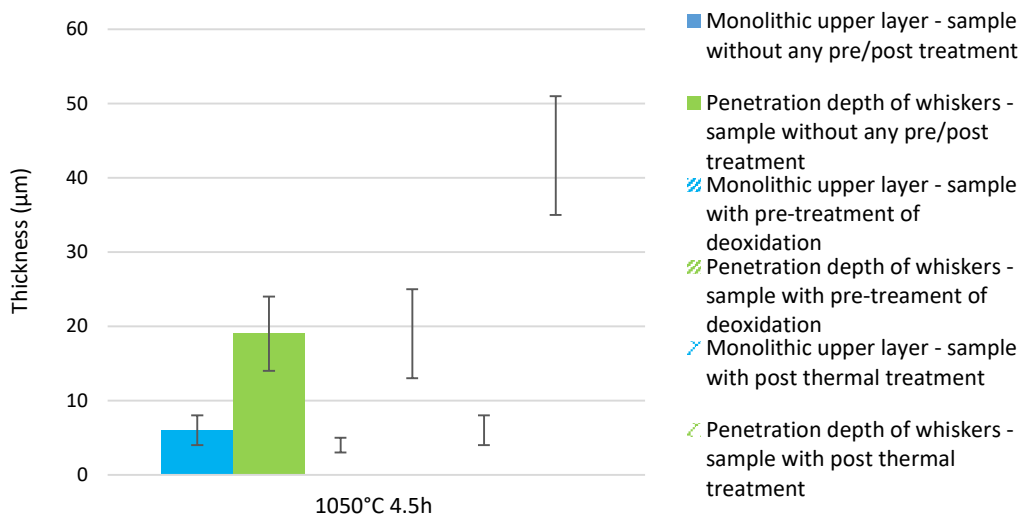


**Figure 5.26 Thickness of samples treated at 1050°C for 4.5 h without any pre/post treatment, with pre-treatment of deoxidation and subjected to the post thermal treatment**

Differently from the deoxidation surface process, that does not lead to any considerable variation in the coating thickness, the post thermal treatment causes a considerable increment of the penetration depth of the whiskers. The average value is  $43 \pm 8 \mu\text{m}$  in comparison to the  $19 \pm 6 \mu\text{m}$  of the samples not subjected to the post thermal treatment.

Last consideration is about the effect of the oxidation surface process on the diffusion of boron. The cross-section and the average thickness of the sample treated at 800°C for 3.5 h with a pre-treatment of oxidation are shown in Figures 5.27 and 5.28.

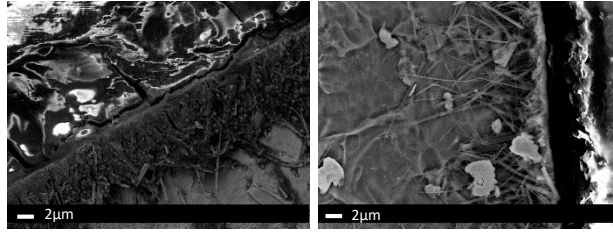


**Figure 5.27** Cross-section FESEM micrographs of the samples treated at 800°C for 3.5 h a) without any pre/post treatment and b) with pre-treatment of deoxidation

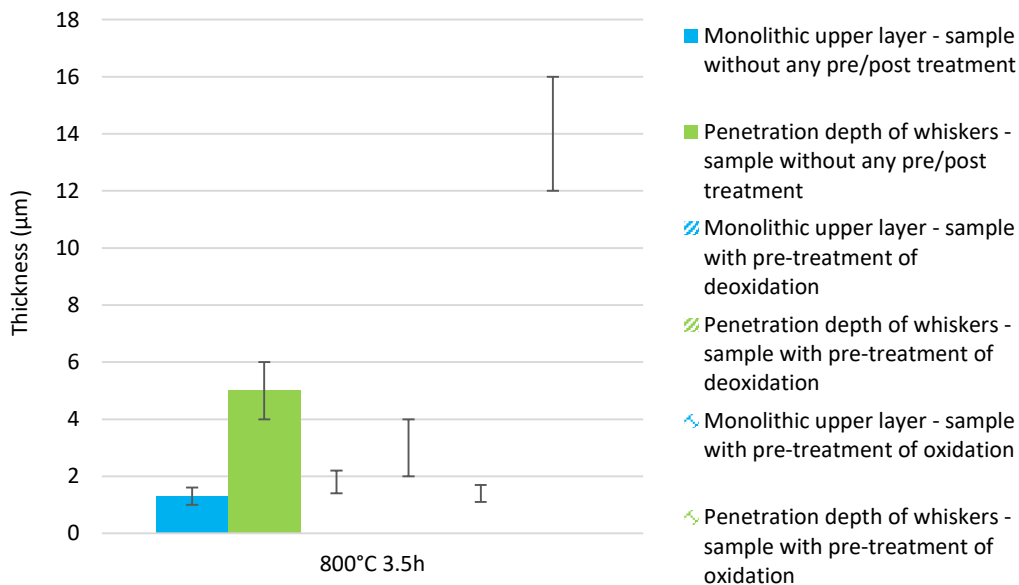


**Figure 5.28** Thickness of samples treated at 800°C for 3.5 h without any pre/post treatment, with pre-treatment of deoxidation and with pre-treatment of oxidation

The penetration depth of the whiskers increases when the thermal treatment is carried out on the samples with a pre-treatment of oxidation in comparison to when the thermal treatment is performed on the samples without any pre/post treatment and with pre-treatment of deoxidation. The penetration depth of the whiskers reaches an average value of  $14 \pm 2 \mu\text{m}$ , in contrast to  $5 \pm 1 \mu\text{m}$  and  $3 \pm 1 \mu\text{m}$  respectively of the samples without any pre/post treatment and with a pre-treatment of deoxidation.

### 5.3.4 Coating hardness

First of all, hardness was evaluated by means of Vickers measurements on the samples without any pre/post treatment. Figure 5.29 shows the hardness values of the samples without any pre/post treatment treated at different temperatures for 4.5 h.

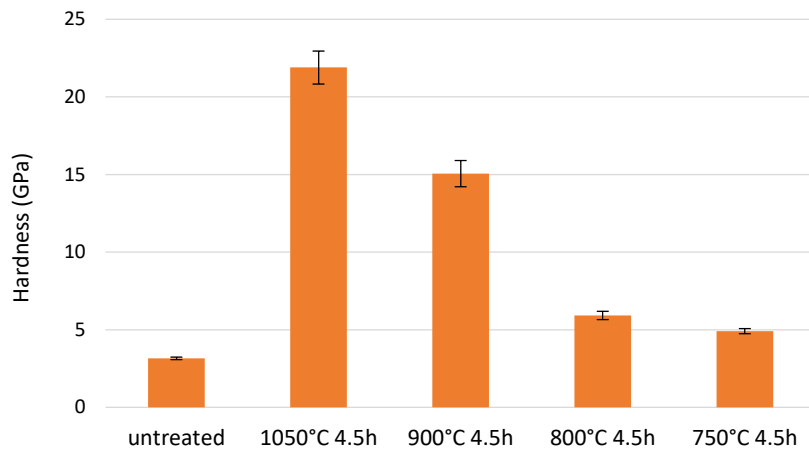


**Figure 5.29 Vickers microindentations: hardness of the samples without any pre/post treatment treated at different temperatures for 4.5 h**

The untreated material results to have a hardness value of about  $3.2 \pm 0.1$  GPa, value closed to the one reported in literature (3.4 GPa) [4]. After the boronizing treatment, hardness increases, in particular there is a considerable increment when the temperature of the treatment is above the  $\beta$  transus temperature. The samples treated at  $1050^\circ\text{C}$  and  $900^\circ\text{C}$  respectively show a hardness of  $21.9 \pm 1.1$  and  $15.1 \pm 0.9$  GPa. For treatments below the  $\beta$  transus temperature, instead, the hardness values slightly increase with respect to the untreated surface. The hardness value is  $5.9 \pm 0.3$  GPa for the samples treated at  $800^\circ\text{C}$  and  $4.9 \pm 0.2$  GPa for the samples treated at  $750^\circ\text{C}$ .

While hardness mainly decreases with the temperature of treatment, the variation of treatment duration has less effects, as it is possible to see in Figure 5.30.

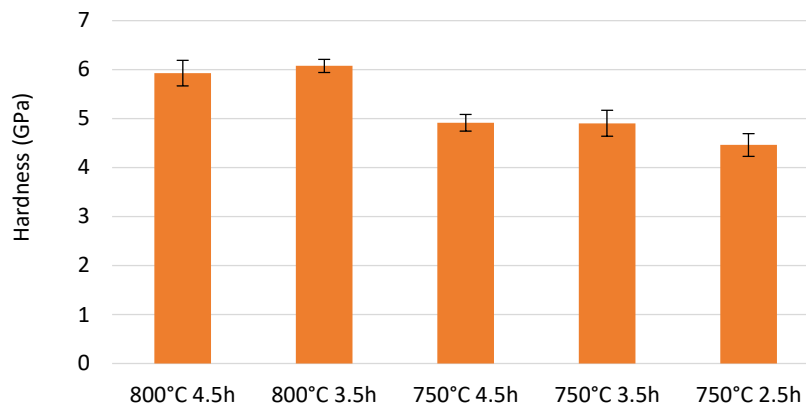


**Figure 5.30 Vickers microindentations: hardness of the samples without any pre/post treatment treated for different times**

Hardness decreases a bit with time, but there are not considerable differences among the treatment times explored till the duration of treatment is reduced at 2.5 h.

As reported by the standard UNI EN ISO 6507, the average thickness of the coating has to be 1.5 times the average dimension of the footprint diagonal to have reliable hardness values. The comparison between the average thickness of the coatings and theoretical values is reported in Figure 5.31.

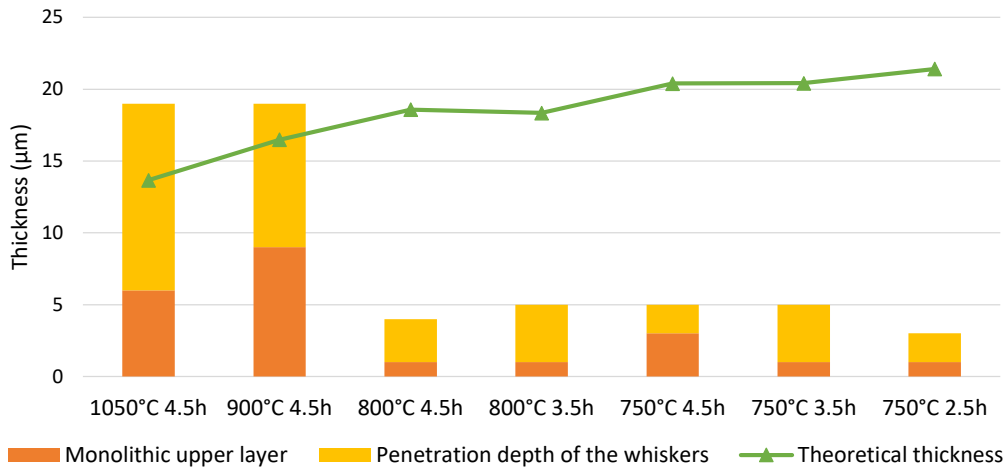


**Figure 5.31 Comparison between the coating thickness and theoretical values**

Observing the data reported in Figure 5.31, we can conclude that some measurements are affected by hardness of the substrate, in particular, in the case of the samples treated at temperatures below the  $\beta$  transus temperature, because the theoretical thickness is much higher than the real thickness, included the penetration depth of the whiskers. Also the measurements, carried out on the samples treated at temperatures higher than the  $\beta$  transus temperature, are partially affected by the substrate because of the theoretical thickness is in the range of the penetration depth of the whiskers, where the harder phase is not continuous and the coating is not compact, but it has a needle-like shape.

Knoop measurements were carried out in a second step. Also in the case of Knoop measurements to verified the values collected, the average thickness of the coatings was compared to the theoretical values, calculated as reported by the standard UNI EN ISO 4516. The data are reported in Figure 5.32.

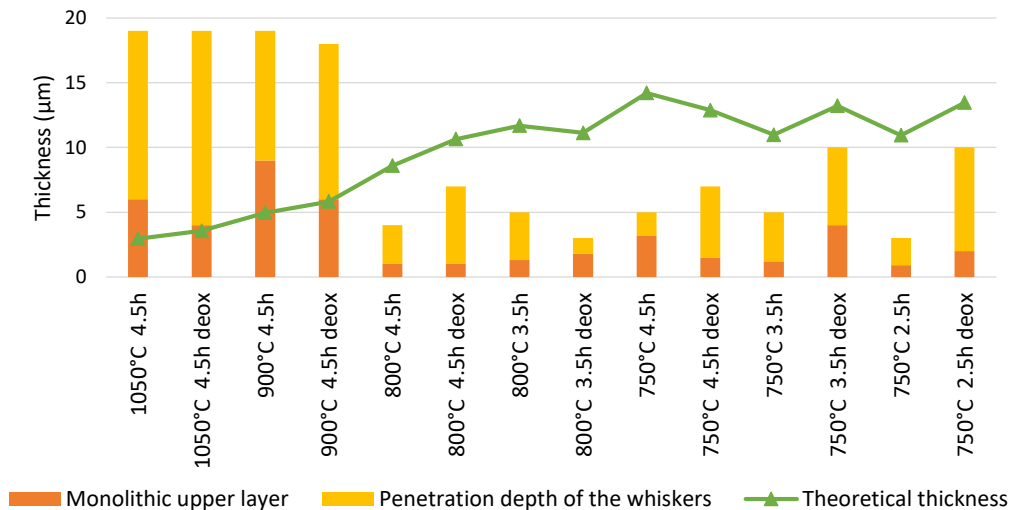


**Figure 5.32 Comparison between the coating thickness and theoretical values**

In this case the thickness values of the coating are in the range of the theoretical values for samples treated at temperatures above of the  $\beta$  transus temperature, while hardness of samples treated at temperatures below the  $\beta$  transus temperature is

affected by the substrate even if in a lower amount than in the case of Vickers measurements.

This test is more suitable for ceramic and brittle materials and for thin coating.

In this case, the measurements were carried out not only on the samples without any pre/post treatment but also on the other kinds of samples (samples with pre-oxidised/oxidised surface and samples subjected to post thermal treatment). As it is possible to see from Figure 5.33 and 5.34, the trend is the same of what collected with Vickers measurements.

Focusing on the samples treated at different temperatures for 4.5 h (Figure 5.33), also in this case, the hardness decreases with the temperature and there is an abrupt change in correspondence of the  $\beta$  transus temperature. The hardness is very higher when the temperature of treatment is above the  $\beta$  transus temperature, while when the temperature of treatment is below the  $\beta$  transus temperature the increment is lower. The samples without any pre/post treatment and with a pre-treatment of deoxidations show the same trend.

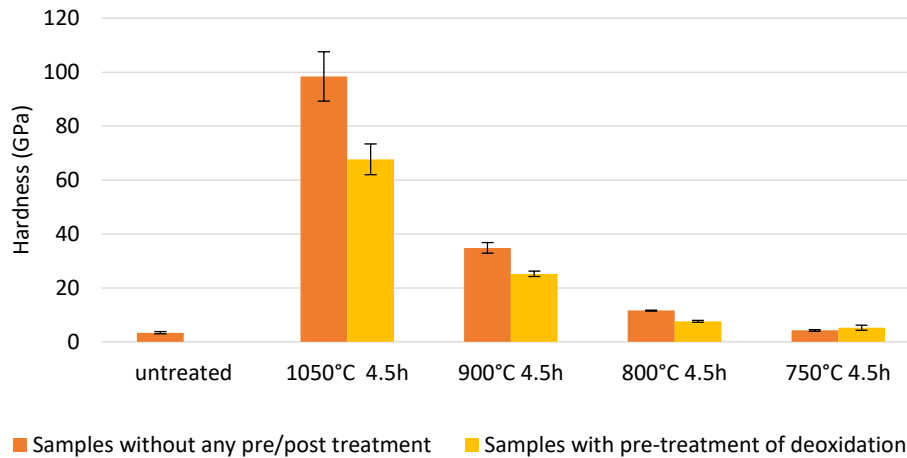


**Figure 5.33 Knoop microindentations: hardness of the samples without any pre/post treatment and with pre-treatment of deoxidation treated at different temperatures for 4.5**

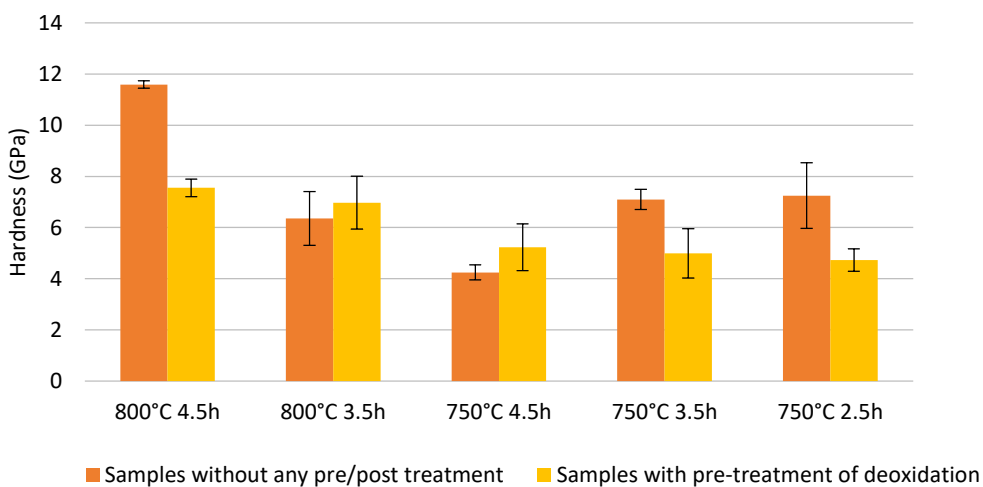


**Figure 5.34 Knoop microindentations: hardness of the samples without any pre/post treatment and with pre-treatment of deoxidation treated for different times**

As in the previous case, the variation of the duration of the treatment carried out at low temperature does not have significant effect on the hardness. Nevertheless, the behaviour of the samples without any pre/post treatment treated for 4.5 h at 800°C and 750°C must be emphasized, because they show respectively the highest and the lowest hardness among the samples treated at temperatures below the  $\beta$  transus temperature. Among the samples with a pre-treatment of deoxidation there are not significant differences, the hardness decreases with temperature but not with the time of treatment.

In general, the samples without any pre/post treatment have a hardness higher than the one with a pre-treatment of deoxidation, except in the case of the samples treated at 800°C for 3.5 h and 750°C for 4.5 h where the trend is reversed; but the hardness values, considering the standard deviations, are in the same range.

Comparing Knoop and Vickers values of hardness, it is possible to see that the hardness of the untreated sample is about  $3.4 \pm 0.4$  GPa similar to the one measured by means of Vickers microindentations ( $3.2 \pm 0.1$  GPa) and the one reported in literature (about 4 GPa) [4]. As expected, the Knoop hardness values of the treated samples are higher than Vickers ones, the values are reported in Table 5.3.

**Table 5.3 Knoop (HK) and Vickers Hardness (HV) of the treated samples**

	1050°C 4.5h	900°C 4.5h	800°C 4.5h	800°C 3.5h	750°C 4.5h	750°C 3.5h	750°C 2.5h
<b>HK (GPa)</b>							
<b>without any pre/post treatment</b>	98.4±9.2	34.8±2.0	11.6±0.1	6.4±1.0	4.2±0.3	7.1±0.4	7.2±1.3
<b>HK(GPa) pre-treatment of deoxidation</b>	67.7±5.7	25.2±1.0	7.6±0.3	7.0±1.0	5.2±0.9	5.0±1.0	4.7±0.4
<b>HV (GPa)</b>	21.9±1.1	15.1±0.9	5.9±0.3	6.1±0.1	4.9±0.2	4.9±0.3	4.5±0.2

As said before, Vickers values are strongly affected by the hardness of the substrate, thus these hardness values are lower than the real ones, while they are reliable in the case of Knoop measurements on the samples treated at temperature equal or higher than 900 °C. The Knoop measurements of the samples treated at temperature below the beta transus, even if still outside the standard requirements, are in any case much more close to the real values.

As concern the effect of the post thermal treatment on the coating hardness, observing Figure 5.35, it is possible to see that there is a reduction of the hardness.

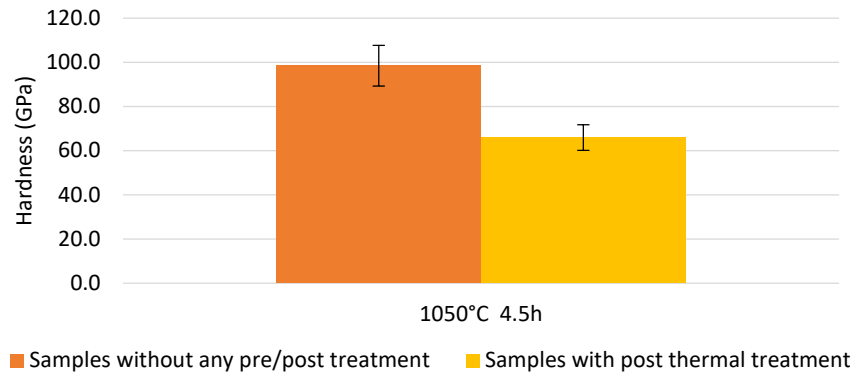


**Figure 5.35 Knoop microindentations: hardness of the sample without any pre/post treatment and the sample subjected to the post thermal treatment**

Hardness of the sample without the post thermal treatment is  $98.4 \pm 9.2$  GPa, as previously reported, while the one of the sample with the post thermal treatment is  $66.0 \pm 5.8$  GPa. The thickness of coating of the samples subjected to the post thermal treatment is in the range 6 – 43  $\mu\text{m}$  (monolithic upper layer – penetration depth of the whiskers), while the theoretical values calculated according to the standard is 4  $\mu\text{m}$ , thus the hardness value is reliable and not affected by the substrate, as well as for the others samples treated above the  $\beta$  transus temperature.

The lower hardness is due to the chemical composition and crystallographic structure of the coating. As shown by the XRD analysis, the samples with the post thermal treatment have a lower fraction of harder phase ( $\text{TiB}_2$ ) than the samples not subjected to the post thermal treatment.

Figure 5.36 shows, instead, the hardness value of the sample with a pre-treatment of oxidation.

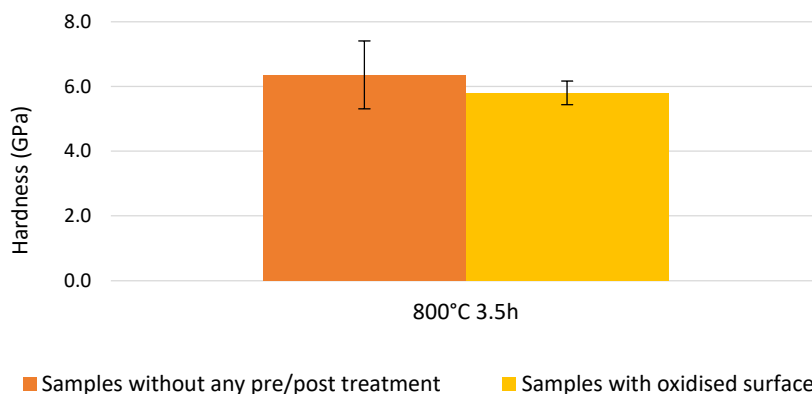


**Figure 5.36 Knoop microindentations: hardness of the samples without any pre/post treatment and with pre-treatment of deoxidation**

Hardness of the samples without any pre/post treatment and with a pre-treatment of oxidation is respectively  $6.4 \pm 1.0$  and  $5.8 \pm 0.4$  GPa. The oxidation surface process has not significant effect on the hardness. In this case, both values are affected by the substrate, as the comparison of the real coating thickness and the theoretical thickness reveals. The coating of the sample with a pre-treatment of



oxidation has a monolithic upper layer of about 1  $\mu\text{m}$  and a penetration depth of the whiskers of about 14  $\mu\text{m}$ , while the theoretical thickness is 12  $\mu\text{m}$ . It is possible to say that the increment of the penetration depth of the whiskers connected to the pre-treatment of oxidation does not have effect on hardness.

Nanoindentation measurements were carried out to evaluate hardness of the samples treated at temperature below the  $\beta$  transus temperature, avoiding the influence of the substrate. Due to the similarity in chemical composition and thickness of these samples the measurements were performed only on the samples treated at 800°C for 3.5 h without any pre/post treatment.

First of all, it was evaluated if it was better to proceed under displacement or load control. The trend of the test under displacement control is shown in Figure 5.37. It is possible to see that the load vs penetration depth curves are not well defined and there is an high data variability of hardness and elastic modulus as Figure 5.38 reports.

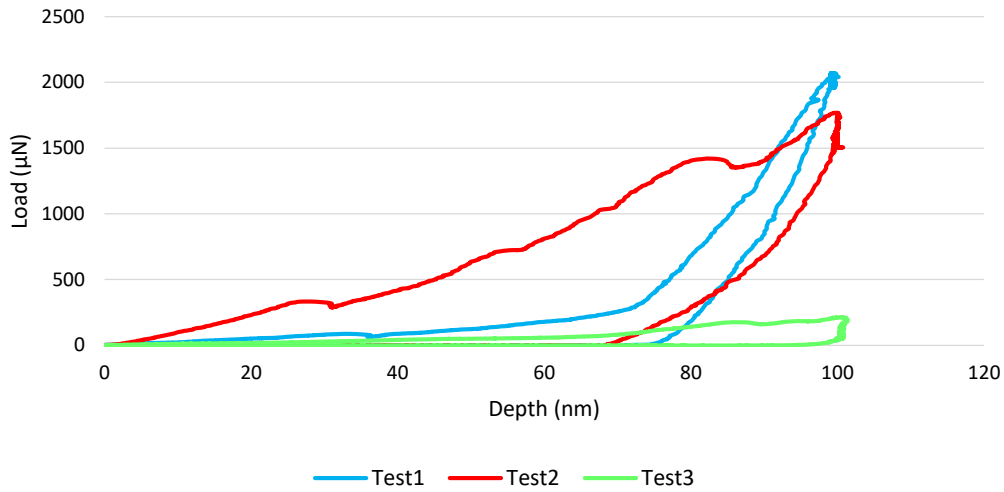
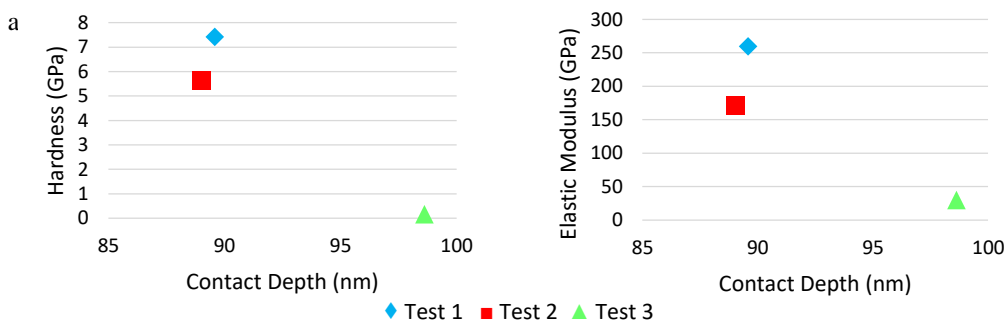
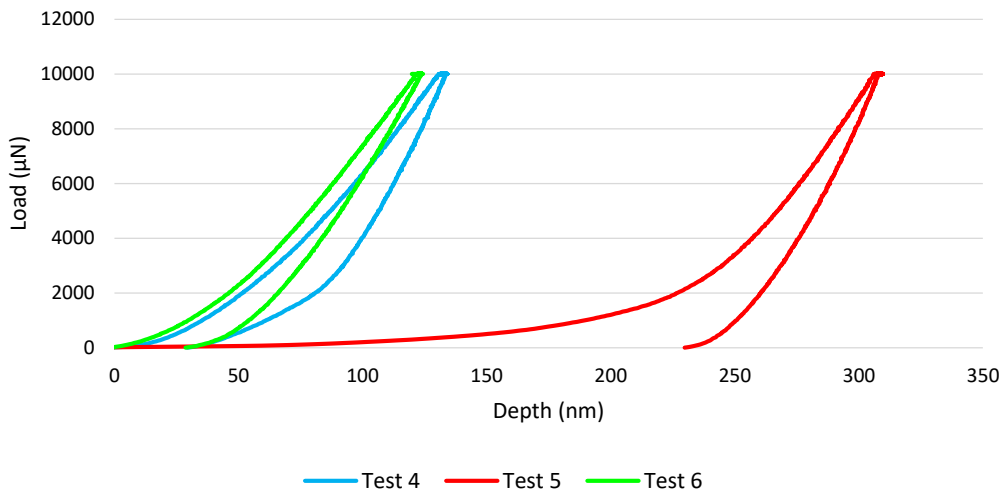


Figure 5.37 Displacement control: load vs penetration depth curves

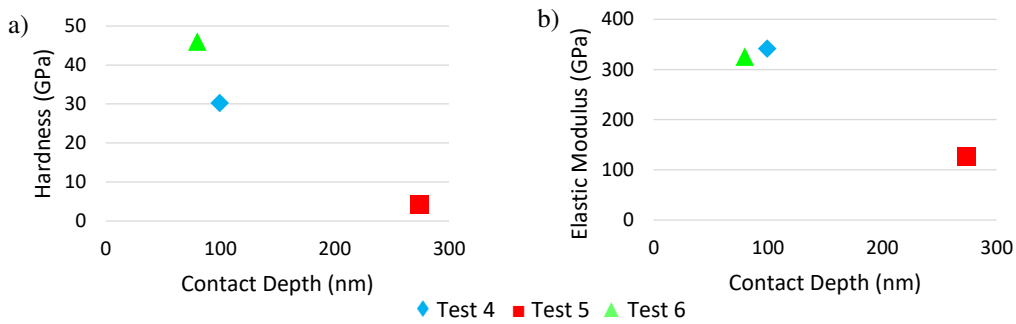


Figures 5.38 a) Hardness vs contact depth and b) elastic modulus vs contact depth

Figure 5.39 shows the trend of the tests performed under load control. The load vs penetration depth curves are well defined but hardness and elastic modulus data are still affected by high variability (Figures 5.40).



**Figure 5.39 Load control: load vs penetration depth curves**



**Figures 5.40 a) Hardness vs contact depth and b) elastic modulus vs contact depth**

Taking into account the results of the preliminary tests, a grid test under load control was carried out on two different zone of the sample, to analyse the data variability.

The hardness and elastic modulus data of the two areas are comparable as it is possible to see on Figures 5.41 and 5.42.

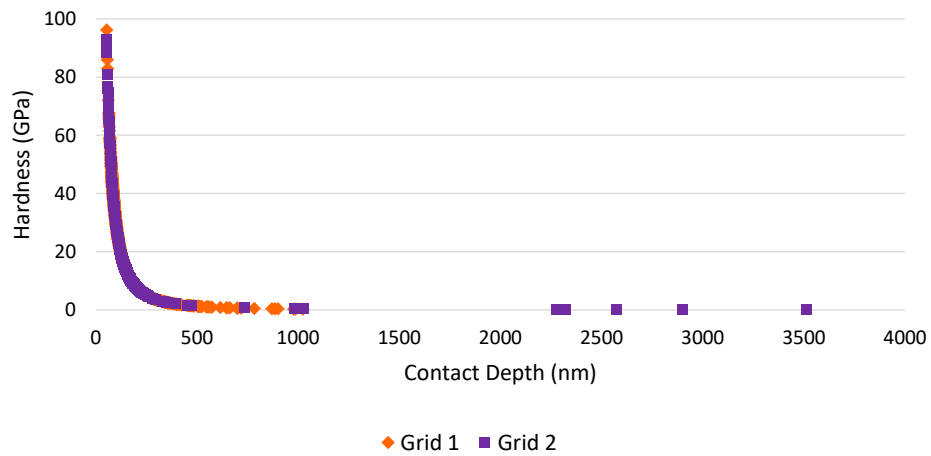


**Figure 5.41 Hardness vs contact depth**

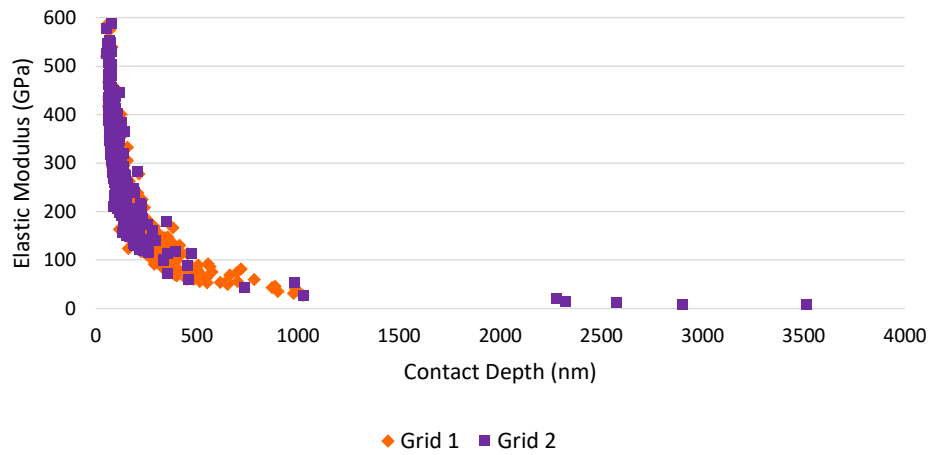


**Figure 5.42 Elastic modulus vs contact depth.**

In both case, hardness decreases with contact depth: the deeper the contact depth is, the lower the hardness. Also the elastic modulus changes with the contact depth and it is lower at deeper contact dept. The average values of hardness, elastic modulus and contact depth are shown in Table 5.4

**Table 5.4 Average values of hardness, elastic modulus and contact depth**

	Hardness (GPa)	Elastic Modulus (GPa)	Contact depth (nm)
<b>Grid 1</b>	23±17	239±93	169±128
<b>Grid 2</b>	29±15	284±91	134±213

The contact depth has a high standard deviation and this reflects on the hardness and elastic modulus values. The high variability of the data was supposed to depend on the surface heterogeneity and mainly on the surface roughness. Roughness has a considerable influence on nano-hardness measurements as it is mentioned in Chapter 4. Literature suggests that average hardness and elastic modulus values converge to a unique set of values and can be considered reliable when the average indentation depth is 5 times the RMS roughness [5].

Roughness of the samples was measured with the nanoindenter Berkovich tip. It is observed that the samples have an average roughness of 163 nm and a RMS roughness of 201 nm, that are in the range of the indentation depth, considering the standard deviation. For this reason, the sample was polished following the protocol described in Chapter 4. The value of roughness after polishing is reported in Table 5.5 together to the value of roughness before polishing, as comparison. Figure 5.43, instead, shows the surface profile scanning.

**Table 5.5 Roughness**

Samples	RMS roughness (Rq) (nm)	Average roughness (Ra) (nm)	Mean Height (nm)	Max Height (nm)	Min Height (nm)	Pick to valley (nm)
unpolished	201	163	0.020	483	-559	1042
polished	170	139	-0.019	287	-757	1044

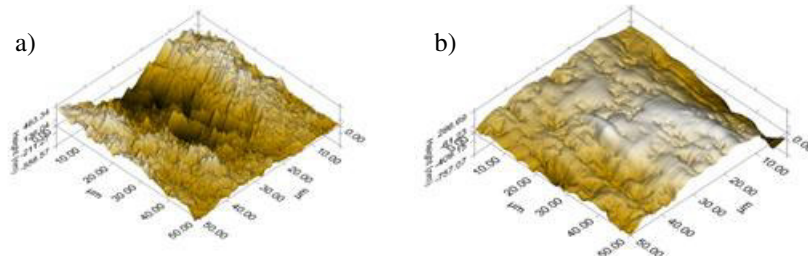


**Figure 5.43 Surface profile scanning of a) unpolished surface and b) polished surface of a samples treated at 800°C for 3.5 h**

After polishing, roughness decreases and the surface appears smoother. To verify the effect of roughness on the variability of the data, the surface profile scanning of the surface was used to select 7 smooth areas where performing the nanoindentations under load control. The surface profile scanning images before and after the test are shown in Figure 5.44.

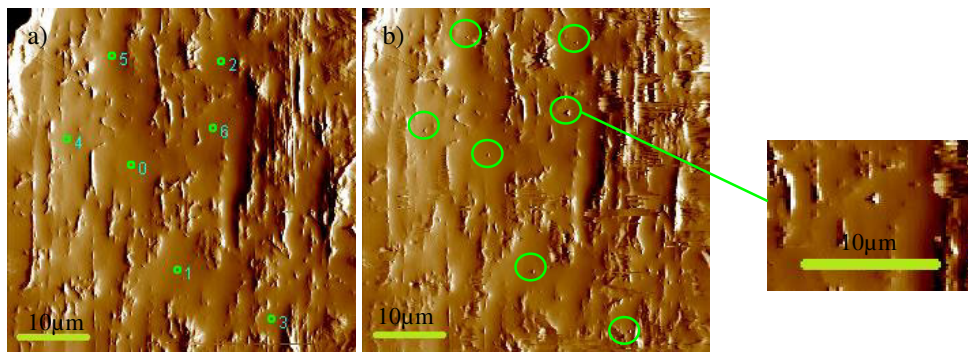


**Figure 5.44 Surface profile scanning a) before and b) after the nanoindentation test (sample treated at 800°C for 3.5 h without any pre/post treatment)**

Figures 5.45 and 5.46 reported respectively the load vs penetration depth curves and the values of hardness and elastic modulus. The data range is closer than before, excluding the 7th nanoindentation, that can be considered an outlier.

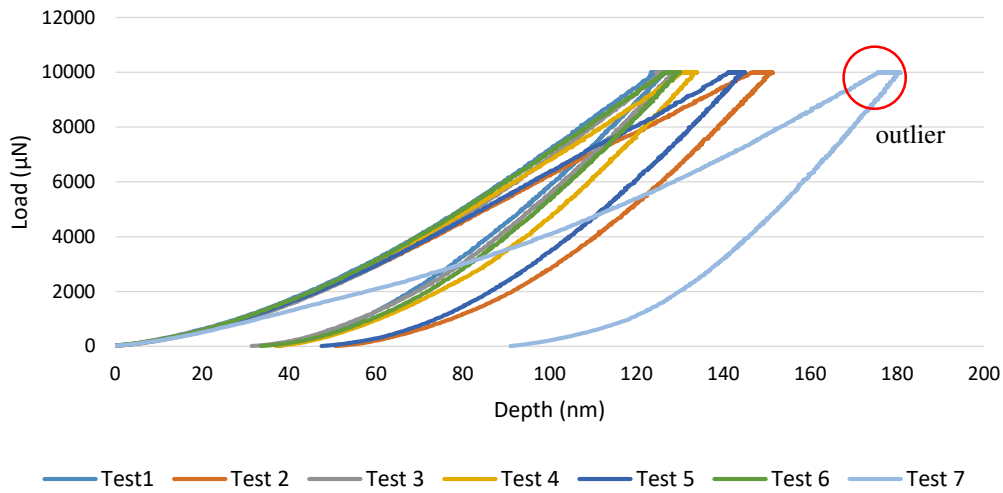
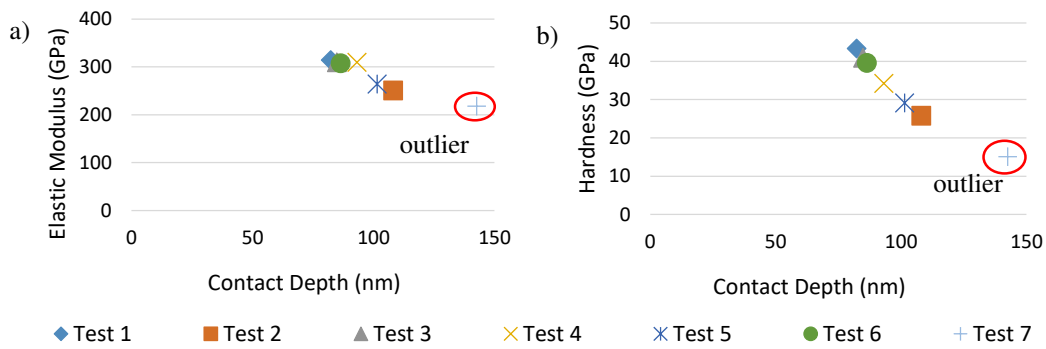


Figure 5.45 Load control: load vs penetration depth curves



Figures 5.46 a) Hardness vs contact depth and b) elastic modulus vs contact depth

Given the apparent reduction of the data variability, a new grid test was performed. Hardness vs contact depth and elastic modulus vs contact depth are plotted on Figures 5.47 and 5.48.

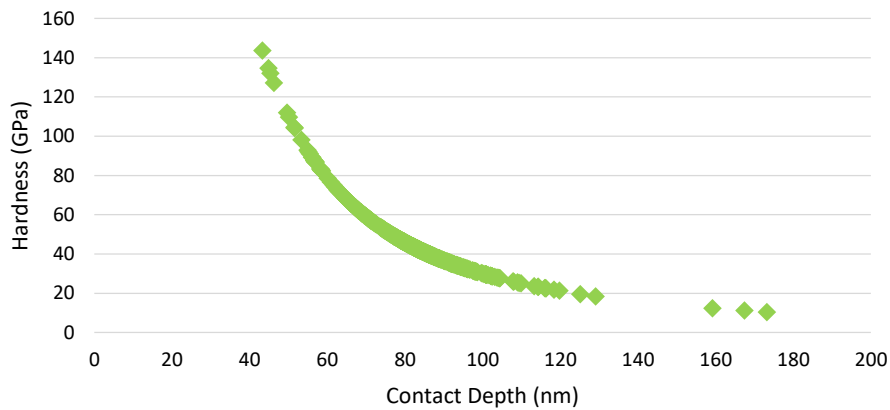
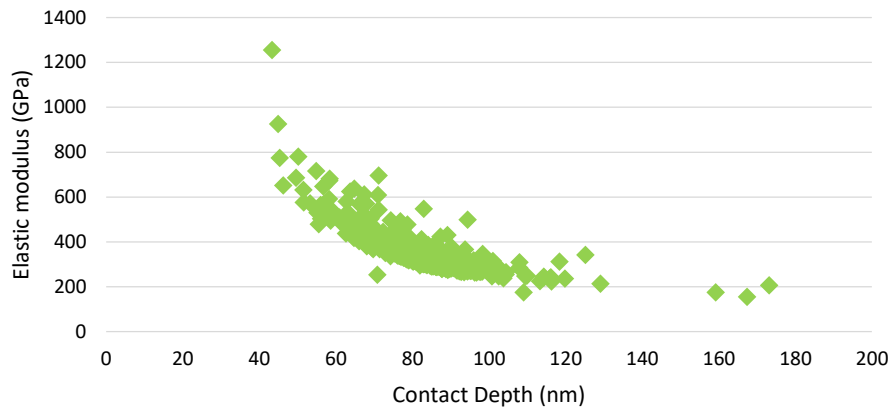


Figure 5.47 Hardness vs contact depth



**Figure 5.48 Elastic Modulus vs contact depth**

The average values of hardness, elastic modulus and contact depth are reported in Table 5.6.

**Table 5.6 Average values of hardness, elastic modulus and contact depth**

Samples		Hardness (GPa)	Elastic Modulus (GPa)	Contact depth (nm)
Polished	Grid 1	46±13	343±81	82±11
	Grid 2	23±17	239±93	169±128
Unpolished		29±15	284±91	134±213

Comparing the data of the sample before and after polishing, it is possible to see the positive effect of the reduction of roughness on the variability of the measurements. The contact depth decreases as well as its standard deviation, the hardness and elastic modulus values increase while their standard deviations decrease slightly. This entails the fall of the data under a closer range and thus their higher reliability.

Taking into account the literature data [4], that are in the same range of the ones measured, the higher hardness values in comparison to the ones collected by means of Vickers and Knoop microindentations and the contact depth in the range of the thickness of the coating monolithic layer, the data can be considered as not affected by the hardness of the substrate.

The last measurements were carried out on the untreated samples as comparison. The load vs penetration depth curves and the hardness and elastic modulus values are shown in Figures 5.49 and 5.50.

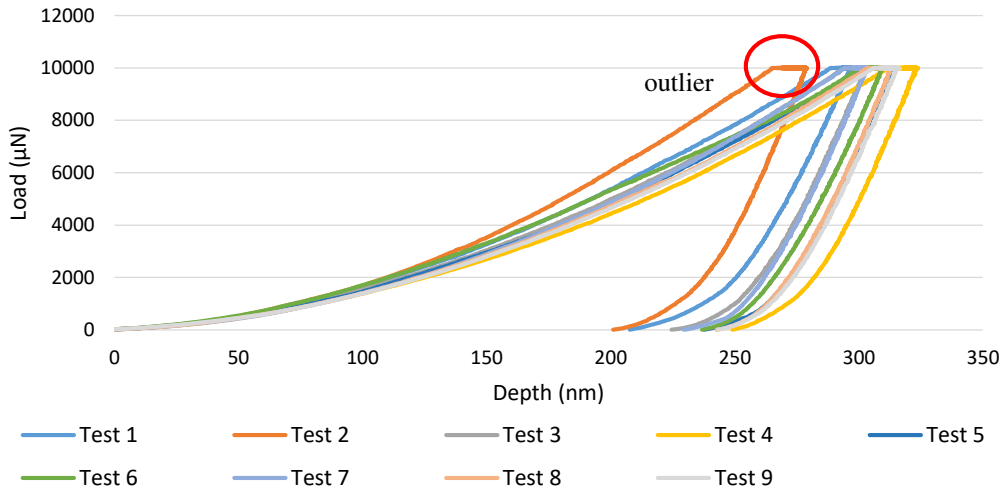
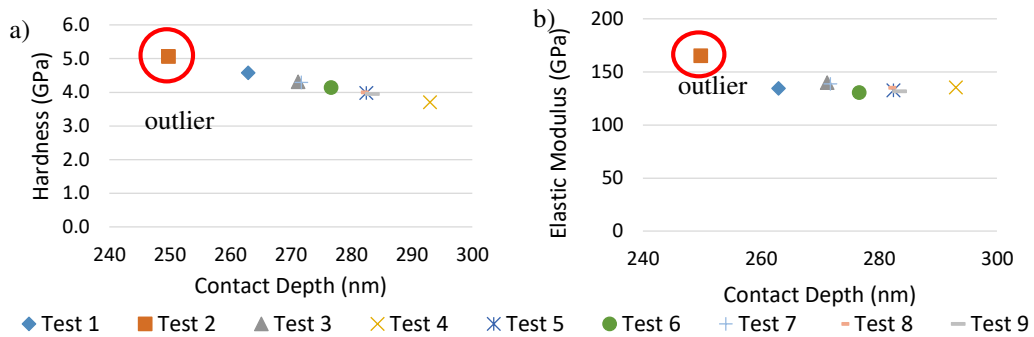


Figure 5.49 Load control: load vs penetration depth curves

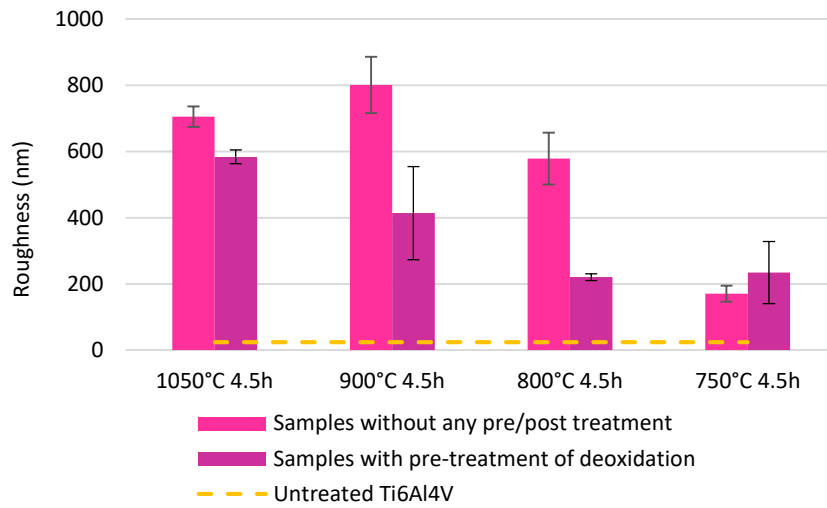


Figures 5.50 a) Hardness vs contact depth and b) elastic modulus vs contact depth

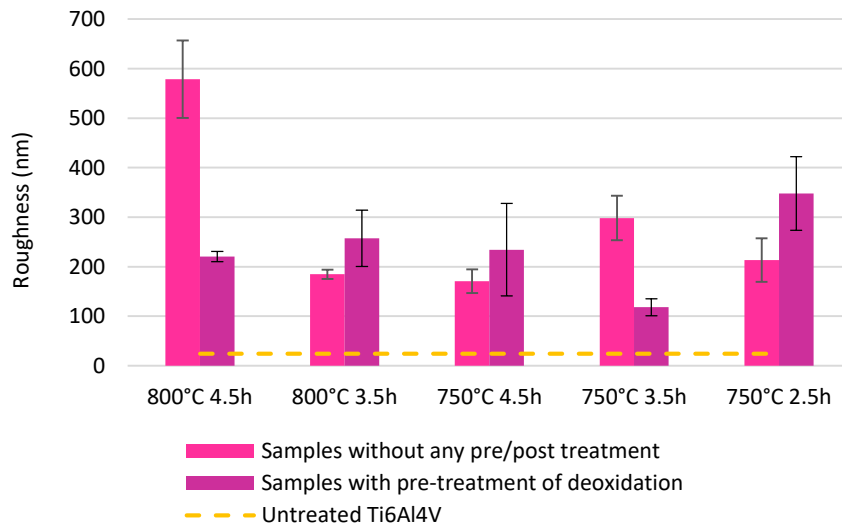
Excluding the values of the test 2, that was considered an outlier, the sample has an average hardness of  $4.1 \pm 0.3$  GPa, an average elastic modulus of  $135 \pm 3$  GPa and an average contact depth of  $278 \pm 9$  nm. As it is possible to see, the standard deviations are very small, this suggest a high reliability of the values. The collected values are a bit higher than the ones measured by means of Vickers and Knoop microindentation and of the ones reported in literature [4], that is not surprising considering that a the difference between micro and nano indentations is usually reported.

### 5.3.5 Roughness

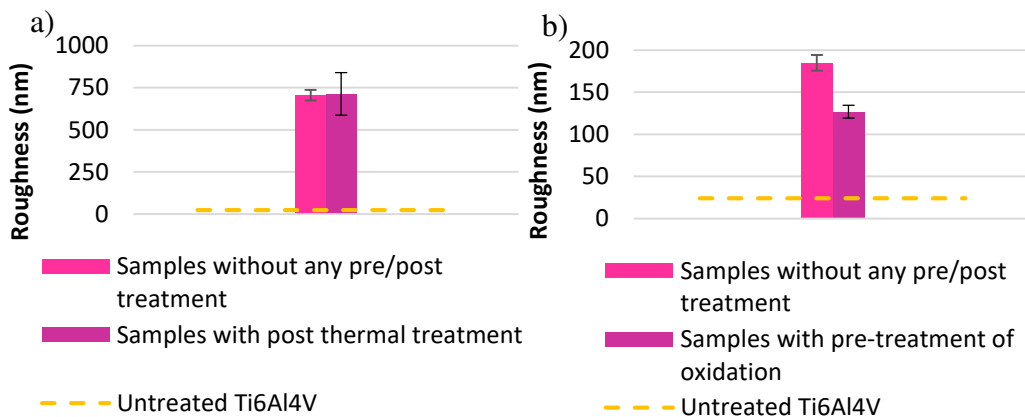
Roughness of the mirror polished untreated Ti6Al4V alloy grade 5 samples was compared with roughness of the unpolished treated samples. The untreated samples have an average roughness of  $24 \pm 3$  nm. While roughness of the treated samples in function of temperature and time of treatment and kind of surface is show in Figures 5.51, 5.52 and 5.53.



**Figures 5.51 Roughness of the samples without any pre/post treatment and with pre-treatment of deoxidation treated at different temperatures for 4.5**



**Figures 5.52 Roughness of the samples without any pre/post treatment and with pre-treatment of deoxidation treated for different times**



**Figures 5.53 Roughness of a) the samples without any pre/post treatment and subjected to the post thermal treatment and b) the samples without any pre/post treatment and with pre-treatment of oxidation**



The boronizing process causes a considerable increment of surface roughness as the Figures shows. The increase of the roughness after the boronizing process is a phenomenon also observed in literature and in particular it is confirmed by Şahin S. in a study on stainless steel [6].

Looking at Figures 5.51 and 5.52 and Table 5.7 it is possible to see that roughness of the samples treated at higher temperatures (1050-900°C) is higher than the one of the samples treated at lower temperatures (800-750°C) but there is not a specific trend in function of the temperature or the time of treatment. This can be observed both in case of the samples without any pre/post treatment and in the case of the samples with a pre-treatment of deoxidation. The only slight discriminant seems to be a temperature below or above the  $\beta$  transus temperature.

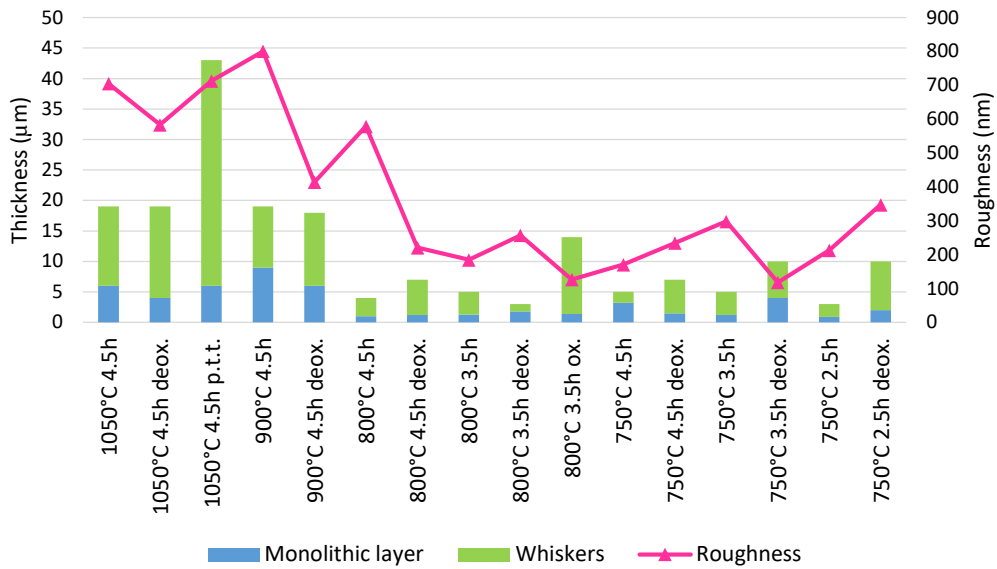
Comparing the samples without any pre/post treatment and with a pre-treatment of deoxidation, can be seeing that the samples with a pre-treatment of deoxidation, treated at temperature above the  $\beta$  transus temperature or at 800°C for 4.5 h have a roughness significantly lower than the samples without any pre/post treatment. While, when the temperature of treatment is below 800°C, roughness of the samples with a pre-treatment of deoxidation is slightly higher than the one of the samples without any pre/post treatment.

**Table 5.7 Roughness of the treated samples without any pre/post treatment and with pre-treatment of deoxidation**

Samples	Surface	1050°C 4.5h	900°C 4.5h	800°C 4.5h	800°C 3.5h	750°C 4.5h	750°C 3.5h	750°C 2.5h
	no pre/post treatment	705±31	801±85	579±78	185±9	171±24	298±45	213±44
<b>Roughness</b>	pre- treatment of deoxidation	584±21	414±141	221±10	257±57	234±94	118±17	348±74

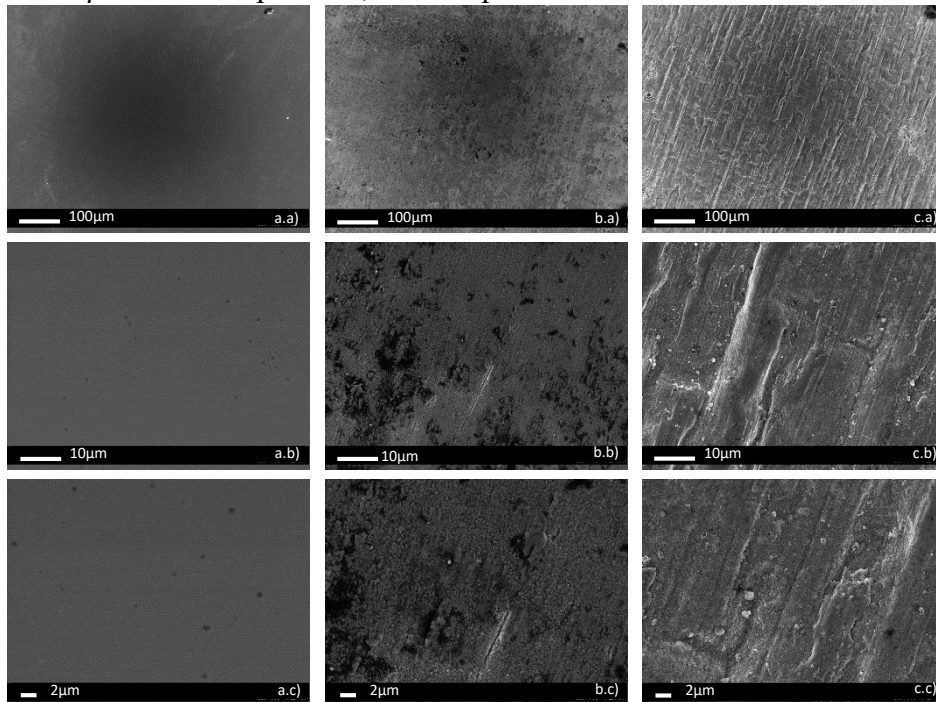
The sample subjected to the post thermal treatment shows roughness in the same range of the one of the samples without any pre/post treatment, respectively 713±127 nm and 705±31 nm (Figure 5.53a). While the samples with a pre-treatment of oxidation have roughness of 127±8 nm a bit lower than the samples without any pre/post treatment, that have roughness of 185±9, nevertheless the roughness increment is in the same range of all the others samples (Figure 5.53b).

In Figure 5.54 the sample roughness was compared with the thickness of the coatings, to verified if there is any correlation.



**Figure 5.54 Comparison between roughness and coating thickness**

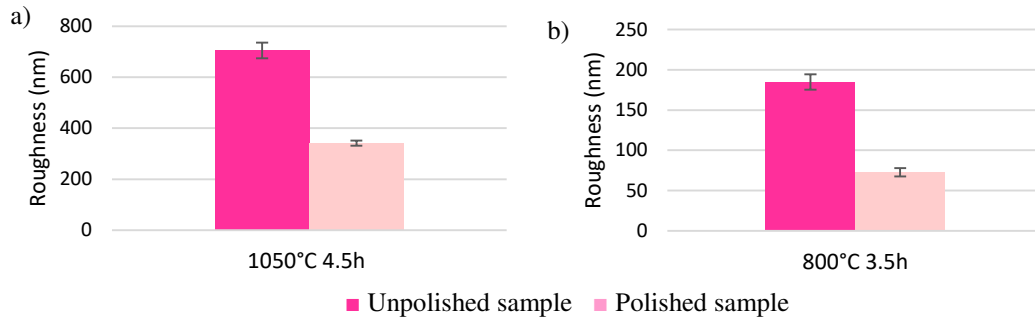
The roughness values of the samples treated at temperature higher than  $\beta$  transus are higher than the ones treated below it, but correlation is probably not related to thickness of the coating, but rather to its composition and crystalline structure. Roughness depends mainly on the amount and kind of formed borided phases, this explains the slight difference observed between the samples treated above or below the  $\beta$  transus temperature, that is the main discriminant on the chemical composition and crystallographic structure of the coatings. Figure 5.55 shows the surface of an untreated sample and two treated samples without any pre/post treatment, one treated above the  $\beta$  transus temperature and one treated below the  $\beta$  transus temperature, as examples.



**Figure 5.55 Surface roughness of the a) untreated sample, b) the sample treated at 750°C for 4.5 h and c) the sample treated at 1050°C for 4.5 h without any pre/post treatment**

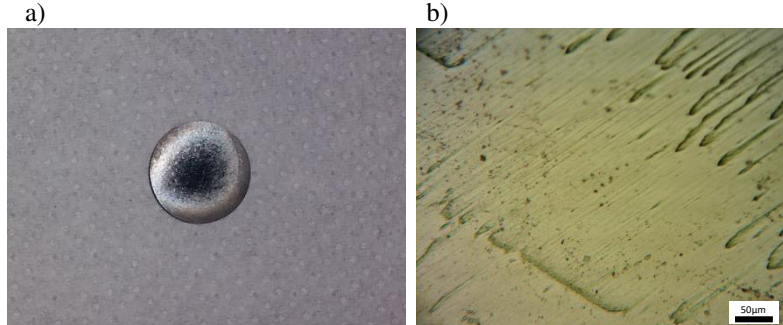
To reduce roughness induced by the boronizing treatment two different polishing protocols were applied on the treated samples as indicated in Chapter 4.

Figure 5.56 shows the effect of polishing using diamond pastes and diamond suspensions.



**Figure 5.56** Comparison between the roughness of the unpolished samples and the polished samples with a) diamond pastes (3+1 $\mu$ m) and b) diamond suspensions (3+1 $\mu$ m) ((a) samples treated at 1050°C for 3.5 h and (b) 800°C for 3.5 h both without any pre/post treatment)

As it is possible to see in Figure 5.56a, diamond pastes allow to reduce roughness with respect to the unpolished surfaces when used on a sample treated at 1050°C; when the diamond pastes are applied on samples treated at temperatures below the  $\beta$  transus temperature, they result to be aggressive and the coating is removed. Through a visual inspection (Figure 5.57a) the coating is still visible on the edges but in the middle of the sample the metal substrate stands out.



**Figure 5.57** a) Sample treated at 750°C for 2.5h after being polished with diamond pastes of 3 and 1  $\mu$ m and b) optical microscope image of an area of the sample surface

Optical microscope observations, in addition, highlight scratches and pits caused by the pastes on the surface (Figure 5.57b).

The second approach consisted on using diamond suspensions. Figure 5.56b shows that, also in this case it is possible to reduce roughness of the samples with respect to the unpolished ones.

In this case it is possible to obtain a more uniform polishing of the surface, but optical microscope observations show also in this case a partial removal of the coating and damages of the surface in case of thin coatings on samples treated below  $\beta$  transus (Figure 5.58).

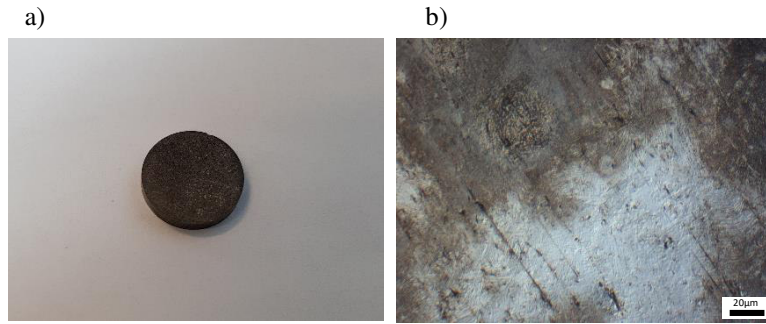


**Figure 5.58** a) Sample treated at 800°C for 3.5h after being polished with diamond suspensions of 3 and 1 µm and b) optical microscope image of an area of the sample

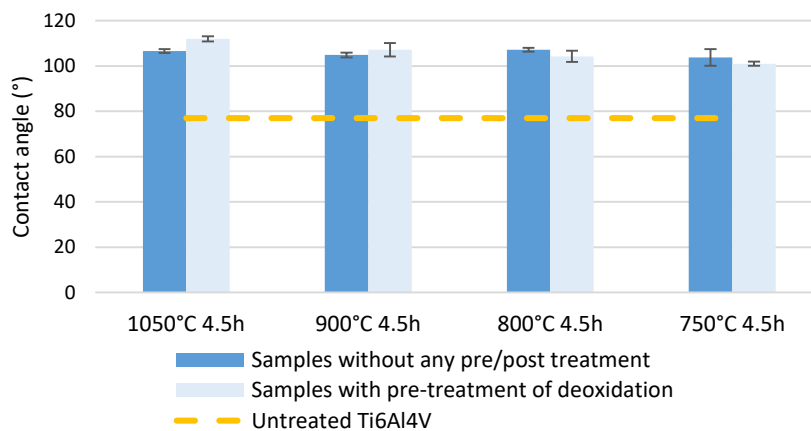
All the polished protocols were carried out performing a manual polishing. Automatic polishing could help to obtain a higher degree of uniformity, while a better degree of surface finishing and lower roughness could be obtained through electropolishing.

The issue related to polishing and roughness is not trivial considering that any application involving friction, wear or fretting is strongly affected by the degree of surface finishing and in some cases ceramic materials are limited in their use because of issues related to their polishing.

### 5.3.6 Wettability

By means of water contact angle measurements, the contact angle of the mirror polished untreated Ti6Al4V alloy grade 5 results to be  $77\pm 1^\circ$ . In literature, the contact angle of Ti6Al4V alloy is reported to be in the range from  $50\pm 3^\circ$  [7] to  $91.34$  [8]. As known by literature, there is a strong correlation between roughness and wettability [9], so the difference in contact angles can be related to the different average roughness of the substrate, that is  $24\pm 3$  nm for the samples used in this research and  $<15$  nm and  $40$  nm for the literature samples [7,8]. In any case, the untreated material is hydrophilic.

The contact angles of the samples after the boronizing treatment are shown in Figures 5.59, 5.60 and 5.61.



**Figures 5.59** Contact angles of the samples without any pre/post treatment and with pre-treatment of deoxidation treated at different temperature for 4.5 h

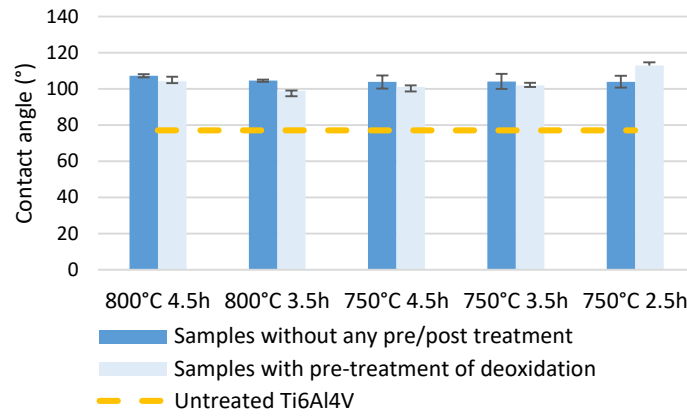


**Figure 5.60** Contact angles of the samples without any pre/post treatment and with pre-treatment of deoxidation treated for different time

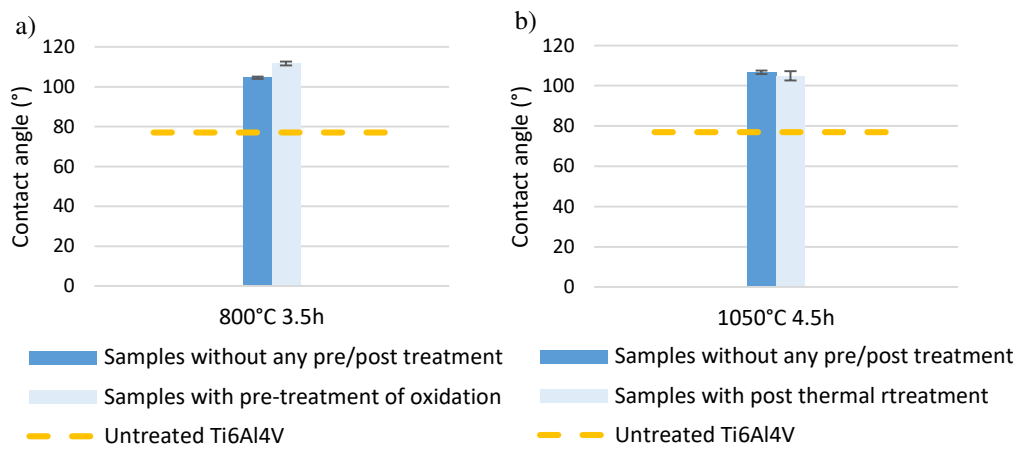


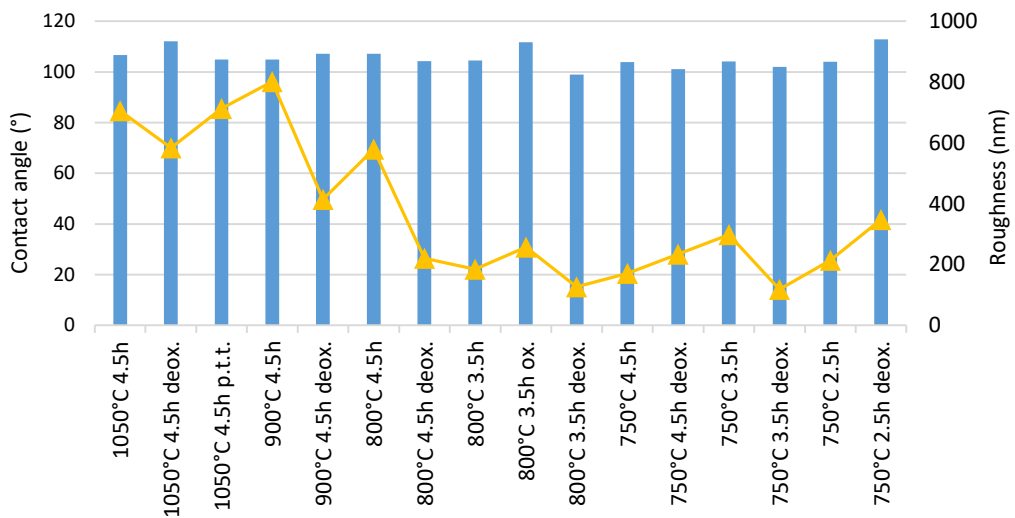
**Figure 5.61** Contact angles of a) the samples without any pre/post treatment and subjected to the post thermal treatment and b) the samples without any pre/post treatment and pre-treatment of oxidation

The surfaces become more hydrophobic after the treatment. All the surfaces have similar values of contact angle independently of the temperature and duration of the treatment. Also the pre-treatment of surface deoxidation and oxidation and the post thermal treatment do not lead a variations of wettability among the treated samples. This effect can be expected, considering that eventual pre-treatments or different times and temperatures of treatment affect the thickness of the coating and its interface with the substrate (penetration depth of whiskers), but not the chemical composition of the external layer that is the same in any case. It can be noted that at this concern, no difference between the two borides phases ( $\text{TiB}$  and  $\text{TiB}_2$ ) is registered on wettability. As it is reported in Table 5.8, all the contact angles are closed to or higher than  $100^\circ$ . The borided coatings result to have an overall average contact angle of  $106 \pm 4^\circ$ .

**Table 5.8 Contact angles of the treated samples**

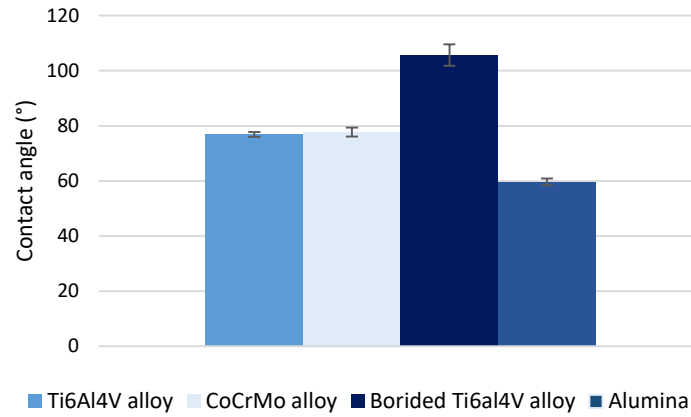
Sample	Contact angle (°)
1050°C 4.5h	106.7±0.9
1050°C 4.5h deox.	112.0±1.1
1050°C 4.5h p.t.t.	104.9±2.3
900°C 4.5h	104.9±1.0
900°C 4.5h deox.	107.2±3.0
800°C 4.5h	107.2±0.9
800°C 4.5h deox.	104.3±2.5
800°C 3.5h	104.5±0.6
800°C 3.5h ox.	111.7±1.0
800°C 3.5h deox.	99.0±0.2
750°C 4.5h	103.8±3.7
750°C 4.5h deox.	101.0±0.9
750°C 3.5h	104.2±4.2
750°C 3.5h deox.	102.0±1.3
750°C 2.5h	103.9±3.3
750°C 2.5h deox.	112.9±1.9

Figure 5.62 compares the wettability trend with the one of roughness. In case of the treated samples, roughness seems not to have any effect on the contact angle, differently from what has been observed on the untreated samples.



**Figure 5.62 Comparison between the contact angles and roughness of the treated samples**

In Figure 5.63, the contact angles of the untreated Ti6Al4V alloy and the borided Ti6Al4V alloy are compared with the ones of CoCrMo alloy and alumina, used as reference materials.



**Figure 5.63 Comparison among the contact angles of the reference materials and the average value of the treated ones.**

It is possible to see that metallic materials have similar average contact angles,  $77\pm 1^\circ$  for untreated Ti6Al4V alloy and  $78\pm 2^\circ$  for CoCrMo alloy. While the ceramic coating and alumina show different wettability behaviour, the first has an average contact angle of  $106\pm 4^\circ$  and the second  $60\pm 1^\circ$ . All the reference materials considered have a hydrophilic behaviour, while the treated Ti6Al4V alloy results to be hydrophobic.

The contact angles of the references materials are in the range of values reported in literature (Table 5.9), the slight differences between one study and another can be related to the different surface finishing of the samples, as demonstrated in literature [9].

**Table 5.9 The contact angles of CoCrMo alloy and alumina**

References	CoCrMo alloy		Alumina	
	Ra (nm)	Water contact angle (°)	Ra (nm)	Water contact angle (°)
Present research	24±6	78±2	39±2	60±1
Literature	320 [10]	61 [10]	110 [10]	40 [10]
Literature	10 [11]	97 [11]		

### 5.3.7 Friction coefficients and scratch resistance derived from scratch tests

The friction coefficient (COF) of the treated Ti6Al4V alloy and the references materials was evaluated in dry condition by means of scratch tests, under the conditions reported in Chapter 4. This type of test has not the aim to simulate friction condition in joint implants, as in the case of the wear tests reported in the next paragraph, but it was used as a useful test for a first evaluation of the tribological properties of the coatings and for a screening of the different treatments explored.

Figure 5.64 shows the trend of the COFs or of the relative acoustic emissions (AE) vs the applied load of the references materials. The AEs are elastic waves, generated when localized sources within the material release energy. They can

provide secondary information about different coating damage level as indicated by the standard C1624 – 05.

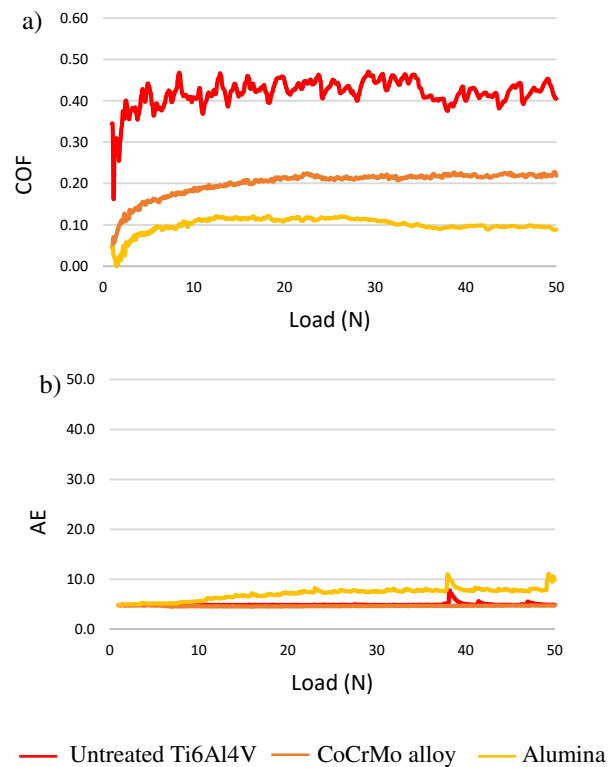


**Figure 5.64 COFs and AEs of the reference materials**

The COFs of the reference materials are about 0.4 (Ti6Al4V alloy), 0.2 (CoCrMo alloy) and 0.1 (Alumina). As known by literature, the Ti6Al4V alloy (such as all the titanium based alloys) has a worst friction behaviour than CoCrMo alloy [12], this is confirmed by the highest COF and this help to explain why the Ti6Al4V alloy is not used in any application involving friction, such as a bearing component. In the evaluation of the COF, roughness of the surfaces was taken into account. The two metallic materials have an average roughness of about 24 nm, so the same surface finish, while the average roughness of the alumina is a bit higher, about 39 nm. The reference materials, in general, have closed average roughness and thus it is possible to compare their COFs. The COF of the untreated Ti6Al4V was used as reference of the substrate and to define the point of removal of the coatings. While the COFs of the CoCrMo alloy and alumina were used as reference of well performing bearing surfaces.

In these cases, the AEs are low and approximately constant due to the absence of a coating and the homogeneity of the surfaces. The slight ripples of the signals can be caused by polishing lines.

Figure 5.65 reports the COFs and AEs of the Ti6Al4V alloy samples without any pre/post treatment treated at different temperatures for 4.5 h.



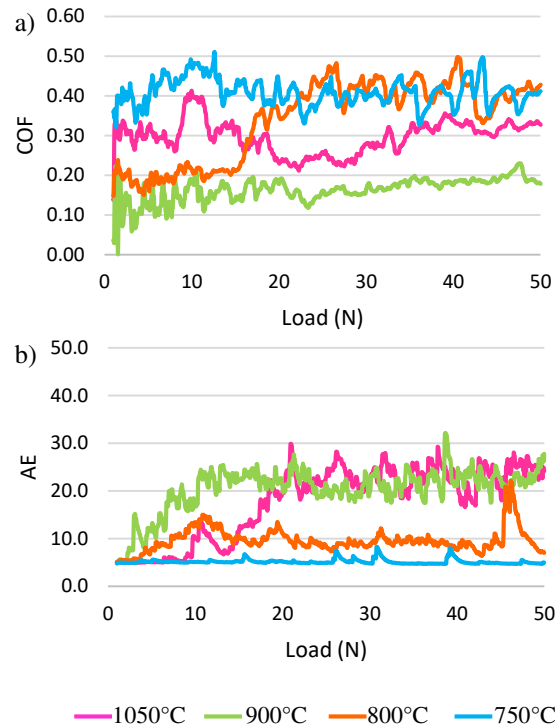


**Figure 5.65** COFs and AEs of the Ti6Al4V alloy samples without any pre/post treatment treated at different temperatures for 4.5 h

The value and trend of the COF change in function of the temperature of treatment. The samples treated at 1050°C and 900°C show a COF respectively of about 0.3 and 0.2. The values are lower than the one of untreated material and approximately constant along the whole test. This suggests that the coating is not removed till the end of the test. The AE signals, instead, present an increment respectively between 13 and 20 N and between 1 and 10 N for the samples treated at 1050°C and 900°C, then they become stable. The increment of the AEs can be due to the penetration of the tip within the coating (which has a gradient of composition and crystallographic texture across thickness) as the applied load increases. The samples treated at 800°C have a COF of about 0.2 up to a load of 15 N, then the COF rises to a value of 0.4, highlighting a removal of the coating at a load of 15 N. The AE signal increases slightly at the beginning of the test and then it shows an approximately linear trend. The AE can be caused by both the removal of the coating and roughness of the sample (~579 nm). The samples treated at 750°C, instead, show the same COF of the untreated material (0.4) and a flat AE, with slight ripples due to roughness of the surface. There is a removal of the coating and exposition of the substrate since the beginning of the test. The critical scratch load in this case is lower than 1 N.

Some variations of the trend of the COFs were introduced by the surface deoxidation pre-treatment. The trend of the COFs and the corresponding AEs are shown in Figure 5.66.

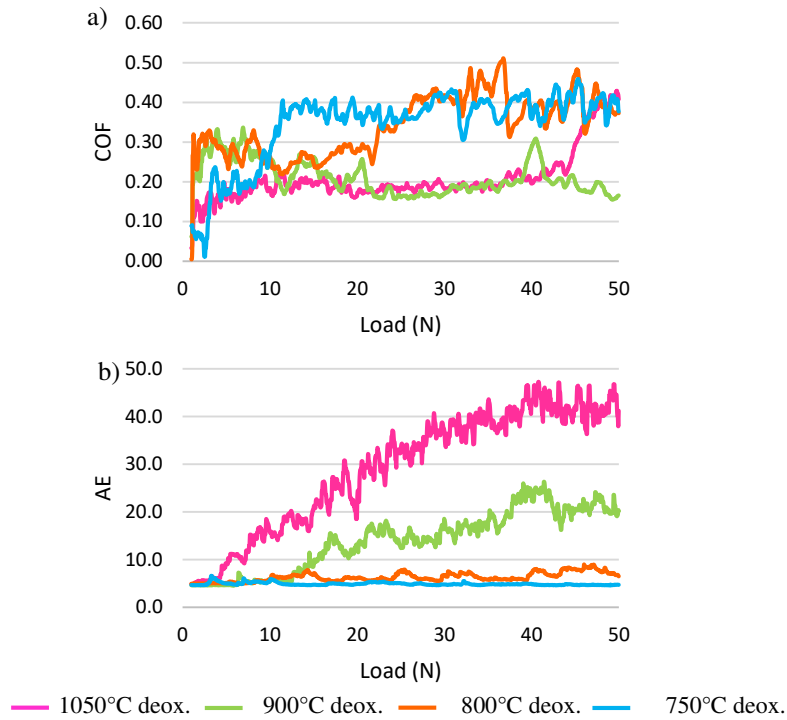


**Figure 5.66** COFs and AEs of the Ti6Al4V alloy samples with pre-treatment of deoxidation treated at different temperatures for 4.5 h

In this case, the sample treated at 1050°C shows a COF of about 0.2, lower than the one of the sample without any pre/post treatment. But, while, in the case of sample without any pre/post treatment there is not detachment of the coating, in this case around 44 N the coating is removed and the COF rises to a values of 0.4, that is the value of the substrate. The COF of the sample treated at 900°C, instead, remains stable around 0.2, as previously registered. Changes can, also, be seen in the case of samples treated at 800°C and 750°C. The sample treated at 800°C shows a detachment load slightly higher than the one of the correspondent sample without any pre/post treatment. It has a COF of about 0.3 up to a load of 20 N. Also in the case of the sample treated at 750°C, the COF is around 0.2 and it rises at 0.4 around 10 N. The coating of the sample at 750°C with pre-treatment of deoxidation shows a higher adhesion than the one of the sample without any pre/post treatment, that detaches at a load lower than 1 N.

The differences can be explained taking into account thickness and roughness of the coatings (Figure 5.67).

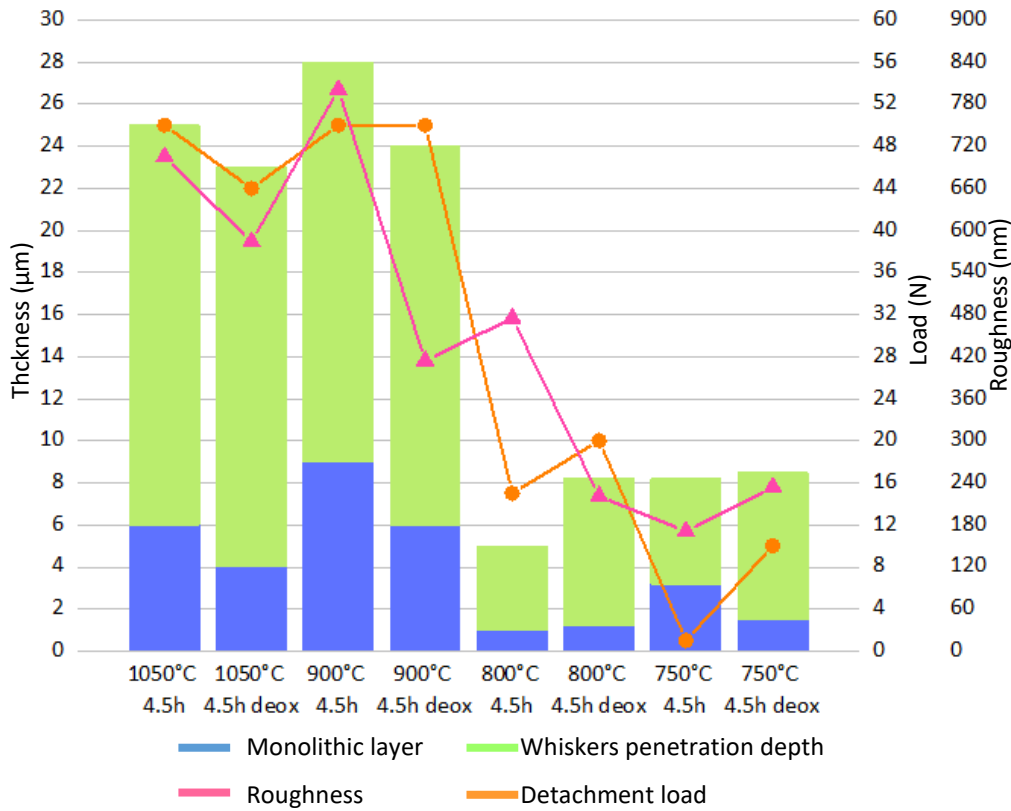


**Figure 5.67 Thickness, roughness and detachment load of samples without any pre/post treatment and with pre-treatment of deoxidation treated for 4.5 h at different temperatures**

The differences in the detachment load can be attributed to the different thickness of the coatings in the case of the samples treated at the same temperature. The monolithic layer of the sample with pre-treatment of deoxidation treated at 1050°C is a bit thinner than the one of the corresponding sample without any pre/post treatment, thus the coating is removed at lower load. The samples treated at 800°C and 750°C with pre-treatment of deoxidation have a penetration depth of the whiskers higher than the corresponding samples without any pre/post treatment. As consequence, the hardened layer is thicker and the coatings delaminated at higher loads. On the other side, roughness affects the registered COF: in the case of the deoxidized surfaces, where lower roughness values are registered, the COFs are much more stable and close to 0.2.

The data obtained allow to reach the following conclusions: the COF of the boride coating is significantly lower than that of the untreated substrate and it is around 0.2 (that is close to that of the CoCr alloy used as standard reference), a lowering of roughness (as derived from treating pretreated surfaces) has a beneficial effect on its stability along the measurement, while a higher thickness of the coating has a beneficial effect on the strength of the interface by enhancing the detachment load (that is close to 40-50 N in the case of the coatings produced at a temperature higher than beta transus).

The AE signals increase as the applied load increases in the cases of the samples treated at 1050°C and 900°C, while the ones of the samples treated at

800°C and 750°C are low and flat. In this case, the AE signal does not give any particular additional information.

Figure 5.68 shows the effect of the duration of the treatment on the samples without any pre/post treatment treated at 800°C and 750°C.

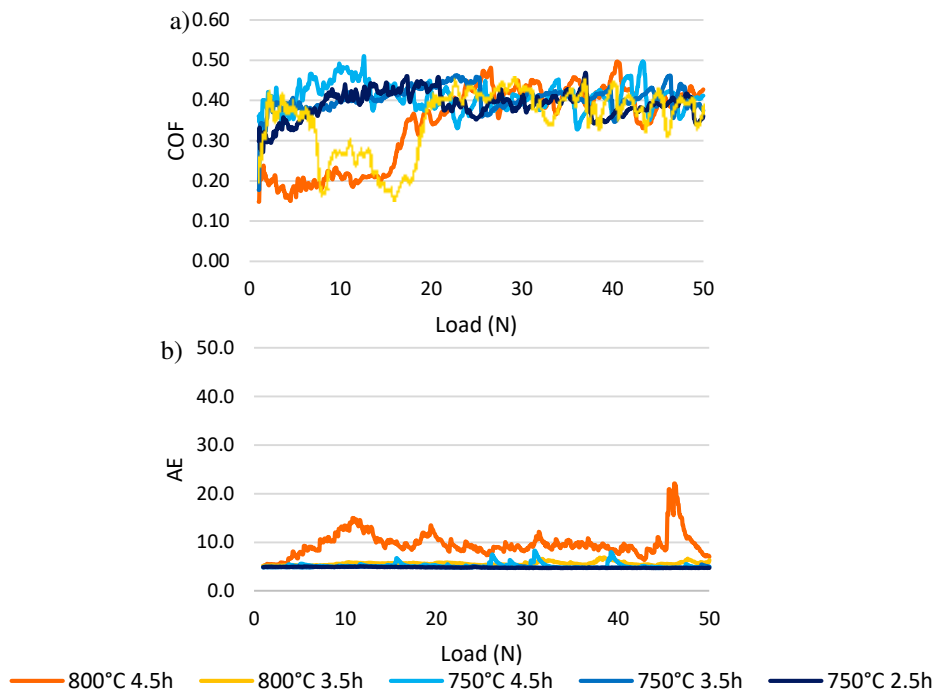


**Figure 5.68 COFs and AEs of the Ti6Al4V alloy samples without any pre/post treatment treated at 800°C and 750°C for different times**

The coatings of the samples treated at 750°C detach at the beginning of the test and the COFs is stable around 0.4 regardless of the duration of the treatment. To evaluate at which load the coatings of these samples detach, a scratch test was performed at lower loads. As example, it was tested the sample treated at 750°C for 3.5 h without any pre/post treatment. The coating delaminates at a load of about  $105 \pm 15$  mN.

The COF of the samples treated at 800°C for 4.5 h is 0.2 up to a load of about 15 N. Then it rises to the same value of the one of the substrate (0.4). The coating of the sample treated at 800°C for 3.5 h has an instable COF: it is around 0.4 at the beginning of the test, then it oscillates between 0.2 and 0.3 and finally it rises again the values of 0.4. Even if a complete removal of the coating occurs around a load of 18N, in this case, due to the instability of the COF also at low load and to an initial value of 0.4, it can be considered that the coating gives up from the beginning of the test.

The AE is flat and low for all the samples, a bit higher is the one of the sample treated at 800°C for 4.5 h, that is the sample with the highest roughness.

The effect of the surface deoxidation pre-treatment on the trend of the COFs of the samples treated at 800°C and 750°C for different duration of the treatment can be evaluated observing Figure 5.69.

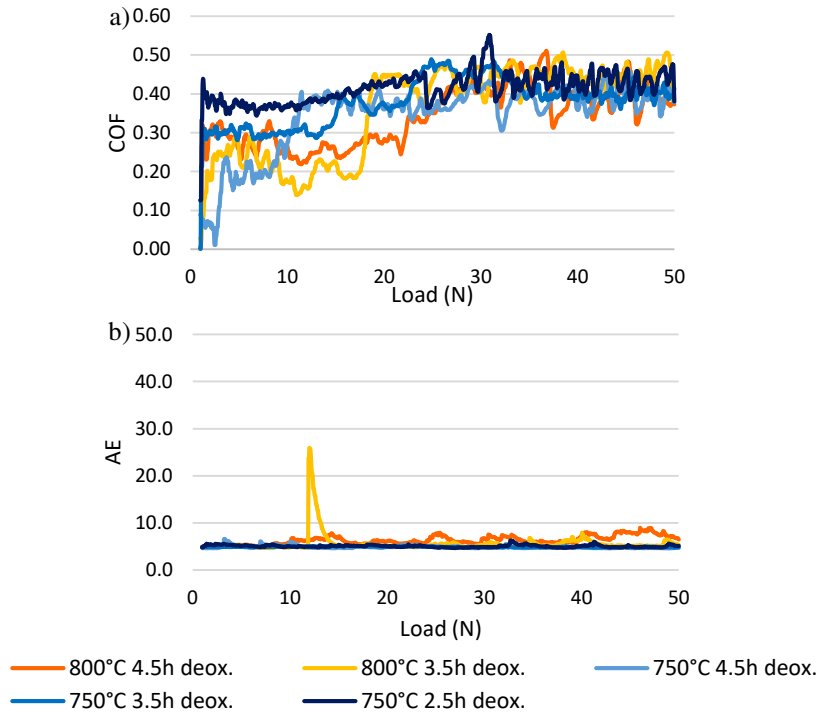


**Figure 5.69** COFs and AEs of the Ti6Al4V alloy samples with pre-treatment of deoxidation treated at 800°C and 750°C for different times

The surface deoxidation process has not effects on the sample treated at 750°C for 2.5 h. The COF is still 0.4, the coating is removed since the beginning of the test as well as in the case of the corresponding sample without any pre/post treatment. The coatings of the samples treated at 750°C for 3.5 h and 4.5 h show a higher adhesion, than the corresponding samples without any pre/post treatment. The sample treated for 3.5 has a COF of about 0.3 up to a load of 15 N, then it rises to a value of 0.4. While the COF of the samples treated for 4.5 h is 0.2 at the beginning of the test and then it rises at 0.4 for loads greater than 10 N. In both cases the thickness of the hardened layer is higher on samples with a pre-treatment of deoxidation than on the corresponding samples without any pre/post treatment (Figure 5.70).

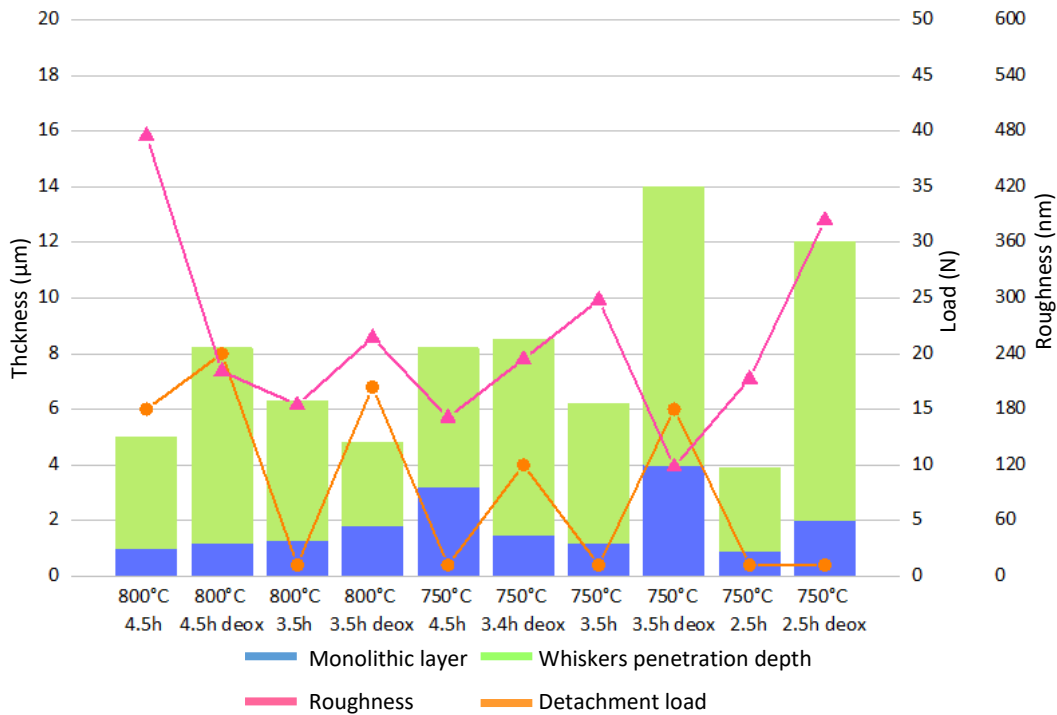


**Figure 5.70 Thickness, roughness and detachment load of the samples without any pre/post treatment and with pre-treatment of deoxidation treated at 800°C and 750°C for different times**

Comparing the three samples treated at 750°C with a pre-treatment of deoxidation the trend of the COF seems to depend mainly on the thickness and roughness of the coating than on the duration of the treatment. The one with the highest adhesion is the coating of the sample treated for 3.5 h, that is the one with the highest thickness and the lowest roughness between the three samples treated at 750°C (Figure 5.70).

The coating of the sample treated at 800°C for 3.5 h has a higher adhesion than the one of the corresponding sample without any pre/post treatment. It detaches around 17 N, load at which the COF rises from a value of 0.2 to a value of 0.4. The compact monolithic layer is thicker than the one of the sample without any pre/post treatment. This can explain the removal of the coating at higher load. The detachment load of the sample treated at 800°C for 4.5 h is about 20 N, it is slightly higher than the one of the correspondent sample without any pre-post treatment. This can be related to a deeper penetration depth of the whiskers in the case of the sample with pre-treatment of surface deoxidation (Figure 5.70).

The AEs are low and flat; no secondary information is given by the signals. The peak of the AE signal of the sample treated at 800°C for 3.5 h maybe is due to a defect of the surface or a transition from a tip-coating contact to a tip-substrate contact.

Figure 5.71 allows to observe the effect of the surface oxidation pre-treatment and post thermal treatment.

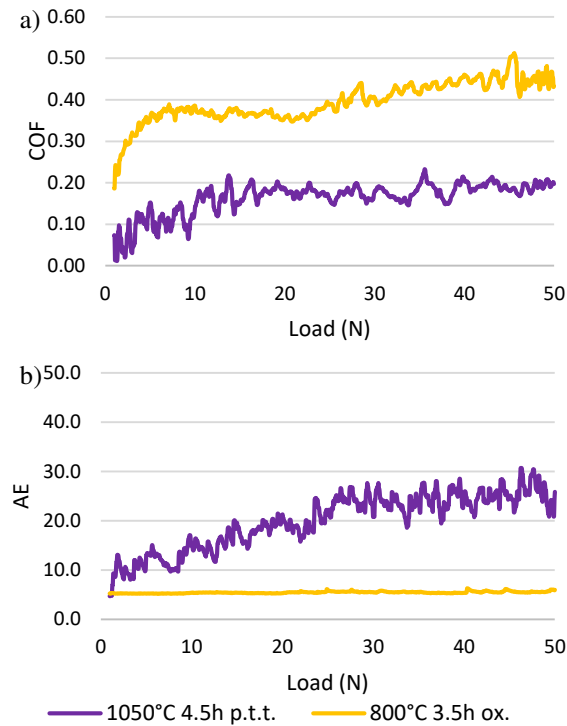


**Figure 5.71 COFs and AEs of the sample with pre-treatment of oxidation treated at 800°C for 3.5 h and of the sample subjected to the post thermal treatment5**

The coating of the sample with a pre-treatment of oxidation is removed since the beginning of the test, the COF is around 0.4, the same of the substrate and the AE is low and flat. In this case, the intermedia oxidised layer dose not promote the adhesion of the coating. While the post thermal treatment, increasing the penetration depth of the whiskers and promoting a thick hardened layer allows to obtain a coating with good adhesion and COF around 0.2. The AE signal increases as the applied load increases, as well as in the case of the others samples treated at 1050°C.

Interesting information was detected performing a nanoscratch test on a sample treated at 800°C for 3.5 h without any pre/post treatment. In Figure 5.72 the normal displacement is plotted in function of the time.

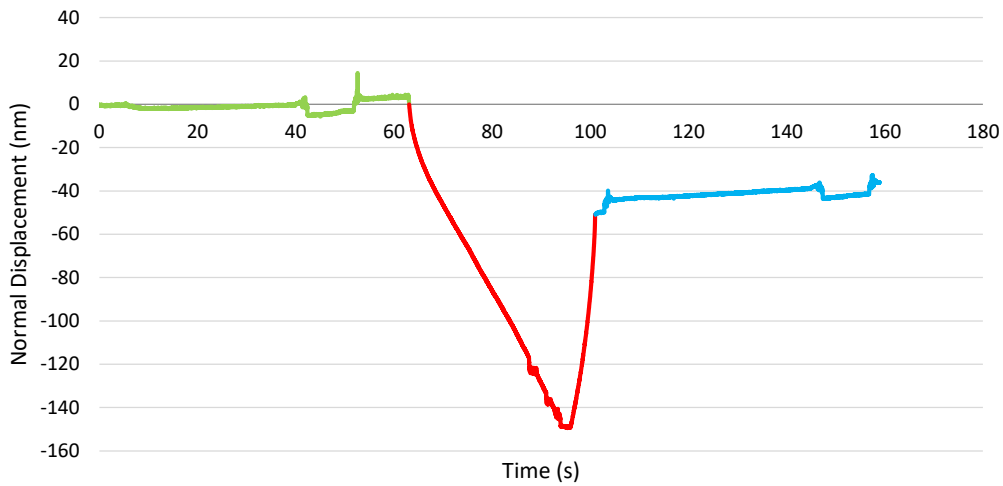


**Figure 5.72 Normal displacement vs time**

The nanoscratch test was performed in three steps. First of all, the probe scanned the surface without applying load (green stroke), then it performed the test applying the progressive load (red stroke) and finally it scanned again the surface without applying load (blue stroke). It is possible to see that the surface profile is the same before and after the test, but there is a displacement of the surface level before and after the test. This suggests that there is not damage of the surface and under the applied load, the treated material shows a plastic deformation.

The behaviour of the coating under the applied load during the scratch test was better analysed by means of FESEM observations. As example, the FESEM images and EDS analyses of the samples treated at 1050°C were reported in Figure 5.73.



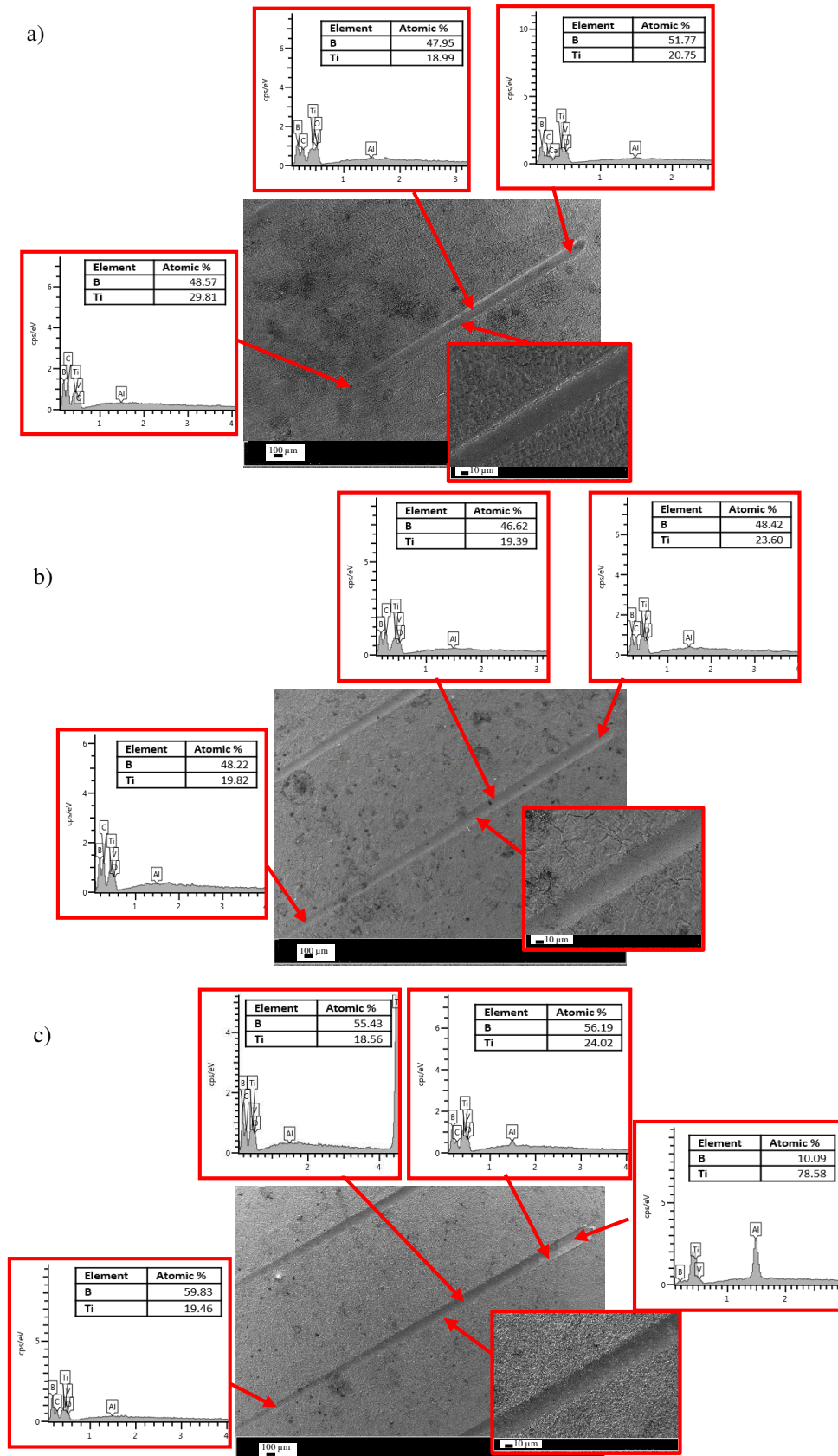


Figure 5.73 FESEM images and EDS analyses of samples treated at 1050°C for 4.5 a) without any pre/post treatment, b) with pre-treatment of deoxidation and c) subjected to post thermal treatment

As FESEM images show the coatings do not have any cracks, they plastically deform following the substrate. During the scratch test the damage of the coatings is not due to detachment or delamination, but the coatings are ploughed by the tip of the probe. The absence of cracks and the plastic deformation can explain why the AE signals gradually increase or are flat and do not have abrupt jumps.

EDS analyses detect a significant and constant amount of boron along all the track, confirming the presence of the coating both in the case of the sample without any pre/post treatment (Figure 5.73a) and in the case of the sample subjected to post thermal treatment (Figure 5.73c). The data agree with the ones of the COF, these samples have COFs lower than the one of the untreated material and approximately constant up to the end of the test. The COF of the sample with a pre-treatment of deoxidation, instead, rises and reaches the values of the one of the substrate around a load of 44 N, as shown in Figure 5.73. EDS analysis (Figure 5.73b) confirms the damage of the coating, showing that at the end of the track the atomic percentage of the boron decreases considerably.

FESEM images and EDS analyses of all others samples lead to the same conclusions and confirm the data of the COFs and AE signals, therefore they were not reported and the data of the samples treated at 1050°C in Figure 5.73 were used as a summary for all samples.

### 5.3.8 Wear tests (soft on hard and hard on hard condition)

#### Friction coefficient

The MoM and MoP couplings used in prostheses, correspond to hard on hard and soft on hard wear conditions; moreover, the neck-head interface corresponds to a hard on hard coupling. Therefore, the COF of the treated material was evaluated by means of pin on disk tests coupled to itself (hard-on-hard) or to UHMWPE (soft-on-hard), in lubricant condition, to mimic the two kinds of coupling.

The untreated Ti6Al4V alloy and CoCrMo alloy were used as reference materials.

The trend of the COF of the untreated Ti6Al4V alloy in hard on hard and soft on hard conditions were reported in Figure 5.74.

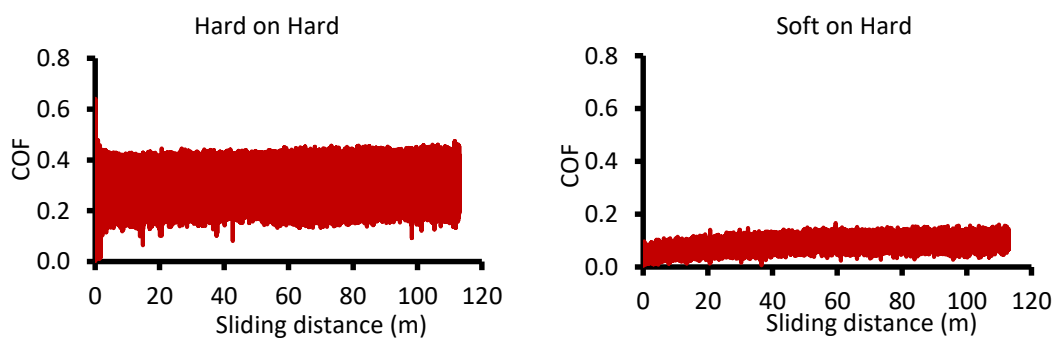
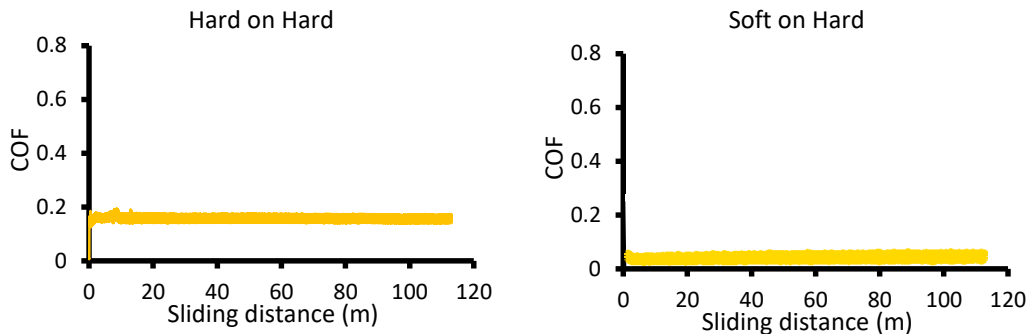


Figure 5.74 COF of the untreated Ti6Al4V alloy in hard on hard and soft on hard conditions

The COF of the untreated Ti6Al4V alloy in soft on hard condition increases slightly during the test and over a sliding distance of about 40 m it became stable with an average value of 0.09 (with a background noise, around 0.02).

In hard on hard condition, the tribological behaviour of the untreated Ti6Al4V alloy is worst. The average COF is 0.28 (with a high background noise, around 0.08), more than twice the one of the soft on hard condition.

In the currently used prostheses with MoM and MoP coupling, CoCrMo alloy is used as metallic material, that has higher hardness (4.2 GPa) and wear resistance than Ti6Al4V alloy (3.4 GPa). The lower COF of the CoCrMo alloy than the one of Ti6Al4V alloy is visible in Figure 5.75.



**Figure 5.75** COF of the CoCrMo alloy in hard on hard and soft on hard conditions

In soft on hard condition, the CoCrMo alloy has an average COF of 0.05 (with a background noise around 0.02). In this condition, the COF slightly increases up to the end of the test, while in hard on hard condition it is stable during all the test. In hard on hard condition, the average value of the COF is 0.16 (with a very low background noise around 0.01), higher than the one in soft on hard contact.

Considering the treated samples, it is possible to see that in soft on hard contact the treated Ti6Al4V alloy without any pre/post treatment has a stable average COF of 0.21 (background noise, around 0.5), while in hard on hard contact the average COF is lower, around 0.12 (background noise around 0.08). Moreover, around a sliding distance of 100 m there is an abrupt jump of the COF that suggest a detachment of the coating. In fact, the COF reaches the values of about 0.4 (Figure 5.76).

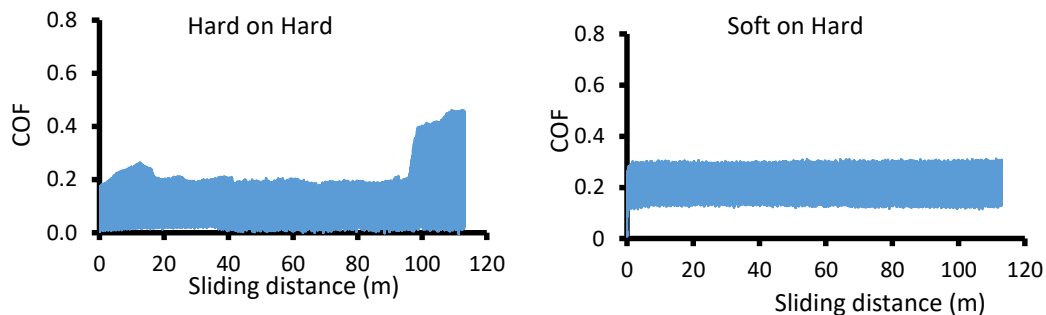


**Figure 5.76** COF of the treated Ti6Al4V alloy without any pre/post treatment in hard on hard and soft on hard conditions

Figure 5.77 reports the trend of the COF in the case of the treated Ti6Al4V alloy with pre-treatment of deoxidation.

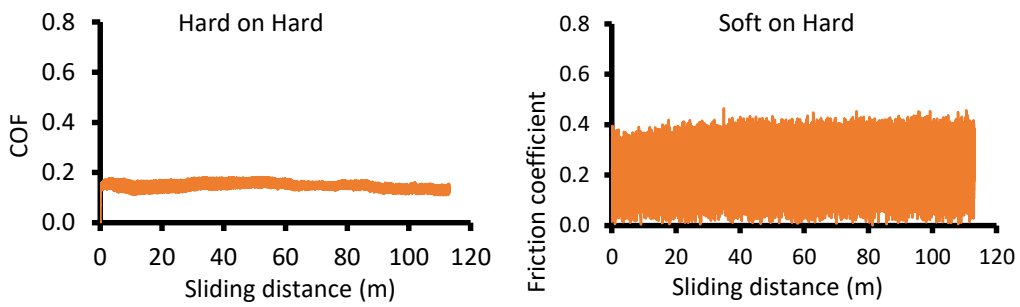


**Figure 5.77 COF of the treated Ti6Al4V alloy with pre-treatment of deoxidation in hard on hard and soft on hard conditions**

In this case, the average COF is 0.27 (with a background noise, around 0.09) in soft on hard contact and 0.15 (with a minimum background noise, around 0.02) in hard on hard contact. The COF is lower in hard on hard contact.

The trend of the COF of the treated Ti6Al4V alloy subjected to post thermal treatment are reported in Figure 5.78.

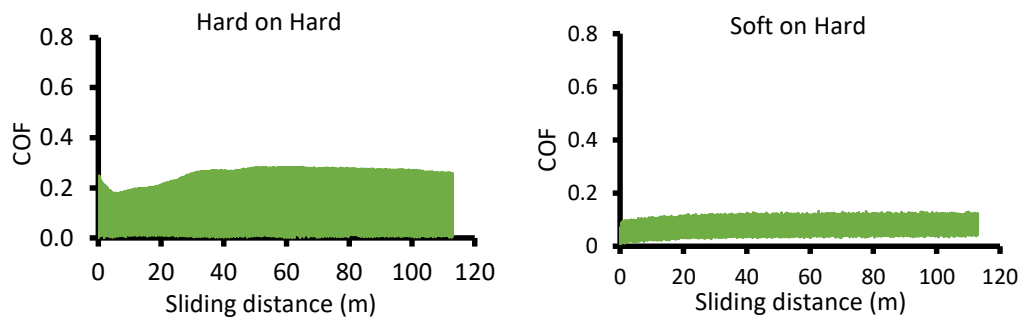


**Figure 5.78 COF of the treated Ti6Al4V alloy subjected to the post thermal treatment in hard on hard and soft on hard conditions**

In soft on hard condition the average COF is 0.08 (background noise around 0.03), while in hard on hard condition the average COF is higher, it is 0.13 (with background noise, around 0.07).

In Figures 5.79 the COF of the different materials (reference materials and treated ones) is compared.

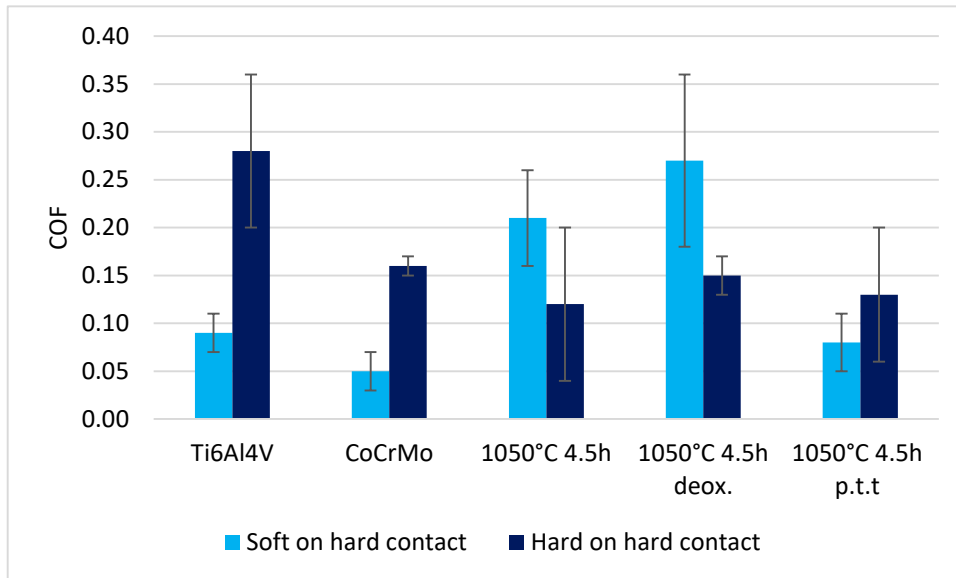
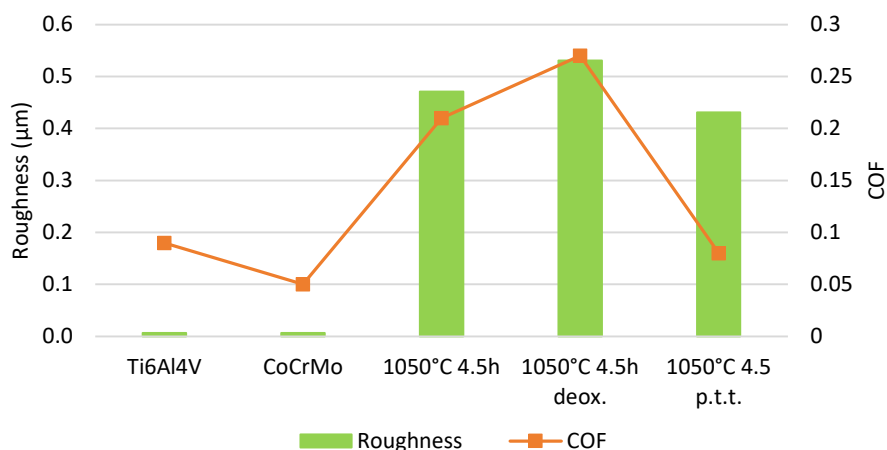


Figure 5.79 Comparison of COFs

Concerning the contact with a UHMWPE counterpart (soft on hard), the untreated Ti6Al4V alloy has a high COF (0.09), as expected because of its low tribological properties, while the CoCrMo has a significantly lower value (0.05) that can be considered as a reference because it corresponds to the majority of the currently used joints. The purpose of this research is to obtain such a value on a material with much higher biocompatibility, as the Ti base alloys are, in order to reduce any risk of toxicity or even to get a lower value in order to enlarge the life of implants, too.

As regards the treated Ti6Al4V alloy, it is of interest to observe that we obtained 3 different values: 0.08 (post thermal treatment), 0.21 (no pre/post-treatment) and 0.27 (deoxidation pre-treatment). We have to consider that we are in the case of a very hard surface (ceramic) in contact with a soft one (UHMWPE); this means that roughness can strongly influence the measured COF and actually it was not possible to optimize it in the present treated samples, as previously explained. So, it was checked if the observed difference in COFs could be related to roughness of the treated disks.

The values of roughness and COF are shown in Figure 5.80.



**Figure 5.80 Average roughness and COF of the disk of the treated samples in soft on hard contact before the test**

As first, roughness of the untreated Ti6Al4V disk is, as expected very low, such as that of CoCr alloy, while it is significantly higher in the case of the treated disks. It must be underlined that all the treated disks have almost the same roughness, so differences in COF among the treated samples cannot be ascribed to this parameter. Other comments about roughness of the pins and disks after the tests will be reported later.

In conclusion, roughness of the treated disks cannot explain the different COF registered on the treated alloys. The difference in the outermost layer of the treated disks is limited to the ratio between the amount of TiB<sub>2</sub>, that is reduced in case of the sample subjected to the post treatment, and of TiB, that is increased by the post-treatment. At this stage, it can be supposed that this compound has a lower COF than the untreated Ti6Al4V. It is interesting to note that this reduction occurs even if roughness of the treated disk with post-treatment was significantly higher than that of the untreated one: it can be speculated that it could be still reduced by optimization of surface polishing. Actually, it was decided to not go much more through this topic within this thesis, but it could worth to explore it much more and details in further works.

When the materials are tested against themselves, the untreated Ti6Al4V alloy is the one with the highest COF (0.28) while the treated Ti6Al4V alloys have COFs closed to the one of CoCrMo alloy (0.16 CoCrMo alloy, 0.12 treated Ti6Al4V alloy without any pre/post treatment, 0.15 treated Ti6Al4V alloy with pre-treatment of deoxidation and 0.13 treated Ti6Al4V alloy subjected to the post thermal treatment).

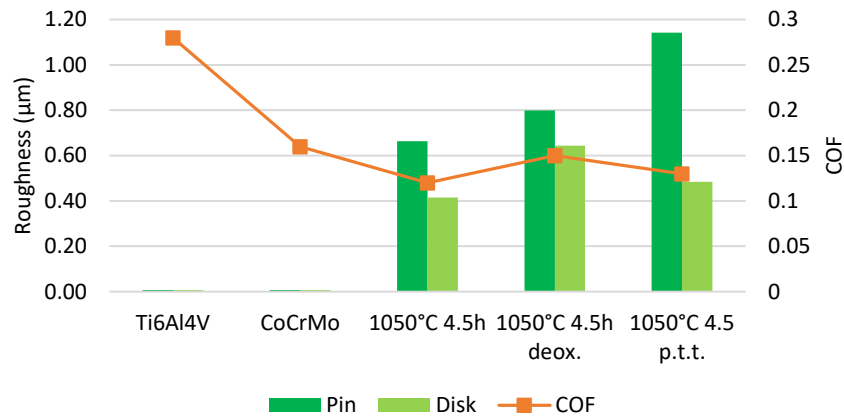


**Figure 5.81** Average roughness and COF of the pin and disk of the treated samples in hard on hard contact before the test

The untreated Ti6Al4V alloy and the CoCrMo alloy have very low roughness while the treated samples have higher roughness values with significant difference according to the different treatments (Figure 5.81). Nevertheless, the treated samples and the CoCrMo alloy sample have similar COFs, while the one of the untreated Ti6Al4V alloy is greater. The COF of the treated samples is much more dependent on the surface chemical composition/structure and hardness than on roughness. Again, it can be speculated that COF could be even more reduced by optimization of surface polishing. Actually, as before mentioned it was decided to not go much more through this topic within this thesis, but it could worth to explore it much more and details in further works.

## Wear resistance

The wear resistance was evaluated by means of the linear wear tests. Figure 5.82 shows the linear wear of the untreated Ti6Al4V alloy in hard on hard and soft on hard conditions.

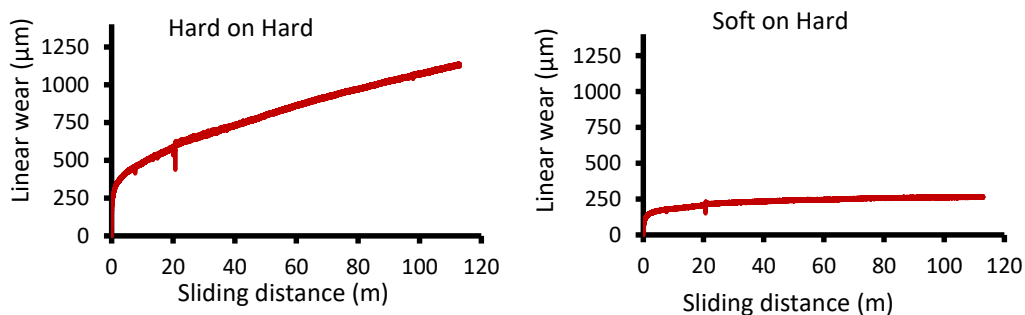


**Figure 5.82** Linear wear of the untreated Ti6Al4V alloy in hard on hard and soft on hard conditions

The linear wear rate of the untreated Ti6Al4V alloy in soft on hard condition increases slightly along the test. The average linear wear results to be around 200 µm.

In hard on hard condition, the linear wear goes on fast, increasing up to the end of the test, with a final value greater than 1000 µm.

As regards the CoCrMo alloy, a better tribological behaviour than the Ti6Al4V is visible in Figure 5.83 with a lower wear rate.

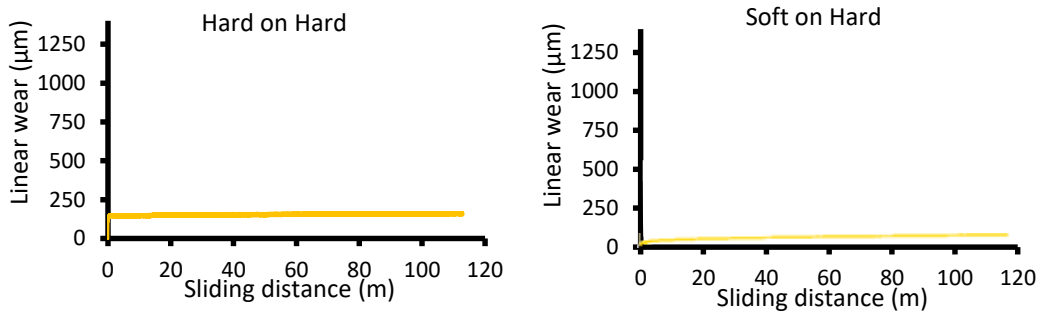


**Figure 5.83** Linear wear of the CoCrMo alloy in hard on hard and soft on hard conditions

In soft on hard condition, the CoCrMo alloy has a linear wear rate lower than  $100 \mu\text{m}$  (with a low background noise) while in hard on hard condition the average linear wear is about  $150 \mu\text{m}$ .

In soft on hard contact, the treated Ti6Al4V alloy without any pre/post treatment has a linear wear of about  $200 \mu\text{m}$ , that slightly increases up to the end of the test. In hard on hard contact, the linear wear is higher, around  $650 \mu\text{m}$  and fast increases along the test, with a further increment around a sliding distance of  $100 \text{ m}$ , maybe due to a detachment of the coating (Figure 5.84).

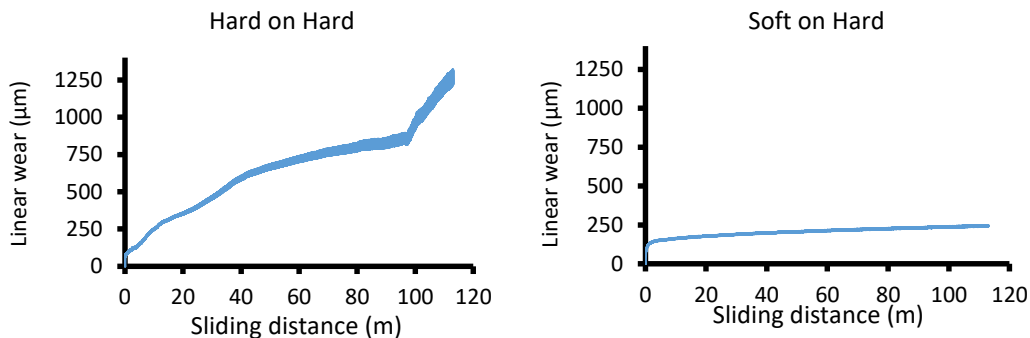


**Figure 5.84** Linear wear of the treated Ti6Al4V alloy without any pre/post treatment in hard on hard and soft on hard conditions

The trend of linear wear in the case of treated Ti6Al4V alloy with pre-treatment of deoxidation is shown in Figure 5.85.

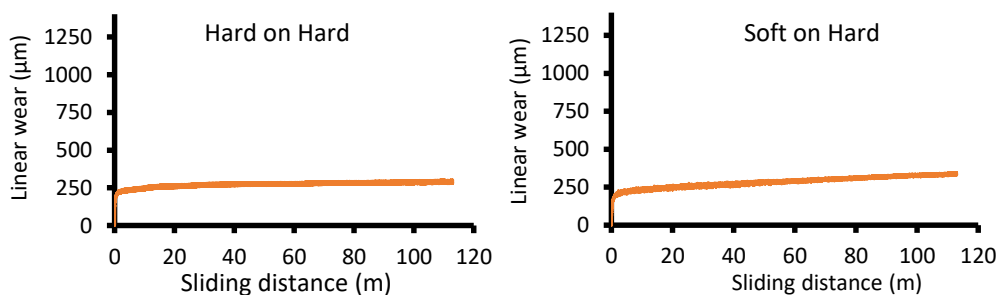


**Figure 5.85** Linear wear of the treated Ti6Al4V alloy with pre-treatment of deoxidation in hard on hard and soft on hard conditions

The average linear wear rate is  $280 \mu\text{m}$  in soft on hard contact and  $270 \mu\text{m}$  in hard on hard contact.



Figure 5.86 shows the trend of the linear wear rate of the treated Ti6Al4V alloy subjected to post thermal treatment.

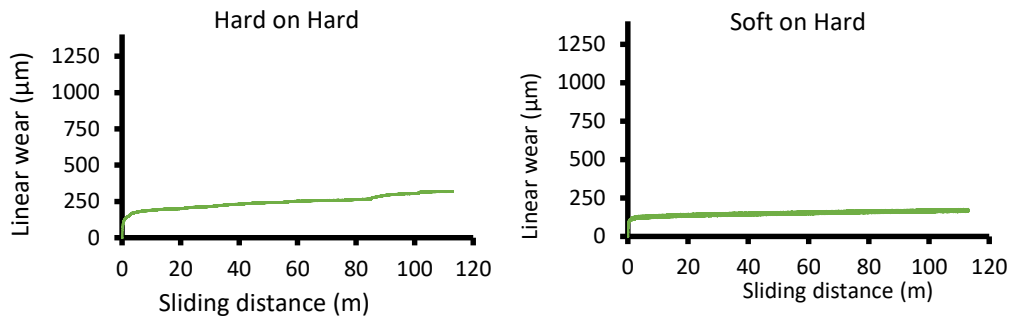


**Figure 5.86** Linear wear of the treated Ti6Al4V alloy subjected to the post thermal treatment in hard on hard and soft on hard conditions

In soft on hard condition, the average linear wear is about 150 µm, lower than the one in hard on hard condition, that is about 250 µm.

Comparing the samples and focusing on the linear wear in soft on hard condition (Figure 5.87), the contact of UHMWPE with CoCrMo alloy gives the lowest wear rate (as expected), while the untreated Ti6Al4V alloy corresponds to a quite higher value. As already underlined in the paragraph related to COF, it is of interest that the treated Ti6Al4V with post-treatment induces a lower wear rate than the untreated Ti6Al4V even if a significantly higher roughness value of the disk.

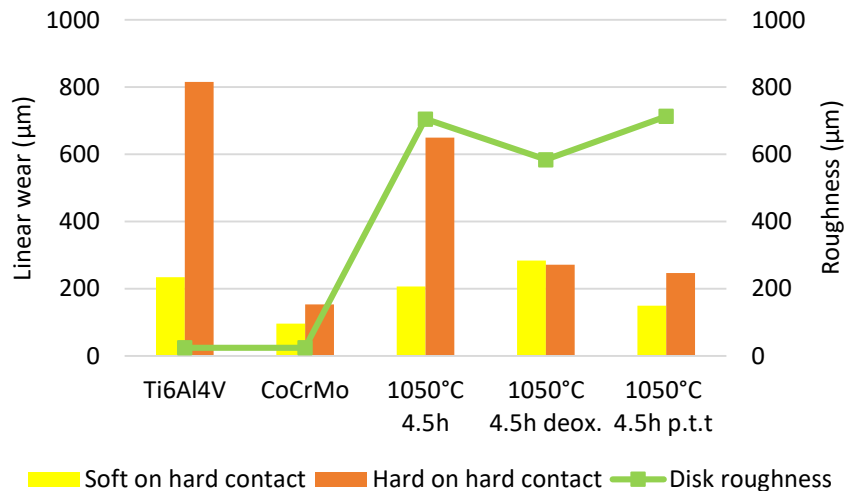


**Figure 5.87** Comparison of linear wear rates

In hard on hard contact, the highest and lowest linear wear rates are respectively the ones of the untreated Ti6Al4V alloy and CoCrMo alloy. The treated Ti6Al4V alloy with no pre-treatment has a consistent linear wear, while the treated Ti6Al4V alloys with pre or post-treatment have a lower linear wear rate, more similar to the one of the CoCrMo alloy. At the moment, no direct correlation was established between wear resistance and presence/absence of pre/post-treatments, considering that imperfect planarity of the pin of the treated Ti6Al4V alloy without any pre/post treatment could affected the measurement.

## Wear mechanisms

Considering the untreated Ti6Al4V alloy samples, both in soft on hard and hard on hard conditions, the surfaces are visibly damaged, as it is possible to observe in Figure 5.88. The 8 figure of the test track is well evident on both the disks surfaces, less evident signs are on the UHMWPE surface, while well visible are the ones on the surface of the metallic pin.

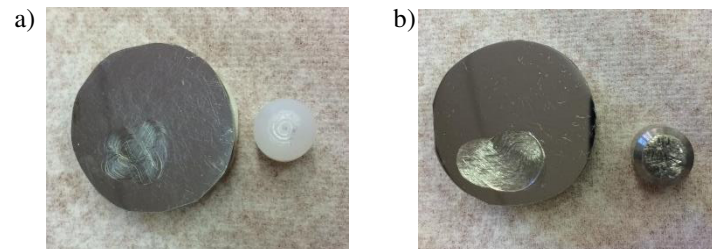


**Figure 5.88** Pins and disks of a) soft on hard and b) hard on hard test of the untreated Ti6Al4V alloy

Optical micrographs and EDS analyses allow to better observe and evaluate the surfaces damage. Figure 5.89 shows the optical images of the surfaces before and after the test in order to evidence how the surfaces are changed.

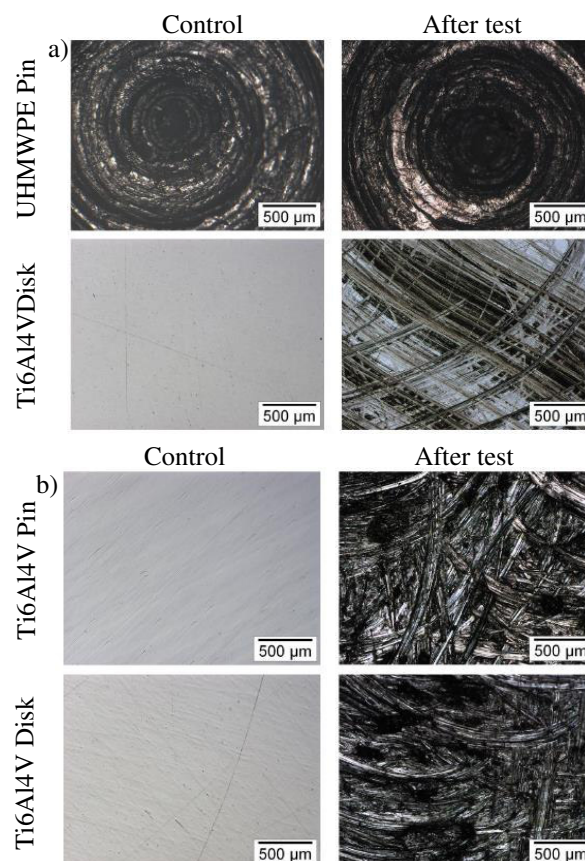


**Figure 5.89** Optical micrographs of the pins and disks surfaces in a) soft on hard and b) hard on hard contact of the untreated Ti6Al4V alloy

In Figure 5.89a the surface of the UHMWPE pin before the test shows visibly working lines: after the test, the working lines are still observable, but they are a bit

warped, that is a sign of wear of the UHMWPE surface. Wear and damage of the UHMWPE can be better observed by means of SEM images (Figure 5.90). Moreover, the EDS analysis on the polymeric surface highlights the presence of Ti and Al, indication of material transfer from the disk surface to the pin one and thus it is an evidence of an adhesion and third body wear mechanism (Figure 5.90).

Element	Atomic %
C	94.69
Ti	0.21
Al	0.02
Contaminants	5.09

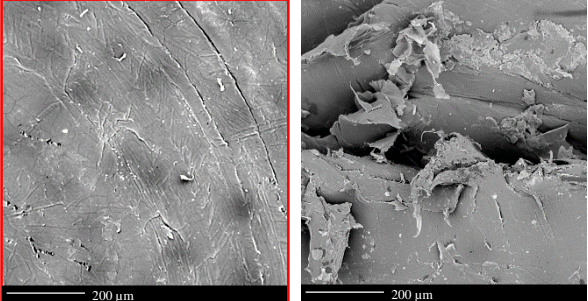


**Figure 5.90** SEM images and EDS analyses of the UHMWPE pin surface tested against the untreated Ti6Al4V alloy disk

It is very interesting to observe that the Ti6Al4V disk, used for the soft on hard test, has a surface very damaged after the test. Evident scratch signs are visible on the disk surface, due to an adhesion and third body mechanism of wear.

In the case of hard on hard contact (Figure 5.89), both the metallic surfaces are severely damaged.

Wear mechanisms and rate of the surfaces are confirmed by the variation of weight of the samples registered before and after the test. The values are reported in Table 5.10.

**Table 5.10** Weight of the pins and disks before and after the wear tests of the untreated Ti6Al4V alloy

Contact	Sample	$\Delta$ weight (mg)
Soft on Hard	Pin	-0.2±0.1
	Disk	-23.8±0.1
Hard on Hard	Pin	-43.2±0.1
	Disk	-58.4±0.1

A loss of material is evident on all the surfaces, this suggests that a reciprocal adhesive mechanism of wear occurs, with the formation and release of debris eventually acting as third body (as evident in the case of UHMWPE). The weight loss is higher in the case of the pin and disk in hard on hard contact and the data agree with the ones about the wear rate, in fact it is greater in the hard on hard contact.

In the case of CoCrMo alloy, there is a lower wear of the surfaces both in soft on hard and hard on hard conditions, as can be observed in Figures 5.91 and 5.92.

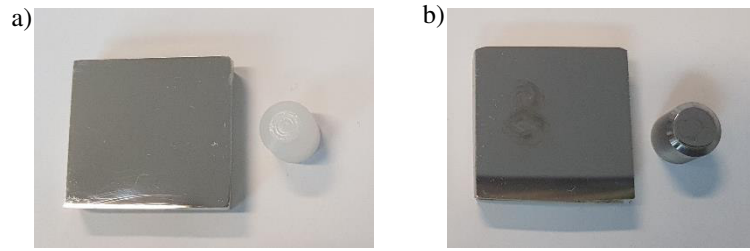


**Figure 5.91** Pins and disks of a) soft on hard and b) hard on hard test of the CoCrMo alloy

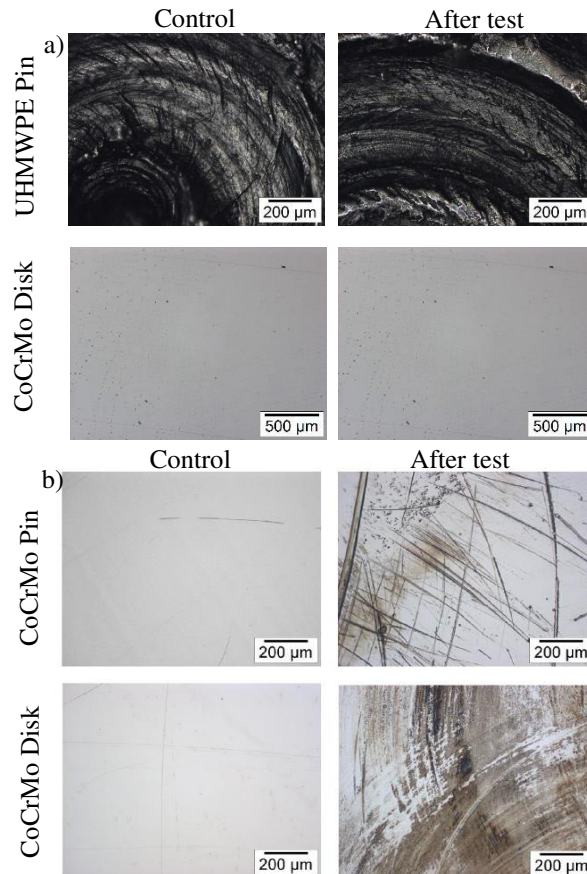


**Figure 5.92** Optical micrographs of the pins and disks surfaces in a) soft on hard and b) hard on hard contact of the CoCrMo alloy

Both visually and at the optical microscope, it is possible to see that the surface of the CoCrMo alloy disk does not present any damage in the soft on hard contact (Figures 5.91a and 5.92a). Also the surface of the UHMWPE pin has not evident damages, after the test the working lines are still well visible.

Even if no evident damage of the surfaces can be observed, EDS analysis detected traces of the elements of the CoCrMo alloy on the polymeric surface. Thus also in this case, adhesive wear occurs even if highly reduced (Figure 5.93).

Element	Atomic %
C	81.50
O	14.86
Cr	3.65

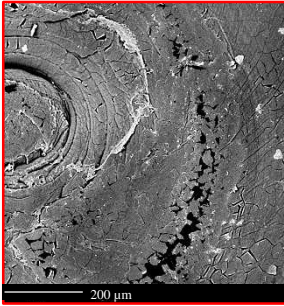


**Figure 5.93 SEM images and EDS analyses of the UHMWPE pin surface tested against the CoCrMo alloy disk**

Considering the surfaces of the pin and disk tested in hard on hard contact, instead, the 8 figure of the track is evident on the surface of the disk as well as scratch signs, that are both on the disk and pin surfaces. The pin surface is not completely damaged, the wear track is limited to a small area. This may be due to a surface not perfectly flat and thus to a not perfectly planarity of the surfaces.

Wear of the surfaces is confirmed by a change in weight of the pins and disks. Table 5.11 reports the values of the variation of weight.

**Table 5.11 Weight of the pins and disks before and after the wear tests of the CoCrMo alloy**

Contact	Sample	$\Delta$ weight (mg)
Soft on Hard	Pin	0.0 $\pm$ 0.1
	Disk	1.4 $\pm$ 0.1
Hard on Hard	Pin	-0.4 $\pm$ 0.1
	Disk	-0.2 $\pm$ 0.1

In soft on hard condition, weight of the pin does not change, while the disk gains weight, in this case the main mechanism of wear that occurs is the adhesive one. In hard on hard condition, instead, both the surfaces loss weight for the adhesive wear and formation of debris.

Looking at the pictures of the UHMWPE pin and disk of the treated Ti6Al4V alloy without any pre/post treatment (Figure 5.93), in soft on hard condition, no evident damage of the surfaces is observed, while it is needed the use of optical microscopy (Figure 5.94) to show that the surface of the UHMWPE is worn out. The working lines are polished due to the rubbing between the two surfaces. The disk surface (with the boride coating), instead, does not show any visible damage after the test.

In hard on hard condition, wear of both the pin and disk surface is evident. On the disk surface, it is possible to see the figure 8 of the wear track, while the pin surface has clean cut-wear signs mainly on half of the surface (Figures 5.94b and 5.95b). This means that the pin surface was not perfectly flat and there was not perfect planarity between the two surfaces. The absence of a perfect planarity can have caused an increase of wear of the surfaces and the detachment of the coating.

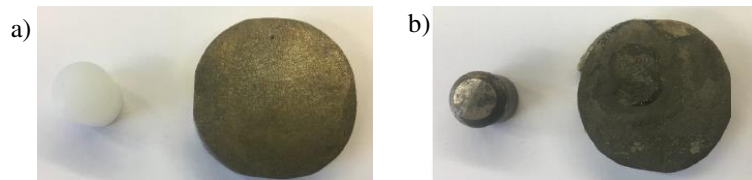


**Figure 5.94 Pins and disks of a) soft on hard and b) hard on hard test of the treated Ti6Al4V alloy without any pre/post treatment**

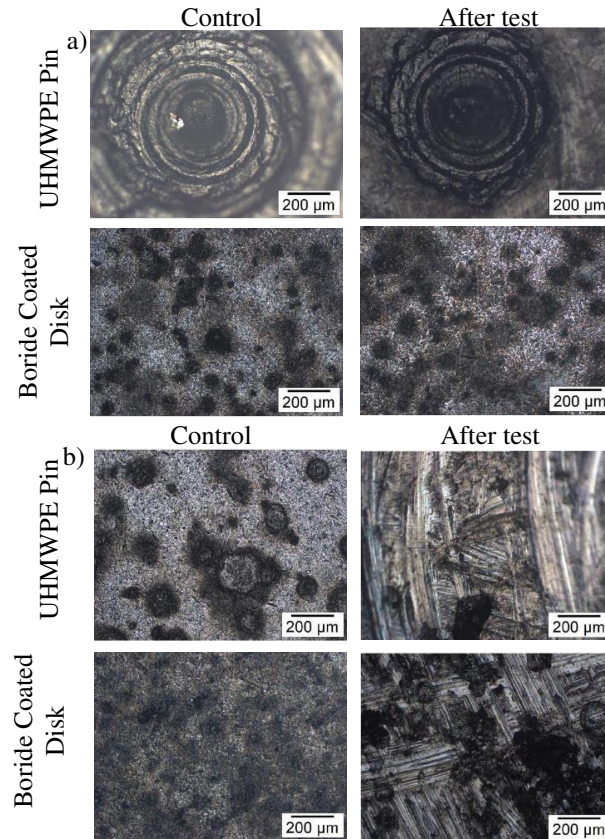


**Figure 5.95 Optical micrographs of the pins and disks surfaces in a) soft on hard and b) hard on hard contact of the treated Ti6Al4V alloy without any pre/post treatment**

SEM observation and EDS analyses (Figure 5.96) allow to better understand wear of the surfaces. Considering the soft on hard condition, the UHMWPE pin has polished working line after the test and on the surface there are traces of boron, due to a material transfer from the disk to the pin. While a EDS linear analysis on the surface of the disk confirms that the coating is still present and there is not any deep sign of wear track.

EDS analysis performed on the pin and disk tested in hard on hard condition, instead, shows that on the wear area of the pin surface the coating is removed (atomic % of B closed to zero), while the coating is still present on the surface of the disk, the amount of boron, however, is reduced within the wear track.

Soft on hard

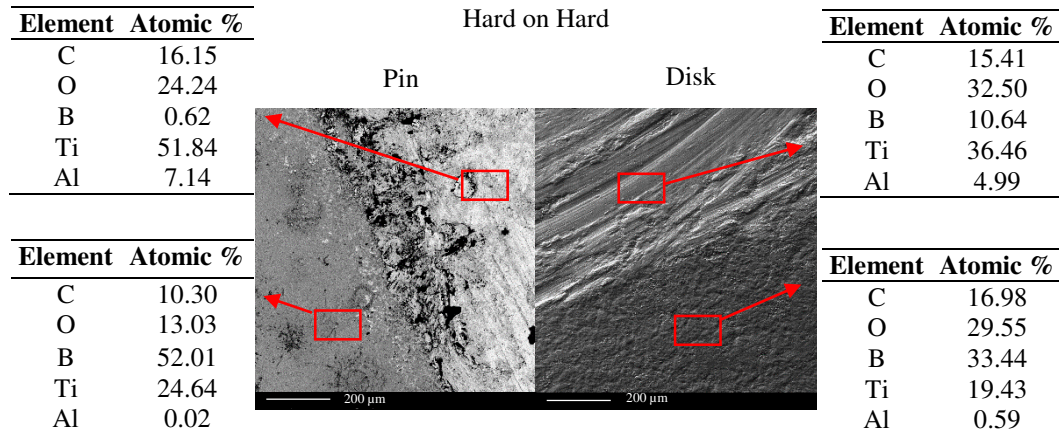
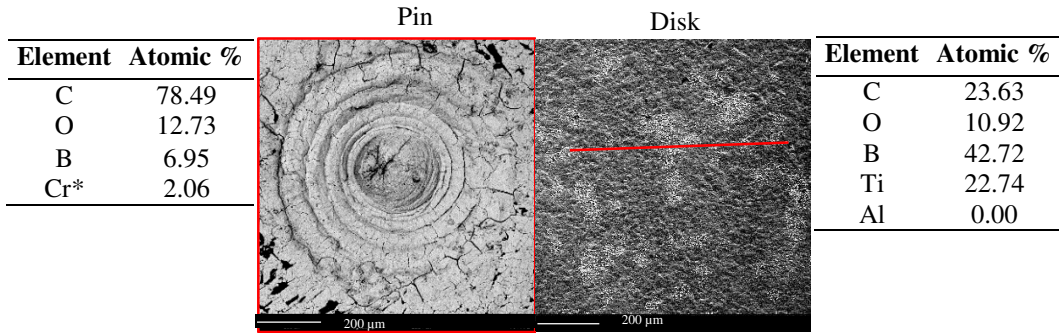


Figure 5.96 SEM images and EDS analysis of the pins and disks surfaces in a) soft on hard condition and b) hard on hard condition of the treated Ti6Al4V alloy without any pre/post treatment

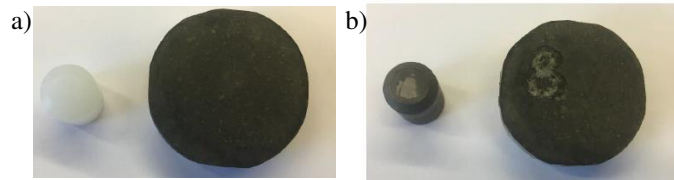
\*Cr is due to the metallic coating performed on the pin to make it conductive for the SEM observation

Table 5.12 Weight of the pins and disks before and after the wear tests of the treated Ti6Al4V alloy without any pre/post treatment

Contact	Sample	Δweight (mg)
Soft on Hard	Pin	-1.0±0.1
	Disk	0.2±0.1
Hard on Hard	Pin	-10.3±0.1
	Disk	-10.4±0.1

The change of weight, reported in Table 5.12, agrees with the previous data. In soft on hard contact, the UHMWPE pin losses weight, while the disk increases a little bit its weight. This suggests that the mechanism of wear is a combination of abrasive and adhesive wear: the pin is worn out and traces of UHMWPE joint to the disk surface. In hard on hard contact, the main wear mechanism is the adhesive one, both the pin and disk loss weight, thus on both surface part of the coating is removed. As highlight by the EDS analysis, the coating is removed on pin surface, while on the disk surface it is still present, but it has been scratched.

Observing the pictures and the optical microscopy images of the treated Ti6Al4V alloy with pre-treatment of deoxidation (Figure 5.97 and 5.98), it is possible to see that, as in the previous case, there is not evident damage of the surfaces in the soft on hard condition, while it is evident wear of the surfaces in hard on hard condition.



**Figure 5.97 Pins and disks of a) soft on hard and b) hard on hard test of the treated Ti6Al4V alloy with pre-treatment of deoxidation**

As before, in soft on hard contact the surface of the pin results to be polished while the disk surface does not show any wear sign. In hard on hard contact, instead, both surfaces are worn out. In particular, the pin surface has scratch signs.

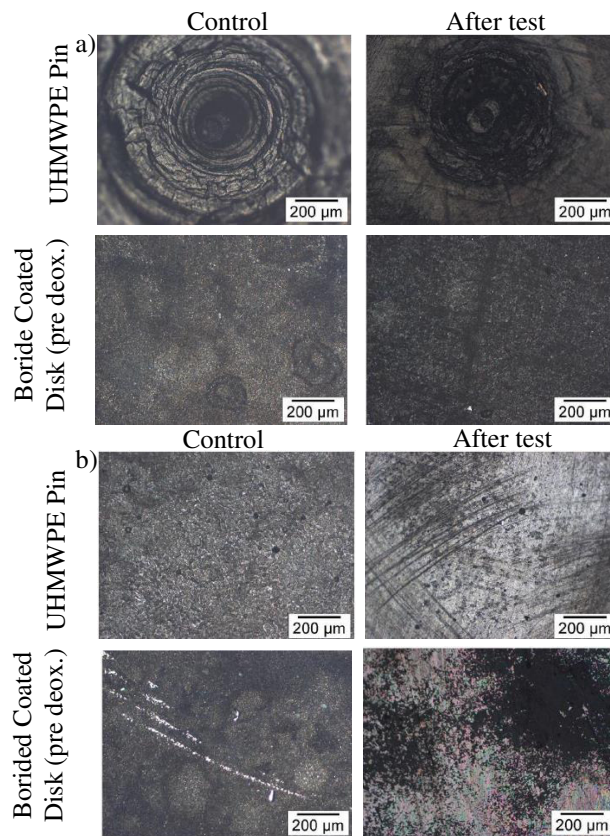


**Figure 5.98 Optical micrographs of the pins and disks surfaces in a) soft on hard and b) hard on hard contact**

EDS analyses (Figure 5.99) and evaluation of the change in weight (Table 5.13) help to understand the mechanism of wear. In soft on hard condition the pin loses weight while the disk gains weight. This means that there is a transfer of material from the pin to the disk due to an adhesive wear mechanism, with a greater wear of





**Table 5.13 Weight of the pins and disks before and after the wear tests of the treated Ti6Al4V alloy with pre-treatment of deoxidation**

Contact	Sample	$\Delta$ weight (mg)
Soft on Hard	Pin	-1.3±0.1
	Disk	1.9±0.1
Hard on Hard	Pin	0.8±0.1
	Disk	4.2±0.1

The pictures and the optical microscopy images of the pins and disks of the treated Ti6Al4V alloy subjected to the post thermal treatment are shown in Figure 5.100 and 5.101.

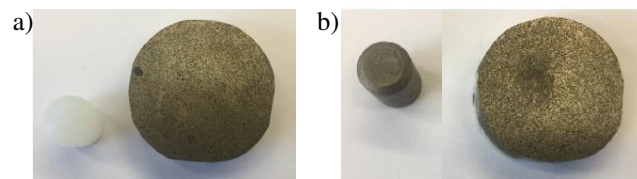


**Figure 5.100 Pins and disks of a) soft on hard and b) hard on hard test of the treated Ti6Al4V alloy subjected to post thermal treatment**

In soft on hard contact, the surfaces of the pin and disk do not show any surface damage at a visual inspection. In the case of hard on hard contact, differently from the previous cases, a well-defined wear track with the shape of a figure 8 is not present, it is visible only a dark spot in correspondence of the treated area.

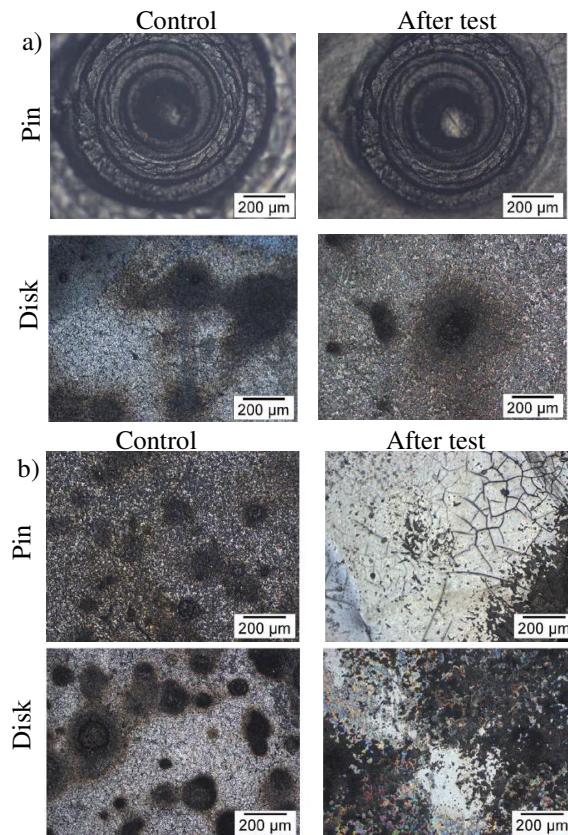


**Figure 5.101 Optical micrographs of the pins and disks surfaces in a) soft on hard and b) hard on hard contact of the treated Ti6Al4V alloy subjected to post thermal treatment**

The optical microscopy images of the pin and disk tested in soft on hard condition do not show any evident damage of the surfaces, except for smoothing of the pin surface. While in the case of hard on hard contact, the surfaces undergo to slight wear, but there is not any scratch sign, the surfaces result only smoothed by the reciprocal rubbing.

Also the SEM observations and EDS analyses (Figure 5.102) show that in soft on hard contact the surfaces do not have evident signs of wear. The presence of boron traces on the UHMWPE surface points out a slight adhesive wear, with transfer of material from the disk to the pin. The disk surface, instead, does not seem to be significantly changed after the test. In hard on hard contact, the main mechanism of wear is the adhesive one. Both the surfaces do not have scratch signs, the disk surface on the wear track is smoother than the area outside the wear track. This is due to the adhesive wear and the transfer of material from the pin to the disk.

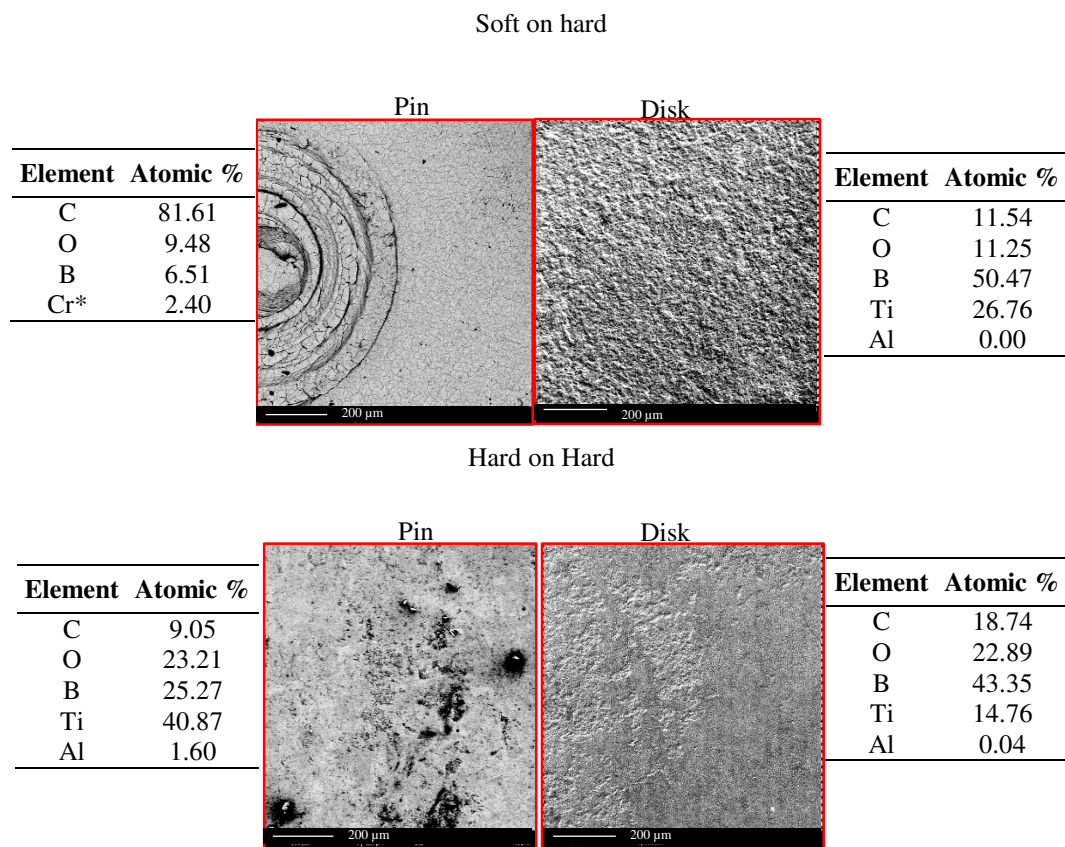


**Figure 5.102** SEM images and EDS analysis of the pins and disks surfaces in a) soft on hard condition and b) hard on hard condition of the Ti6Al4V alloy subjected to the post thermal treatment

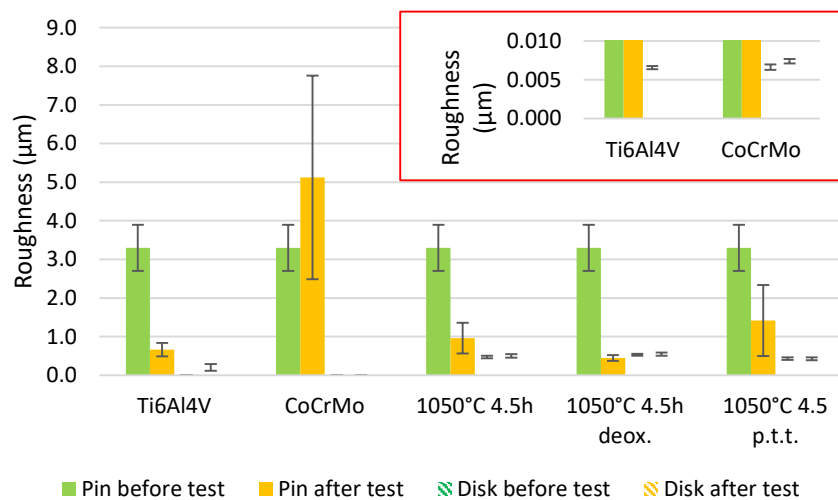
\*Cr is due to the metallic coating performed on the pin to make it conductive for the SEM observation

**Table 5.14 Weight of the pins and disks before and after the wear test of a treated Ti6Al4V alloy with post treatment**

Contact	Sample	$\Delta$ weight (mg)
Soft on Hard	Pin	-0.6±0.1
	Disk	0.4±0.1
Hard on Hard	Pin	1.0±0.1
	Disk	3.6±0.1

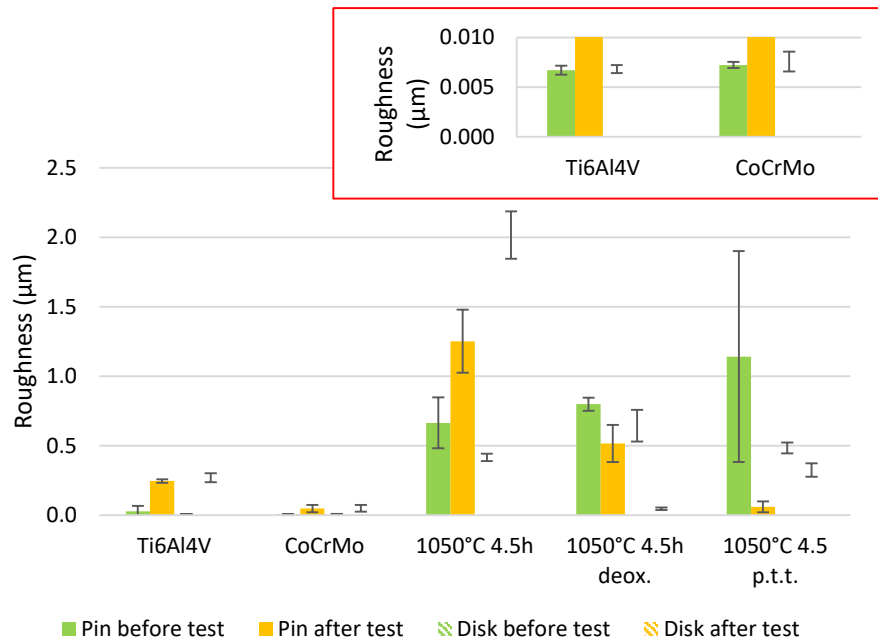
Table 5.14 reports the variation of weight. In soft on hard condition the pin losses weight while the disk gains weight. This confirms that even if wear of the surfaces is not visible, there is transfer of material from the pin to the disk. In hard on hard contact, instead, both the pin and the disk gain weight and this suggests that the adhesive phenomenon is reciprocal between pin and disk.

Figure 5.103 and 5.104 show the roughness values of the pins and disks surfaces before and after the wear test.



**Figure 5.103 Roughness of pins and disks surface in soft on hard contact**

As regards the soft on hard contact (Figure 5.103), in the case of UHMWPE vs untreated Ti6Al4V alloy, roughness of the pin decreases, while roughness of the disk increases during the test. In this case, the surface of the Ti6Al4V alloy disk is scratched, even if harder, by the softer pin of the UHMWPE, that is polished, due to adhesive wear with third body effect, as described in Chapter 2. As concern the CoCrMo alloy, there is a considerable increase of the roughness value of the pin, while roughness of the disk does not change significantly. This means that there is adhesion from the pin surface to the disk one. Looking at the data of the treated Ti6Al4V alloy, it is possible to observe that in all the three cases roughness of the UHMWPE decreases, while roughness of the disk surface is stable. In these cases, the surfaces of the pin are smoothed while the surface of the disk is not damaged. In these cases, the main wear mechanism is an abrasive polishing process of the UHMWPE pin.



**Figure 5.104 Roughness of pins and disks surface in hard on hard contact**

Considering the hard on hard contact, it is possible to see that as regards the untreated Ti6Al4V alloy, the treated Ti6Al4V alloy without any pre/post treatment and the CoCrMo alloy, the roughness values of both the pin and disk increase considerably after the test (Figure 5.104). This is due to adhesive wear, with detachment of materials that goes to abrade the counterpart in a reciprocal way. The treated Ti6Al4V alloy with pre or post treatment show a reduction of surfaces roughness after the test: reciprocal rubbing occurs, causing smoothing and polishing of the surfaces.

### ICP analysis and ion release evaluation

The fetal serum bovine used as lubricant in the wear test of the untreated and treated Ti6Al4V alloys was analysed by means of ICP analyses to evaluate the amount of ions release.

It is known that high concentrations of metallic ions in the blood are dangerous and toxic for the body, nevertheless specific threshold for these ions have not been fixed. In literature, as reported in Chapter 1, it is possible to find a lot of cases of diseases related to the release and the high concentration of metallic ions, but the toxic concentration and the effects must be correlated to the age, the gender, the health state and the physical activity rate of the patient.

The amount of released B, Ti, Al and V is reported in Figure 5.105.

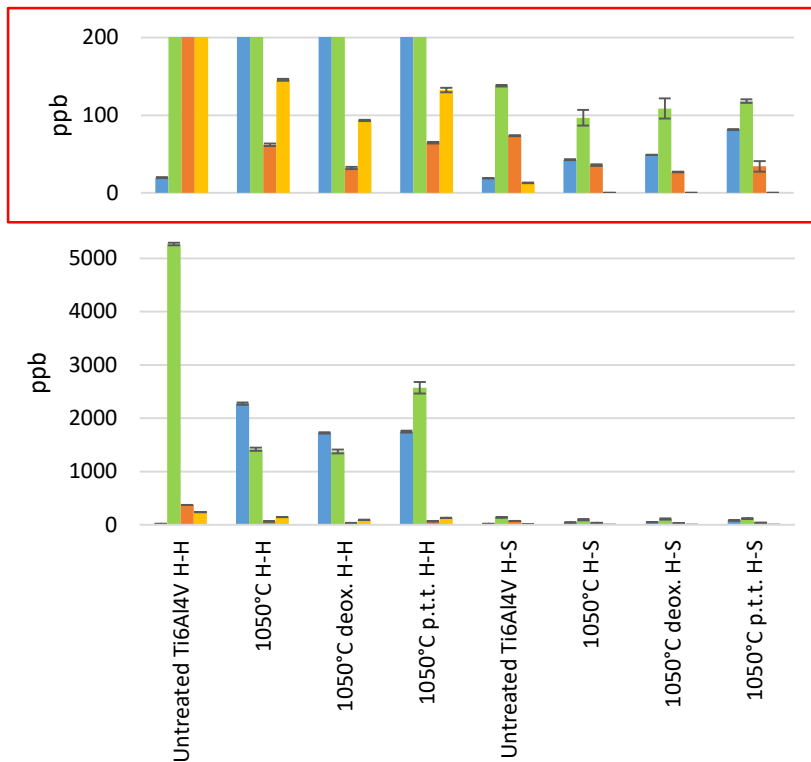


**Figure 5.105 Metallic ion release of the untreated Ti6Al4V alloy and the three cases of treated Ti6Al4V alloy tested under hard on hard and soft on hard wear condition**

Release of ions is due to wear of the surfaces during the test. As expected, all the samples show a greater ion release in hard on hard condition than in soft on hard condition. This agrees with data about the linear wear rate, where wear is higher in the hard on hard contact than in soft on hard contact.

Comparing the three treated Ti6Al4V alloys with the untreated one (hard on hard condition), it is possible to see that in all of them the amount of released Ti, Al and V ions is lower than the ones of the untreated Ti6Al4V alloy. In these cases, also B is released: the release of B ions is higher than that of Ti ions in the case of the treated Ti6Al4V alloy without any pre/post treatment and of the pre-treated alloy, while it is the opposite in the case of the treated Ti6Al4V alloy with post-treatment. The difference can be explained taking into account the XRD analyses, that show that the treated Ti6Al4V alloy without any pre/post treatment and that with pre-treatment have an external layer composed only of  $TiB_2$  while the treated Ti6Al4V alloy with post-treatment has an external layer that is a combination of  $TiB_2$  and TiB. Moreover, the amount of released V is greater than the one of Al. This can suggest a reorganisation of alloy elements on the surface during the B diffusion as well as it occurs in the case of surface oxidation of Ti6Al4V alloy substrate [13].

Focusing on the soft on hard condition, also in this case, the release of Ti, Al and V is lower for the treated samples than for the untreated one. The difference in this case is less evident because on all the samples wear is very low. For the same reason, the release of B by the treated samples is lower than in the soft on hard contact. Moreover, the release of B ions is lower than that of Ti ions in all the three treated alloys. This may be due to the fact that in soft on hard contact wear is limited

to the outermost layer of the surface with respect to hard on hard contact. Ti is very reactive in an oxygen-rich environment, thus the most external layer is composed of a very thin amorphous  $Ti_2O$  layer, that is removed as first. The treated samples, in addition, do not release V.

### 5.3.9 Fretting tests

#### Friction coefficients

Fretting tests were performed in order to verify behaviour of the treated surface in a condition close to cemented prostheses: friction at the interface between the metal (such as a stem of a hip prostheses) and the bone cement was simulated.

The condition was simulated by means of pin on plate test. Pins of AISI 316L, untreated Ti6Al4V and Ti6Al4V alloy treated at  $1050^{\circ}C$  for 4.5 h, without any pre/post treatment, were rubbed against plates of polymethyl methacrylate (PMMA). Cemented prostheses are mainly composed of an AISI 316L stem, thus in this case medical stainless steel was considered as reference material.

First of all, it was evaluated the COFs, that are reported in Figure 5.106 and 5.107. The first image corresponds to the data not elaborated, while the second to the data after application of median filter.

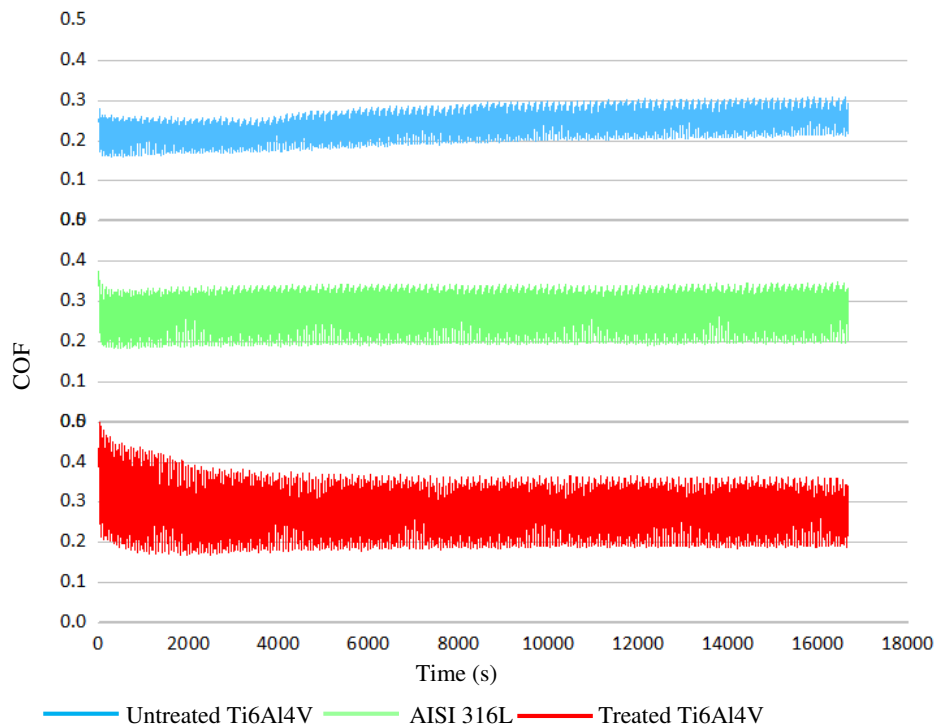


**Figure 5.106** COFs of the untreated Ti6Al4V alloy, AISI 316L and Ti6Al4V alloy without any pre/post treatment treated at  $1050^{\circ}C$  for 4.5 h

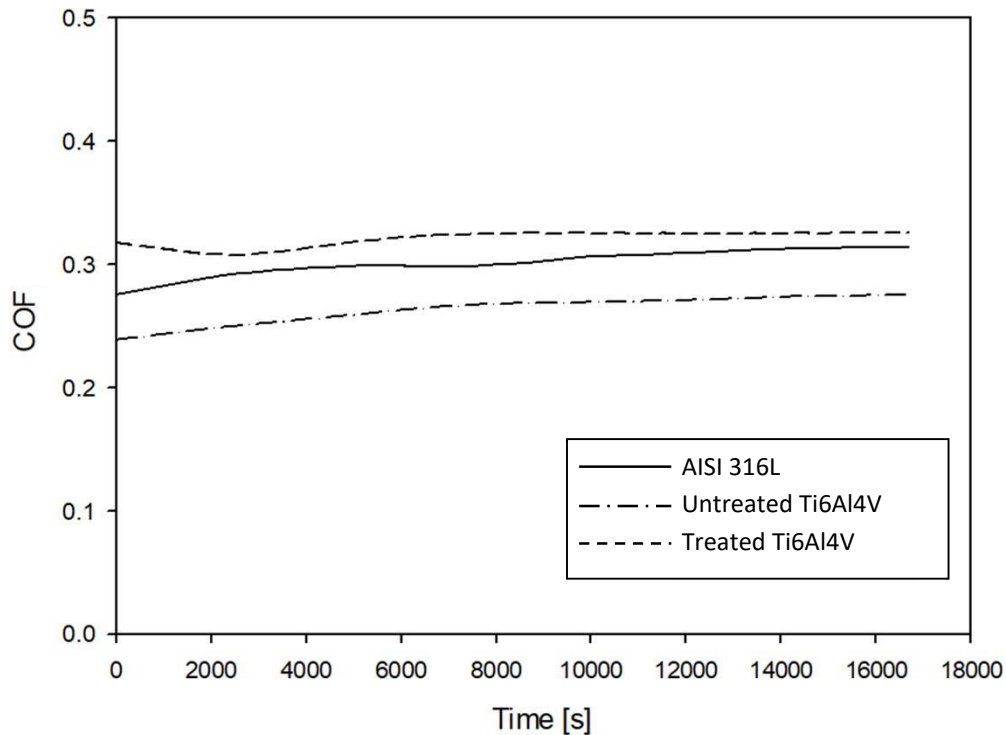


**Figure 5.107** COFs of the untreated Ti6Al4V alloy, AISI 316L and Ti6Al4V alloy without any pre/post treatment treated at 1050°C for 4.5 h after median filter

The untreated Ti6Al4V alloy, AISI 316L and treated Ti6Al4V alloy have respectively an average COF of  $0.24 \pm 0.04$ ,  $0.28 \pm 0.05$  and  $0.28 \pm 0.07$ , when tested against the PMMA.

Comparing the materials, it is possible to see that the untreated Ti6Al4V has the lowest COF, while the AISI 316L and treated Ti6Al4V have the same COF. The untreated Ti6Al4V is also the one with the lowest standard deviation, while the treated Ti6Al4V alloy has the highest standard deviation.

The variability of the data can be related to the wear mechanism. Looking at the trends of the COFs in Figure 5.107, it is possible to observe that the COFs of the untreated Ti6Al4V alloy and AISI 316L slightly increases along the test. This suggests an adhesive wear mechanism of the pins, that causes an increment of the surface roughness and thus of the COF, due to the worst fretting condition.

The COF of the treated Ti6Al4V alloy decreases at the beginning of the test and becomes stable around 6000 s. In this last case, it is possible to suppose an abrasive wear mechanism of the pin, where the asperities of the coating were polished and thus the surface becomes smoother and the COF decreases. The wear mechanism can be better understood in the following paragraph, observing the images of the surfaces. Differences of the COFs can be also related to different surface roughness of the pins. The average Ra values, collected on an area of  $9000 \times 200 \mu\text{m}$  before the tests, are reported in Table 5.15.



**Table 5.15 Average values of Ra for the cement plate and the AISI 316L, untreated and treated Ti6Al4V alloy pins before the fretting test**

Material	Cement	Untreated Ti6Al3V alloy	AISI 316L	Treated Ti6Al4V alloy
<b>Ra</b>	19.58 $\mu\text{m}$	0.78 $\mu\text{m}$	1.92 $\mu\text{m}$	2.56 $\mu\text{m}$

Table 5.15 shows that the untreated Ti6Al4V alloy pin has the lowest roughness, followed by the AISI 316L pin and the treated Ti6Al4V alloy pin. Comparing the average values of the COFs and roughness, it is possible to observe that the higher roughness is, the higher the COF (Figure 5.108).

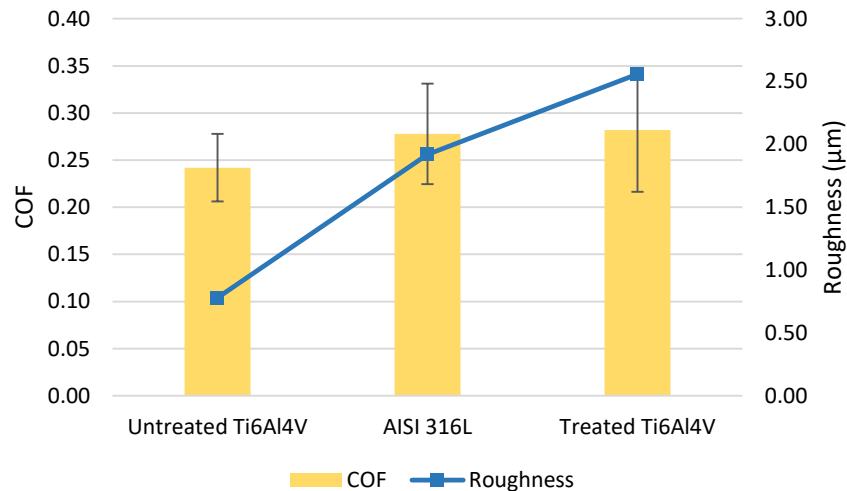


**Figure 5.108 Comparison between COFs and roughness of the untreated Ti6Al4V alloy, AISI 316L and Ti6Al4V alloy without any pre/post treatment treated at 1050°C**

This suggests a relevant correlation between the roughness values and the COF. If the treated metal does not induce wear of the cement, because of its roughness, a higher COF could limit the reciprocal movement between the implant and cement, otherwise the COF of the treated Ti6Al4V alloy can be reduced by decreasing surface roughness, if this can reduce cement wear.

## Wear mechanism

Figure 5.109 shows the optical micrographs of the surfaces of the untreated Ti6Al4V alloy pin and cemented plate after the fretting test.

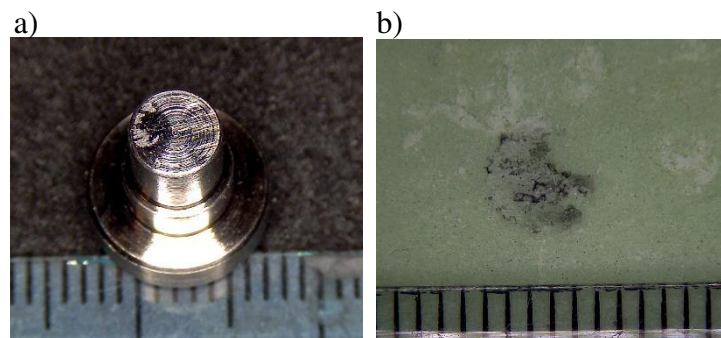


**Figure 5.109 Untreated Ti6Al4V alloy pin and PMMA plate**

Looking at the images, it is possible to observe material transfer from the pin to the plate (dark spots on the cement) on 2/3 of the contact area and material transfer from the plate to the pin on 1/3 of the contact area (dark area on the pin). An adhesive mechanism of wear with transfer of material from the pin to the plate and vice versa occurs in the case of the untreated Ti6Al4V alloy.

EDS analyses and SEM images (Figure 5.110) confirm that there is transfer of material from the pin to the plate and the opposite and thus an adhesive wear mechanism. Moreover, the surface of the cement plate results to be abraded, while the surface of the pin shows several grooves. This indicates that an abrasive wear mechanism overlaps the adhesive one, moreover the presence of the grooves suggests a third body abrasive wear mechanism, due to the wear debris. Nevertheless, the abrasion of the surface pin can also be due to zirconium particles, present into the cement as radio-opacifiers. The abrasion of the cement surface allows to the zirconium particles be exposed, as consequence they engrave the softer surface of the untreated Ti6Al4V alloy pin.

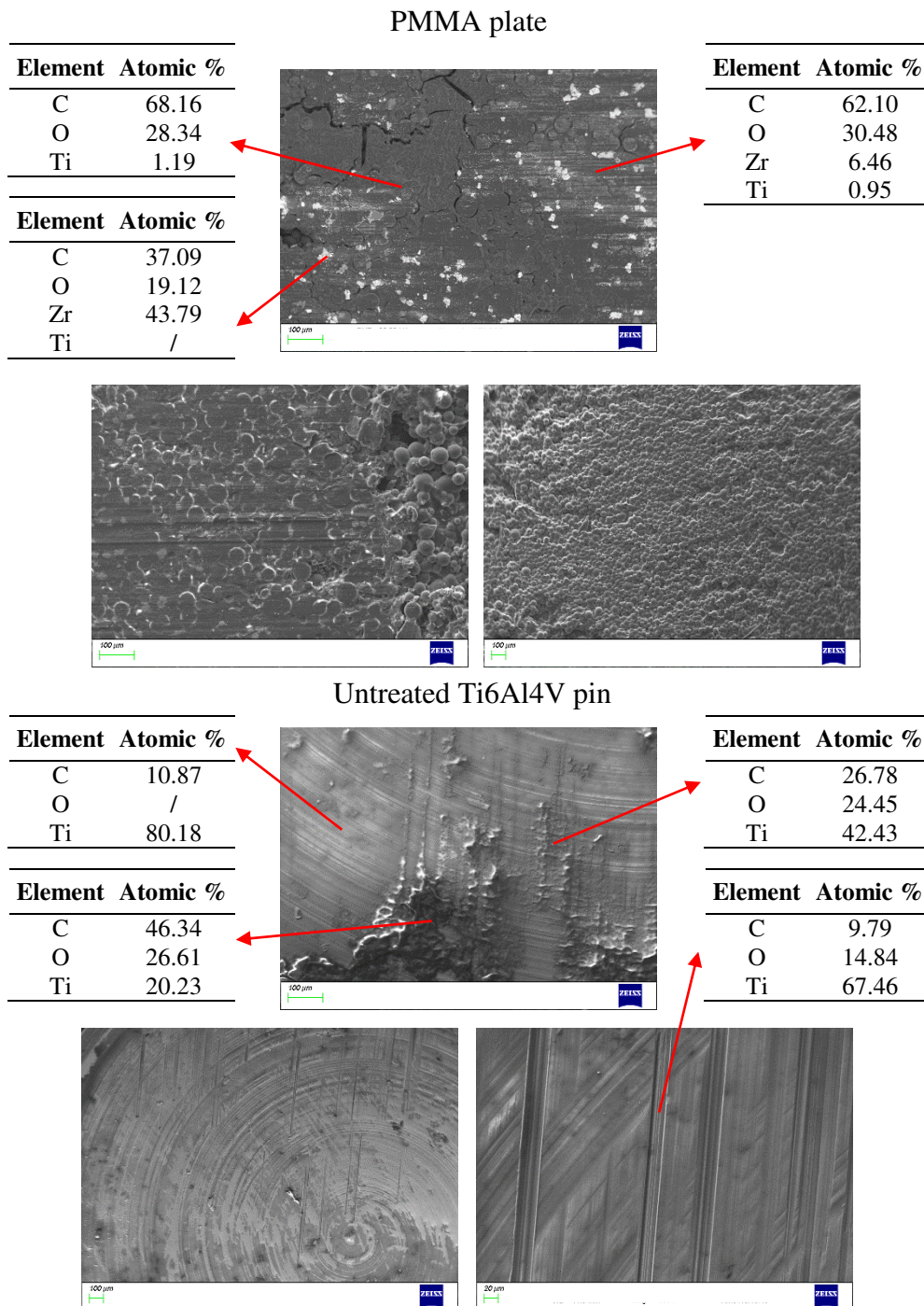


Figure 5.110 SEM images and EDS analyses of untreated Ti6Al4V pin and PMMA plate

The roughness and weight values of the cement plate and the untreated Ti6Al4V alloy pin are reported in Table 5.16. As it is possible to see, the variation of weight is not relevant, the slight increment of weight of the cement can be attributed to adsorption of the FBS solution used as lubricant. As regards roughness, instead, roughness of the cement surface increases due to the transfer of material from the pin, while roughness of the pin increases on some areas, while decreases in others, because of the wear process.

**Table 5.16 Average values of Ra and weight of the cement plate and the untreated Ti6Al4V alloy pins**

		Roughness ( $\mu\text{m}$ )	Weight (g)
PMMA plate	Before test	19.58	3.913
	After test	21.13	3.921
Untreated Ti6Al4V pin	Before test	0.78	1.834
	After test	0.91	1.837
		0.61	

Similar consideration can be done for the AISI 316L. Figure 5.111 shows the optical microscopy images of the plate and the pin.

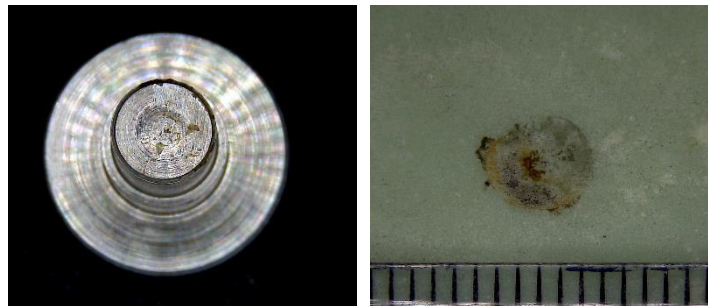


**Figure 5.111 AISI 316L pin and PMMA plate after the fretting test**

As before, there is transfer of material from the pin to the plate. The read spots correspond to ferrous particles detached from the pin surface and then oxidized.

Figure 5.112 reports the EDS analyses and the SEM images. They confirm the transfer of material from one surface to the others and that both surfaces are also subjected to abrasive wear, in fact scratches are visible on both surfaces. The surface of the pin has deeper grooves than the correspondent surface of the cement plate, as consequence of the abrasive action of the zirconium particles embedded into the cement. As in the case of the untreated Ti6Al4V alloy, the harder zirconium, engraves the softer AISI 316L.

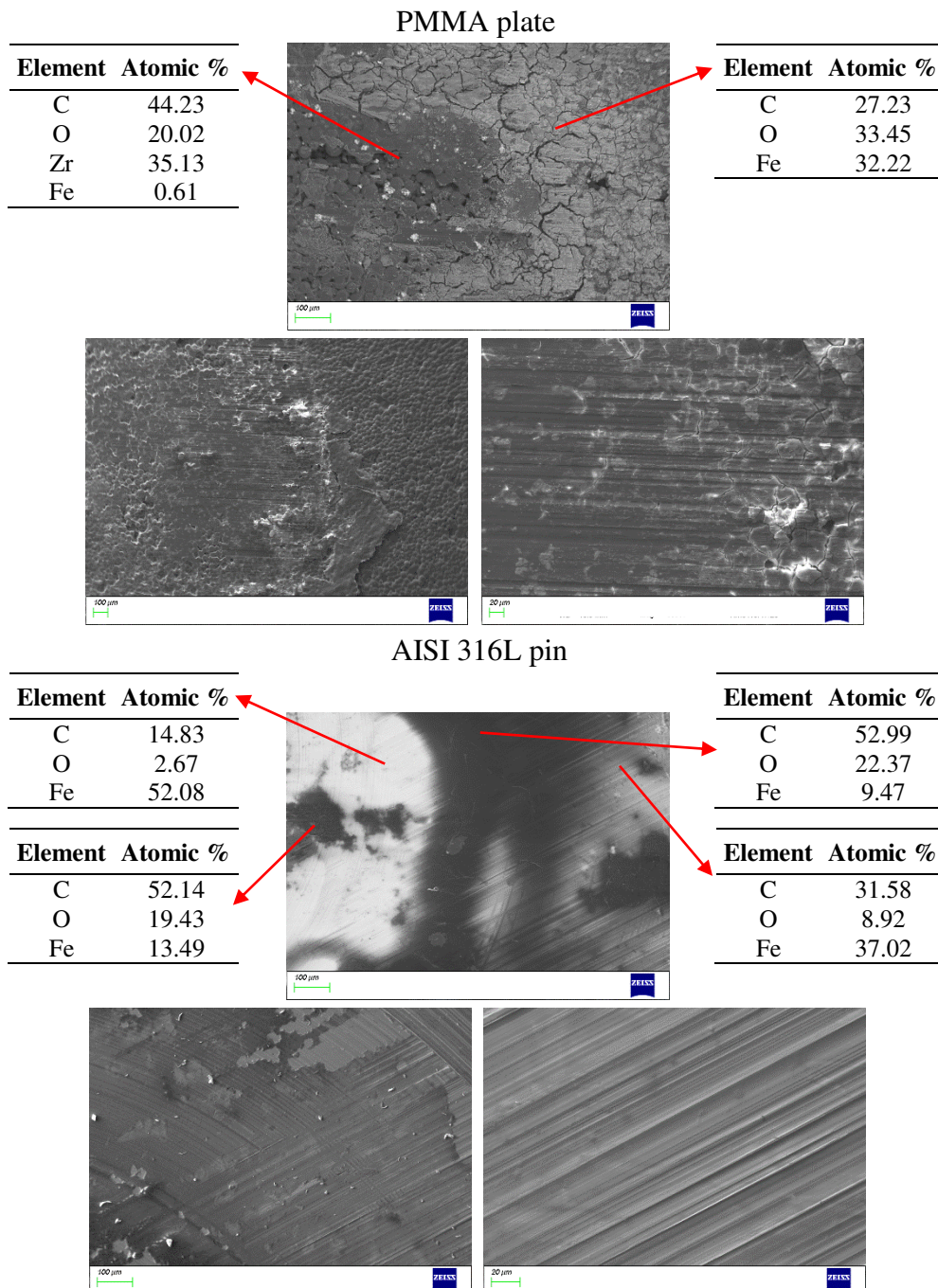


**Figure 5.112 SEM images and EDS analyses of AISI 316L pin and PMMA plate after the fretting test**

Looking at Table 5.17, it is possible to see that roughness of the cement surface decreases for a polishing abrasive process, while roughness of the pin increases. The increment of roughness is related to the adhesion of cement spots, detachment of metal spots (adhesive wear mechanism) and grooves (abrasive wear mechanism).

The change of weight is not relevant as in the case of untreated Ti6Al4V alloy.

**Table 5.17 Average values of Ra and weight of the cement plate and the AISI 316L pins**

		<b>Roughness (<math>\mu\text{m}</math>)</b>	<b>Weight (g)</b>
<b>PMMA plate</b>	<b>Before test</b>	19.58 $\mu\text{m}$	3.427
	<b>After test</b>	18.52 $\mu\text{m}$	3.442
<b>AISI 316L pin</b>	<b>Before test</b>	1.92 $\mu\text{m}$	4.033
	<b>After test</b>	2.74 $\mu\text{m}$	4.034

Different behavior was observed in the case of the treated Ti6Al4V alloy. Figure 5.113 shows that in this case there is not any evident transfer of material from the pin to the plate and the pin surface does not have any visible damage.

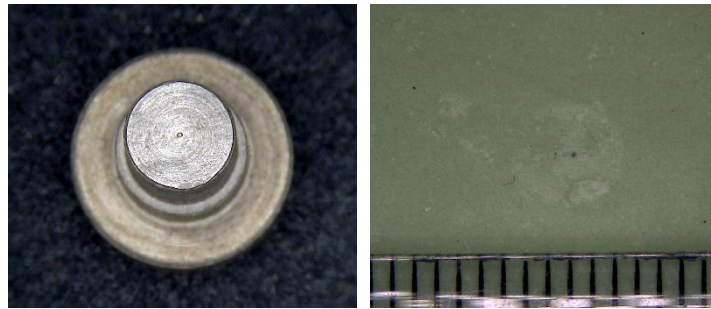


**Figure 5.113 treated Ti6Al4V alloy pin and PMMA plate after the fretting test**

EDS analyses and SEM images are reported in Figure 5.114 and are very interesting. Focusing on the cement surface, a deep socket is visible in the middle of the wear track. It is due to the abrasion process performed by a burr (residual of the turning process) of the pin. This is a phenomenon, which does not occur in the case of untreated Ti6Al4V alloy and AISI 316L, even if these pins have the same shape, because the burr was worn during the test. Inside this socket, some traces of titanium were detected, while outside there are not traces of titanium. This suggests that there is no evident transfer of material from the pin to the plate. As regards the pin surface, instead, relevant traces of carbon were detected, in this case, there is a relevant transfer of cement to the pin surface.

The wear mechanism is still composed of a combination of adhesive and abrasive wear, but the transfer of material is in this case unilateral, from the plate to the pin. In addition, no scratch signs are visible on the pin surface, that appears not damaged.

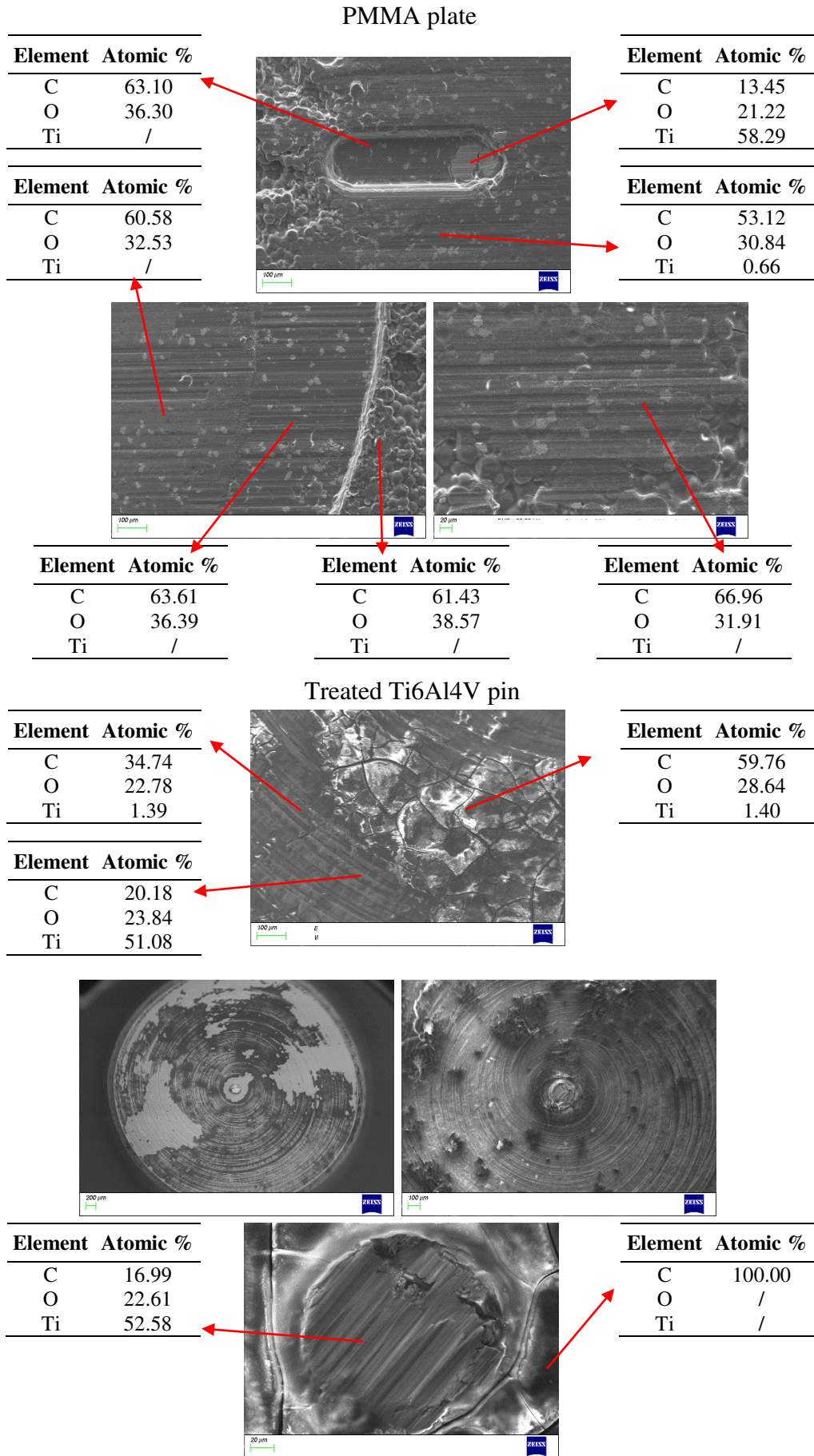


Figure 5.114 SEM images and EDS analyses of treated Ti6Al4V alloy pin and PMMA plate after the fretting test

More information is given by the roughness values (Table 5.18), the wear process increases roughness of the cement surface, while roughness of the pin surface decreases, index of a polishing abrasive mechanism of the asperities of the surface.

**Table 5.18 Average values of Ra and weight of the cement plate and the treated Ti6Al4V alloy pins**

		<b>Roughness (<math>\mu\text{m}</math>)</b>	<b>Weight (g)</b>
<b>PMMA plate</b>	<b>Before test</b>	19.58 $\mu\text{m}$	3.680
	<b>After test</b>	23.65 $\mu\text{m}$	3.689
<b>Treated Ti6Al4V pin</b>	<b>Before test</b>	2.56 $\mu\text{m}$	1.825
	<b>After test</b>	1.26 $\mu\text{m}$	1.828

As regards the change of weight, instead, also in this case the variation is not significant.

In conclusion, the untreated Ti6Al4V alloy and AISI 316L have an adhesive and abrasive mechanism of wear, with a relevant damage of the surfaces, that show evident scratch signs. The treated Ti6Al4V alloy, instead, does not show any damage of the surfaces, even if a slight abrasive mechanism of wear acts on its surface. In this last case, it is the cement, that shows a mechanism of adhesive wear.

## **Wear resistance**

Wear rate was calculated on the base of profilometric images of cement plates and metallic pins. These images give also further information about the wear mechanism of the surfaces.

Figures 5.115 and 5.116 show respectively the profilometric images of the cement plates and metallic pin before and after the fretting tests. While the rate of wear is reported in Figure 5.117.



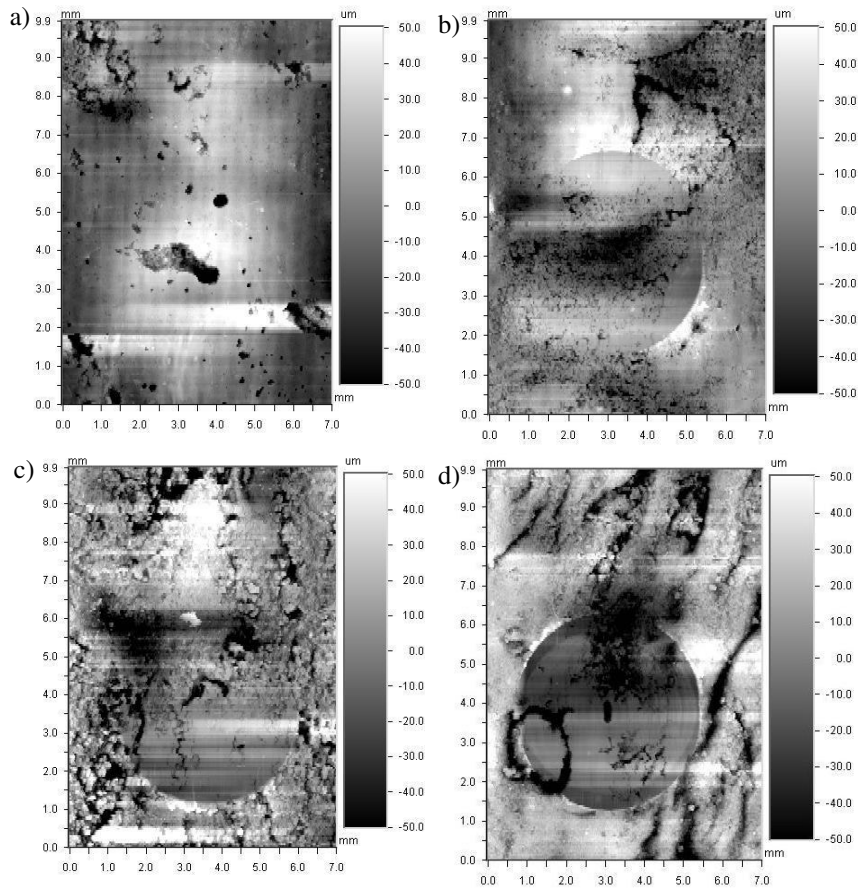


**Figure 5.115** Profilometric images of cement plate a) before the fretting test, b) after the fretting test against AISI 316L pin, c) after the fretting test against untreated Ti6Al4V alloy pin and d) after the fretting test against treated Ti6Al4V alloy pin

Figure 5.115 shows that there is a well-defined wear track on the cement plate, corresponding to the pin area, when tested against the treated Ti6Al4V alloy pin. While, in the case of cement plates tested against untreated Ti6Al4V alloy and AISI 316L pins, an incomplete edge of wear within the contact area is observable. In addition, the wear track due to the burr is visible only on the cement plate tested against the treated Ti6Al4V alloy pin, as mentioned before.

Focusing on the profilometric images of the pins (Figure 5.116), it is possible to see that the AISI 316L and untreated Ti6Al4V alloy pins show polished working lines and scratch signs, on the surfaces after the test, due to a wear mechanism of both adhesion and abrasion. Moreover, the untreated Ti6Al4V alloy pin has a very small burr, that, instead, is well-evident on the AISI 316L pin, but in any case it does not engrave the cement surface and it is worn out during the test. Differently, the treated Ti6Al4V alloy pin shows well-defined working lines and no surface damage after the test, nevertheless the big burr on its surface strongly abrades the cement surface.

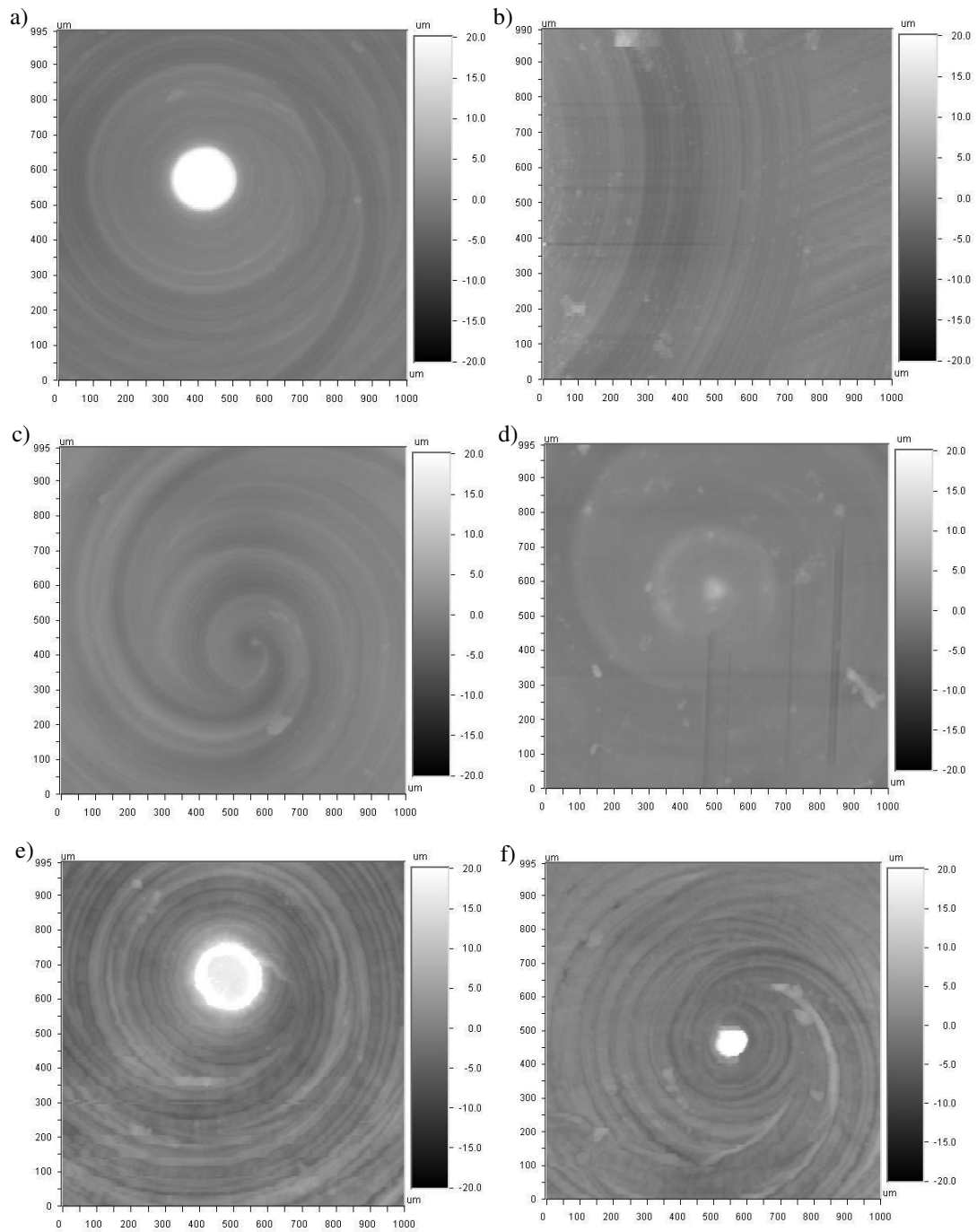


**Figure 5.116** Profilometric images of AISI 316L pin a) before the fretting test and b) after the fretting test; untreated Ti6Al4V alloy pin c) before the fretting test and d) after the fretting test; treated Ti6Al4V alloy pin e) before the fretting test and f) after the fretting test

Figure 5.117 reports wear rate and shows that the order of magnitude of the wear rate is the same for all the three samples, nevertheless the wear rate of the treated Ti6Al4V alloy is higher even if the surfaces are less damaged. The higher wear rate can be related to the deep socket caused by the burr on the cement surface. It is possible to suppose that removing the burr, the wear rate can decrease.

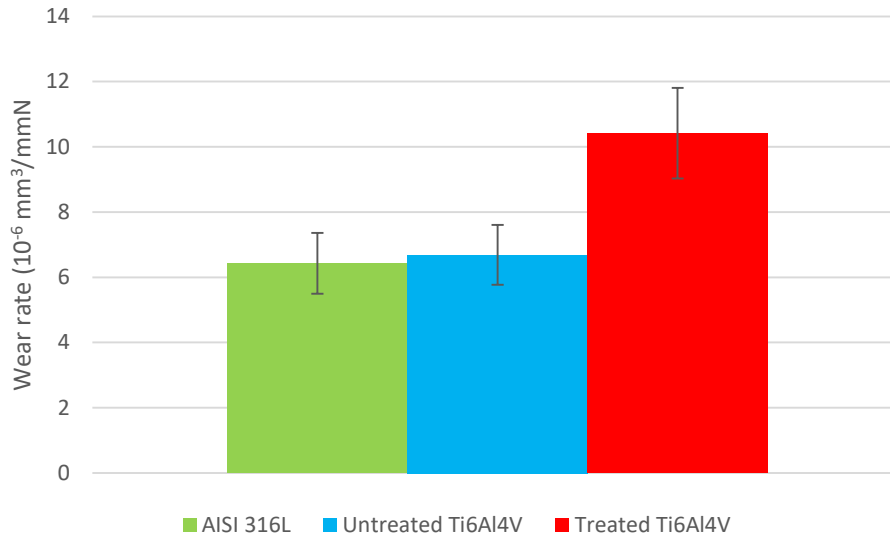


**Figure 5.117** Wear rate of AISI 316L pin, untreated Ti6Al4V alloy pin and treated Ti6Al4V alloy pin

Comparing the data of wear and fretting tests and XPS analyses, that are described in the paragraph 5.3.11, it can be supposed that the titanium borided coating chemically bonds the PMMA  $((\text{C}_5\text{O}_2\text{H}_8)_n)$  by means of C-O and C=O functional groups, as well as it does in the case of proteins [14]. While in the case of UHMWPE  $((\text{C}_2\text{H}_4)_n)$ , there is not a chemical bond between the boride coating and the polymer due to the absence of C-O and C=O functional groups in the polymer. In the first case, the chemical interaction between the borided surface and cement can lead to a more stable interface with a reduction of micromotion between the stem and the cement. In the second case, instead, the absence of a chemical interaction between the borided surface and UHMWPE can avoid an adhesive wear of the polymeric surface in a MoP coupling.

### 5.3.10 Summary of titanium borided coatings properties

Table 5.19 summarizes the characteristic collected in the previous paragraphs of the developed coatings.

**Table 5.19 Characteristics of the borided coatings**

Substrate	Composition	Thickness ( $\mu\text{m}$ )	Hardness HK (GPa)	Roughness (nm)	Wettability ( $^\circ$ )	COF
no pre/post treatment		3-19	7-98	171-801	104-107	
pre-treatment of deoxidation		3-19	5-68	118-584	99-113	
Pre-treatment of oxidation	TiB/TiB <sub>2</sub>	~4	~6	~127	~112	~0.2
Post thermal treatment		~43	~66	~713	~105	

As the Table 5.19 shows, thickness of the coating and hardness depend on boron diffusion rate and, as expected, are significantly affected by the time/temperature of the process. On the other side, all the coatings have similar chemical composition and crystallographic structure on the surface external layer and, as a consequence, similar wettability and friction coefficient.

According to these results, it was decided to evaluate, as an example, the behaviour of the coating in contact with protein solutions only in the case of the treated samples at the highest temperature and for the longest time of treatment without any pre/post treatment.

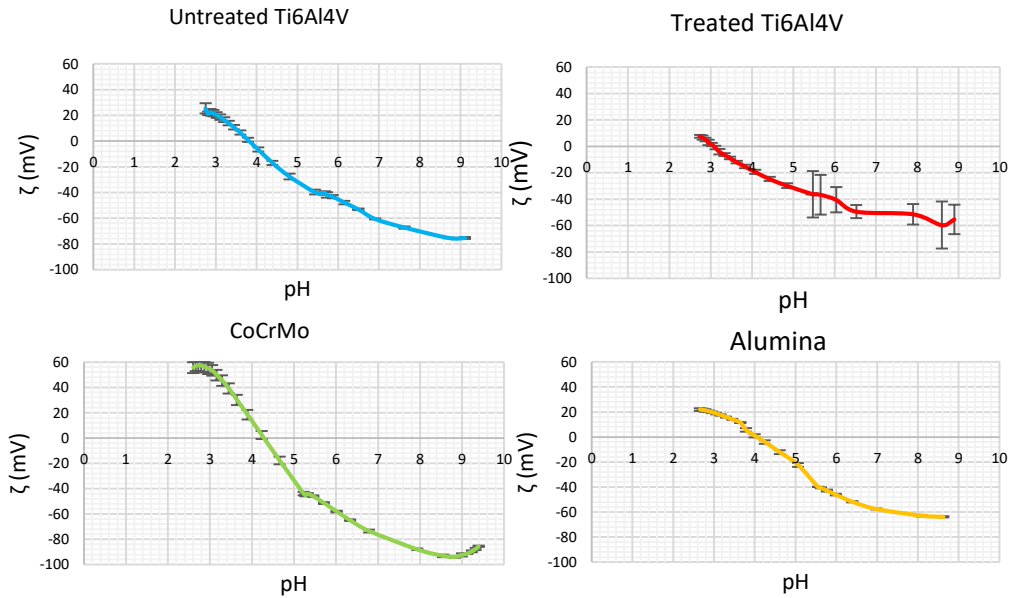
### 5.3.11 Protein adsorption evaluation

The developed coating was thought to be used in arthroprostheses and contact with biological fluids (containing proteins) is expected to occur; in particular synovial fluid can act as lubricant within the artificial articulation even it is not known in details in which amount and condition. Thus, surface interaction of the coating with proteins was evaluated. In particular, the effect of a surface net charge and the presence/configuration of adsorbed proteins on the coating were taken into account.

The behaviour of the untreated and Ti6Al4V alloy grade 5 treated at 1050°C for 4.5 h without any pre/post treatment were compared with that one of CoCrMo alloy and alumina, used as reference standard materials for arthroprostheses.

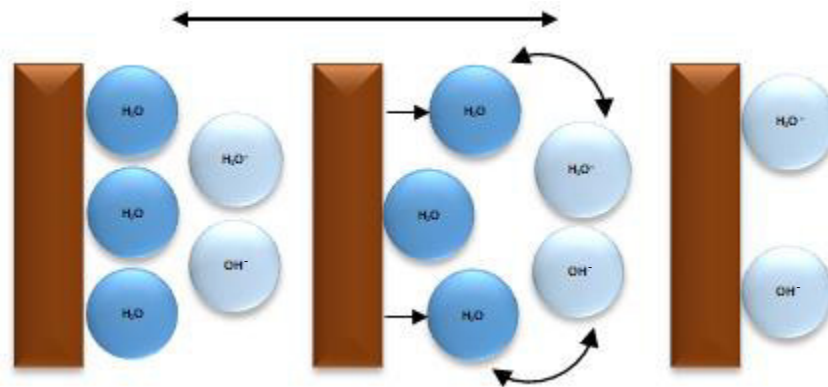
## Zeta potential analysis: before protein adsorption

Figure 5.118 reports the zeta potential curves in function of pH of untreated and treated Ti6Al4V alloy, CoCrMo alloy and alumina, before protein adsorption.



**Figure 5.118** Zeta potential curves before protein adsorption

The pH at which the material has a zero net surface charge, thus a zeta potential of 0 mV, correspond to the isoelectric point (IEP) of the material. It gives information about the ratio (or eventual absence) of acidic and basic functional groups on the surface. Generally speaking, a IEP of 4 corresponds to hydrophobic material, such as polymers, that has not any functional surface groups. In this case, the surface material adsorbs water molecules and at the pH of 4 there is a balance between the concentration of adsorbed hydroxide ions ( $\text{OH}^-$ ) and adsorbed hydronium ions ( $\text{H}_3\text{O}^+$ ) (Figure 5.119). These materials are also hydrophobic because of the absence of polar groups. They show zeta potential curves with high slope because they easily desorb water molecules with increasing/decreasing pH of the solution and adsorb higher amount of hydroxyl groups (or hydronium groups) following their increase in the solution: a rapid increase of the absolute value of zeta potential by changing pH occurs because of the great change of the surface charge and the slope of the titration curve is high.



**Figure 5.119** Charge at the solid-liquid interface for hydrophobic materials

On the other side, the presence of a high amount of surface polar groups leads to a hydrophilic behaviour of the material with strong attraction of water molecules along all the titration curve and low adsorption of hydroxyl or hydronium groups from the solution (low slope, low absolute values of zeta potential). If these polar groups have acid-basic reactions by changing pH, a shift of the IEP towards  $\text{pH} < 4$  occurs (if strong acidic groups are preponderant on the surface) or towards  $\text{pH} > 4$  (if strong basic groups are preponderant - Figure 5.120).

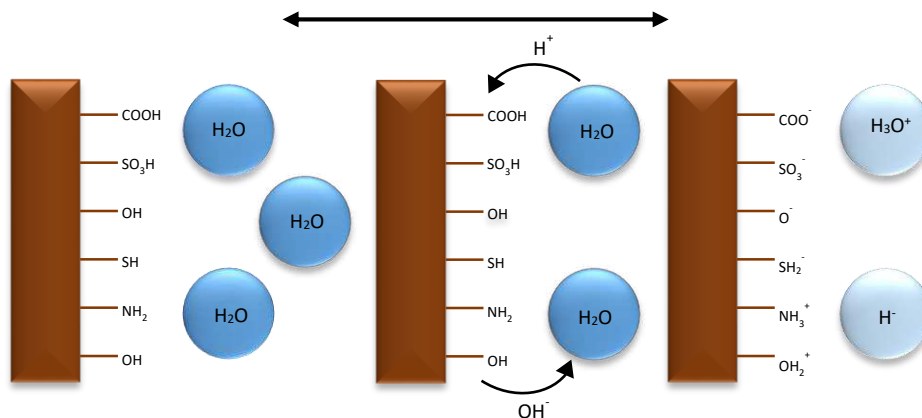


**Figure 5.120** Charge at the solid-liquid interface for hydrophilic materials

The IEP value depends on the balance between acid or basic functional groups, based on their strength and thus on their  $\text{pK}$  value: higher shifts of IEP point are expected with increasing the strength of acid/basic behaviour of functional groups.

The completed protonation or dissociation of functional groups with the same strength leads to a plateau of the zeta potential. When the material has weak or different types of functional groups, it is possible that the plateau is not reached also at very high or low values of  $\text{pH}$  due to the inhibition of the dissociation/protonation of one functional group by the neighbour group [15].

As regards the material used in this study, the untreated Ti6Al4V alloy has an isoelectric point (IEP) of 3.8 (Figure 5.118). This suggests that there is a small prevalence of acidic functional surface groups due to a IEP value very close to 4. At about  $\text{pH}$  6.5, the curve changes slightly slope for the dissociation of part of these acidic functional groups: a real constant value and a plateau is not reached by the curve. It can be supposed that the acidic functional groups on the untreated

Ti6Al4V alloy are weak and they show a range of different acidic strength. A second change of slope can be observed with the onset of a plateau at pH 8.8.

Data about the treated samples show that the IEP is 3.0. It is shifted to more acidic values compared to the IEP of the untreated material, thus there are acidic groups with higher strength on the treated material than on the untreated one. According to this hypothesis, around pH 5.5, there is a significant change of the slope of the zeta potential curve; the standard deviation of the points at higher pH is high, but it is possible to consider the last part of the curve as a unique plateau and to suppose that the material exposes strong acid functional groups which are almost completely dissociated above pH 5.5.

CoCrMo alloy, used as metallic reference material, has a IEP of 4.3. The IEP slightly higher than 4 suggests that there is a slight prevalence of basic functional groups. In this case, the zeta potential curve shows plateaus both in the basic and in the acid range at the pH respectively of 3.1 and 7.7. This confirms the presence of basic functional groups, but also reveals the presence of minority of acid functional groups with a not negligible strength (deprotonation observable in the explored pH range). Considering the trend of the curve for pH below 3.1 and above 7.7 it is possible to say that the basic and acid functional groups are, respectively, almost completely protonated and dissociated respectively below and above these pH values.

Alumina, the second reference material, has a IEP of 4.0. Both in the acid and basic range, the zeta potential curve has a change of slope at pH 3.1 and 6.6, respectively. The curve does not reach a plateau in both cases, this means that the basic and acid functional surface groups have different basic/acid strength and there is not a complete protonation/dissociation of the functional groups at any specific pH. In this material, the IEP is at 4.0 because this is the pH value at which positive and negative surface charges are balanced, that is a different case with respect to a hydrophobic surface without any surface functional groups.

The zeta potential curves before protein adsorption were compared in Figure 5.121.

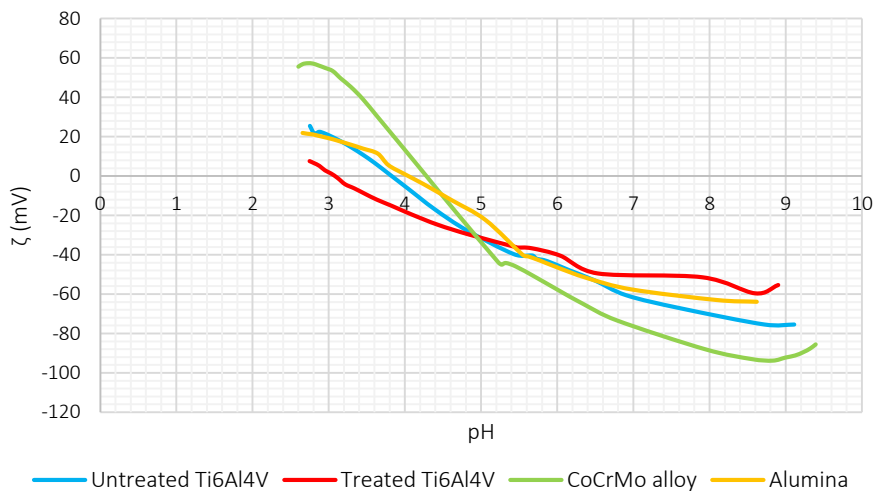


**Figure 5.121 Comparison of the zeta potential curves before protein adsorption**

Considering the slope of the curves around the IEP, in the range before the eventual change of slope or presence of plateau, it is possible to see that the curve of alumina and untreated Ti6Al4V alloy have similar slope. Zeta potential data suggest that alumina and untreated Ti6Al4V alloy have similar hydrophilicity, that means similar ability to attract water molecules through the presence of polar groups on the surface. Both materials result to be hydrophilic by contact angle measurements (Paragraph 5.3.6, Figure 5.63) even if wettability is not really the same (contact angle on the untreated Ti6Al4V:  $77\pm 1^\circ$ ; Alumina:  $60\pm 1^\circ$ ). This is not surprising, considering that wettability and zeta potential are quite different techniques, measuring different phenomena. As first, wettability data can be affected by surface roughness [16] while the zeta potential measurement is a dynamic analysis dependent mainly on surface chemistry [15]. Furthermore, wettability is usually performed only at one pH and it depends on balance between solid, liquid and gas surface energies.

CoCrMo alloy and treated Ti6Al4V alloy have a hydrophilic behaviour according to the shift of the IEPs at values different from 4. Taking into account the slope of the curves, the treated Ti6Al4V alloy is more hydrophilic than CoCrMo alloy: the lower slope of the treated Ti6Al4V curve points out a strong bond between the surface and the water molecules

CoCrMo alloy has a more hydrophobic behaviour in the titration curve due to the higher slope of the curve, while the treated Ti6Al4V alloy is more hydrophilic according to the lower slope. Actually, this is not in agreement with wettability data, where a contact angle of  $78\pm 2^\circ$  was measured on CoCrMo alloy and of  $106\pm 4^\circ$  on the treated Ti6Al4V. As previously explained, the correlation between titration curves and wettability measurements must be investigated much more in details and cannot be completely explained at this stage.

The characteristics of the surfaces are summarised in Table 5.20.

**Table 5.20 Summary of material surface characteristic**

Material	IEP	Hydrophilicity	Acidic groups (strength)	Basic groups
CoCrMo	4.3	++	+ (onset of the plateau @ pH 7.7)	++ (onset of the plateau @ pH 3.1)
Allumina	4.0	+	+++ (onset of the plateau @ pH 6.6)	++ (onset of the plateau @ pH 3.1)
Untreated Ti6Al4V	3.8	+	++ (onset of the plateau @ pH 6.5-8.8)	/
Treated Ti6Al4V	3.0	+++	++++ (onset of the plateau @ pH 5.5)	/



## Zeta potential analysis: after BSA adsorption

The zeta potential curves of all the materials after adsorption of BSA are compared to the curves before protein adsorption. The protein adsorption process was carried out dissolving the protein once in PBS and once in double distilled water, both the zeta potential curves are reported in Figure 5.122. Moreover, the zeta potential curve of each material after BSA adsorption was compared to the titration curve of BSA, obtained in solutions buffered at different pH (Figure 5.123). The last curve was obtained through a different equipment of zeta potential measurement as described in Chapter 4.

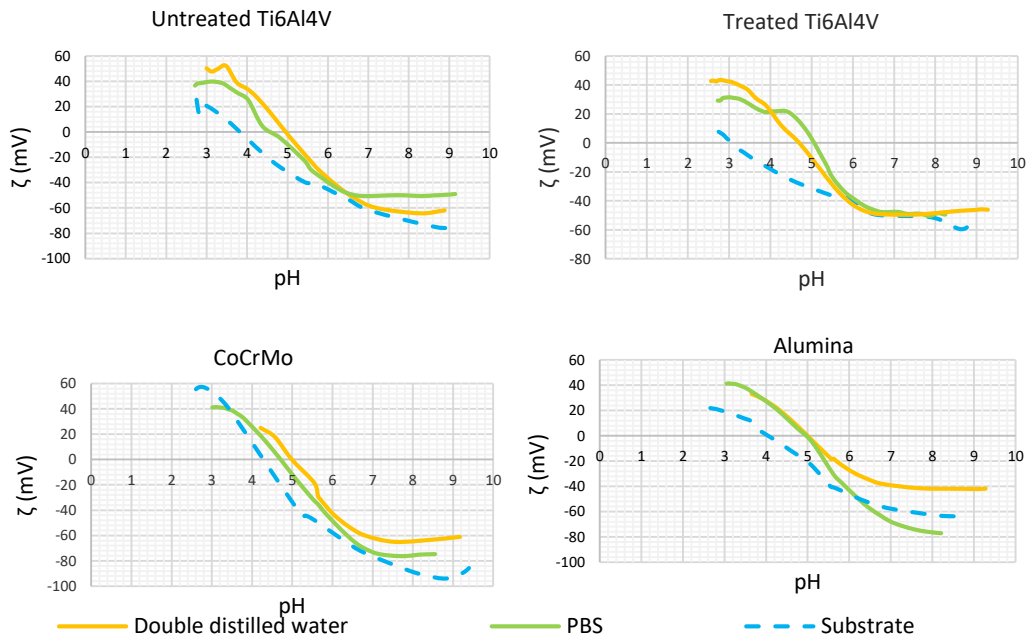
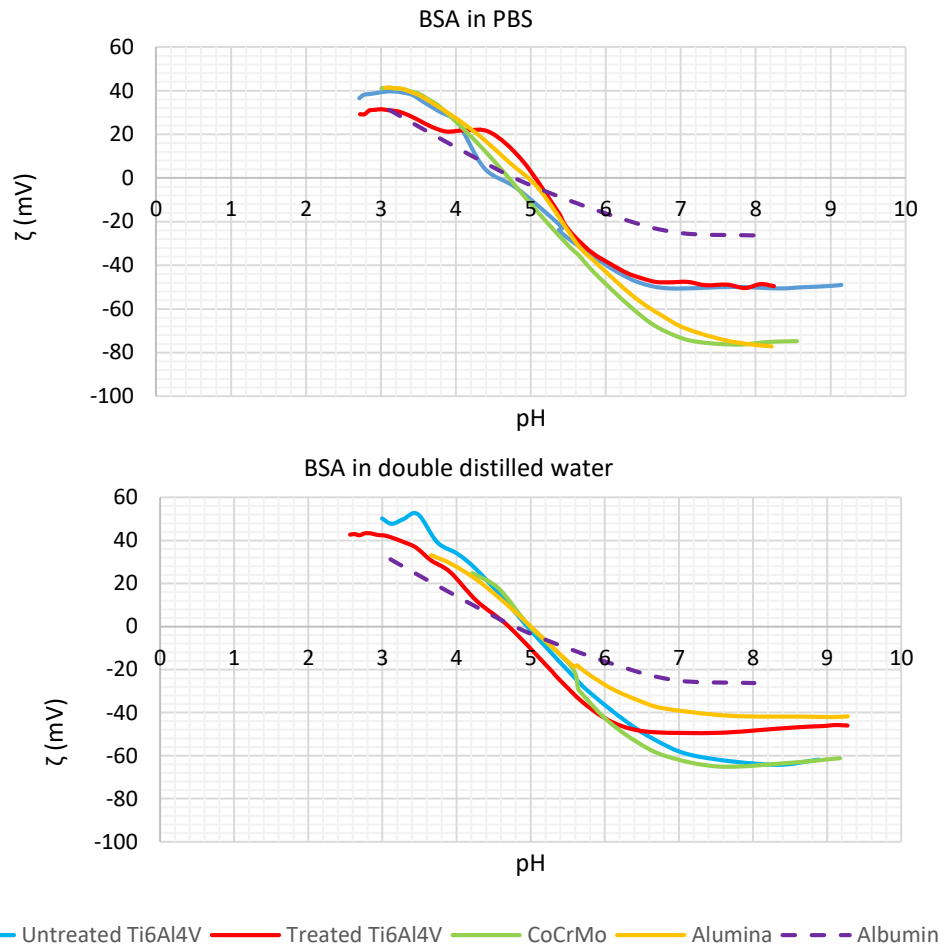


Figure 5.122 Comparison of the zeta potential curves before and after BSA adsorption



**Figure 5.123 Comparison of the zeta potential curves of materials after protein adsorption and pure BSA**

The protein in aqueous solution shows IEP 4.8, that is within the range reported in literature [17]. At this pH, the protein has a zero net surface charge density, the negative functional groups ( $\text{COO}^-$ ) of the protein and the positive ones ( $\text{NH}_3^+$ ) are balanced. In the basic range, at pH 6.7 the curve of BSA in aqueous solution has the onset point of a plateau. This points out the presence in the protein of acid functional groups ( $\text{COO}^-$ ), that are completely dissociated above pH 6.7. In the acidic range, no plateau is evident. BSA is composed by both acid ( $\text{COOH}$ ) and basic ( $\text{NH}_2$ ) groups [18] and the absence of a plateau in the acidic range points out the presence of very weak basic functional groups ( $\text{NH}_2$ ), whose complete protonation occurs at pH lower than 3 and it is not detectable by the measurement. The scenario is outlined in Figure 5.124.

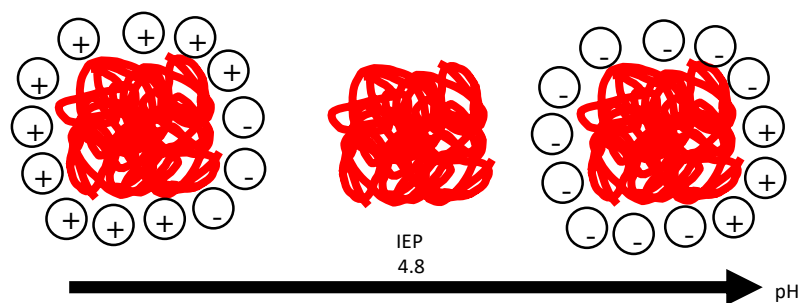


Figure 5.124 Outline of the BSA in solution

Considering that pH of BSA dissolved in PBS is around 7, in this solution the protein shows completely dissociated COOH functional groups ( $\text{COO}^-$ ) during the adsorption process. Moreover, the secondary structure, spatial surface positive and negative potential distribution and the hydrophobic/hydrophilic region of the BSA at pH close to 7 (6.9) are shown in Figure 5.125.

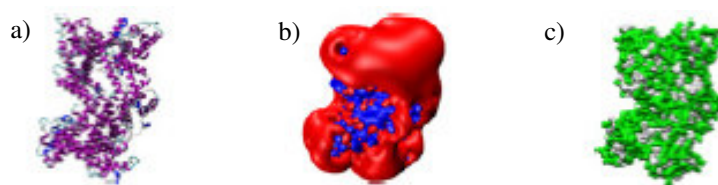


Figure 5.125 a) secondary structure, b) spatial surface potential distribution (red: negative potential and blue: positive potential) and c) hydrophilic/hydrophobic regions (green: hydrophilic and white: hydrophobic) [19]

At pH around 7 also the explored surfaces which have acid functional groups, that dissociate at pH lower than 7, have negative charged groups exposed to the liquid environment in PBS. On the other side, when adsorption is performed dissolving the protein in double distilled water, the pH is close to 5. In this condition, the protein is almost neutral (positive and negative groups are balanced) and most of the surfaces are almost lacking of negative charged functional groups (the surfaces are at pH that is below the onset of the plateau). An exception is due to the treated Ti6Al4V that has a plateau with onset point almost at the same pH value of double distilled water.

Considering all the curves of the different surfaces after adsorption (both at pH 5 and 7), it is possible to observe that in all the surfaces after adsorption there is a shift of the IEP (with respect to the curve of the same material before adsorption) and a change of the curve slope, suggesting that adsorption of the protein occurred. As reported in Table 5.21, all the materials after BSA adsorption show a IEP around 5, that is close to the IEP of albumin: this means that the coverage of the surface is complete and a uniform layer of protein covers the surface of the materials. Moreover, there is an increase of the curves slope (with respect to the curve of the materials before adsorption), that involves a more hydrophobic behaviour of the adsorbed surfaces, in agreement with a complete coverage of the metal/ceramic surface by an organic compound.

**Table 5.21 IEP of the materials after BSA adsorption, dissolving the protein once in PBS and once in double distilled water**

Material	IEP (BSA in PBS)	IEP (BSA in double distilled water)
Untreated Ti6Al4V	4.5	4.9
Treated Ti6Al4V	5.0	4.7
CoCrMo alloy	4.7	4.9
Alumina	5.0	5.0

Furthermore, all the curves obtained after adsorption are different with respect to the titration curve of albumin in aqueous solution, evidencing that albumin acts as a soft protein which changes configuration after adsorption. As known by literature, BSA is a soft protein [20], in contact with the materials it loses its ternary structure and changes conformation to interact with the surfaces. Much more in details, the curves of the adsorbed protein have higher slope with respect to the curve of the protein in solution probably because, while in solution albumin exposes to the liquid environment its hydrophilic domains in order to minimise the energy of the system, after adsorption these domains are much more oriented to the surfaces (which, even if in different degree, are all hydrophilic) and the hydrophobic domains of the adsorbed protein comes much more in contact with the solution. In contact with hydrophobic surface the protein reorganises its structure to reduce the free energy of the system and it exposes mainly the hydrophobic core toward the surface and the hydrophilic regions away from the surface (Figure 5.126a).

As last, a plateau in the acidic range is almost always observable after adsorption while it was absent in the titration curve of the protein in solution, evidencing that, in the new configuration, the  $\text{NH}_2$  groups of the adsorbed protein change their reactivity increasing their basic strength: they become completely protonated at lower pH values that are within the explored range. In contact with hydrophilic surfaces the interaction between the reorganised protein and surface occurs through electrostatic forces, charge transfer and/or hydrogen bonds. Ions from the solution can be adsorbed and stabilise eventual charge repulsion forces between the surface and the protein (Figure 5.126b).

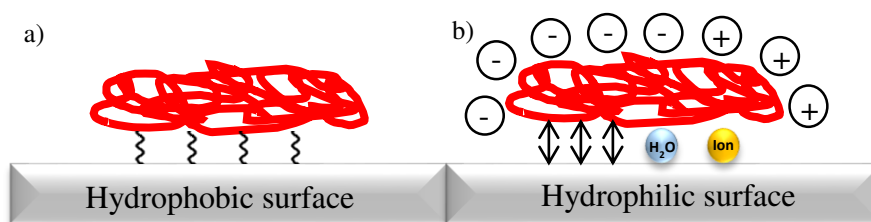


**Figure 5.126 Interaction between the BSA and hydrophobic/hydrophilic surfaces**

Comparing the zeta potential curves of each material after adsorption in different solvents, it is possible to observe that in the case of alumina the two curves are significantly different. This suggests that in this case there is an influence of the pH of the solvent on the adsorption process and on the configuration of the adsorbed protein. This is in agreement with the presence on the surface of both albumin and alumina of charged groups (deprotonated acidic groups) at pH 7: in this case a hydrophilic/electrostatic interaction between protein and surface occurs, while at pH 5 interaction is mainly hydrophobic.

In the case of the untreated Ti6Al4V alloy and CoCrMo alloy, the curves obtained after adsorption at different pH are much more similar. This is in agreement with the absence (or low) presence of charged groups on these materials at pH 7: a hydrophobic interaction mainly occurs at both pH values.

A different case is that of the treated Ti6Al4V alloy, where there are strong acidic groups and they are dissociated at both the pH values of the solutions used for adsorption. In these cases, both curves are similar, but probably because hydrophilic/electrostatic interaction occurs in both cases.

Focusing on adsorption in PBS, the zeta potential curves of the materials after adsorption, have a plateau in the basic range similarly to the curve of BSA in solution. Untreated Ti6Al4V alloy and treated Ti6Al4V alloy have the onset of a plateau respectively at pH 6.4 and 6.3. The shift of the onset of the plateau at a pH lower than the one of BSA in solution (6.7) suggests that, because of the rearrangement of the protein and the electrostatic interaction with the surface, there is a small change in the electron charge distribution within the protein after adsorption (to be confirmed): the COOH groups of the adsorbed protein act as a slight stronger acid.

Looking at the curve of the CoCrMo alloy, it is possible to see that the curve has the onset of the plateau at the same pH of BSA (6.7), this means that at pH above 6.7 the functional groups completely dissociates, as well the COOH groups of BSA in solution: this is in agreement of the absence of an electrostatic interaction with the surface.

The curve of albumin adsorbed on alumina has the onset of the plateau at pH 7.1 and in this case the plateau is not well-developed, thus the COOH groups are only partially dissociated above this pH and their acid strength decreases with respect to BSA in solution. This difference is to be investigated in much more details.

In the acid range, all the zeta potential curves of the materials after adsorption show a plateau, that is not present on the zeta potential titration curve of BSA in solution. The occurring of basic group protonation at pH values analysable by zeta potential means that after adsorption the basic strength of  $\text{NH}_3^+$  changes, becoming stronger. The onset of the plateau respectively occurs at pH 3.4 (untreated Ti6Al4V alloy), 3.5 (CoCrMo alloy and alumina) and 4.4 (treated Ti6Al4V alloy). The treated Ti6Al4V alloy is the material with the basic functional groups of the adsorbed proteins showing the strongest basic strength and highest modification with respect to the protein in solution: this effect can be related to the presence on this material of the acid functional group with the strongest acid strength.

Similar consideration can be done as regard the adsorption in double distilled water. In the basic range, all the curves have a plateau with onset point at almost the same pH (6.6 CoCrMo alloy; 6.7 alumina and BSA in solution; 6.9 untreated Ti6Al4V), except the treated Ti6Al4V alloy that starts the plateau at a lower pH, 6.2. The presence of the plateau, as before, points out that the COOH functional groups are completely dissociated above the onset of the plateau. Nevertheless, the protein adsorbed on the treated Ti6Al4V alloy shows acid functional groups with a stronger acid strength than the ones of BSA in solution (the onset of the plateau is at a lower pH value): the configuration of the protein was changed after absorption with a change in charge distribution and electrostatic interaction with the surface. While the other materials have the onset points of the plateau around the same pH of BSA in solution, therefore, in these cases the reorganisation of the protein after adsorption does not cause a change in the electron charge distribution and the strength of the acid functional groups does not change too.

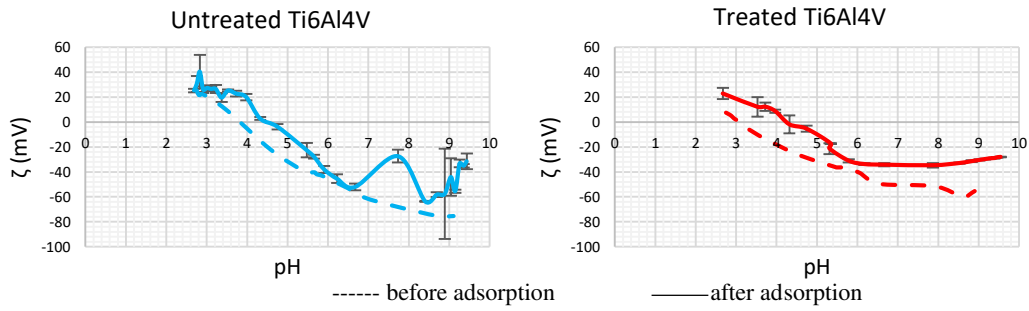
These data underline that a strong electrostatic interaction between albumin and the Ti6Al4V treated surface can be derived from zeta potential titration curves. This type of interaction is much closer (even stronger) to that of ceramic surfaces (like alumina) than to metals (untreated Ti6Al4V or CoCr alloy) and usually ceramic surfaces show better lubrication ability in artroprostheses than metals.

A study performed by Scholes et al. shows that CoC joint has a full fluid film lubrication while MoM and MoP joint show a mixed lubrication when tested in carboxy methyl cellulose, that has rheological properties similar to synovial fluids. This is due to the low roughness and good wettability of the ceramic material. Nevertheless, when the CoC joint is tested in FBS there is an increment of friction coefficient and the lubrication condition shift to a predominately mixed regime. This is caused by the interactions between the ceramic surface and the proteins, that leads to an increment of the surface roughness. In conclusion real lubricant ability depend strongly from the viscosity of the lubricant and the amount of adsorbed proteins on surface [21].

Otherwise, the direct experimental determination of the lubricant performance of the surface in physiologic liquid cannot be immediately derived by these data.

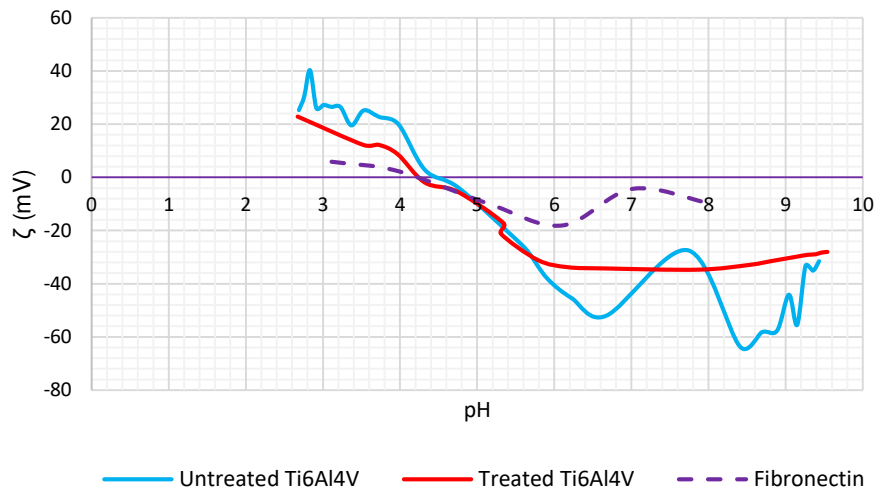
### **Zeta potential analysis: after FN adsorption**

Figure 5.127 shows and compares the zeta potential curves of the different materials before and after adsorption of FN in PBS solution. The analysis was carried out only focusing on the materials finalised to osseointegration, such as the untreated and treated Ti6Al4V alloy.



**Figure 5.127 Comparison of the zeta potential curves before and after FN adsorption**

Also in this case, it is possible to observe the occurrence of absorption. After protein adsorption, the zeta potential curves of the surface change and the IEP moves toward the basic range (actually toward the IEP of the protein in solution). In Figure 5.128 the zeta potential titration curve of the protein dissolved in PBS is compared to the ones of the materials after protein adsorption.



**Figure 5.128 Comparison of the zeta potential curves of materials after protein adsorption and FN in PBS solution**

The measurement of the pure FN in solution was carried out twice to confirm the particular trend in the basic range. The obtained IEP of the protein is 4.0 and it is a bit lower than data from literature [22]. At pH of 3.9, there is a slight change of slope of the curve without the formation of a net plateau. This means that the protein in solution has weak basic functional groups, that are not completely protonated in the explored pH range. In the basic range, there is a peak with onset at pH 6.1, that is different from the plateau observed on the other curves: a changing in protein configuration can be supposed, but it must be confirmed.

Adsorption of FN as performed in PBS, thus the adsorption process was carried out at pH around 7 and there is no evidence in the case of FN of exposition of acidic functional groups completely dissociated, unlikely BSA.

Comparing the curve of FN with the ones of the materials with the adsorbed protein, it is possible to see that the untreated and treated Ti6Al4V alloy move their IEP after adsorption to a value closed to the one of FN, respectively 4.5 and 4.25.

As for BSA, this suggest that there is an adsorbed continuous layer of protein on the material surface. The slope of the curve of the material after adsorption change compared to the one of FN. The slope of the curve of the protein after adsorption slightly increases pointing out a more hydrophobic behaviour of the protein after adsorption. In solution, the protein behaves in a hydrophilic way as well as BSA.

Considering the basic range, the zeta potential curve of the protein adsorbed on the untreated Ti6Al4V alloy behaves similar to the zeta potential curve of FN in solution. The shape of the curves is similar and absorption without a relevant change of configuration can be supposed: FN can be considered a hard protein in this case. The only difference can be related to the onset of the peak that is at pH 6.7: this value is higher than in the case of FN in solution (6.1).

The zeta potential curve of the protein adsorbed on the treated Ti6Al4V alloy is completely different from the one of FN in solution. The protein changes conformation and exposes acid functional groups that are completely deprotonated (COO<sup>-</sup>) at pH higher than 6.2. In the acid range, the curve of the untreated Ti6Al4V alloy is similar to that of FN in solution (change of slope at pH 3.9), while the curve of the protein adsorbed on the treated Ti6Al4V alloy does not change slope in the acid range: thus in this last case the basic strength of the functional group decreases after adsorption.

FN acts in this case as a hard protein on the untreated Ti6Al4V alloy and as a nearly soft one on the treated alloy. The effects of this specific surface interaction on the biological response to the treated Ti6Al4V surface cannot be directly inferred by these data, but it can be derived a potential interest to the application of the treatment also in case of surfaces finalized to osseointegration.

### **Zeta potential analysis: after FBS adsorption**

The zeta potential curves before and after adsorption of FBS are reported and compared in Figure 5.129.



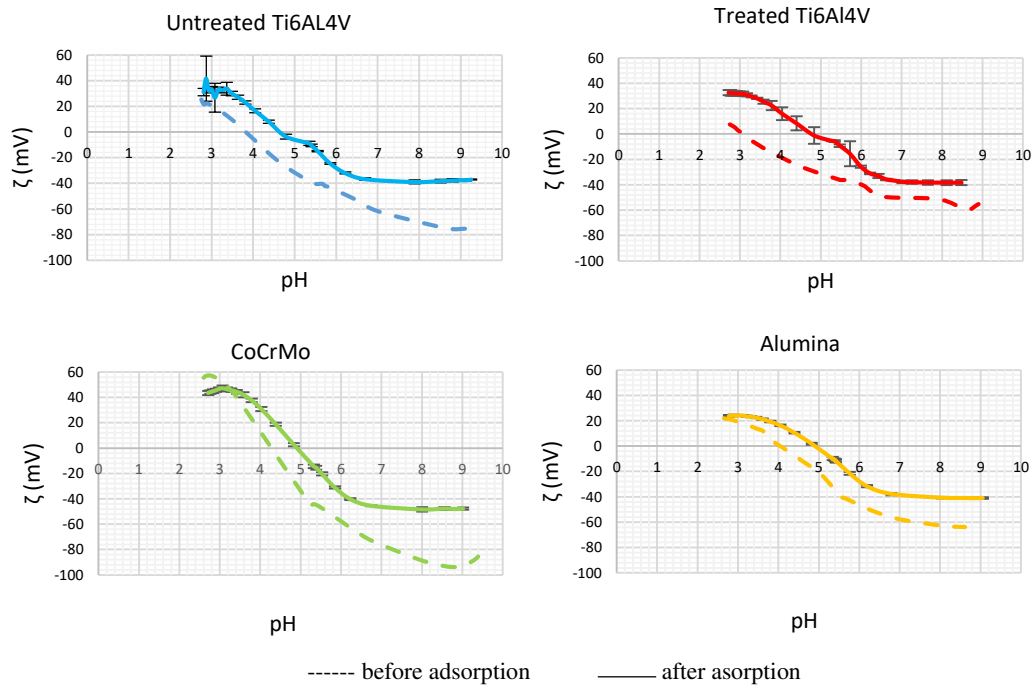


**Figure 5.129** Comparison of the zeta potential curves before and after FBS adsorption

All the curves show a shift of the IEP toward pH 5 after absorption and a plateau both in the acid and basic range.

In Figure 5.130 the zeta potential curves of the materials after FBS adsorption were compared to the one of FBS in solutions buffered at different pH.

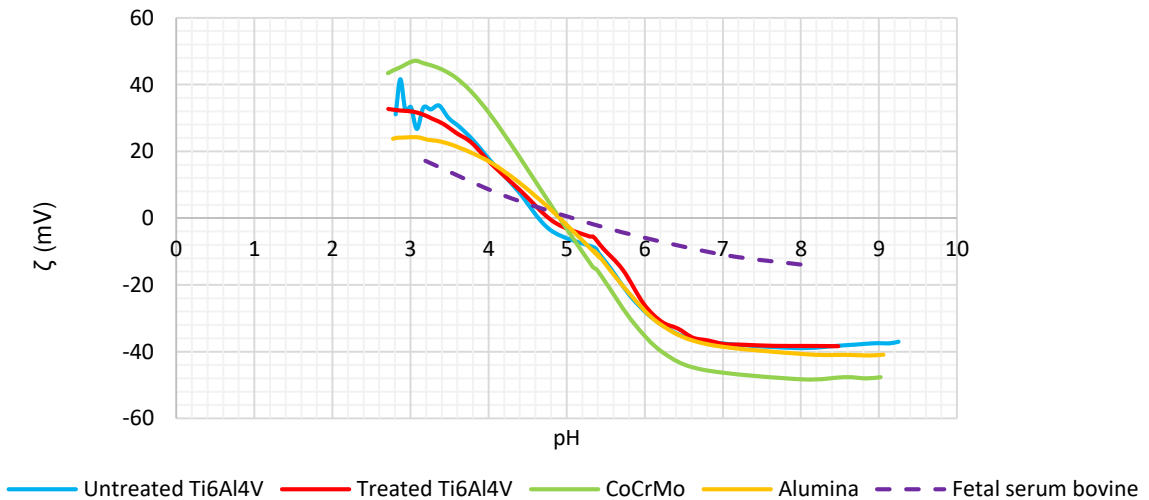


**Figure 5.130** Comparison of the zeta potential curves of materials after protein adsorption and FBS.

The IEP of the pure FBS results to be 5.1. The curve does not present any plateau neither in the basic or acid range. FBS is a mix of proteins, that expose functional groups with different pK, thus it is expected that the zeta potential titration curve of FBS does not show any plateau.

The adsorption process was performed using FBS as received, as consequence the adsorption of proteins on material surface occurs at a pH around 5. Condition at which the FBS overall has a zero net surface charge density.

It is possible to state that there is an adsorbed continuous layer of proteins on the materials surface. This can be deduced by the variation of the IEP of the materials after the FBS adsorption. The IEP are 4.7, 4.8, 4.9 and 4.9 respectively for untreated Ti6Al4V alloy, treated Ti6Al4V alloy, CoCrMo alloy and alumina.

The curve slope of all materials is similar and diverges from the one of the FBS, that shows a lower slope. As well as in the previous cases, the FBS proteins behave in a hydrophilic way, while after being adsorbed on a surface, they behave in a more hydrophobic way. The curve of CoCrMo alloy shows a slightly higher slope and so a more hydrophobic behaviour.

Both in the basic and acidic range, the zeta potential curves of all the materials after adsorption develop a plateau. The plateau in the basic range has an onset point at pH 6.7, 6.6, 6.3 and 6.9 respectively for the untreated Ti6Al4V alloy, treated Ti6Al4V alloy, CoCrMo alloy and alumina. The onset of the plateau in the acidic range occurs at pH 3.5, 3.3, 3.5 and 3.6 respectively for untreated Ti6Al4V alloy, treated Ti6Al4V alloy, CoCrMo alloy and alumina. The presence of the plateau points out that the adsorbed proteins expose acid functional groups with the same pK. The presence of a plateau, absent on the FBS titration curve, suggests that there is a selection of the adsorbed proteins from the mixture of FBS or a variation of the acid strength of the functional groups of the adsorbed proteins that become stronger.

FBS, as said before, is a mix of proteins, with high concentration of BSA. Interesting is the comparison between the zeta potential curves of the materials after adsorption of BSA and FBS and between the pure BSA and FBS in solution (Figures 5.131 and 5.132).

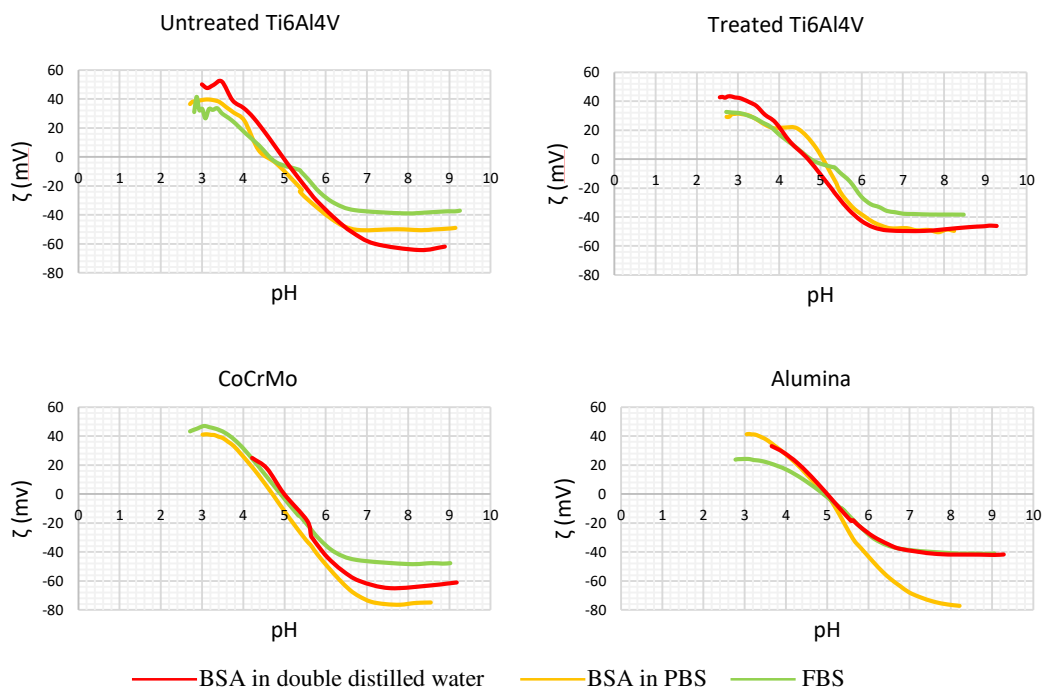


**Figure 5.131 Comparison of the zeta potential curves of materials after BSA and FBS adsorption**

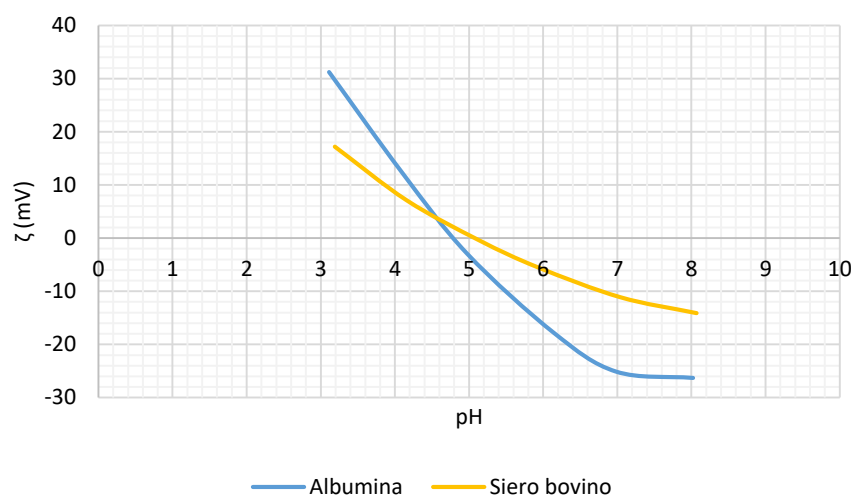


**Figure 5.132 Comparison of the zeta potential curves of pure BSA and FBS in solution**

Even if BSA is the highest concentrated protein of FBS, the zeta potential curves of the materials after adsorptions in BSA (in both solvents) and FBS are different; only in the case of the untreated Ti6Al4V, the titration curves of BSA (in PBS) and FBS are closer. The slope of the zeta potential curves of adsorbed FBS is lower than the one of the zeta potential curves of adsorbed BSA regardless of the solvent: the mix of adsorbed proteins from FBS is more hydrophilic after adsorption than BSA. The curves of the untreated Ti6Al4V alloy and CoCrMo alloy develop plateaus at different pH values in the case of adsorption of BSA or FBS, thus the adsorbed proteins expose functional groups with different acid/basic strength with respect to BSA. In the case of alumina, instead, the curve of adsorbed FBS overlaps the curve of adsorbed BSA (from a solution in double distilled water) in the basic range, while differs in the acid range: an electrostatic interaction of the  $\text{NH}_2$  groups of some proteins different from BSA (and probably with a different IEP) can be supposed. The Vroman effect described in Chapter 3 has to be taken into account: FBS is a solution containing more than one protein and different proteins compete in adsorption over time.

In any case, as Figure 5.132 shows, curve of pure BSA and the one of pure FBS are different, even if the albumin is the main protein present in the FBS. Pure BSA behaves in a more hydrophobic way than pure FBS (higher slope of the curve), this suggest a strong influence of the proteins present at a lower concentration. Therefore, a difference of the curves after BSA and FBS adsorption can be expected.

### **XPS analyses: survey analysis**

The surfaces of the different materials were also evaluated by means of XPS analyses in order to confirm the presence of the adsorbed proteins.

Data refer to XPS analyses after adsorption in BSA, FN and FBS solutions using PBS as solvent for BSA and FN, while FBS was used pure.

Table 5.22 reports the atomic % of the elements detected on the surfaces by means of survey analysis.

A relevant amount of carbonaceous contaminant can be detected on all the substrates (see the C content on the substrates in Table 5.22): this can affect also the data on the surfaces after adsorption and it must be taken into account.

It is possible to observe a variation of the atomic percentage of all the elements after protein adsorption, in particular an increment of the nitrogen atomic percentage and a decrement of the atomic percentage of the elements of the substrate is mainly evident: this is first evidence of the presence of adsorbed proteins.

The highest amount of proteins adsorption occurs in the case of soaking in FBS on all the substrates: the surface layer of adsorbed proteins is so thick that the elements of the substrates are no more detected. Only in the case of the treated Ti6Al4V alloy, a small amount of B is still detected.

In the case of albumin adsorption, the lowest values of the elements of the substrates (that can be roughly ascribed to the highest protein coverage) can be observed on the treated Ti6Al4V and untreated Ti6Al4V, while CoCrMo alloy and alumina seem to adsorb less albumin.

Following the same criteria, an almost equal amount of FN seems to be adsorbed on both treated and untreated Ti6Al4V and it is lower than the amount of adsorbed albumin on the same substrates; at this concern, the lower concentration of the solution used for FN adsorption (that is 2 orders of magnitude lower than that used for albumin adsorption, in agreement with the concentration of FN in the human plasma) must be considered.

**Table 5.22 Atomic % from the survey analyses**

Materials		C1s	O1s	N1s	Ti2p	B1s	Cr2p3	Co2p3	Mo3d	Al2p	Contaminants
Untreated Ti6Al4V	unsoaked	65.5	25.2	0.7	4					1.5	3.1
	BSA	74.6	14.6	8.6	0.4						1.4
	FN	51.7	30.1	6.9	1.5					0.5	7.7
	FBS	74.3	14.6	9.7							1.0
Treated Ti6Al4V	unsoaked	52.5	24.4	2.6	3.8	14.7					2.3
	BSA	68.3	16.1	12.5	0.1	0.9					1.1
	FN	51.4	26	6.6	1.9	3.8					7.3
	FBS	75.8	13.4	8.6		1.1					
Alumina	unsoaked	42.1	41.8	1.5						11.4	3.3
	BSA	54.8	26.5	8.2						8.7	1.5
	FBS	70.4	16.7	10.3							2.0
CoCrMo	unsoaked	51.9	26.4				13.1	6.7	1.2		0.7
	BSA	62.9	18.6	6.8			7	3.1	0.7		0.9
	FBS	75.6	14.2	9							0.7

The N/Metal and N/C<sub>tot</sub> ratios were calculated from the data of the survey analyses in order to respectively confirm the degree of coverage of the surfaces and to evaluate the occurrence of carbonaceous contamination on the surfaces after protein adsorption. Theoretical N/C<sub>tot</sub> values for fibronectin and albumin is 0.27 in both cases [23,24]. The theoretical value for the FBS can be considered the same of the BSA, due to the fact that albumin is the protein present in the highest amount in the FBS [25]. N was selected as the reference element for evaluating the proteins amount because it is almost absent in the carbonaceous contamination. B was selected as the reference element for evaluating the presence of the substrate in the case of the treated Ti6Al4V alloy (instead of Ti) because it is the last observable element on the surface when there is a very thick layer of proteins such as after adsorption of FBS. The values are shown in Table 5.23.

**Table 5.23 N/Metal and N/C ratios**

Protein	Albumin		Fibronectin		Fetal Serum Bovine	
	N/Metal	N/C <sub>tot</sub>	N/Metal	N/C <sub>tot</sub>	N/Metal	N/C <sub>tot</sub>
<b>Untreated Ti6Al4V</b>	21.50	0.12	4.60	0.13	∞	0.13
<b>CoCrMo</b>	0.97	0.11	/	/	∞	0.12
<b>Alumina</b>	0.94	0.15	/	/	∞	0.15
<b>Treated Ti6Al4V</b>	13.89 (B)	0.18	1.74 (B)	0.13	7.82 (B)	0.11

∞: the elements of the substrate (Ti, Cr and Al) were not detected, thus the N/Metal ratios cannot be calculated.

According to the N/metal ratio, the highest degree of surface coverage is reached on the reference materials (untreated Ti6Al4V alloy, CoCrMo alloy and alumina) after FBS adsorption. The homogeneity and the thickness of the adsorbed protein layer is such high that the substrate is no more detected: it can be supposed that not only albumin, but even other proteins are adsorbed when these substrates are exposed to a mixture of different proteins such as in the case of FBS. A progressive lower amount of adsorbed proteins is detected in the case of albumin on the untreated Ti6Al4V alloy; in the case of treated Ti6Al4V alloy, there is a similar degree of coverage both in the case of BSA and FBS adsorption. It is of interest note that the treated Ti6Al4V alloy only slightly decreases the amount of adsorbed proteins when exposed to a mixture of different proteins, with a peculiar behaviour with respect to the other substrates. In any case, both the tested Ti6Al4V alloys has a higher affinity for albumin than the other substrates. Then, a still lower amount of adsorbed protein occurs in the case of FN adsorption on the untreated and treated Ti6Al4V alloy. As last, the lowest amount of adsorbed protein is detected on CoCrMo and alumina after soaking in albumin: these substrates show a very low affinity for this protein.

It must be considered (as described in Chapter 4) that the concentration of FN in the solution used for adsorption was 2 order of magnitude lower than that of

BSA: this means that Ti based materials have a strong ability to bind FN even if from diluted solutions. These considerations concerning the coverage degree (based on the N/Metal ratio) are in agreement and confirm the previous ones based only on the amount of the elements of the substrates detected after adsorption.

It is not easy to compare these data with literature because of the wide range of different experimental conditions used; moreover, concerning alumina, it was much more analysed as a powder (with great difference in surface charge with respect to the bulk material considered in this work) rather than a bulk material. Several factors play a role in the amount of adsorbed proteins including hydrophobicity/hydrophilicity, surface chemistry, presence and reactivity of surface functional groups, polar component of surface charge. The range of materials explored in this work is wide, with a wide range of surface properties, and it is not possible to find a direct correlation between a specific surface properties and the amount of adsorbed proteins. In any case, it is of interest to notice that a low amount of adsorbed albumin is observed in this work and it is reported in literature on negatively surface charge alumina [19].

As regards the  $N/C_{tot}$  ratio, looking at Table 5.23, the calculated ratios are lower than the theoretical ones. This suggests that organic contaminations are present on the surfaces even after adsorption.

### XPS analyses: high resolution analysis of surfaces before protein adsorption

High resolution analyses were also performed for the carbon, oxygen, nitrogen and titanium regions of the substrates before and after protein adsorption.

In Figure 5.133 is reported the high resolution analysis of the carbon region for the substrates before protein adsorption.

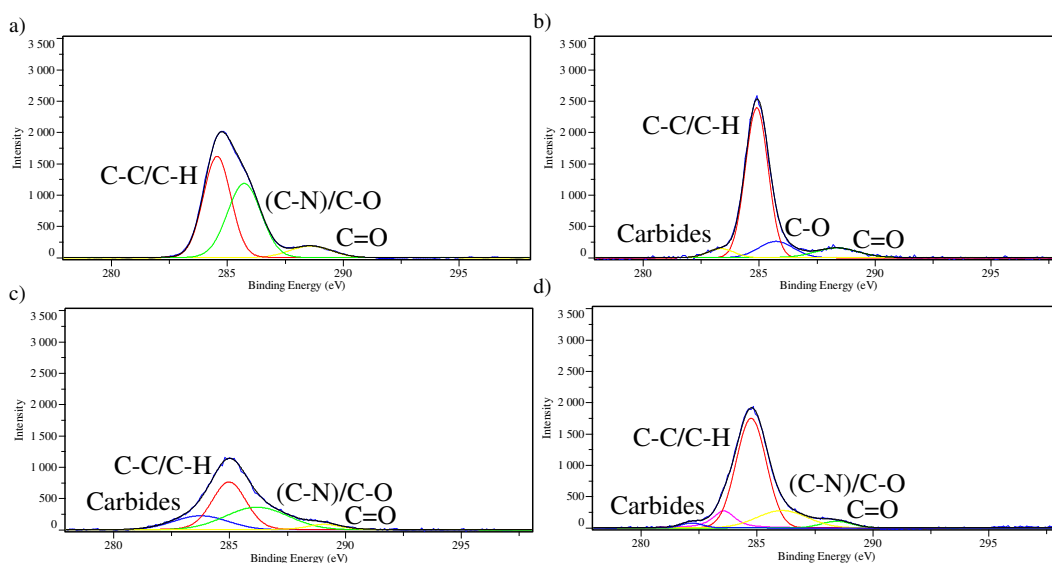


**Figure 5.133 Carbon region of the a) untreated Ti6Al4V alloy, b) CoCrMo alloy, c) alumina and d) treated Ti6Al4V alloy before protein adsorption**

The spectra of the carbon region show that in all cases there are three main peaks around the binding energy of 284 eV, 285 eV/ 286 eV and 288 eV, that correspond respectively to C-C/C-H, C-N/C-O and C=O bonds [26,27]. The hydrocarbon, carbides and carbonate signals on the bare materials before protein adsorption are due to contaminations of the surface, that are unavoidable on reactive surfaces. The peak in the range of energies between 285 eV and 286 eV is due to the signals of C-N and C-O bonds, that are very close to each other. The main contribution can be ascribed to the C-O bond, according to the low percentage of nitrogen on all the substrates (Table 5.22), in particular there are no traces of nitrogen on the CoCrMo alloy, thus the signal at 285.7 eV is only due to the C-O bond of surface contaminants. Small peaks are also visible at low energies, around 282/283 eV, they correspond to the signals of carbides, maybe due to contaminations from the abrasive paper used for polishing.

The spectra of the oxygen region before protein adsorption are reported in Figure 5.134.

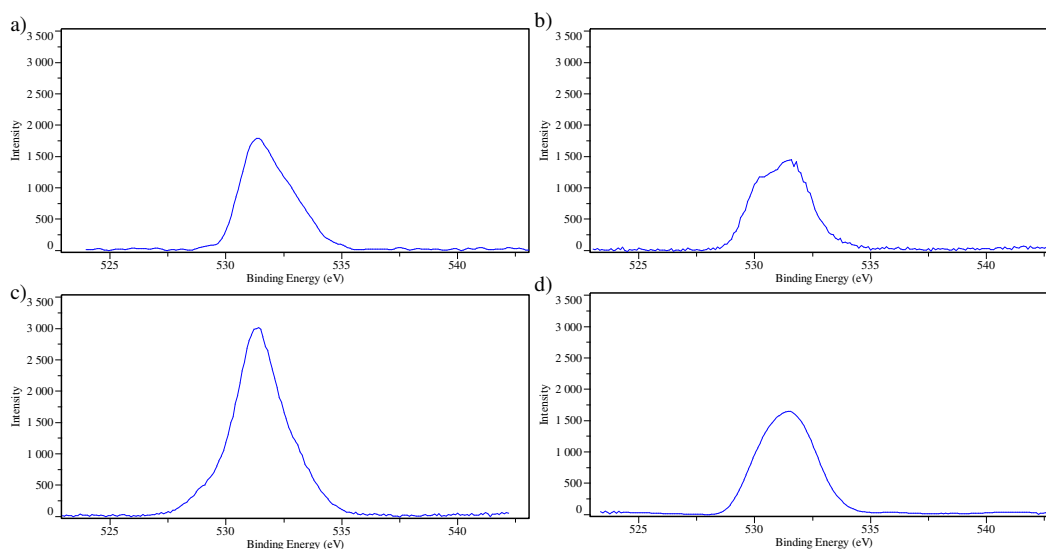


**Figure 5.134 Oxygen region of the a) untreated Ti6Al4V alloy, b) CoCrMo alloy, c) alumina and d) treated Ti6Al4V alloy before protein adsorption**

As reported by the Handbook of X-ray photoelectron spectroscopy [27] signals of metal oxides, OH groups, C=O and C-O bonds fall in a close range of binding energies. The signal of the metal oxides is in the energy range between 529.8 eV and 530.9 eV, the range of energies of OH groups is 530.9 – 532 eV, while C=O and C-O bonds fall respectively at the binding energies of 532.2 eV and 532.8 eV. Taking into account this information, the deconvolution of this region results to be very complex and arbitrary, thus the O1s spectra were not de-convoluted. In this case, it was evaluated the shape and the width at the half height of the signals, that are reported in Table 5.24.

**Table 5.24 Width at the half height of the signals before protein adsorption**

Material	Untreated Ti6Al4V	CoCrMo	Alumina	Treated Ti6Al4V
Width	2.58	2.81	2.59	2.87



In all cases there is the contribution both of the substrate (metal oxides) and the organic contaminants (C=O and C-O bonds). The contribution of the substrate is the main one in the case of alumina, where the signal is more intense and the maximum of the intensity falls toward lower energies. In the case of the untreated Ti6Al4V alloy and CoCrMo alloy the signals have a hump toward the higher energy, due to the C=O and C-O bonds of the organic contaminations on the surfaces. As regards the treated Ti6Al4V alloy, the signal is almost symmetric, this suggests a major contribution of the substrate and a minor contribution of the contaminants. The width at the half height of the signals will be used for the comparison of the surface chemistry after protein adsorption.

Figure 5.135 shows the spectrum of the nitrogen region before protein adsorption of the treated Ti6Al4V alloy. This is the material with the highest amount of nitrogen before protein adsorption, due to surface contaminations (Table 5.22). The spectrum of the nitrogen region in the case of CoCrMo alloy was not collected because no trace of nitrogen was detected on the surface (Table 5.22), while in the case of untreated Ti6Al4V alloy and alumina the spectra result to be flat, only the noise of the background was detected, thus the spectra were not reported, because there were not any evident signals.

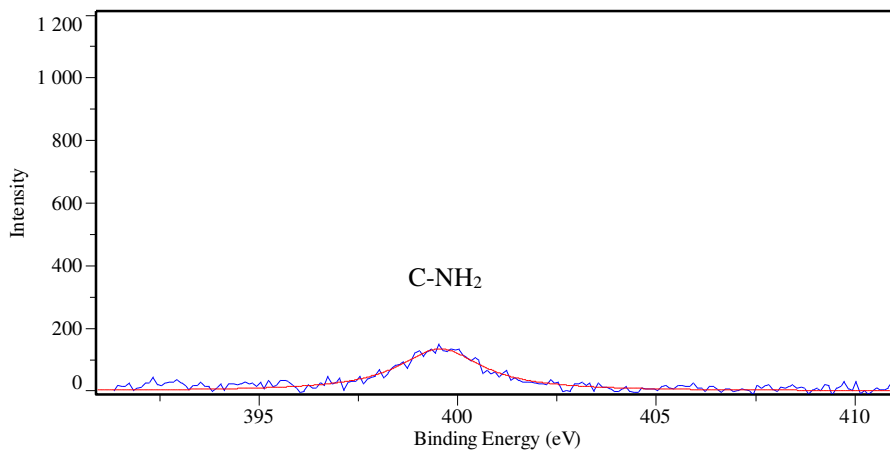


**Figure 5.135 Nitrogen region of the treated Ti6Al4V alloy before protein adsorption**

The treated Ti6Al4V alloy spectrum shows a small peak of the C-NH<sub>2</sub> bond of the organic contaminants at the binding energy of 399.6 eV [28].

The spectra of the titanium region of the untreated and treated Ti6Al4V was compared in Figure 5.136.

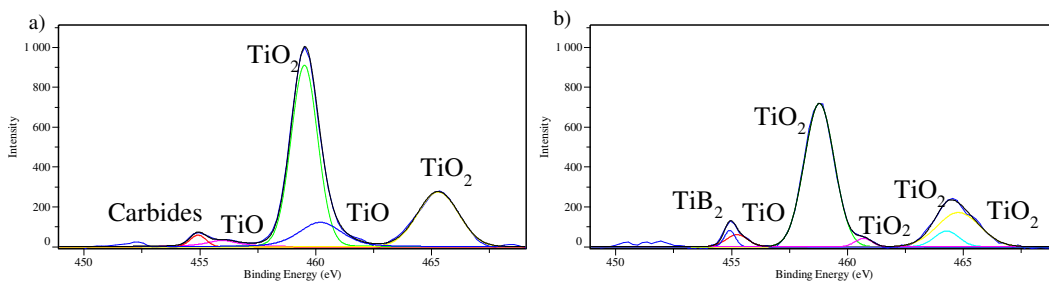


**Figure 5.136 Titanium region of the a) untreated and b) treated Ti6Al4V alloy before protein adsorption**

The spectrum of the titanium region of the untreated Ti6Al4V alloy before protein adsorption show the main peaks of TiO<sub>2</sub> at the binding energy of 459.5.3 eV and 465 eV and two small peaks of the TiO bond at the energies of 455.9 eV (Ti2p3/2) and 460.2 eV (2p1/2). Moreover, it possible to see a small peak at the binding energy of 454.9 eV (Ti2p2/3) due to carbides, related to surface contaminations [27,29]. In the case of treated Ti6Al4V alloy, the spectrum shows the peaks of the coating: TiB<sub>2</sub> (454.9 eV), TiO (455.2 eV) and TiO<sub>2</sub> (458.8 eV, 460.7 eV, 464.3 eV and 464.8 eV). The presence of TiO and TiO<sub>2</sub> signals allows to suppose that the borided layer is subjected to oxidation in air environment, as well as the untreated Ti6Al4V alloy, developing a thin TiO<sub>2</sub> layer on the surface. Literature data, in fact, report that the oxidation product of the TiB<sub>2</sub> are TiO<sub>2</sub> and B<sub>2</sub>O<sub>3</sub>, the latter maybe in the amorphous phase [14].

### XPS analyses: high resolution analysis of surfaces after BSA adsorption

After protein adsorption the high resolution analysis was focused on the carbon, nitrogen and oxygen region.

In the case of BSA adsorption the spectra of carbon region are shown in Figure 5.137.

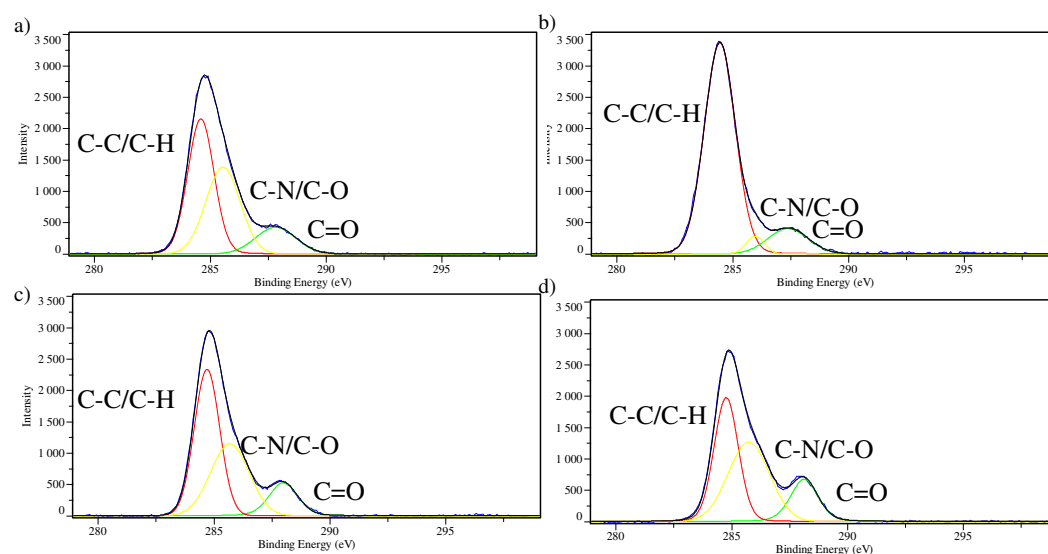


**Figure 5.137 Carbon region of the a) untreated Ti6Al4V alloy, b) CoCrMo alloy, c) alumina and d) treated Ti6Al4V alloy after BSA adsorption**

All the spectra have three peaks: C-C/C-H bond (~284.4-284.9 eV), C-N/C-O bonds (285-286 eV) and C=O (287-288 eV), as well as in the spectra of the substrate before BSA adsorption [26,27]. In this case, these signals are due to both surface contaminations and the presence of the proteins. A consistent contribution from the adsorbed proteins can be supposed, observing the intensity of the C=O bond, that increases in all the substrates after adsorption.

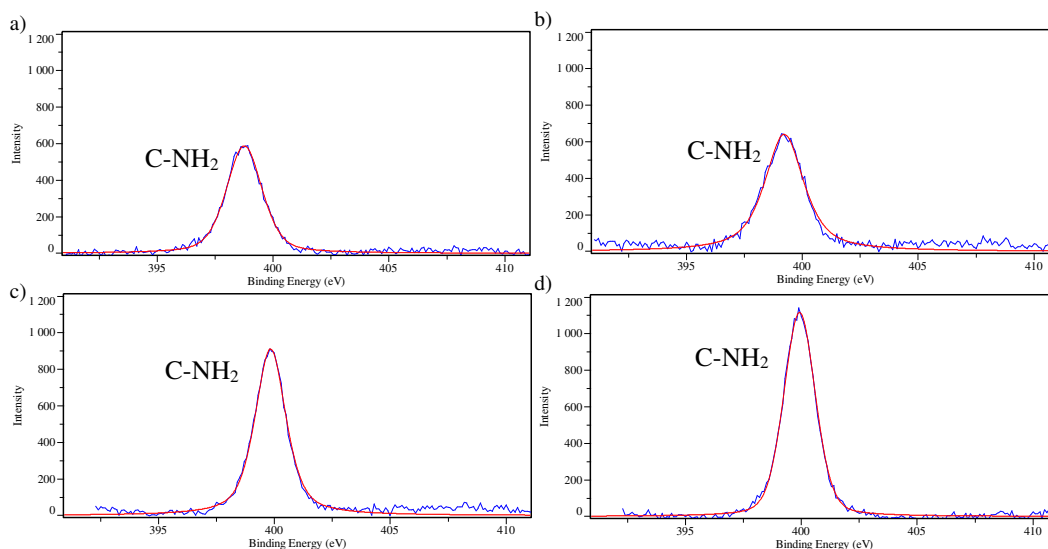


**Figure 5.138 Nitrogen region of the a) untreated Ti6Al4V alloy, b) CoCrMo alloy, c) alumina and d) treated Ti6Al4V alloy after BSA adsorption**

All the spectra of the nitrogen region (Figure 5.138) show the peaks of the C-NH<sub>2</sub> bond of the adsorbed protein. The signals of the untreated Ti6Al4V alloy and CoCrMo alloy are respectively at the binding energy of 398.7 eV and 399.2 eV, while the ones of the treated Ti6Al4V alloy and alumina fall respectively at the binding energy of 399.9 eV and 399.8 eV [28]. It is visible a shift of the signals of the ceramic materials (alumina and treated Ti6Al4V alloy) after adsorption in comparison to the ones of the substrates before adsorption and of the metallic materials (untreated Ti6Al4V alloy and CoCrMo alloy) after adsorption. This shift of the C-N bond is not observable in the carbon region, where the peaks of the C-N/C-O bond are at the binding energy of 285.8 eV, 285.9 eV, 285.7 eV and 285.7 eV respectively for the untreated Ti6Al4V alloy, CoCrMo alloy, alumina and treated Ti6Al4V alloy. This may be due to the overlap of the binding energy region of the C-O bond to the one of the C-N, that do not allow to point out the shift of the signals. The shift to higher energies in the nitrogen region suggests a chemical interaction between the protein and the surfaces in case of treated Ti6Al4V alloy and alumina than on the metals alloys. This is in agreement with the hypothesis formulated on the basis of the zeta potential titration curves after adsorption in solutions at different pH. Moreover, the absence of NH<sub>3</sub><sup>+</sup> in the XPS signal indicates that the type of the chemical interaction is not electrostatic: BSA does not bond to the ceramic materials through donation of H<sup>+</sup> from the acidic OH functional groups on the ceramic surfaces to the NH<sub>2</sub> groups of the protein, as it could be supposed. According to all the acquired data, it can be supposed that a chemical interaction between the COOH groups of the protein and the OH acidic groups of the surfaces occurs; the formation of the chemical bond between the protein and the surface seems to affect, as a consequence, also the energy of the C-N bonds within the protein, as it can be deduced from the analysis of the nitrogen region.

As regards the oxygen region, as already explained, the spectra were not deconvoluted and the evaluation was based on the shape (Figure 5.139) and width at the half height of the main peaks (Table 5.25).

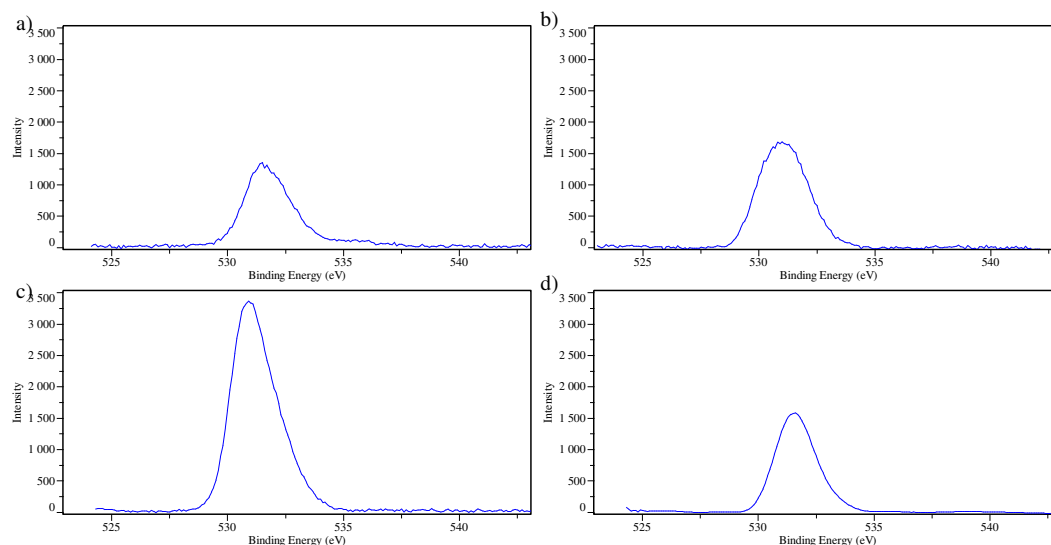


**Figure 5.139** Oxygen region of the a) untreated Ti6Al4V alloy, b) CoCrMo alloy, c) alumina and d) treated Ti6Al4V alloy after BSA adsorption

**Table 5.25** Width at the half height of the signals after BSA adsorption

Material	Untreated Ti6Al4V	CoCrMo	Alumina	Treated Ti6Al4V
Width	2.22	2.46	2.23	2.02

The signals are due to the contribution of the oxygen of the substrates and the C=O and C-O bonds of the protein and organic contaminants. It can be noted that the width at the half height of the signals is consistently lower than it was on the substrates: a consistent contribution from oxygen within BSA can be hypothesized. Taking into account the N/Metal ratio (Table 5.23), it is possible to say that the contribution of the oxygen of the substrate is higher in the case of alumina and CoCrMo alloy (ratio of 0.94 and 0.97 respectively), while it is lower in the case of untreated and treated Ti6Al4V alloy (ratio respectively of 21.50 and 13.89). In addition, the signal of the treated Ti6Al4V alloy is the one with the minor width at half height, this indicates a less dispersion of the signal and that in this case the main contribution is the one of the oxygen within the protein bonds. In any case, it is difficult to make any hypothesis on the basis of this region where so many chemical bonds can contribute.

### **XPS analyses: high resolution analysis of surfaces after FN adsorption**

As regards the FN adsorption, Figure 5.140 reports the spectra of carbon region.

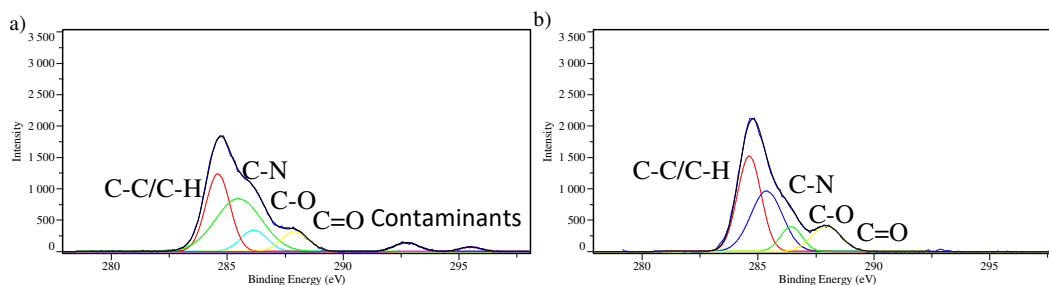


**Figure 5.140 Carbon region of the a) untreated and b) treated Ti6Al4V alloy after FN adsorption**

The two spectra show the peaks of C-C/C-H (284.6 eV), C-N (285.5 eV), C-O (around 286 eV) and C=O (around 288 eV), as well as in the previous spectra [26,27]. As in the case of BSA adsorption, these signals are due to both surface contaminations and the presence of the proteins. The untreated Ti6Al4V alloy has a more evident hump due to the C-N/C-O bond of protein, while the treated Ti6Al4V alloy has a more pronounced hump of the C=O signal. On the spectrum of the untreated material two small peaks are also visible at high energies, they are due to surfaces contaminants but they were not attributed.

The nitrogen region is shown in Figure 5.141.

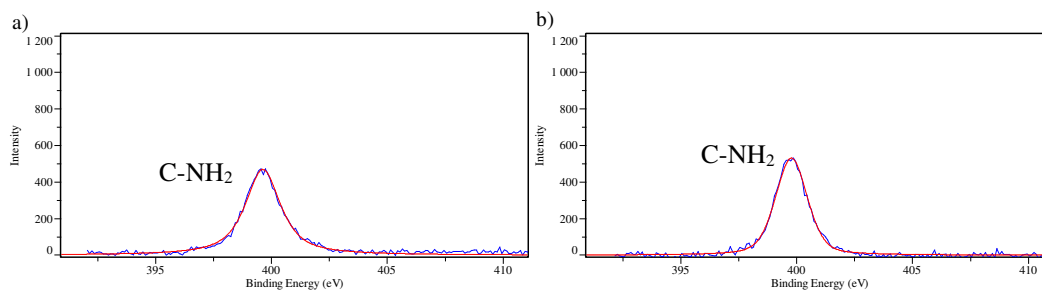


**Figure 5.141 Nitrogen region of the a) untreated and b) treated Ti6Al4V alloy after FN adsorption**

The C-NH<sub>2</sub> signal of the protein is well-defined on both spectra and it falls at the binding energy of 399.6 eV and 399.8 eV respectively for the untreated and treated Ti6Al4V alloy [28]. Differently to the case of the BSA, the C-NH<sub>2</sub> bond peak falls at the same binding energy for the two substates, in this case there is no significant shift of the signal. Considering all the data acquired, a chemical interaction between the protein and the treated Ti6Al4V surface can be hypotized (according to zeta potential data), but no donation of H<sup>+</sup> from the acidic OH functional groups on the ceramic surfaces to the NH<sub>2</sub> groups of the protein occurs (according to XPS data in nitrogen region). Again, the chemical interaction seems to occur through the COOH groups of the protein, but, in the case of FN, it does not affect the energy of the bond of the C-NH<sub>2</sub> groups within the adsorbed protein.

Figure 5.142 reports the oxygen region, as in the previous cases, the spectra were not deconvoluted and only the shape and width at the half height of the main peaks (Table 5.26) were evaluated.

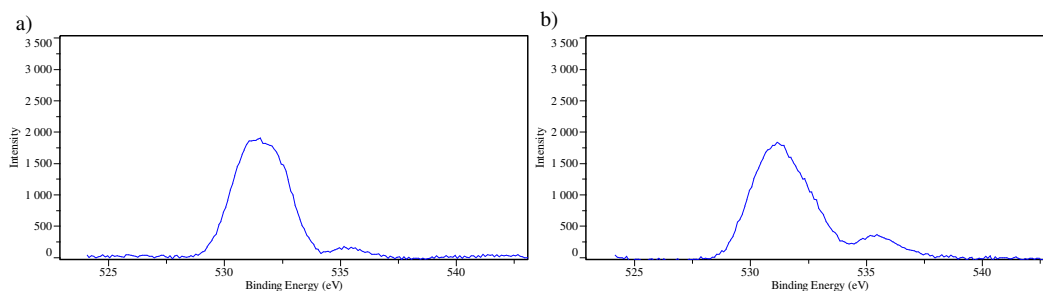


**Figure 5.142 Oxygen region of the a) untreated and b) treated Ti6Al4V alloy after FN adsorption**

**Table 5.26 Width at the half height of the signals after FN adsorption**

Material	Untreated Ti6Al4V	Treated Ti6Al4V
Width	2.73	2.85

The two signals have different shape, but similar width at half height (that is not far from that of the substrates before absorption). Both the spectra show a main peak due to the contribution of the oxygen of the substrate and the C=O and C-O bonds of the protein and organic contaminants and a small peak that is related to adsorbed water [29]. The N/Metal ratios (Table 5.23) suggest that the contribution of the oxygen of the substrate is predominant and no further consideration can be done in this case

### XPS analyses: high resolution analysis of surfaces after FBS adsorption

Figure 5.143 shows the carbon region of the materials after FBS adsorption.

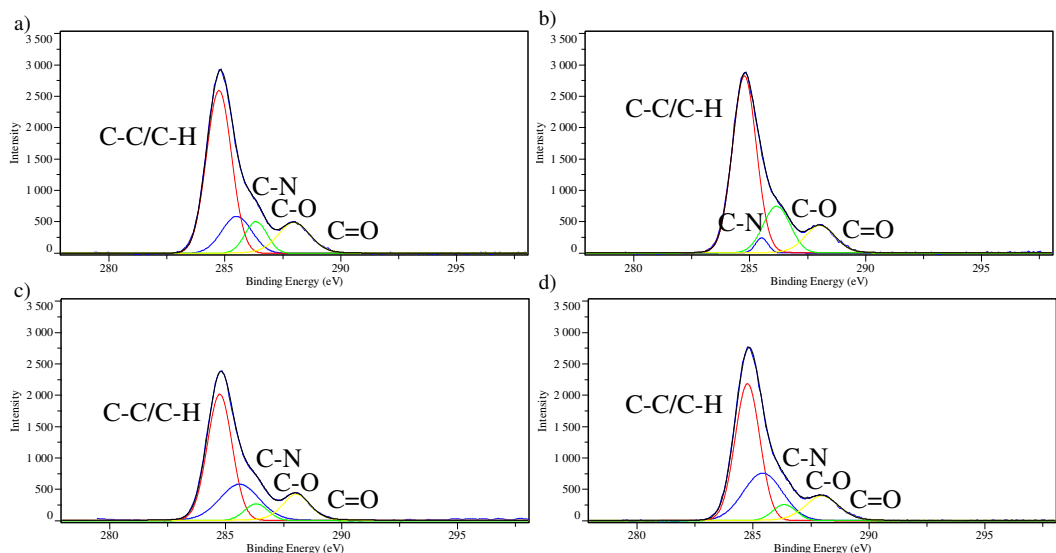


**Figure 5.143 Carbon region of the a) untreated Ti6Al4V alloy, b) CoCrMo alloy, c) alumina and d) treated Ti6Al4V alloy after FBS adsorption**

All spectra show the peaks of C-C/C-H bond (~284.6-284.8 eV), C-N (~285.1-285.5 eV), C-O bonds (~286.0-286.2 eV) and C=O (~288.0 eV) [26,27]. As in the case of BSA and FN adsorption, these signals are due to both surface

contaminations and the presence of the proteins. All the spectra have a similar shape with a well-defined hump of the C=O bond. No evident differences are visible among the spectra, this suggests a great coverage of the surface and that only the signals of the protein layer are detected.

The nitrogen region is shown in Figure 5.144.

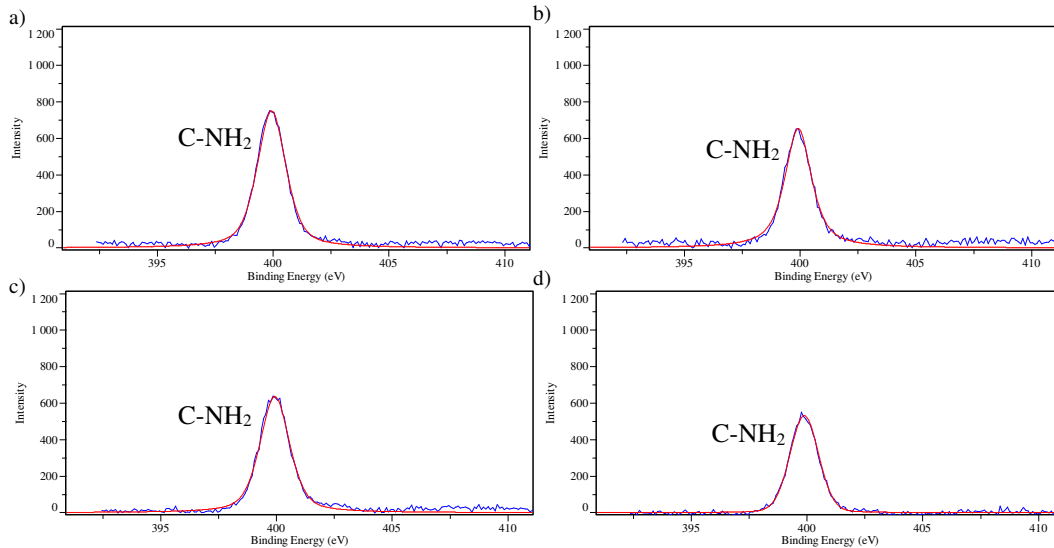


**Figure 5.144** Nitrogen region of the a) untreated Ti6Al4V alloy, b) CoCrMo alloy, c) alumina and d) treated Ti6Al4V alloy after FBS adsorption

Also in this case, only the peak of the C-NH<sub>2</sub> bond of the adsorbed protein is detected on all the spectra. The signals fall all at the binding energy of 399.9 eV. As in the case of carbon region, no differences are observed among the spectra. This is a further confirmation of the high amount of adsorbed protein on the surfaces.

Focusing on the oxygen region (Figure 5.145), also in this case there are not any significant differences among the spectra. All the spectra have a prominent tail towards the high energies.

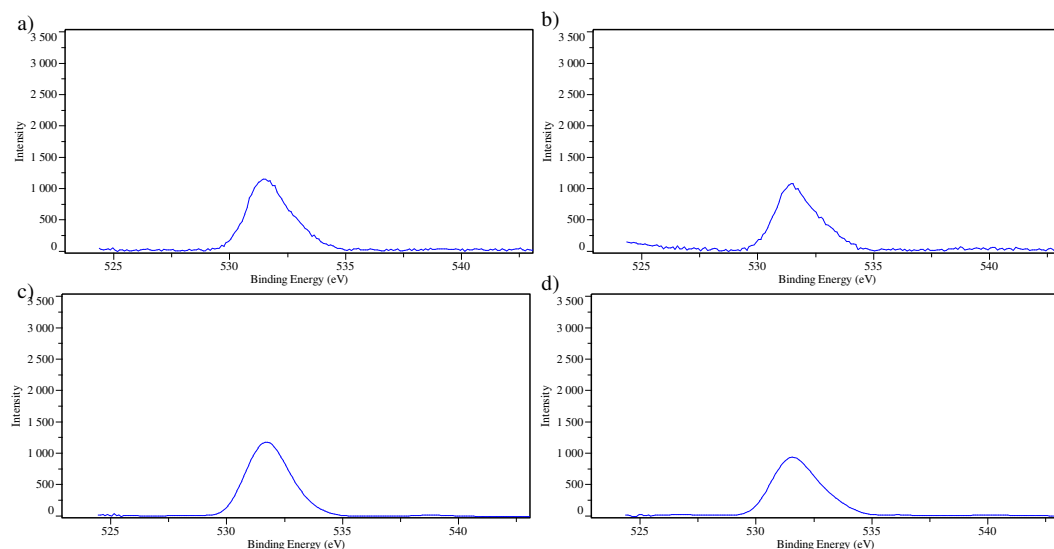


**Figure 5.145** Oxygen region of the a) untreated Ti6Al4V alloy, b) CoCrMo alloy, c) alumina and d) treated Ti6Al4V alloy after FBS adsorption

As previously, only the shape and the width at half height were taken into account. The widths are reported in Table 5.27. In this case, analogously to the surfaces after adsorption of BSA, the width of the peak is quite lower and probably the contribution of the bonds within the protein are dominant. In any case, it is difficult to make any hypothesis on the basis of this region where so many chemical bonds can contribute.

**Table 5.27 Width at the half height of the signals after FBS adsorption**

Material	Untreated Ti6Al4V	CoCrMo	Alumina	Treated Ti6Al4V
Width	2.15	2.11	2.20	2.36

### XPS analyses: high resolution analysis of boron region

The boron region of the treated Ti6Al4V alloy before and after protein adsorption is interesting to be analysed as shown in Figure 5.146.

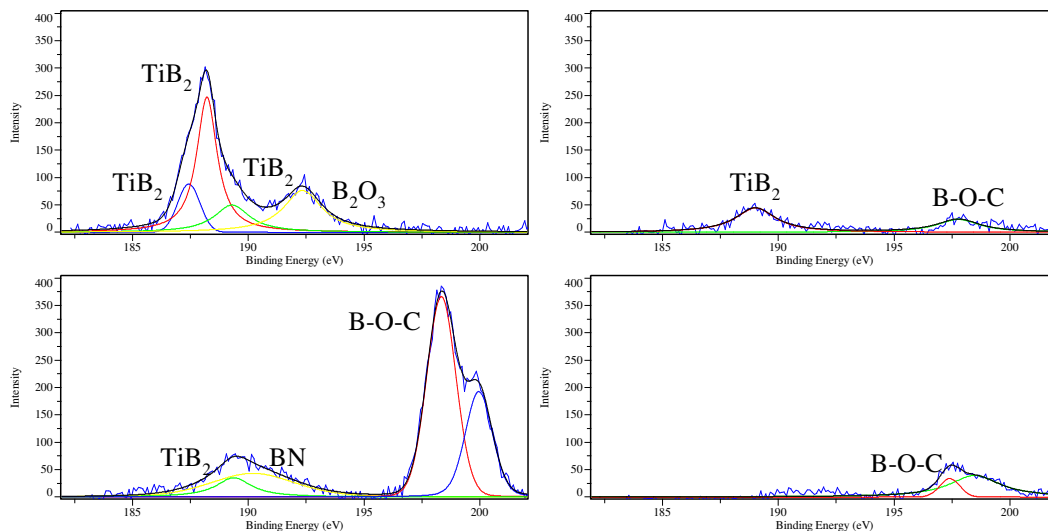


**Figure 5.146 Boron region of the treated Ti6Al4V alloy a) before protein adsorption b) after BSA adsorption, c) FN adsorption and d) FBS adsorption**

It is possible to observe a significant difference between the spectrum of the treated material before and after protein adsorption.

The spectra of the treated Ti6Al4V alloy before protein adsorption shows the signals of the  $TiB_2$  and  $B_2O_3$  bonds [27]. The first is the compound already detected by XRD in the coating, while the second indexes a thin boron oxide layer on the surface. The contribution of  $TiB_2$  is significantly lower after protein adsorption, as expected. On the spectra of the treated material after BSA and FN adsorption, a small peak of the  $TiB_2$  is still present while in the case of FBS it is not visible any more: this is in agreement with the thicker layer of adsorbed protein in the case of soaking in FBS.

After protein adsorption, on all the spectra, a peak composed by two signals is visible around the binding energy of 197-199 eV, while the signal of  $B_2O_3$  is no more detected. The signal at lower energy (in the range 197-199 eV) can be



assigned to the C–O–B bond and it indicates the formation of a specific bond between the proteins and the boride layer. In fact, in literature it is reported that borate ions can form chemical covalent bonds with several groups containing oxygen such as carboxyl groups [30]. It is supposed that also the second signal, the one at higher energy (in the range 197-199 eV), is related to the bond between the proteins and the surface, but it was not attributed. The peak in the region of 197-199 eV has a low intensity in the case of the treated Ti6Al4V alloy after BSA and FBS adsorption, in particular in the case of BSA the peak is so small, that the two signals cannot be splitted. In the case of the treated Ti6Al4V alloy after FN adsorption, the spectrum shows the peak of the BN bond and a very intense peak of the B-O-C bond are present. This suggests that the borided layer interacts both with the COOH and NH<sub>2</sub> groups with formation of covalent bonds. The higher intensity of this peak, even if the amount of adsorbed protein is lower in the case of FN (according to the lower N/Metal ratio -Table 5.23) than in the case of BSA and FBS, allows to suppose that the bond between B of the surface and FN is stronger in the case of FN than for BSA.

In conclusion it is possible to say that:

- BSA is bonded differently on metals alloys (Ti6Al4V and CoCr) and ceramic materials (alumina and treated Ti6Al4V alloy). A chemical interaction between the COOH groups of BSA and the OH acidic groups of the ceramic surfaces occurs; the formation of the chemical bond between the protein and the ceramic surface seems to affect, as a consequence, also the energy of the C-N bonds within the protein. In the case of the treated Ti6Al4V alloy, a contribution to the bond of BSA with the surface comes from the B-O-C covalent bond.
- In the case of FBS, the spectra of the materials do not show any evident differences, they seem behave in the same way.
- The FN interacts strongly with the treated Ti6Al4V alloy. The chemical interaction seems to occur mainly through the COOH groups of the protein with a strong contribution due to the formation of B-O-C covalent bond (higher than in the case of BSA) and a small contribution of the B-N bond. The chemical bond between the surface and FN does not affect the energy of the bond of the C-NH<sub>2</sub> groups within the adsorbed protein.

XPS analyses give also information about the most external layer of the titanium borided coating. It results to be subjected to oxidation in contact with air environment, developing two oxide products: TiO<sub>2</sub> and B<sub>2</sub>O<sub>3</sub>. Both these compounds are not visible by means of XRD analyses, while their signals are observed on the titanium and boron region of XPS analyses. Probably, on one side, the external oxide layer, composed of TiO<sub>2</sub> and B<sub>2</sub>O<sub>3</sub>, is too thin to be detected through diffraction analyses, the signals are hidden by the most intense signals of TiB and TiB<sub>2</sub>. On the other side, as literature suggests the crystallographic structure of the B<sub>2</sub>O<sub>3</sub> can be amorphous [14]. In conclusion it can be ipotised a structure of the coating as shown in Figure 5.147.



Figure 5.147 Scheme of the titanium borided coating for the samples without any pre/post treatment

## BCA Protein Assay Kit analysis

The BCA Protein Assay method was used to quantify the amount of adsorbed proteins in the case of pure FBS adsorption.

Figure 5.148 shows the diluted standard from the most concentrated to the blank and the solution of detached protein of the samples of the different materials (untreated and Ti6Al4V alloy treated at 1050°C for 4.5 h without any pre/post treatment) after being incubated for 30 minutes at 37°C with the working reagent of the BCA kit.

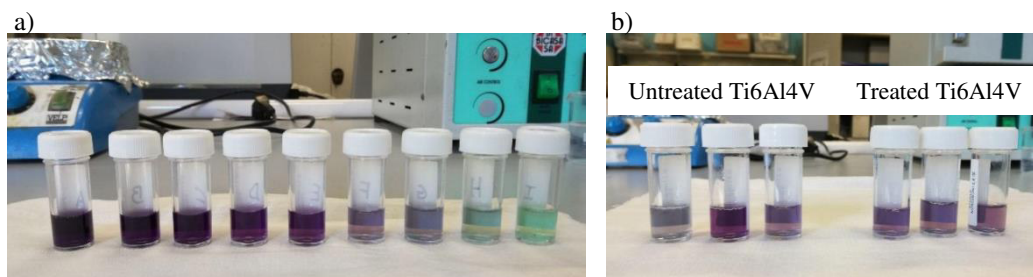


Figure 5.148 a) Standards and b) samples

The standard curve of BSA (obtained through UV spectroscopy as described in Chapter 4) and the obtained concentrations of the protein solutions detached by the examined surfaces are reported in Figure 5.149.

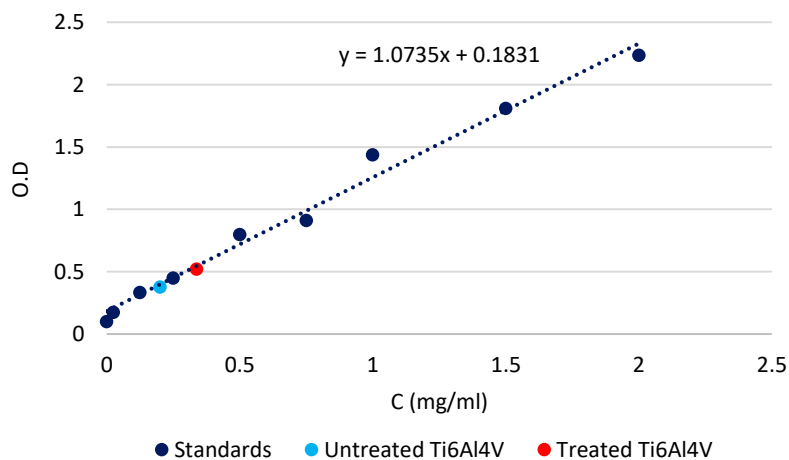


Figure 5.149 Standard curve and concentration of untreated and Treated Ti6Al4V alloy

The amount of adsorbed proteins on the untreated Ti6Al4V alloy surface is  $0.8 \pm 0.4 \mu\text{g}/\text{mm}^2$  while the one of the treated Ti6Al4V alloy surface is  $1.3 \pm 0.2 \mu\text{g}/\text{mm}^2$ . The amount of adsorbed proteins has the same magnitude order in both cases. Nevertheless, the untreated alloy has a lower protein adsorption with a higher standard deviation than the treated alloy. The higher variability of data of the untreated Ti6Al4V alloy is also evident looking at Figure 5.148, where it is possible to observe a different colour of the three replicates of untreated Ti6Al4V sample. The different colours suggest a different protein concentration into the solutions.

It can be concluded that no huge difference in the amount of protein adsorption can be expected on the boride coating with respect to the substrate, while it mainly differs (as previously described) for the type of bond between the surface and proteins and configuration of adsorbed proteins on it.

### 5.3.12 In vitro bioactivity evaluation

According to the presence on the treated Ti6Al4V alloy of a consistent amount of OH groups with acidic behaviour and complete dissociation at physiological pH, bioactivity of the borided alloy was tested in Simulated Body Solution. Actually, the main purpose of this thesis was not osseointegration, but considering the great relevance of this topic concerning Ti6Al4V alloy it was briefly evaluated. Bioactivity of the treated Ti6Al4V alloy without any pre-post treatment (treated at  $1050^\circ\text{C}$  for 4.5 h) was evaluated at 14 and 28 days by soaking the samples in simulated body fluid for (SBF), as described in Chapter 4.

Table 5.28 reports the pH values of the SBF solution collected each 7 days.

**Table 5.28 pH values of SBF**

	pH sample 1	pH sample 2	pH sample 3	pH sample 4
<b>0 day</b>	7.41	7.41	7.41	7.41
<b>7 days</b>	7.21	7.21	7.26	7.22
<b>14 days</b>	7.22	7.22	7.22	7.20
<b>21 days</b>			7.13	7.04
<b>28 days</b>			7.34	7.34

The SBF had an initial pH of 7.41, the standard pH of Kokubo solution [31]. After 7 days the pH is decreased and after 14 days it is stable. After 7 days the pH is decreased and after 14 days it is stable. After 21 days it is possible to observe a further decrement of the pH, that increases again after 28 days. The pH values are homogenous on the 4 samples with small fluctuations.

FESEM observation and EDS analyses were carried out to evaluate the presence of hydroxyapatite. Figure 5.150 shows the surface of the sample 1 after 14 days of SBF incubation. Both samples 1 and 2 were observed, no difference was detected between the two samples, thus only the images of one sample were reported as example.

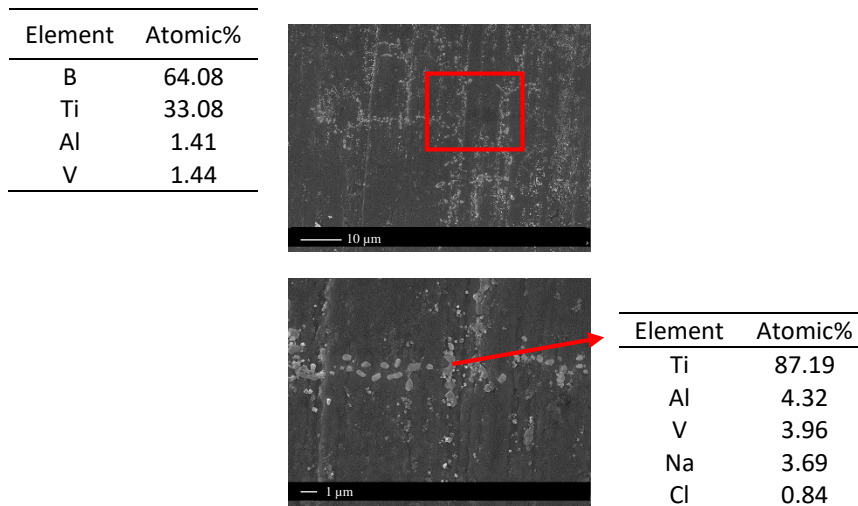


**Figure 5.150** FESEM images and EDS analyses of the surface of a Ti6Al4V alloy sample without any pre/post treatment treated at 1050°C for 4.5 h and soaked in SBF for 14 days

On the surface some deposits are visible, nevertheless EDS analyses do not detect any traces of Ca and P, thus of the hydroxyapatite. On the surface there is only salts precipitation, indexed by the presence of Na and Cl coming as contaminations from the SBF solution.

The images of the surface of the sample soaked for 28 days are shown in Figure 5.151. Also in this case, the two samples incubated for 28 days do not show any differences, thus only the images of one sample were reported.

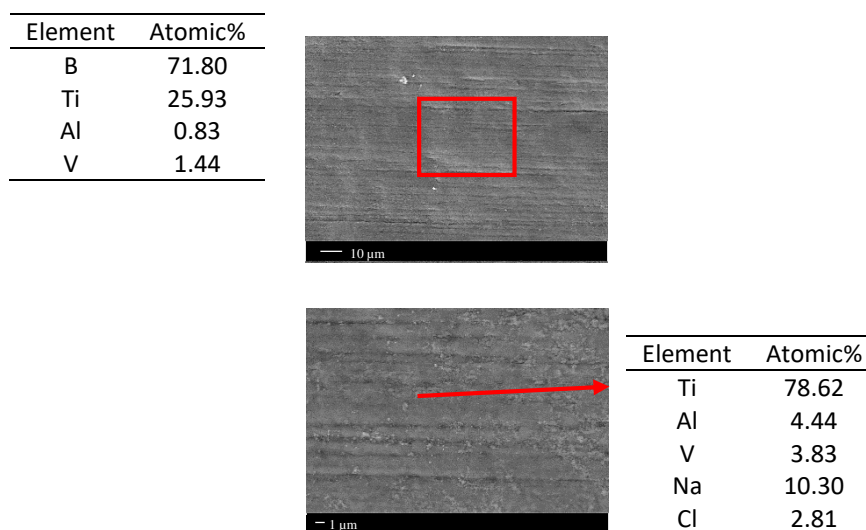


**Figure 5.151** FESEM images and EDS analyses of the surface of a Ti6Al4V alloy sample without any pre/post treatment treated at 1050°C for 4.5 h and soaked in SBF for 28 days.

Also after 28 days there is no trace of hydroxyapatite, on the surface there is only deposition of salts.

In conclusion, it is possible to say that the borided coating has not in vitro bioactive behaviour and thus it is not able to induce faster osseointegration. This observation can contribute to the discussion about the surface factors able to induce apatite precipitation on the treated Ti based material: according to these results, the

only presence of strong acidic OH groups is not enough and the concomitant role of surface porosity on the nanoscale or other factors must be evaluated.

## 5.4 Analysis of further mixtures of powders

In parallel to the characterization of the samples treated with the first powder composition, other powder compositions were studied, in order to obtain coatings with the same properties, but through treatments at lower temperature in order to avoid significant modification of the microstructure of the substrate. The mixtures of powders taken into account are derived from commercial powders for boronizing of steel. The rationale of this section is to explore boriding processes in salt mixtures which melt during the process in order to enhance boron diffusion depth even at lower temperature.

### 5.4.1 Characterization of the Ti6Al4V alloy grade 5 samples treated with the second composition of powder mixture (90%wt B<sub>4</sub>C – 10%wt KBF<sub>4</sub>)

Figure 5.152b shows one of the samples treated at 800°C for 3.5h with the second composition of powder mixture. The temperature of 800°C was selected in order to make the treatment below the beta transus temperature. Samples appear covered by a dark layer, deformed and no longer flat. The coating results to be brittle and in some cases it detached.

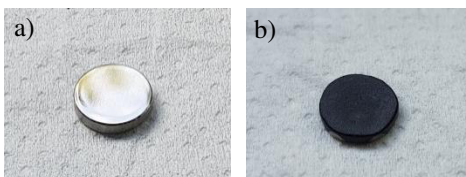
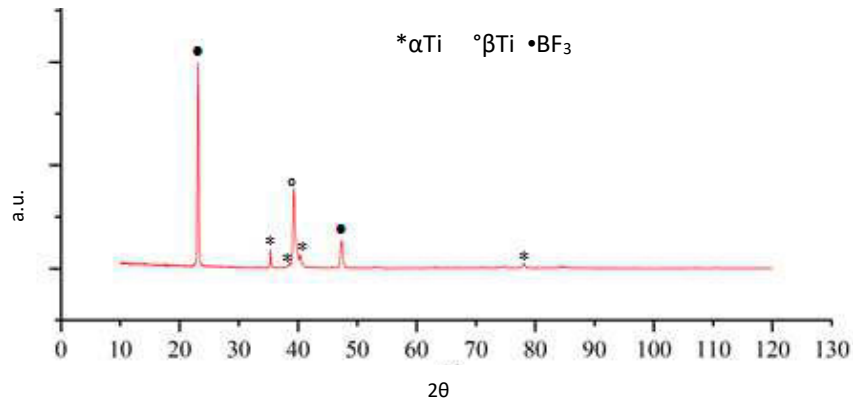


Figure 5.152 Picture of a) untreated sample and b) treated sample

XRD analysis (Figure 5.153) shows the peaks corresponding to Ti $\alpha$  and Ti $\beta$  phases, related to the substrate and the peaks of BF<sub>3</sub>. The dark layer visible on the substrates results to be composed of BF<sub>3</sub>.



**Figure 5.153 XRD patterns collected with Bragg-Brentano geometry on a sample treated at 800°C for 3.5 h**

It can be supposed that, during the thermal treatment, around 530°C, the  $\text{KBF}_4$  melts, dissociating in gaseous  $\text{KF}$  and  $\text{BF}_3$  that solidifies on the substrate during the cooling.

The damage of the samples is due to the presence of fluorides that are aggressive for Ti alloys. As consequence, this powder mixture is not suitable for boronizing Ti6Al4V alloy substrates.

### **5.3.2 Characterization of the Ti6Al4V alloy grade 5 samples treated with the third composition of powder mixture (5% wt $\text{B}_4\text{C}$ – 90% wt $\text{SiC}$ – 5% wt $\text{KBF}_4$ )**

The third composition of powder mixture has a lower amount of  $\text{KBF}_4$  than the second one, so it was supposed to be less aggressive than the previous one. In addition, the treatment was carried out for 3.5 h at two temperatures (800°C and 700°C) to evaluate if at lower temperature less damage of the substrate occurs. By means of visual investigation it is possible to see that the sample treated at 800°C is not deformed in shape and shows a not uniform pearlescent coating while the sample treated at 700°C show a dark coating and a thick layer of melted salts on surface. The samples are shown in Figure 5.154.



**Figure 5.154 Picture of a) untreated sample, b) sample treated at 800°C for 3.5h and c) samples treated at 700°C for 3.5h**

Samples treated at 700°C were subjected to polishing using SiC abrasive sheet of 4000 grit to remove the melted salts on surface. After the polishing, as Figure 5.155 shows, the sample still has a dark surface.

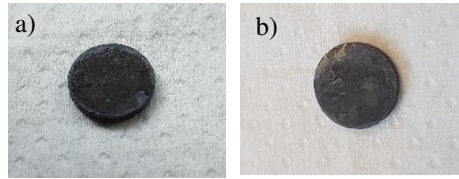


Figure 5.155 Picture of samples treated at 700°C with a) unpolished surface and b) polished surface

XRD analysis was carried out on a sample treated at 800°C and on a polished sample treated at 700°C. XRD patterns are reported in Figure 5.156.

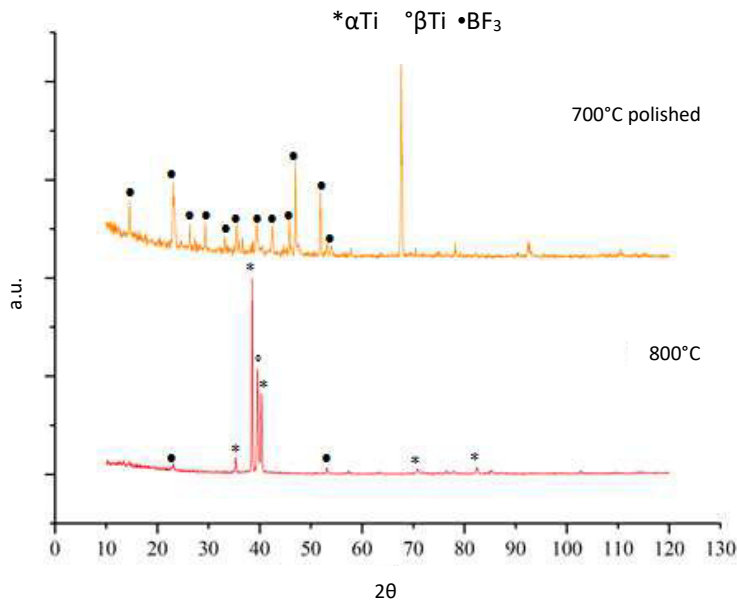


Figure 5.156 XRD patterns collected with Bragg-Brentano geometry of the sample treated at 800°C and at 700°C, the last one after polishing

The two samples present completely different patterns. The peaks of the substrate and the  $\text{BF}_3$  phase are visible on the pattern of the sample treated at 800°C, while the samples treated at 700°C results to be covered by a thick layer of  $\text{BF}_3$  and another unidentified compound.

No further investigation was performed and it was concluded that also in this case this kind of powder mixture is not suitable to treat a Ti6Al4V alloy substrate.

### 5.4.3 Characterization of the Ti6Al4V alloy grade 5 samples treated with the fourth composition of powder mixture (5% wt B<sub>4</sub>C – 95%wt KCl+KBF<sub>4</sub>)

The fourth composition of powder mixture was introduced to perform the treatment at even lower temperature in order to avoid corrosion of the surface, deformations and strong adhesion of the salt mixture to the surface. The treatment was carried out at 550°C for 3.5h and one of the treated samples is shown in Figure 5.157.

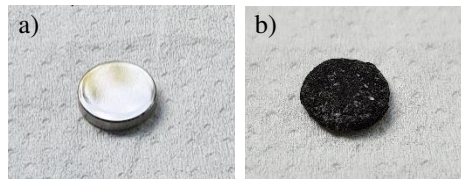


Figure 5.157 Picture of a) untreated sample and b) sample treated at 550°C for 3.5 h

By means of visual analysis it is possible to see that the sample is strongly damaged by the treatment. The sample is deformed in shape, not more planar and it shows residues of melted salts on surface, that are brittle and detaches from the surface.

The powder mixture contains mainly KBF<sub>3</sub>. It can be supposed that during the treatment BF<sub>3</sub> and KF are developed and chemically attach the substrate.

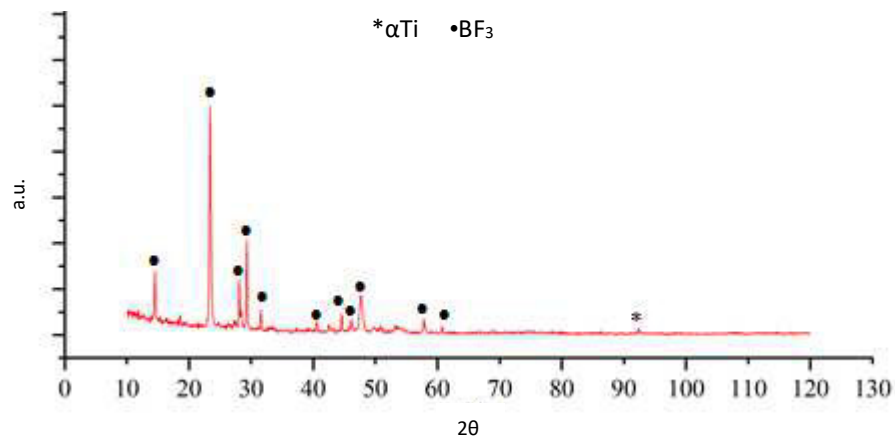


Figure 5.158 XRD patterns collected with Bragg-Brentano geometry of the sample treated at 550°C for 3.5 h

Figure 5.158 shows the pattern of the treated samples, also in this case the BF<sub>3</sub> phase was detected and the powder mixture cannot be used to boronizing Ti6Al4V alloy substrate, as in the previous cases.



#### 5.4.4 Characterization of the Ti6Al4V alloy grade 5 samples treated with the fifth composition of powder mixture (30% wt B<sub>2</sub>O<sub>3</sub> – 35% wt Activated Charcoal – 35% wt LiCl+KCl)

The fifth composition of powder mixture was introduced both to further lower the temperature of treatment and to avoid the corrosion of the surface by means of the fluorides. The samples were treated at 500°C and 400°C for 3.5 h in both cases. The activator based on F was substituted with an activator based on Cl, in order to be less aggressive for the substrate.

Figure 5.159 shows the sample after the treatment.

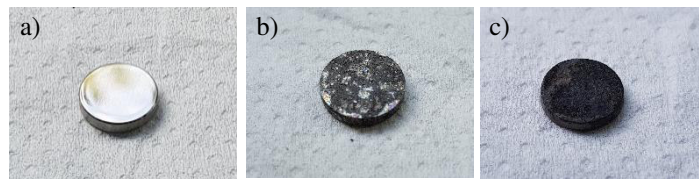


Figure 5.159 Picture of a) untreated samples, b) sample treated at 500°C and c) sample treated at 400°C

Both the samples show melted salts solidified on surface, in case of samples treated at 500°C, the melted salts layer was brittle and part of them detached during the washing, in case of sample treated at 400°C the melted salts layer is still visible on surface after the washing.

In this case XRD analysis does not give any indication about the external melted salts layer (probably amorphous) but only the peaks of the substrate elements were detected as Figure 5.160 shows.

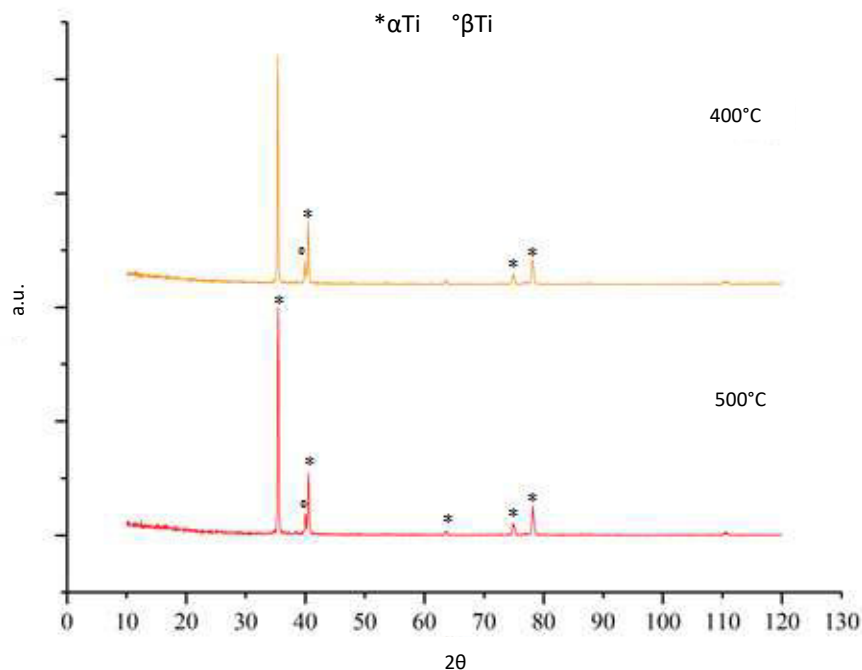


Figure 5.160 XRD patterns collected with Bragg-Brentano geometry of the samples treated at 500°C and at 400°C

It can be concluded that it was not possible to obtain a boride coating on Ti6Al4V through a process in the liquid state at a temperature below beta transus, because the explored salt mixtures induce corrosion of the surface (mainly in the presence of F), deformation of the substrate, strong attachment of the melted salts to the surface after solidification without any evidence of formation of the titanium boride layer. This strategy was not explored much more even if it could be still considered in the future.

# References

- [1] Sarma B, Tikekar NM, Ravi Chandran KS. Kinetics of growth of superhard boride layers during solid state diffusion of boron into titanium. *Ceramics International* 2012;38:6795–805. doi:10.1016/j.ceramint.2012.05.077.
- [2] Aich S, Ravi Chandran KS. TiB whisker coating on titanium surfaces by solid-state diffusion: Synthesis, microstructure, and mechanical properties. *Metallurgical and Materials Transactions A* 2002;33:3489–98. doi:10.1007/s11661-002-0336-6.
- [3] Gammon LM, Briggs RD, Packard JM, Batson KW, Boyer R, Dombay CW. *Metallography and Microstructures of Titanium and its Alloys*. Materials Park, OH: ASM International, 2004. 2004;9:899–917. doi:10.1361/asmhba0003779.
- [4] Niinomi M. Mechanical properties of biomedical titanium alloys. *Materials Science and Engineering A* 1998;243:231–6. doi:10.1016/S0921-5093(97)00806-X.
- [5] Miller M, Bobko C, Vandamme M, Ulm FJ. Surface roughness criteria for cement paste nanoindentation. *Cement and Concrete Research* 2008;38:467–76. doi:10.1016/j.cemconres.2007.11.014.
- [6] Şahin S. Effects of boronizing process on the surface roughness and dimensions of AISI 1020, AISI 1040 and AISI 2714. *Journal of Materials Processing Technology* 2009;209:1736–41. doi:10.1016/j.jmatprotec.2008.04.040.
- [7] Ponsonnet L, Reybier K, Jaffrezic N, Comte V, Lagneau C, Lissac M, et al. Relationship between surface properties (roughness, wettability) of titanium and titanium alloys and cell behaviour. *Materials Science and Engineering C* 2003;23:551–60. doi:10.1016/S0928-4931(03)00033-X.
- [8] Rupp F, Scheideier L, Olshanska N, De Wild M, Wieland M, Geis-Gerstorfer J. Enhancing surface free energy and hydrophilicity through chemical modification of microstructured titanium implant surfaces. *Journal of Biomedical Materials Research - Part A* 2006;76:323–34. doi:10.1002/jbm.a.30518.
- [9] Kubiak KJ, Wilson MCT, Mathia TG, Carval P. Wettability versus roughness of engineering surfaces. *Wear* 2011;271:523–8. doi:10.1016/j.wear.2010.03.029.
- [10] Pawlak Z, Urbaniak W, Oloyede A. The relationship between friction and wettability in aqueous environment. *Wear* 2011;271:1745–9. doi:10.1016/j.wear.2010.12.084.
- [11] Yan Y, Yang H, Su Y, Qiao L. Albumin adsorption on CoCrMo alloy

surfaces. *Scientific Reports* 2015;5:1–10. doi:10.1038/srep18403.

- [12] Ryu JJ, Shrotriya P. Mechanical load assisted dissolution response of biomedical cobalt-chromium and titanium metallic alloys: Influence of in-plane stress and chemical environment. *Wear* 2015;332–333:662–8. doi:10.1016/j.wear.2015.01.071.
- [13] Brice DA, Samimi P, Ghamarian I, Liu Y, Brice RM, Reidy RF, et al. Oxidation behavior and microstructural decomposition of Ti-6Al-4V and Ti-6Al-4V-1B sheet. *Corrosion Science* 2016;112:338–46. doi:10.1016/j.corsci.2016.07.032.
- [14] Pletinx S, Marcoen K, Trotochaud L, Fockaert L-L, Mol JMC, Head AR, et al. Unravelling the Chemical Influence of Water on the PMMA/Aluminum Oxide Hybrid Interface In Situ. *Scientific Reports* 2017;7:13341. doi:10.1038/s41598-017-13549-z.
- [15] Luxbacher T. *The Zeta Guide Principles of the streaming potential technique*. 2014.
- [16] Quéré D. Rough ideas on wetting. *Physica A: Statistical Mechanics and Its Applications* 2002;313:32–46. doi:10.1016/S0378-4371(02)01033-6.
- [17] Salis A, Boström M, Medda L, Cugia F, Barse B, Parsons DF, et al. Measurements and Theoretical Interpretation of Points of Zero Charge / Potential of BSA Protein. *Langmuir* 2011;27:11597–604.
- [18] Xiao Min H, Carter DC. Atomic structure and chemistry of human serum albumin. *Nature* 1992;358:209–15.
- [19] Meder F, Daberkow T, Treccani L, Wilhelm M, Schowalter M, Rosenauer A, et al. Protein adsorption on colloidal alumina particles functionalized with amino, carboxyl, sulfonate and phosphate groups. *Acta Biomaterialia* 2012;8:1221–9. doi:10.1016/j.actbio.2011.09.014.
- [20] Norde W. My voyage of discovery to proteins in flatland ...and beyond. *Colloids and Surfaces B: Biointerfaces* 2008;61:1–9. doi:10.1016/j.colsurfb.2007.09.029.
- [21] Scholes SC, Unsworth A, Hall RM, Scott R. The effects of material combination and lubricant on the friction of total hip prostheses. *Wear* 2000;241:209–13. doi:10.1016/S0043-1648(00)00377-X.
- [22] Boughton BJ, Simpson AW. The biochemical and functional heterogeneity of circulating human plasma fibronectin. *Biochemical and Biophysical Research Communications* 1984;119:1174–80.
- [23] Galtayries A, Warocquier-Cle´rout R, Nagel M., Marcus P. Fibronectin adsorption on Fe–Cr alloy studied by XPS. *Surface and Interface Analysis: An International Journal Devoted to the Development and Application of Techniques for the Analysis of Surfaces, Interfaces and Thin Films* 2006;38:186–90. doi:10.1002/sia.

- [24] Huang Z, Gengenbach T, Tian J, Shen W, Garnier G. Effect of Bovine Serum Albumin Treatment on the Aging and Activity of Antibodies in Paper Diagnostics. *Frontiers in Chemistry* 2018;6:161. doi:10.3389/fchem.2018.00161.
- [25] Hang R, Ma S, Ji V, Chu PK. Corrosion behavior of NiTi alloy in fetal bovine serum. *Electrochimica Acta* 2010;55:5551–60. doi:10.1016/j.electacta.2010.04.061.
- [26] Das SK, Dickinson C, Lafir F, Brougham DF, Marsili E. Synthesis, characterization and catalytic activity of gold nanoparticles biosynthesized with *Rhizopus oryzae* protein extract. *Green Chemistry* 2012;14:1322–34. doi:10.1039/c2gc16676c.
- [27] John F Moulder, William F Stickle, Peter E Sobol KDB. *Handbook of X-ray photoelectron spectroscopy*. 1995.
- [28] Ahmed M, Byrne JA, McLaughlin J a. D. Glycine Adsorption onto DLC and N-DLC Thin Films Studied by XPS and AFM. *E-Journal of Surface Science and Nanotechnology* 2009;7:217–24. doi:10.1380/ejssnt.2009.217.
- [29] Naumkin AV, Kraut-Vass A, Gaarenstroom SW, Powell C. NIST X-ray Photoelectron Spectroscopy Database 2000. [srdata.nist.gov](http://srdata.nist.gov).
- [30] Soyekwo F, Zhang Q, Zhen L, Ning L, Zhu A, Liu Q. Borate crosslinking of polydopamine grafted carbon nanotubes membranes for protein separation. *Chemical Engineering Journal* 2018;337:110–21. doi:10.1016/j.cej.2017.12.079.
- [31] Kokubo T, Takadama H. How useful is SBF in predicting in vivo bone bioactivity? *Biomaterials* 2006;27:2907–15. doi:10.1016/j.biomaterials.2006.01.017.



## **Chapter 6**

### **Conclusions and future trends**

Summarizing the conclusions, five mixtures of powders were investigated for the boronizing treatment, in order to obtain a uniform boron coating on Ti6Al4V alloy substrate. Only one of them allows to reach the aim. The mixture of powders composed of B, Na<sub>2</sub>B<sub>4</sub>O<sub>7</sub> and activate charcoal leads to the development of a uniform coating composed of TiB and TiB<sub>2</sub>. On the other side, the mixtures of powders containing fluorides result to be too aggressive for titanium substrates, causing corrosion and distortion of the substrate. A strong attachment of salts to the surface without any evidence of formation of the titanium boride layer was observed in case of boriding in liquid phase.

Focusing of different parameters of the treatment, the effects of a range of different temperatures and times were tested. Microstructure of the substrate depends mainly on the temperature of treatment. A treatment at temperature above  $\beta$  transus leads to the development of Widmanstratten microstructure (1050°C) or acicular grains (900°C), while a treatment below  $\beta$  transus causes only growth of grain dimensions (800°C and 750°C). At these low temperatures, variations of time of treatment do not have any significant effect on microstructure of the substrate.

Different pre/post treatments (pre-treatment of deoxidation or oxidation and post thermal treatment) were also tested.

As regard the chemical composition and crystallographic structure of the coatings, in all cases, the coating results to be composed of TiB and TiB<sub>2</sub> phases. XRD analyses show that the intensity of the signals of the borides decreases with temperature, but time of treatment and pre-treatments have no effect on the composition of the coating. A greater fraction of TiB than TiB<sub>2</sub> was detected on samples subjected to post thermal treatment: the post thermal treatment causes a further transformation of the TiB<sub>2</sub> phase in TiB phase.

Moreover, all the coatings have the same multilayer sequence: they are composed by a compact monolithic TiB<sub>2</sub> upper layer and whiskers of TiB penetrating the substrate. The thickness of the coating changes mainly in function of temperature and time of the process. The thickness of the compact layer and the penetration depth of the whiskers are lower for temperatures of process below the  $\beta$  transus temperature. Time of treatment seems to have effect on the coating thickness mainly at the lower temperatures: the thickness decreases with it. XPS analyses, detected also the formation of a thin external surface layer of TiO<sub>2</sub> and B<sub>2</sub>O<sub>3</sub>. Pre-treatment of deoxidation slightly increases the penetration depth of the whiskers for temperatures below the  $\beta$  transus temperature, while post thermal treatment and pre-treatment of oxidation allow to increase the penetration depth of the whiskers.

A consistent increase of hardness is due to the ceramic coating, as expected. Hardness of the samples treated at temperature above the  $\beta$  transus temperature is higher than the one of the samples treated at temperature below it. The difference can be related to the thickness of the coating and the higher influence of the substrate in case of treatment below the  $\beta$  transus temperature. Variation of time of treatment, as well as a pre-treatment of surface oxidation/deoxidation, have no significant effect on hardness. Hardness decreases in the case of post thermal treatment. In this case, the decrement is related to the lower fraction of TiB<sub>2</sub> phase on the surface.

Roughness depends mainly on the borided phase present on surface, there is not a trend in function of temperature and time of treatment. In fact, roughness of the samples subjected to post thermal treatment is slightly higher than the corresponding sample without any pre/post treatment.

Wettability has no correlation with temperature or time of the process, roughness, pre/post treatments and type of boride phase on the surface. All the samples have similar wettability, with an average contact angle of 106°: the surface becomes hydrophobic after the treatment.

Scratch tests indicate that generally the borided coating has a friction coefficient around 0.2, lower than the one of the untreated Ti6Al4V alloy (0.4) and closed to the one of the CoCrMo alloy (0.2), used as reference material. Nevertheless, the adhesion of the coating changes in function of the temperature of treatment. Adhesion is greater at temperatures of treatment above the  $\beta$  transus temperature. Adhesion is higher for coatings with higher thickness and lower roughness. Adhesion of the coating is enhanced when pre-treatment of deoxidation or post thermal treatment increase the penetration depth of the whiskers. While the pre-treatment of oxidation has a negative effect on coating adhesion: hardness and brittleness of the TiO<sub>2</sub> inter-layer cause an early detachment of the coating.

Considering that the borided coating has almost the same chemical composition, structure, wettability and friction coefficient independently from



temperature and time of treatment, the wear/fretting behaviours were evaluated only on the samples treated at the highest temperature and for the longest time without and with pre/post treatments. While, the interaction of the borided surface with biological fluids was performed only on the samples treated at the highest temperature and for the longest time of treatment (without any pre/post treatment).

Focusing on the wear tests, it was observed that, independently from pre/post treatments, in soft on hard contact (coated disk and UHMWPE pin) an abrasive wear of the pin occurs: this is a significant difference with respect to the standard reference materials where adhesive wear is usually detected. While in the hard on hard contact (coated disk and pin), a reciprocal polishing abrasive wear occurs on the disk and pin surfaces. Generally, the wear mechanism of the three treated Ti6Al4V alloys (with different pre/post treatments) can be considered the same.

In fretting tests, the treated samples showed different wear behaviour in comparison to the reference materials (untreated Ti6Al4V alloy and AISI 316L) coupled to PMMA (bone cement). Reference materials show a wear mechanism due to a combination of adhesion and three body abrasion, while the main wear mechanism is abrasion of the borided surface and adhesion of the cement surface in the case of the treated Ti6Al4V alloy. It can be speculated the development of a chemical bond between the borided surface and cement one.

Zeta potential titration curves evidenced the presence of strong acidic functional groups (which can be attributed to OH groups) on the surface of the treated Ti6Al4V alloy (as well as on alumina). As regards the evaluation of protein adsorption, zeta potential analyses show that in all the three cases (albumin solution, fibronectin solution and fetal serum bovine) there is a change of slope of the titration curve and a shift of the isoelectric point to the one of the protein after protein adsorption: the treated Ti6Al4V alloy (as well as the reference untreated Ti6Al4V and CoCrMo alloys) is covered by a surface layer of proteins after soaking. An electrostatic interaction occurs between albumin and the borided surface or alumina, while it is a hydrophobic interaction in the case of the untreated Ti6Al4V and CoCrMo alloys. Fibronectin interacts as a soft protein on the borided surface while as a hard protein on the untreated Ti6Al4V alloy. In the case of fetal serum bovine, the treated Ti6Al4V alloy and the reference materials (untreated Ti6Al4V alloy, alumina and CoCrMo alloy) have a similar trend in the titration curves.

These data were confirmed by XPS analyses, from which can be deduced that ceramic materials (alumina and treated Ti6Al4V alloy) bound albumin through a chemical interaction between the COOH groups of albumin and the OH acidic groups of the ceramic surfaces. Moreover, a B-O-C covalent bond links albumin on the treated Ti6Al4V alloy surface. No difference can be detected by XPS between the adsorption of the treated material and the reference ones in case of fetal serum bovine. XPS analyses confirm that fibronectin interacts strongly with the treated Ti6Al4V alloy, through the COOH groups of the protein, with formation of B-O-C covalent bond (with higher intensity than in the case of BSA) and a small contribution of B-N bond.

A similar amount of adsorbed proteins from fetal serum bovine is also confirmed by BCA assay kit analysis on the treated and untreated Ti6Al4V alloys.

Finally, it was observed that the borided coating has not in vitro bioactive behaviour and thus it is not able to induce osseointegration at 28 days, even if there are acid OH groups on the surface: this factor is not enough to promote the deposition of hydroxyapatite.

Summarizing, the advantages and disadvantages of the boride coating are reported and compared to the ones of the commercial coatings in Table 6.1.

**Table 6.1 Characteristics of the boride coating and commercial coatings**

Technique	Thickness	Hardness	Adhesion	Wear mechanism (hard on soft)	Substrate microstructure
Boronizing below $\beta$ transus temperature	+	+	-	/	No variation of substrate microstructure
Boronizing above $\beta$ transus temperature	++	+++	+	Abrasion of the pin/ No spallation or delamination	Variation of substrate microstructure
Nitriding	+	+	-	Three body abrasion with spallation and delamination	No variation of substrate microstructure
DLC	+	+	-	Three body abrasion with spallation and delamination	No variation of substrate microstructure

According to these observations, some open issues can be identified. Firstly, it is necessary to find a method to polish the coating, in order to reduce roughness: a way can be an electropolishing process. The reduction of roughness can allow to further reduce the friction coefficient and wear rate of the coating.

Secondly, a way to enhance boron diffusion at temperature below beta transus should be identify in order to form a thick coating avoiding to change microstructure of the substrate. As an alternative, long treatments at low temperature can be tested.

Finally, in order to the potential valorisation of the developed coating further tests should be carried out such as: standard fatigue test, specific fatigue test to evaluate the implant - cement interface, mechanical test to compare the mechanical resistance of Ti6Al4V alloy and the one of CoCrMo alloy, dry wear test and biocompatibility test, even if the boride coating does not want to be used directly in contact with bone cells or soft tissues.

Considering the potential of application of the coating, a cemented hip joint implant fully made of Ti6Al4V alloy with a titanium borided coating (head, head–neck taper connection and stem) can be hypothesized. The borided head could induce low wear of UHMWPE (through absence of adhesion wear mechanism, as shown by soft-on-hard wear tests), low wear rate at the neck-head connection could derive from coupling of boride on boride coating (as shown by hard-on-hard wear tests), and a chemical bond of the stem to PMMA (as shown by fretting tests) could reduce the mobilization risk of the stem as well as its damage by fretting. The strong chemical interaction of the boride coating with proteins could ensure a good lubrication of the joint.